Induced interactions between dressed impurities in one-dimensional ultracold quantum gases

Dissertation
zur Erlangung des Doktorgrades
an der Fakultät für Mathematik, Informatik und Naturwissenschaften
Fachbereich Physik
der Universität Hamburg

vorgelegt von

Friethjof Theel

Hamburg

2025

Gutachter/innen der Dissertation:	Prof. Dr. Peter Schmelcher Dr. Thore Posske
Zusammensetzung der Prüfungskommission:	Prof. Dr. Daniela Pfannkuche Prof. Dr. Peter Schmelcher Dr. Thore Posske Prof. Dr. Ludwig Mathey PD Dr. Tim Laarmann
Vorsitzende/r der Prüfungskommission:	Prof. Dr. Daniela Pfannkuche
Datum der Disputation:	03.07.2025
Vorsitzender Fach-Promotionsausschusses PHYSIK:	Prof. Dr. Wolfgang J. Parak
Leiter des Fachbereichs PHYSIK:	Prof. Dr. Markus Drescher
Dekan der Fakultät MIN:	Prof. Dr.-Ing. Norbert Ritter

To my family

Abstract

Quantum gases at ultracold temperatures have been proven over the last three decades to be ideal platforms for studying fundamental aspects of quantum mechanics and many-body systems. The success of this field is primary due to the exquisite experimental control over relevant system parameters. By applying magnetic and electric fields, the atoms can be confined in arbitrary external potential landscapes, and the interatomic interaction is tunable via Fano-Feshbach resonances. The realization of several species of atoms or different hyperfine states of the same isotope expands the number of adjustable parameters and opens up the possibility to explore highly particle-imbalanced ultracold mixtures, which is the main subject of this dissertation. In these systems, a majority species is coupled to a minority one consisting of impurity atoms that can become dressed by the excitations of the majority species. This gives rise to the notation of quasi-particles such as polarons. An intriguing aspect is the possibility to intuitively understand the properties and microscopic mechanisms of the dressed impurities in terms of simple few-body models, while the overall system remains essentially many-body.

We focus on the static and dynamical properties of impurities immersed into an ultracold bosonic gas in one dimension. The first publication investigates the counterflow dynamics of two bosonic impurities confined in a double-well potential and coupled to a majority species trapped in either a box or harmonic oscillator potential. We classify the emerging two-body correlation patterns and extract the ensuing phase diagram, which highly depends on the interspecies and impurity-impurity coupling parameters as well as the underlying trapping potential of the medium. For repulsive or attractive interspecies coupling strengths the medium induces a bunching behavior between the impurities such that at strong attractions we find signatures of a bound state among the impurities signaling the formation of a bipolaron. The bunching behavior can be converted into an anti-bunching tendency by increasing the repulsion between impurities, in this way, overcoming the effects of the induced attraction. To trigger the counterflow between the impurities, the central barrier of the double-well potential is ramped down. For a box confined medium, in a region where the induced attraction dominates the internal impurity-impurity repulsion, the impurities collide at the trap center where they remain localized. However, in case of a harmonically confined medium, the impurities perform a periodic oscillation and at large impurity-medium repulsions they are expelled from the trap center.

Inspired by the tunability of the induced impurity-impurity correlation patterns, the next three works investigate in more detail the mediated interactions between the impurities. In the first work of this series, we consider two distinguishable and non-interacting impurities coupled to a harmonically confined bosonic gas. This setup features two impurity-medium coupling parameters that can be tuned individually. Exploiting this flexibility, we find an anti-bunching tendency emerging in the two-body correlation function if one impurity attracts the medium and the other repels it. When both impurities couple with the same sign to the majority species, the expected bunching behavior between the impurities is recovered. Importantly, the mediation of an anti-bunching behavior in such settings is reserved to mixtures with three or more components and, therefore, is absent in binary mixtures. By constructing an effective two-body model, which approximates the induced interaction between the mobile impurities in terms of a contact interaction potential, we are able, for the first time, to associate the anti-bunching behavior with an effective repulsive interaction and the induced bunching behavior with an effective attraction. Moreover, we study the formation of a dimer and trimer state in the strongly attractive regime by inspecting three-body correlation functions. In a subsequent work, we investigate the dynamical response of the impurities by linearly ramping the impurity-medium interaction parameters in time. In this course, we devise effective one- and two-body models in order to gain an intuitive understanding of the induced interplay between the impurities. First, we focus on the effective description of the dynamics of one impurity. We find the best agreement with the emergent many-body dynamics for a model consisting of a time-dependent effective mass and trap frequency. These time-dependent effective parameters are determined by an optimization process which enables the model to account even for temporal effects imprinted by impurity-medium correlations. Building on the success of the effective one-body model, we simulate the induced interplay between two impurities with different types of effective two-body models. The best agreement with the two-body correlation function of a many-body approach achieves the two-body model which includes a time-dependent contact interaction potential with an optimized interaction strength. Evaluating the evolution of the effective interaction strength, we are able to track the crossover from an induced attraction to an induced repulsion and vice versa. Importantly, this study provides a stepping stone for the effective description of the many-body dynamics of impurities by relying on time-dependent parameters rather than static ones. Instead of quantifying the induced interactions between the impurities in terms of two-body correlation functions, in another study, we pursue a different direction and interpret the induced interactions in the context of bipolaron and three-polaron energies. The system under investigation consists of up to three impurity atoms confined in a tilted double-well potential and coupled to a bosonic gas on a ring potential. The effective two- and three-body interaction parameters are determined by fitting the energies of the respective two- and three-body models to the polaron energies obtained within a many-body approach. Remarkably, we are able to explicate the presence of mediated two- and three-body interactions by measuring the impurities' density population at the energetically elevated well. The many-body results of the above mentioned studies are obtained by the *ab initio* multi-layer multi-configuration time-dependent Hartree method for atomic mixtures.

Ultracold quantum gases not only offer the possibility to study imbalanced particle mixtures, but also allow us to gain insights into other fascinating models such as the Anyon-Hubbard model, to which the final work of this dissertation is dedicated. We consider particles with anyonic exchange statistics distributed on a finite lattice with open boundary conditions. In the absence of on-site interactions the eigenspectrum exhibits a degenerated zero-energy subspace with chiral symmetry that is even preserved under variations of the statistical angle. We demonstrate that the chiral symmetry is responsible for the emergence of a checkerboard pattern in the experimentally accessible one-body density. Next, we adiabatically evolve the zero-energy subspace while cyclically tuning the statistical parameter from a value corresponding to Bose statistics to a value associated with pseudo-fermions and back to Bose statistics. We find that this loop in control space produces nontrivial Berry phases and holonomy matrices. Finally, we provide a protocol to steer any initial number state into the zero-energy subspace only by temporally varying the statistical parameter.

Zusammenfassung

Quantengase im ultrakalten Temperaturbereich haben sich in den letzten Jahrzehnten als ideale Plattformen für die Untersuchung von grundlegenden Aspekten der Quantenmechanik sowie von Vielteilchensystemen erwiesen. Der Erfolg dieses Wissenschaftszweigs kann in erster Linie auf die exquisite experimentelle Kontrolle der relevanten Systemparameter zurückgeführt werden. Durch die Anwendung von magnetischen und elektrischen Feldern können die Atome in beliebigen externen Potentialen gefangen werden. Weiterhin sind die interatomaren Wechselwirkungen mittels Fano-Feshbach-Resonanzen regulierbar. Das Einfangen mehrerer atomarer Spezies ermöglicht es zudem Mischungen von Quantengasen zu erzeugen, welche sich stark in ihrer Teilchenzahl unterscheiden. Letzteres stellt das Hauptthema dieser Dissertation dar. In diesen Systemen ist eine größere Spezies an eine Spezies mit wenigen Teilchen gekoppelt, welche aus Fremdatomen besteht. Ein einzelnes Fremdatom zusammen mit den Anregungen der größeren Spezies kann als Quasiteilchen verstanden werden, welches auch Polaron genannt wird. Ein faszinierender Aspekt besteht hierin aus der Möglichkeit, die Eigenschaften und mikroskopischen Mechanismen der Quasiteilchen mit Hilfe von vereinfachten Modellen intuitiv zu verstehen, während das gesamte System im Wesentlichen ein Vielteilchenproblem bleibt.

In der ersten Publikation wird die Dynamik zweier bosonischer Fremdatome in einem Doppeltopfpotential untersucht. Die beiden Atome sind mit einer bosonischen Majoritätsspezies gekoppelt, welches sich entweder in einem eindimensionalen Kasten- oder harmonischen Oszillatorpotential befindet. In Abhängigkeit von den Wechselwirkungsstärken zwischen den Fremdatomen, sowie zwischen der Majoritätsspezies und den Fremdatomen, wird ein Phasendiagramm erstellt, das die Zweiteilchendichte bezüglich ihrer Korrelationsmuster klassifiziert. Bei abstoßenden oder anziehenden Kopplungsstärken zwischen den beiden Spezies, induziert die Majoritätsspezies eine attraktive Wechselwirkung zwischen den beiden Fremdatomen, welches zu einer Ballung in der Zweiteilchendichte führt. Bei starken Wechselwirkungen sorgt die induzierte Anziehung für die Formation eines gebundenen Zustands, dem Bipolaron. Wird die Abstoßung zwischen den Fremdatomen erhöht, kann das Korrelationsmuster der Zweiteilchendichte in ein anti-korreliertes Muster überführt werden. Um das System in einen dynamischen Zustand zu versetzen, wird die zentrale Barriere des Doppeltopfpotentials heruntergefahren. In einem Bereich, in dem die induzierte Anziehung überwiegt, kollidieren die beiden Fremdatome in der Mitte des Potentials, wo sie im weiteren Zeitverlauf lokalisiert bleiben. Im Falle einer harmonisch eingeschlossenen Majoritätsspezies und für geringe Wechselwirkungsstärken führt das Verringern der Barriere zu einer periodischen Oszillation der Fremdatome, die für großen Abstoßungen in eine Phasenseparation übergeht.

Inspiriert durch die Möglichkeit, die Korrelationsmuster der Fremdatome mittels Wechselwirkungsparameter zu kontrollieren, konzentrieren sich die nächsten drei Arbeiten auf die explizite Quantifizierung der zugrunde liegenden induzierten Wechselwirkung. In der ersten Arbeit dieser Reihe werden zwei unterscheidbare und nicht wechselwirkende Fremdatome untersucht, welche an eine harmonisch eingeschlossene Majoritätsspezies gekoppelt sind. Eine Besonderheit ist, dass die Kopplungsstärken der beiden Fremdatome individuell eingestellt werden können. Diese Flexibilität ermöglicht es, ein Fremdatom attraktiv an die Majoritätsspezies koppeln zu lassen, während das andere Fremdatom Letztere abstößt, welches schlussendlich zu einem anti-korrelierten Muster in der Zweiteilchen-Korrelationsfunktion führt. Sobald beide Fremdatome mit dem gleichen Vorzeichen an die Majoritätsspezies koppeln, zeigt das Korrelationsmuster wieder das bekannte Ballungsverhalten auf. Der Kern dieser Arbeit besteht darin, mithilfe eines effektiven Zweiteilchenmodells die Korrelationsmuster mit einer induzierten attraktiven und abstoßenden Wechselwirkung in Verbindung zu bringen. Darüber hinaus wird die Bildung eines Dimer- und Trimerzustandes im stark anziehenden Bereich unter Zuhilfenahme der Dreiteilchen-Korrelationsfunktionen untersucht.

Aufbauend auf diesen Erkenntnissen widmet sich die nächste Arbeit dem dynamischen Fall. Die Dynamik wird durch eine zeitlich lineare Veränderung der Wechselwirkungsparameter hervorgerufen. Für ein intuitives Verständnis werden entsprechende Ein- und Zweiteilchenmodelle entwickelt und miteinander verglichen. Das Einteilchenmodel, welches die beste Übereinstimmung mit den Resultaten einer Vielteilchenmethode erlangt, besteht aus einer zeitabhängigen effektiven Masse und Fallenfrequenz. Die beiden effektiven Parameter entstammen einem Optimierungsprozess, das in der Lage ist, jene zeitlichen Effekte mit zu berücksichtigen, welche von Korrelationen zwischen dem Fremdatom und der Majoritätsspezies hervorgerufen werden. In einer ähnlichen Weise wird das induzierte Wechselspiel zwischen den beiden Fremdatomen mit einem effektiven Zweiteilchenmodell bestimmt. Dafür werden zwei Einteilchenmodelle mit einem zeitabhängigen Kontaktwechselwirkungspotential miteinander verbunden. Die entsprechende zeitabhängige Wechselwirkungsstärke ergibt sich aus einer Optimierung bezüglich der Zweiteilchen-Korrelationsfunktion. Angewandt auf verschiedene dynamische Systeme, konnte mittels des effektiven Zweiteilchenmodells der Übergang von einer induzierten Anziehung hin zu einer induzierten Abstoßung beobachtet werden, sowie der umgekehrte Fall. Insbesondere liefert die Vorgehensweise, in welcher die Dynamik der Quasiteilchen im Sinne von zeitabhängigen effektiven Parametern modelliert wird, einen neues Werkzeug für das intuitive Verständnis solcher Systeme.

Die dritte Studie erforscht eine alternative Methode zur Bestimmung der induzierten Wechselwirkung. Anstatt Letztere auf der Grundlage von Zweiteilchen-Korrelationsfunktionen zu quantifizieren, wie in den beiden vorherigen Studien getan, basiert in dieser Arbeit ihre Spezifizierung auf den Polaronenergien. Das zu untersuchende System besteht aus bis zu drei Fremdatomen, welche in einem gekippten Doppeltopfpotential eingeschlossen und an ein bosonisches Gas in einem Ringpotential gekoppelt sind. Das effektive Verhalten der Fremdatome wird mit entsprechenden Zwei- und Dreiteilchenmodellen erfasst, wobei die jeweiligen Zwei- und Dreiteilchen-Wechselwirkungsparameter so justiert werden, dass die effektiven Modelle den Polaronenergien entsprechen. Letztere werden mittels eines Vielteilchenmodells bestimmt. Des Weiteren erlaubt das gekippte Doppeltopfpotential den Einfluss der induzierten Wechselwirkungen auf die Einteilchendichte der Fremdatome zu messen. Die Berechnungen der Vielteilchenmodelle der oben erwähnten Studien werden mit der Multi-Layer Multi-Configuration Time-Dependent Hartree-Methode für atomare Mischungen durchgeführt.

Ultrakalte Quantengase bieten nicht nur die Möglichkeit, Michungen mit stark variierender Teilchenzahl zu untersuchen, sondern erlauben auch Einblicke in andere faszinierende Modelle, wie z.B. das Anyon-Hubbard-Modell, welches Gegenstand der letzten Arbeit dieser Dissertation ist. Insbesondere werden Teilchen mit anyonischer Vertauschungsrelation betrachtet, welche in einem Gitterpotential mit offenen Randbedingungen gefangen sind. Für den Fall, dass die Teilchen nur über einen dichteabhängigen Kopplungsterm miteinander wechselwirken, weist das Eigenspektrum einen entarteten Unterraum auf, welcher aus Eigenzustände mit verschwindender Eigenenergie besteht. Es stellt sich heraus, dass die Eigenzustände in diesem Unterraum eine chiralen Symmetrie beitzen, welche erhalten bleibt, auch wenn der statistische Parameter variiert wird. Zudem führt die chirale Symmetrie zu einem Schachbrettmuster innerhalb der Einteilchenkorrelationsfunktion. Eine weitere interessante Eigenschaft des Unterraums ist die Realisierung von nicht-trivialen Berry-Phasen und Holonomiematrizen, welche aus einer adiabatische Entwicklung des Unterraums hervorgehen. Während dieser Entwicklung durchläuft der statistische Parameter einen Zyklus vom bosonischen zum pseudo-fermionischen und wieder zurück zum bosonischen Fall. Im letzten Schritt dieser Arbeit wird ein Protokoll vorgestellt, welches in der Lage ist, nur mithilfe von Variationen des statistischen Parameters einen simplen Anfangszustand in einen Eigenzustand mit verschwindender Energie zu überführen.

Contents

List of Abbreviations

BEC	**B**ose **E**instein **C**ondensate
DOF	**D**egree **O**f **F**reedom
EOM	**E**quation **O**f **M**otion
DVR	**D**iscrete **V**ariable **R**epresentation
FBR	**F**inite **B**asis-set **R**epresentation
LAPACK	**L**inear **A**lgebra **PACK**age
SPF	**S**ingle-**P**article **F**unction
MCTDH(B)	**M**ulti-**C**onfiguration **T**ime-**D**ependent **H**artree method (for **B**osonic particles)
ML-MCTDHX	**M**ulti-**L**ayer **M**ulti-**C**onfiguration **T**ime-**D**ependent **H**artree method for mi**X**tures
PPT	**P**ositive **P**artial **T**ranspose
MB	**M**any **B**ody
sMF	**s**pecies **M**ean-**F**ield

Preface

This cumulative thesis is based on the publications Refs. [FT1–FT5] listed below.

Publications covered by this thesis

[FT1] F. Theel, S. I. Mistakidis, K. Keiler, and P. Schmelcher, "Counterflow dynamics of two correlated impurities immersed in a bosonic gas", Phys. Rev. A **105**, 053314 (2022).

[FT2] F. Theel, S. I. Mistakidis, and P. Schmelcher, "Crossover from attractive to repulsive induced interactions and bound states of two distinguishable Bose polarons", SciPost Phys. **16**, 023 (2024).

[FT3] F. Theel, S. I. Mistakidis, and P. Schmelcher, "Effective approaches to the dynamical properties of two distinguishable Bose polarons", Phys. Rev. A **111**, 013306 (2025).

[FT4] F. Theel, A. G. Volosniev, D. Diplaris, F. Brauneis, S. I. Mistakidis, and P. Schmelcher, "Effective two- and three-body interactions between dressed impurities in a tilted double-well potential", `10.48550/arXiv.2503.20624` (2025), preprint, submitted to Phys. Rev. Research.

[FT5] F. Theel, M. Bonkhoff, P. Schmelcher, T. Posske, and N. L. Harshman, "Chirally-protected state manipulation by tuning one-dimensional statistics", `10.48550/arXiv.2412.01517` (2024), preprint, submitted to Phys. Rev. Lett.

Further publications

[FT6] F. Theel, A. Karamatskou, and R. Santra, "The fractal geometry of Hartree-Fock", Chaos **27**, 123103 (2017).

[FT7] F. Theel, K. Keiler, S. I. Mistakidis, and P. Schmelcher, "Entanglement-assisted tunneling dynamics of impurities in a double well immersed in a bath of lattice trapped bosons", New J. Phys. **22**, 023027 (2020).

[FT8] F. Theel, K. Keiler, S. I. Mistakidis, and P. Schmelcher, "Many-body collisional dynamics of impurities injected into a double-well trapped Bose-Einstein condensate", Phys. Rev. Research **3**, 023068 (2021).

Declaration of personal contributions to the publications

The idea for the project [FT1] emerged from Dr. Kevin Keiler and Prof. Dr. Simeon I. Mistakidis. The numerical calculation and analysis was done entirely by myself. I generated the first draft of the paper which Prof. Dr. Simeon I. Mistakidis revised. Dr. Kevin Keiler participated in the discussions during the first half of the project.

The main findings of the publication [FT2] evolved during the research process and were not foreseen at the beginning of this project. The numerical calculation as well as the analysis was done entirely by myself. I devised the effective models and implemented the major part of the analysis tools. During the project Prof. Dr. Simeon I. Mistakidis and I had regular meetings in which we discussed the recent progress and planned the next steps. I wrote the manuscript myself, which has been significantly revised and improved by Prof. Dr. Simeon I. Mistakidis.

The work [FT3] is a follow-up project of the work [FT2]. The numerical calculations as well as the implementation of the time-dependent effective one- and two-body models were done by myself. I wrote the manuscript, which has subsequently been revised and optimized by Prof. Dr. Simeon I. Mistakidis. During the process I had regular meetings with Prof. Dr. Simeon I. Mistakidis.

The publication [FT4] was triggered by a conservation with Dr. Fabian Brauneis, Prof. Dr. Artem Volosniev and Prof. Dr. Simeon I. Mistakidis. M.Sc. Dimitrios Diplaris joined the project when we had settled on the setup considered in Ref. [FT4]. M.Sc. Dimitrios Diplaris has performed the mean-field and many-body calculations, which I have analyzed. In particular, we stayed in close contact almost on a daily basis. The codes for the analysis tools have been developed by me, which includes also the effective two- and three-body models. I devised all figures and wrote the results part of the manuscript as well as the majority of the appendices. In general, all of the above-named authors significantly contributed to the writing and revising process of the manuscript and have participated in weekly meetings.

The project [FT5] has been initiated by Dr. Thore Posske. Together with Prof. Dr. Nathan L. Harshman and Dr. Martin Bonkhoff, we worked out in a collaborative effort the main results of the work and discussed the progress in regular meetings. Prof. Dr. Nathan L. Harshman, Dr. Martin Bonkhoff and Dr. Thore Posske devised the concept of the work, while I contributed the numerical simulations. In this course, I devised the computer program which solves the anyon-Hubbard model via exact diagonalization and implemented all observables. The manuscript has been written mainly by Prof. Dr. Nathan L. Harshman and Dr. Martin Bonkhoff. I devised all figures and wrote the parts concerning the implementation, the adiabatic evolution, as well as, the steering protocol. Dr. Thore Posske revised and optimized the manuscript.

In all cases Prof. Dr. Peter Schmelcher supervised the research progress, took part in the discussions and contributed to the revision of the manuscripts.

Outline of this thesis

The present dissertation is organized as follows. Chapter 1 gives a short overview of the field of ultracold atoms with the emphasis on impurity physics. It concludes with remarks on the recent progress made in terms of the one-dimensional anyon-Hubbard model. In Chapter 2, the basic experimental concepts inherent in ultracold quantum gases are introduced. In Chapter 3 the focus is set on the theoretical description of one and two impurities immersed into a bosonic medium and a selection of the commonly used effective models is discussed. Chapter 4 introduces the numerical methods employed to treat the many-body systems considered in this thesis. In particular, we elaborate on the exact diagonalization method and the multi-configuration time-dependent Hartree method as well as its multi-layered variant. Since the many-body methods outlined Chapter 4 are intended to capture all relevant correlations present in a system, it is important to quantify and classify them. Therefore, Chapter 5 is devoted to the quantification of the interparticle as well as interspecies correlations and introduces the methods applied in the framework of this thesis. In Chapter 6 we give a brief overview of the one-dimensional anyon-Hubbard model. In Chapter 7 we outline the scientific contributions which are subsequently presented in Chapter 8. Finally, we summarize in Chapter 9 the results and provide an outlook to further research possibilities.

Chapter 1

Introduction

Since the first realization of a Bose-Einstein condensate (BEC) in 1995 [1, 2], the field of ultracold quantum gases has experienced a rapid growth boasting experimental and theoretical advances. A major contribution to the success of this field lies in the unprecedented experimental control of ultracold quantum gas parameters, rendering them the most suitable testbeds to emulate a plethora of quantum many-body phenomena. Specifically, it is nowadays possible to tune continuously the interaction strength between the individual atoms by manipulating their scattering length optically [3, 4] or magnetically [4–6]. For instance, tuning the interatomic interaction strength toward the strongly attractive regime, two atoms can bind and form Feshbach molecules [4, 6–8]. Apart from having access to the internal degrees of freedom (DOFs) of ultracold gases, it is also possible to externally trap the atoms in optical potentials and even restrict their motion to one or two spatial dimensions [9–11]. These features add extra flexibility and allow the systematic study of a variety of complex setups such as box [12] and double-well potentials [13–16], lattice structures [17, 18] or any other arbitrary static or dynamically varying potentials [19]. In addition, by exploiting different kinds of trapping techniques experimentalists have attained control over the number of participating particles and paved the way for a detailed study of few-body systems [15, 20–24]. In this sense, using Pauli's exclusion principle, the number of trapped fermions can be controlled by lowering the threshold of the external potential so that only a precise number of atoms are realized [22]. A similar technique has been applied to study the crossover from a few- to many-body system by successively adding fermions to an impurity in order to observe the formation of a Fermi sea [23]. Other methods to enter the few particle regime consists of trapping individual atoms in optical tweezer arrays [15, 25, 26]. In such setups, the tunneling behavior of two atoms in an effective double-well trap has been studied by bringing two optical tweezers close to each other and allowing the single-particle functions to overlap [15]. In such setups, the entanglement between the atoms can be controlled by employing a time-dependent protocol [25]. These developments in terms of experimental control render the platforms of ultracold quantum gases the most favorable and promising candidates for quantum simulation. The implementation of disparate physical models in ultracold quantum simulators allows to gain insights into previously elusive properties [10, 27, 28]. For example, ultracold atoms in optical lattices can mimic condensed matter systems [29–31] such as Hubbard models [32, 33] as well as reveal the existence of exotic phases, e.g., supersolid states [34–36] or even explore lattice gauge theories [37, 38].

Moreover, ultracold quantum gases are intriguing platforms on their own since they can provide for insights into fundamental aspects of quantum mechanics. Some of the earliest experiments after the first realization of a BEC were devoted to the investigation of collective excited states such as dipole-like and breathing-like motions [39, 40], or the generation of dark [41–43] and bright solitons [44, 45], where the latter corresponds to spatially localized excitations appearing either as density dips (accompanied by a phase jump) or humps [46]. Since a BEC can inherit properties of a superfluid, quantized topological vortices may emerge in rotating gases [40, 46] which can be generated by optically modulating the external confining potential to induce a rotation into the BEC [47, 48] or by spatially merging three independent BECs together [49]. The emergence of vortices has been utilized in order to demonstrate the presence of superfluidity in a paired fermionic gas [50].

Another fruitful research direction arises when adding more complex optical confining potentials to the system, e.g., an optical lattice. Here, the underlying idea is to understand phenomena appearing in condensed matter physics from the perspective of a highly controllable ultracold setup [51, 52]. The simplest variant of a lattice potential consists of two sites, forming a double-well potential [24, 53–59]. Such setups allow the realization of a Josephson junction, i.e., the back and forth oscillation of ultracold particles from one site to the other, or a macroscopic self-trapping behavior at one site. The transition between these regimes can be controlled by tuning the interparticle interaction strength and the initial population imbalance regarding the wells [13]. Additionally, a maximally entangled Bell state has been generated by optimally ramping up the potential barrier of the double-well [60]. Experimentally, extending the double-well potential to a periodic lattice is usually done by superimposing two counter-propagating laser beams, which realizes another intriguing branch in ultracold quantum physics [10, 52, 61]. The ground-state and dynamics of ultracold atoms in optical lattices are well described by the Bose-Hubbard model which assumes nearest-neighbor hopping and on-site interactions [29, 62]. The ratio between the hopping amplitude and the interaction strength determines whether the particles correspond to a superfluid (dominant hopping term) or a Mott-insulator (dominant interaction term). The respective transition between a Mott-insulator and a superfluid has been experimentally demonstrated in three- [63], two- [64, 65] and one-dimensional setups [66]. Other studies investigated the formation of a Tonks-Girardeau gas [67], the pairing of fermions [68] or more exotic superfluid phases in higher bands [69, 70]. Adding disorder to a lattice leads to fundamental changes in the transport and correlation properties of the trapped atoms. For instance, in the non-interacting case disorder leads to the localization of the wave-packet, the so-called Anderson localization [71, 72], while for interacting particles many-body localized states emerge [73]. An example denotes the so-called Bose glass which is a many-body localized state lying in between the usual superfluid and Mott-insulating phases in a disordered system [74, 75].

So far, we have provided a glimpse of the intriguing physics inherent in one-component ultracold setups. However, going beyond this, the study of multi-component ultracold quantum gases promises an even richer phenomenology [11, 76, 77]. In such setups two or more atomic species are simultaneously trapped in the same or different external potentials and interact with each other [78–82]. Experimentally, two-component Bose-Bose [16, 83–85], Bose-Fermi [86, 87] and Fermi-Fermi [50, 88] mixtures have been realized. In such setups, a two-component mixture can be prepared by transferring a fraction of an ultracold gas into a different hyperfine state via a radio-frequency pulse [16, 50, 88, 89] or by simultaneously trapping two different atomic elements such as ^{41}K and ^{87}Rb atoms [80, 83, 85], ^{6}Li and ^{23}Na atoms [86] or ^{6}Li and ^{133}Cs atoms [87]. Specifically, the addition of another atomic component extends the experimentally available parameter space which, for instance, includes the number of tunable interaction parameters. Depending on the inter- and intraspecies repulsion different kinds of miscible and immiscible phases can be realized [90, 91], such as composite fermionization [92, 93] or full fermionization [94]. In the case of attractively coupled mixtures, the components can form a self-bound quantum droplets [95, 96]. These objects owe their existence to competing effects between inter-component attractive and internal repulsive forces [97, 98]. One of the most fascinating properties of quantum droplets is the necessity to incorporate higher-order correlation effects, such as the Lee-Huang-Yang correction [99], in order to maintain these many-body self-bound states, making them pure quantum objects. Experimentally, quantum droplets have been observed in Bose-Bose mixtures [100, 101] and theoretically studied, e.g., in terms of their dynamical properties [102–104], within optical lattices [105, 106] or in the presence of three-body interactions [107]. Other ways of exploiting the increased complexity of a two-component mixture include the generation of different kinds of solitons such as dark-dark [108], dark-bright [109–111] or dark-antidark solitons [112, 113] as well as the spatially and temporally localized Peregrine soliton which belongs to the rouge wave family [114, 115].

In multi-component systems, a major focus has been placed on highly particle-number imbalanced mixtures, where a minority species of impurity atoms is embedded in a majority component. In the extreme case, a single impurity atom is coupled to an ultracold host and can become dressed by the excitations of the latter. The dressed impurity gives then rise to a quasi-particle, i.e., a polaron [11, 116–119]. Experimentally, Bose [85, 120–122] and Fermi [82, 88, 123, 124] polarons, i.e. dressed impurities interacting with either a bosonic or a fermionic environment, respectively, have been realized in mass-balanced [88, 120] or mass-imbalanced [82, 85] setups. These studies, for instance, provided evidences for an increased effective mass of ^{41}K impurities immersed into a bosonic gas of ^{87}Rb atoms [85] or, in a three-dimensional setup, allowed to study the attractive and repulsive polaron branch as well as the lifetime of the respective quasi-particle [120]. Moreover, finite temperature effects on the polaronic properties were studied in terms of ^{40}K impurities immersed into a ^{23}Na BEC where the breakdown of the quasi-particle picture has been observed near the critical temperature of the BEC [122]. In other experiments where impurities coupled are coupled to an ultracold gas [125, 126] investigated the motion of the impurities through a strongly interacting Bose gas [89, 127], the bath-induced decoherence effects on the impurities [86] or the possibility to extract information about the bath from internal impurity states [128]. In another experiment consisting of a ^{41}K impurity confined in an optical tweezer and immersed into a cloud of ultracold ^{87}Rb atoms, the control over the impurity's position as well as over the impurity-medium interaction strength has been demonstrated [129].

On the theoretical side, the Bose polaron problem in three dimensions is adequately described by the Fröhlich model assuming a weakly interacting impurity [119, 130, 131]. However, for strong impurity-medium interactions, i.e. in the vicinity of a Feshbach resonance, the Fröhlich model looses its validity and more sophisticated approaches are required [132–135], e.g., perturbative methods [136, 137] or field theoretical approaches [138]. Particular focus has been put on the polaron spectrum, which exhibits a repulsive and an attractive branch. In the strong coupling regime, the attractive branch is expected to evolve into a molecular dimer state [120, 121, 138, 139]. However, a more recent work based on a variational scheme suggests additional many-body bound states to emerge in the attractive branch [140].

In one-dimensional setups, the problem of an impurity coupled to a weakly interacting bath has been extensively studied in term of homogeneous potentials [130, 141–150]. In this course, various numerical approaches have been applied including analytical techniques [146], Monte Carlo calculations [143, 144] and mean-field [141, 142, 146–150] as well as beyond mean-field [149] approaches. These endeavors have led to the characterization of the effective mass and residue of the dressed impurity [143, 145] as well as to a profound knowledge of the impurity's self-trapping behavior [85, 130, 141, 148, 149, 151]. The situation becomes more involved when considering additional trapping geometries or when triggering the dynamics. Especially, in the dynamical case interparticle correlations are expected to have an increased impact [11]. For example, in a system where an impurity performs an oscillatory motion within a harmonically trapped bosonic gas, the presence of interspecies correlations leads to an accelerated energy transfer from the impurity to its host [152]. Other works studied the impact of correlations on the motion of an impurity in terms of a harmonic confinement [153], a double-well [FT7, FT8, 154, 155] or lattice potential [156–159]. In general, external confining potentials can crucially affect the emergent dynamics, trigger dipole-like [152] or dissipative motions [153] of the impurity and even lead to temporal orthogonality catastrophe events [160]. The latter emerge in the strongly repulsive regime and are characterized by a vanishing residue of the impurity.

Increasing the number of impurities interacting with a bosonic medium gives rise to intriguing phenomena which are not present in the single-impurity case. For example, in one-dimensional setups the medium can induce an attractive interaction between the impurities given that they couple with the same sign to their host, i.e., the impurities are either both attractively or repulsively coupled to the medium [161–173]. In the strong coupling regime, this mediated attraction leads to the formation of a bound state, the so-called bipolaron [150, 174–176]. The shape of the induced interaction potential takes, for impurity-impurity distances smaller than the healing length of the bath, the form of a Yukawa-type potential [150, 161, 162, 167, 168]. At large impurity separations, quantum fluctuations are the dominant mediator of the induced interaction and give rise to a Casimir-type interaction [167, 177]. However, the relevance of the latter is still under debate since the impact of the Cassimere-type interaction turns out to be comparatively small [150, 170]. In Ref. [170] it has been shown that the mediated interaction can be adequately modeled by a contact interaction potential with a strength derived from mean-field arguments. On the other hand, models based on a mean-field description fail to predict the entanglement entropy between the impurities [170]. Similarly, in Ref. [178] it was shown that also beyond mean-field effects lead to an induced interaction.

The presence of an external harmonic confinement has an additional impact on the mediated interaction between the impurities and leads, e.g., in the case of strong interactions, to the coalescence of the impurities at the edges of the bath [165, 169]. Besides the mediation of an induced interaction, the majority species can also influence the transport and correlation properties of the impurities confined in a lattice potential [156, 157, 179] or impact the impurities' localization behavior in the presence of a harmonic external potential [169]. In Ref. [FT1] we have continued the ongoing research of impurity physics and studied the counterflow of two atoms in the presence of a superimposed bosonic medium. In this sense, our work combines the idea of colliding ultracold particles [180–184] within the concept of dressed impurities. Specifically, we study the impact of an induced attraction on the dynamical behavior of the colliding impurities, which turns out to be strongly dependent on the applied interaction parameters as well as on the particular external trapping potential. In general, collisions of ultracold particles are an intriguing branch of ultracold physics since the out-of-equilibrium dynamics can offer additional insights into the structure of the many-body wave function which, in the static case, is otherwise hidden. Experimentally, such collision processes can be induced by first spatially separating atoms in a harmonic trap according to different hyperfine states and, subsequently, letting the separated atoms collide in the trap center. In the corresponding experiment, this protocol led to the formation of dark-bright soliton trains [185]. An alternative approach consists of trapping two ultracold ensembles in two spatially separated external potentials and letting the traps collide [FT8, 182–184, 186]. A similar approach is to prepare an ultracold gas in a double-well potential and ramping down the central barrier to initiate the counterflow dynamics [180, 181, 187] leading to the formation of dark solitons [181].

An additional research direction beyond the field of one- and two-component ultracold quantum gases, which has recently gained more attention, refers to three-component mixtures. Experimentally, triple mixtures have already been realized in terms of Bose-Fermi-Fermi mixtures which consist of bosonic ^{87}Rb and fermionic ^{6}Li and ^{40}K atoms [79] or with bosonic ^{41}K and fermionic ^{40}K and ^{6}Li atoms [82], where in these experiments the third species mainly served as a sympathetic coolant in order to reach degeneracy. Besides the creation of ultracold hetero-nuclear mixtures, it is also possible to create a three-component mixture by populating different hyperfine states, e.g., as reported in Refs. [188, 189]. In these experiments, three hyperfine levels of ^{87}Rb have been populated in order to study dark-bright-bright and dark-dark-bright solitons [188] or the collision of two vector solitons [189]. On the theoretical side, the focus has been mainly on the study of the interplay between impurities coupled to a Bose-Bose mixtures in various setups [190–195]. For instance, the two-component host has been subjected to a harmonic confinement [191, 193], a double-well [194] and lattice potential [196], or has formed a two-component quantum droplet [192, 197]. In the case of particle balanced three-component mixtures, the formation of a shell-shaped droplet has been predicted [198, 199] as well as a plethora of different phases beyond the two-component paradigm [200].

Other highly unexplored three-component mixture settings are represented by two distinguishable impurities interacting with a bosonic gas [201–203]. This setup is fundamentally different from the related two-component scenario in the sense that the impurities can couple with distinct interaction strengths to the majority species, i.e., one impurity may be attractively coupled to the bosonic medium while the other repels it. This is an important feature, since this interaction configuration facilitates a mediated repulsive interaction between the impurities [167, 168, 177, 202] and, therefore, goes beyond the induced attractive behavior observed in two-component setups. Signatures of the repulsive character of the mediated interaction have been found in terms of two static impurities with an infinite mass confined on a ring potential within a flow equation approach [202]. In particular, one impurity has been considered to repel the bath with an infinite interaction strength while the other impurity attracts the medium. However, the implications of the induced repulsion and attraction on the behavior of mobile impurities, as well as the role of interparticle correlations on the induced interplay, have remained elusive. In Ref. [FT2] we aim at filling this gap and study the ground state behavior of two distinguishable impurities with finite mass coupled to a bosonic medium. By devising an effective two-body model we quantify the induced attraction and repulsion between the impurities and make the connection to the induced pattern appearing in the two-body correlation function. We base our analysis on many-body calculations obtained by the *ab initio* multi-layer multi-configuration time-dependent Hartree method for atomic mixtures (ML-MCTDHX) [204–206]. This method is capable of taking all relevant inter- and intraspecies correlations into account and provides to access the underlying many-body wave function of the system. In Ref. [FT3], we build on the findings made in [FT2] and study the dynamical response of the impurities upon linearly ramping their interaction strengths to the medium in time. In previous studies, the effective description of the impurities' dynamical response has been restricted to static effective parameters, which has limited the applicability to small impurity-medium interaction strengths and short propagation times [170]. In Ref. [FT3] we significantly improve the effective description of the induced interplay between the impurities by devising a time-dependent effective model consisting of time-dependent effective parameters. The application of these effective models eventually results in the observation of the dynamical crossover from an induced attraction to an induced repulsion and vice versa. While in Refs. [FT2, FT3] we identify the mediated interactions in terms of a bunching or anti-bunching pattern in the two-body correlation function, in Ref. [FT4] we quantify the induced interaction by relying exclusively on polaron energies [207]. Specifically, we consider up to three impurities confined in a tilted double-well potential [FT7, 208–210] which are coupled to a majority species trapped in a ring potential [211, 212]. The tilt applied to the double-well potential leads to a population imbalance of the impurities regarding the two wells and facilitates the detection of the induced interaction by means of the one-body density. Based on this, we construct effective two- and three-body models and extract the impact of an induced two- and three-body interaction imprinted on the impurities' one-body density.

As mentioned above, the exquisite experimental control over the system parameters renders ultracold platforms ideal testbeds for quantum simulation. This feature, has been impressively demonstrated in a recent experiment reported in Ref. [213]. In this experiment, a Floquet scheme has been applied to two ultracold ^{87}Rb atoms confined in a tilted optical lattice potential to simulate the one-dimensional anyon-Hubbard model. The latter model is a generalization of the Bose-Hubbard model and describes a system consisting of lattice trapped anyons which, similar to bosons, can interact via an onsite-interaction potential and propagate through the lattice via hopping between neighboring sites. In general, abelian anyons are particles for which the describing wave function picks up a statistical phase $e^{i\theta}$ when two particles are interchanged. The angle of this phase is denoted by θ and defines the particular exchange statistics [214–219]. When the additional phase factor is 1 or -1, the underlying particle statistics corresponds to bosons ($\theta = 0$) or fermions ($\theta = \pi$), respectively. One of the most prominent examples associated with the appearance of anyons is the fractional quantum Hall effect [220–223]. This effect can be observed in ultracold two-dimensional electron systems with an additional perpendicular magnetic field. Measuring the Hall resistance gives an insight into the filling factors of the Landau levels, which can be either integer or fractional. The emergence of a fractional filling factor is then explained with the concept of identical quasi-particles obeying a fractional exchange statistics [220, 221].

The aforementioned one-dimensional anyon-Hubbard model is expected to exhibit a rich physics, including the formation of exotic phases that are absent in the Bose-Hubbard model. Recall that in the bosonic case ($\theta = 0$), depending on the chemical potential, the system enters a superfluid phases, when J is much larger than U, corresponding to a delocalization of the particles over the lattice. On the other hand, if U is dominant, the particles localize with an integer number on individual lattice sites and the system is in a Mott-insulating state [62, 63, 224, 225]. Besides the appearance of a superfluid and Mott-insulting phase [226], the anyon-Hubbard model exhibits more exotic phases that are entered by varying the statistical angle. For instance, in the absence of triple occupations, the emergence of a dimer, a pair-superfluid or a partially paired phase have been predicted [227]. In Ref. [228] it has been shown that a negative statistical parameter induces an attraction between the anyons which eventually leads to the formation of a quantum-statistical condensate and turns out to be even more robust than a BEC. Moreover, when tuning the statistical angle from bosons to fermions, the fermionization of the anyons can be observed in terms of Friedel oscillations [229], a signature occurring also in the bosonic continuum limit [230, 231]. Another property which distinguishes the anyon-Hubbard model from the bosonic one, is the breaking of the spatial inversion and time reversal symmetry [232], leading to an asymmetric particle transport [213, 233]. Additionally, great interest has been paid to one-dimensional hard-core anyons [234–237], which undergo dynamical fermionization after a free time evolution [234] and reveal an asymmetric quasi-momentum distribution [235–237]. Remarkably, such a system has been recently realized in terms of a strongly-interacting quantum gas which relies on spin-charge separations [238].

In Ref. [FT5] we extend the field of one-dimensional anyons and study the spectral properties of the anyon-Hubbard model. Specifically, we find a degenerate zero-energy subspace whose dimension is independent of variations in θ. The root of this property is found in the conservation of chiral symmetry a property, which is also responsible for the emergence of a checkerboard pattern in the one-body density function. Moreover, by preparing the system in the zero-energy space and adiabatically tuning the statistical angle from bosons to fermions back to bosons, i.e. from $\theta = 0$ to 2π, we reveal nontrivial Wilcek-Zee phases and holonomies which could be used for state manipulation purposes.

Objectives of this thesis

In this cumulative thesis, our main goal is to study the correlated static and dynamical properties of ultracold atomic ensembles in one-dimensional setups at ultracold temperatures, where the focus is put on strongly particle-number imbalanced mixtures. The numerically exact results for the systems discussed in [FT1–FT4] are obtained by employing the ML-MCTDHX method [204–206]. The primary interest is put on the induced interplay between impurities coupled to a majority species. We intend to characterize the induced interaction in terms of their impact on polaron energies, one-body observables and higher-order correlation functions. In order to quantify the respective induced interactions, the strategy is to construct two- and three-body effective models with the ultimately goal to provide an intuitive understanding of the underlying physics and to reveal the presence of induced attraction and repulsion.

An additional focus is put in [FT5] on the spectral properties of the anyon-Hubbard model in one-dimension. The emphasis is on characterizing the zero-energy subspace and relating its properties to the presence or absence of chiral symmetry. Additionally, we aim at providing a scheme that is able to evolve an initial number state into a zero-energy eigenstate by temporally tuning the statistical parameter. A main goal is to realize nontrivial state transformations by exploiting the dimensional stability of the zero-energy subspace and to adiabatically tune the statistical parameter in the control space.

Chapter 2

General Aspects of Ultracold Atoms

Materials can have different phases depending on the external pressure and temperature. The most prominent phases are the liquid, solid and gas phase. Beyond these classical phases there exists numerous other exotic phases of matter which occur only either within special materials or at extreme temperatures. In the case of extreme large temperatures, the atoms dissolve into nuclei and electrons and form a plasma. On the other hand, at very low temperatures quantum effects become relevant and enable, for instance, the formation of a so-called Bose-Einstein condensate, named after S. N. Bose who theoretically predicted the phase in terms of massless photons [239] and A. Einstein who extended his work to massive particles [240]. The general idea of a BEC is that at very low temperatures the de Broglie wavelength of massive particles λ_T becomes comparable to the interparticle distance of the atoms in the cloud and the individual matter waves of the atoms overlap. This eventually leads to the condensation of the atoms into a BEC. In the case of bosonic particles, the atoms occupy the same state such that even a large atomic ensemble can be described by a single wave function making it the ideal testbed to study fundamental quantum effects. Still, it took over 70 years from its first prediction in 1924 until the cooling techniques had advanced enough to realize such a BEC. Important contributions to the development of the cooling and trapping techniques have been made by S. Chu, C. Cohen-Tannoudji and W. D. Williams who received for their work the Nobel Prize in Physics in 1997 [241]. In 1995, the group under the direction of E. Cornell and C. Wiemann created for the first time a BEC with ^{87}Rb atoms [1], followed by the realization of a BEC with ^{23}Na atoms by the group led by W. Ketterle [2]. In 2001, their achievements were awarded with the Nobel Prize in Physics. These early endeavors set a milestone in the history of ultracold physics and ignited a rapid growth of the field.

In the following, we introduce the basic properties of ultracold atoms and provide in Section 2.1 a brief overview of the different trapping techniques used to cool an atomic ensemble into the ultracold regime. The impact of optical light on the of ultracold ensemble is shortly discussed in Section 2.2. In Section 2.3 we introduce different control mechanisms employed in experiments to tune the interatomic interactions.

2.1 Cooling an Atomic Ensemble into the Ultracold Regime

In order to experimentally cool down an atomic ensemble and realize a BEC, an advanced trapping machinery is required [241–244]. Nowadays, there exist a number of ways of cooling an atomic gas to ultracold temperatures ($\sim$ nK), e.g, through the application of optical and magnetic fields [244, 245] and/or the collision with a buffer gas [246]. The starting point of a typical experimental sequence is given by a hot gas of atoms emitted from an oven. These atoms are then decelerated via a Zeeman slower [244] in which the atoms move along a magnetic field gradient that splits the internal level structure of the atoms, while a counterpropagating laser slows down the atoms. It is crucial that the magnetic field gradient is matched with the Doppler effect such that the atoms are always resonant with the applied laser. After passing through the Zeeman slower the atoms posses a temperature of around 1 K.

Subsequently, the atoms can be loaded into a magneto-optical trap consisting of a quadrupolar magnetic field that varies in space and vanishes at the trap center. The concept of such a setup is as follows. Once the atoms move away from the center, their energy levels get shifted by the magnetic field gradient according to the Zeeman effect and, importantly, become resonant with optical lasers installed around the trap center. The frequencies and polarization of the laser beams are adjusted such that they are only resonant with the atoms propagating towards them and leave the other atoms unaffected. Once an atom absorbs a photon, it receives a kick back to the trap center. Note that this effect of pushing the atoms back to the center is an average over many absorption and emission processes, i.e., the absorption of an incoming photon leads to the kick towards the trap center, while the emission of the photon leads to a kick in a random direction. This mechanism denotes at the same time also its limitation, i.e., it is not possible to cool the ensemble below the momentum kicks invoked by the laser light, known as the Doppler limit. Eventually, a magneto-optical trap is able to cool the atoms into the μK regime [247–249].

In order to cool the gas below the Doppler limit and convert a macroscopic fraction of the gas into the condensed phase, other cooling techniques are required such as Sisyphus or evaporative cooling [241, 242, 244, 245, 250]. The former procedure constitutes of two polarized counter-propagating laser beams, where the idea is to convert kinetic energy to potential energy which is then absorbed by a photon. Here, the atoms move along a spatially varying potential landscape. In case an atom reaches a potential maximum, part of the kinetic energy is converted to potential energy. Polarized laser beams then pump the internal state of the atoms to a different hyperfine state corresponding to a different potential landscape with inverted minima and maxima. By doing so, the optical pump lowers the overall energy of the atom. After the Sisyphus cooling the temperature can be further reduced by employing an evaporative cooling scheme. In this method, the atoms are loaded into an optical dipole trap, whose depth is subsequently lowered such that highly energetic atoms can escape the trap. The loss of a small fraction of highly energetic atoms significantly lowers the temperature and can cool the remaining ensemble into the nK regime [251].

2.2 Optical Confinement of Atoms

Once the atoms are trapped and cooled to ultracold temperatures, they can be further manipulated via optical light. This light is used to generate potential landscapes for the atoms, in this way, opening the possibility to study quantum processes in almost arbitrary setups [10, 19, 252]. The interaction of an atom with an electric field $\mathbf{E}(\mathbf{r}, t)$ is given by [40, 61],

$$\hat{H}^{\mathrm{atom-light}} = -\mathbf{d} \cdot \mathbf{E}(\mathbf{r}, t), \tag{2.1}$$

where $\mathbf{d}$ is the electric dipole operator. Here, we have assumed that the electric field with frequency ω_L does not vary on scales of the atomic size, also known as the *dipole approximation*. The external electric field induces a dipole polarization $\alpha(\omega_L)$ on the atom, which leads to an energy-shift, known as *Stark shift*. This spatially dependent energy shift acts as an effective potential and after time-averaging obtains the form,

$$V^{\mathrm{atom-light}}(\mathbf{r}) = -\frac{1}{2}\alpha(\omega_L)\overline{\mathbf{E}(\mathbf{r}, t)^2}, \tag{2.2}$$

where $\alpha(\omega_L) \approx |\langle e|\mathbf{d} \cdot \epsilon|g\rangle|^2/(E_e - E_g - \hbar\omega_L)$ is the atomic polarizability and $|g\rangle$ ($|e\rangle$) refers to the ground (first excited) state of the atom with energy E_g (E_e) and ϵ denotes a unit vector pointing in the direction of $\mathbf{E}$ [40]. Since the electric field varies much faster than the atomic motion, it is sufficient to consider only the time-average of the intensity, i.e., $\overline{\mathbf{E}(\mathbf{r},t)^2}$. Depending on the sign of the polarizability $\alpha(\omega_L)$ the atom either seeks or avoids an intensity maximum. In this sense, the optical light leads to a spatially dependent energy shift that gives rise to a spatially dependent potential.

By exploiting the effect of optical light on neutral atoms, various potential landscapes can be realized, e.g. box [253] and a double-well potentials [16, 17] or optical lattices [254, 255]. The latter can be generated by superimposing counter-propagating optical laser beams, where the distance between the sites is determined by the wavelength of the laser. Furthermore, when rapidly moving a laser beam faster than the dynamical response of the atoms, it is even possible to generate arbitrary and time-dependent potential landscapes [19].

2.3 Interactions Between Neutral Atoms

Interactions in ultracold gases are vital for the generation of correlation and the formation of complex phases. Therefore, it is pivotal to understand and control interparticle interactions. The scattering of two low-energetic neutral particles is already textbook knowledge, see for instance [4, 61, 256, 257]. Here, we focus on the most relevant aspects of ultracold collisions which lay the ground for the following discussion.

We distinguish between two types of interactions occurring between neutral atoms, i.e., Coulomb and van der Waals interactions, where their relevance depends on the interatomic distance. For instance, at short distances, meaning at the order of the spatial extension of an atom ($\sim 0.5\,\mathrm{nm}$ for Rb atoms), the interaction is governed by the Coulomb repulsion between the electrons residing in the outer shell of each atom. Increasing the interatomic distances to large values, the internal structure of the atom becomes less relevant and the atoms appear effectively neutral. For distances above $\sim 10^2\,\mathrm{nm}$, the instantaneous polarizability of the moving internal charges, i.e. the electrons, gives rise to an attractive van der Waals interaction potential which scales as $-1/R^6$ with R being the interparticle distance [257]. In ultracold experiments the interatomic distances are much larger than the atomic radii so that it is sufficient to consider only van der Waals interactions.

2.3.1 Two-Body Scattering in Three Dimensions

The scattering process of two colliding neutral particles is a widely celebrated quantum mechanically problem which is tackled by solving the two-body Schrödinger equation constructed from a two-body interaction potential $V(\mathbf{r_1},\mathbf{r_2})$ [40, 61]. As starting point, two particles with masses m_1 and m_2 are prepared in a plane wave with a relative energy of $E=\frac{k^2}{2\mu}$ and absolute momentum $\hbar k$, where $\mu=\frac{m_1 m_2}{m_1+m_2}$ denotes the reduced mass. For an isotropic potential, i.e., the potential depends only on the absolute distance R between the atoms, it is convenient to expand the solution of the Schrödinger equation in terms of spherical harmonics Y_{lm} and radial functions $u_l(R)$, leading to the relation [4, 40, 256],

$$\left(-\frac{\hbar^2}{2\mu}\frac{\mathrm{d}^2}{\mathrm{d}R^2}+\frac{\hbar^2}{\mu R}\frac{\mathrm{d}}{\mathrm{d}R}+V(R)+\frac{\hbar^2 l(l+1)}{2\mu R^2}\right)u_l(R)=Eu_l(R), \tag{2.3}$$

where l denotes the relative angular momentum between the two atoms. The last term on the left-hand side denotes the centrifugal barrier, which vanishes for $l=0$. At large interatomic distances, in the limit of $R\to\infty$, the radial wave function takes the form,

$$u_l(R)\approx\frac{1}{kR}\sin\left(kr-\frac{\pi}{2}l+\delta_l(E)\right) \tag{2.4}$$

where $\delta_l(E)$ is the scattering phase shift. As it turns out, for small momenta k all phase shifts with $l > 0$ vanish such that the scattering cross section is governed by the $l = 0$ contribution, also referred to as *s-wave scattering*. The scattering length a is defined from the relation $\delta_0(E) = -ka$ in the limit $k \to 0$ [4]. Note that the scattering length is an important quantity in ultracold physics due to its direct relation to the scattering properties between two particles.

Instead of using a van der Waals-type interaction potential, it is often sufficient to use a more simplified effective interaction potential. Typically, ultracold systems are very dilute meaning that the interatomic distance is much larger than the size of an atom so that the short-range behavior of the interaction potential can be simplified. A prominent example is given by Huang's pseudopotential [258]

$$U(r) = \frac{2\pi\hbar^2 a}{\mu}\delta\mathbf{r}\frac{\partial}{\partial r}(r\,\cdot), \tag{2.5}$$

where the operator $\frac{\partial}{\partial r}(r\,\cdot)$ accounts for the regularization at small distances. This description is exact in the limit of vanishing energies and facilitates a bound state for positive scattering lengths, $a > 0$, with energy $E = \hbar^2/(2\mu a^2)$ [4].

2.3.2 Tuning the Scattering Length via Feshbach Resonances

As we have seen in the previous Section 2.3.1, the scattering length a is the decisive parameter defining the interaction between two particles. Therefore, it is crucial to gain an experimental control over this scattering length. A possibility is given by tuning over a Feshbach resonance.

A Feshbach resonance is present when the energy of a molecular bound state, corresponding to a closed channel (E_c), approaches the asymptotic energy of two separated atoms in an open channel (E_o). In the vicinity of such a Feshbach resonance, two atoms in an open channel can undergo a second-order transition and scatter to a state in the closed channel and decay back to the open channel, a process which impacts the scattering length a [40]. In particular, the impact scales with the inverse of the difference between the entrance energy and the bound state energy of the closed channel, i.e., $\sim 1/(E_o - E_c)$ [40]. The impact on the scattering length is especially large at the Feshbach resonance, where the energy difference vanishes. Conveniently, this energy difference is tunable by applying an external magnetic field and, thus, also the scattering length which reads as [4, 259],

$$a(B) = a_{\mathrm{bg}}\left(1 - \frac{\Delta}{B - B_0}\right), \tag{2.6}$$

where a_{bg} denotes the background scattering length while B_0 and Δ correspond to the position and width of the resonance, respectively. At the position of the resonance, a diverges towards negative or positive infinite values depending on the site from which one approaches the resonance. The fact that the scattering length can be almost arbitrarily tuned, implies that the interaction strength between two ultracold atoms is likewise tunable. Note that, besides controlling the scattering length via magnetic fields, it is also possible to apply optical or radiofrequency fields in order to mix the two collision channels and trigger a resonant coupling between the atoms [3, 260–263].

In a BEC, a Feshbach resonance was observed for the first time at the MIT for ^{23}Na atoms [5] via non-destructive *in situ* phase-contrast images. Nowadays, this technique belongs to the standard tool-kit in ultracold experiments, in this way, enabling the full control over the interaction between two atoms [4]. Moreover, a Feshbach resonance facilitates the formation of a bound state between two atoms, known as a Feshbach molecule. In this context, homonuclear molecules such as Cs_2, [7, 264], K_2 [265] and Rb_2-molecules [266] as well as heteronuclear ones, e.g. ^{85}Rb-^{87}Rb [267] and NaK*-molecules [268] have been realized and which were detected via laser- or radiofrequency-induced dissociation [264, 265] or via a Stern-Gerlach separation [7].

2.3.3 Two-Body Scattering in One Dimension

One-dimensional ultracold gases are usually realized by tightly confining the atoms in two spatial directions such that the motion of the atoms along these directions is suppressed and only one axis remains available [10, 39, 67, 269]. The strong external confinement along the two spatial dimensions makes it necessary to adjust the scattering length a to the one-dimensional case, which was done by M. Olshanii in 1998 [9]. Starting from a Huang's pseudopotential [see Eq. (2.5)] and considering a harmonic confinement along the axial direction with a frequency of $\omega_\perp$, the following expression for the one-dimensional scattering length $a_{1\mathrm{D}}$ can be derived,

$$a_{1\mathrm{D}} = -\frac{a_\perp^2}{2a}\left(1 - C\frac{a}{a_\perp}\right), \tag{2.7}$$

where C denotes a constant and $a_\perp = \sqrt{\hbar/(\mu\omega_\perp)}$ the size of the ground state of the transverse Hamiltonian. To prevent a transverse motion, the energy of the atoms has to be smaller than the energy required to excite a transverse vibrational state given by $\hbar\omega_\perp$. The above considerations result in the expression for the two-body interaction potential in one dimension,

$$U_{1\mathrm{D}}(r) = g_{1\mathrm{D}}\delta(r), \tag{2.8}$$

where $g_{1\mathrm{D}} = -\frac{\hbar^2}{\mu a_{1\mathrm{D}}}$ denotes the interaction strength and $\delta(r)$ corresponds to a contact delta potential.

The expression for the two-body interaction potential [Eq. (2.8)] reveals an important experimental feature, namely, that the one-dimensional interaction strength can be tuned not only by controlling the magnetic or optical field strength, but also via modulating the transverse confinement frequency $\omega_\perp$.

Chapter 3

Impurities Immersed in One-Dimensional Bose Gases

In this chapter, we introduce the basic concepts required to treat systems consisting of impurities which are immersed in one-dimensional ultracold bosonic ensembles. We begin in Section 3.1 with a description of the many-body Hamiltonian of a single-component species and continue in Section 3.2 with the effective description of a dressed impurity immersed into a bosonic bath. In Section 3.3 we elaborate on the case of two impurities interacting with a bosonic host and put a special emphasis on the mediated interaction between the impurities.

3.1 Single-Component Ultracold Bose Gases

In the following, we consider a bosonic ensemble consisting of N atoms with mass m confined to one spatial dimension. The respective many-body Hamiltonian describing this system reads [51],

$$\hat{H}^A = \sum_{i=1}^{N} \hat{h}_i(x_i) + g \sum_{i<j} \delta(x_i - x_j), \tag{3.1}$$

where $\hat{h}_i(t)$ corresponds to the one-body Hamiltonian of particle i which are pairwise interacting with a two-body contact interaction potential of strength g corresponding to a s-wave scattering process (see Section 2.3.3). The one-body Hamiltonian is composed of a kinetic and a potential term,

$$\hat{h}(x_i) = -\frac{\hbar^2}{2m}\frac{\mathrm{d}^2}{\mathrm{d}x_i^2} + V(x_i) \tag{3.2}$$

where $V(x_i)$ is the spatially dependent potential [cf. Section (2.2)]. Note that in this expression we have neglected three- or higher-body interactions terms, which are suppressed in dilute systems. Moreover, we remark that the potential and interaction strength, in principle, could be time-dependent so that the Hamiltonian in Eq. (3.1) does not necessarily conserve energy.

3.1.1 Homogeneous Case

A special case of the Hamiltonian $\hat{H}^A$ presented in Eq. (3.1) denotes the homogeneous case, where $V(x) = 0$, known as the Lieb-Liniger model [270]. This model is exactly solvable via a Bethe ansatz [271, 272]. For a given particle density n the system is characterized by a single dimensionless parameter,

$$\gamma = \frac{mg}{\hbar^2 n}, \tag{3.3}$$

which reflects the ratio of kinetic energy $\hbar^2 n^2/(2m)$ and the mean-field interaction energy ng. If the gas is confined along a ring potential of length L, the density is given by $n = N/L$. There are two limiting cases of this model, one case appears at high densities n and corresponds to weak interaction strengths ($\gamma \ll 1$), while the other regime emerges at low densities corresponding to large interaction strengths ($\gamma \gg 1$). In the case of weak interactions, the energy per particle is found to be $\epsilon(n) = \frac{\hbar^2 n^2}{2m}$, which leads to the mean-field theory in the thermodynamic limit ($N, L \to \infty$). On the other hand, in the strongly interacting regime the system consists of impenetrable bosons and can be mapped to the case of non-interacting spinless fermions, known as Tonks-Girardeau gas [273, 274]. Note that this rather counter-intuitive relation between density and interaction is unique to the one-dimensional case and inverted in three dimensions [10, 61, 257]. This property can be used to realize strongly correlated ensembles by reducing the atomic density [67, 269, 275].

3.1.2 Harmonic Confinement

Let us briefly elaborate on the properties of a finite bosonic gas confined in a harmonic oscillator potential represented by $V(x) = \frac{1}{2}m\omega^2 x^2$ with trap frequency ω. The eigenfunctions of the one-body problem can be constructed from Hermite polynomials, while the eigenspectrum consists of equidistant energy levels $E_n = \hbar\omega(n + \frac{1}{2})$. An analytical solution exists for the case of two interacting particles, which can be obtained by solving the relative and the center-of-mass Hamiltonian individually [276]. Experimentally, such a two-particle system has been studied in Ref. [277]. For systems consisting of three or more interacting particles confined in a harmonic oscillator potential, there exists *a priori* no exact analytical solution. However, in the case of three atoms with equal mass, a similar procedure as in the two-body case can be employed to decrease the numerical cost, i.e., a center of mass Hamiltonian can be decoupled from the relative parts using Jacobian coordinates [278–281]. The respective spectrum has similar properties as the two-body solution featuring dimer-atom energies that diverge to negative infinity for increasing attractions and for strong repulsive interactions the spectrum shows signatures of fermionization. Employing an *ab initio* many-body variational approach, such as the MCTDHB method (see Section 4.4), for few atoms a N-body bound state has been conjectured to emerge in the attractive regime [282]. Additionally, using a correlated pair wave-function, the ground state of a few particles can be reliably predicted [283].

In the following, we briefly discuss some of the most common dynamical patterns that can emerge in a one-dimensional, harmonically trapped Bose gas. The dynamics are usually triggered by varying a system parameter in time. For instance, in a two-atom setup quenching the interaction strength leads to a breathing-like motion [284], while carefully driving the interaction strength between the atoms, the system can be steered into higher excited states of the relative motion with a high degree of controllability [285]. A similar breathing motion is triggered by quenching the trap frequency. In the two-particle case, this quench protocol leads to a beating behavior in the time-evolved spatial variance, where a Fourier analysis reveals the presence of two dominant frequencies which are accompanied by multiple sidebands [286]. The two dominant frequencies merge into a single-frequency behavior when increasing the particle number, consistent with respective experiments [39, 287]. The latter frequency was found to correspond to the energy gap between the ground state and an excited state [288].

3.2 Single Impurity Interacting with a Bosonic Ultracold Gas

A natural extension to the case of a single-component Bose gas is the addition of a second atomic species offering a plethora of novel phases [11, 76, 77]. A widely celebrated branch is given by strongly particle-number imbalanced mixtures, where in the extreme case a single impurity interacts with a majority species. The respective many-body Hamiltonian reads as,

$$\hat{H}^{\text{bath}-1\text{imp}} = \hat{H}^A + \hat{h}^B + g_{AB} \sum_{i=1}^{N_A} \delta(x_i^A - x^B). \tag{3.4}$$

where $\hat{H}^A$ describes the bosonic majority species with the form of Eq. (3.1) and $\hat{h}^B$ denotes the impurity Hamiltonian of the form of Eq. (3.2). The interaction potential between the impurity and the medium is modeled by a contact interaction potential with strength g_{AB}.

One relevant property of the bath-impurity Hamiltonian is the possibility to study so-called Bose polaron. The latter denotes a quasi-particle that is composed of the impurity and the excitation of the bath. The origin of the polaron concept has its roots in solid state physics, where the aim was to effectively describe the motion of an electron through a crystal [289]. While moving through the crystal, the electron distorts the positions of the surrounding nuclei via Coulomb interaction and, in this way, excites phonons which, in turn, impact the electron's motion. The overall behavior of the electron is then a combination of its bare movement and the phonon excitations. In this sense, the electron becomes dressed by the phonons giving rise to a quasi-particle with an effective mass and energy that deviate from the bare mass and energy of the electron [289]. This effective model has been successfully employed in the field of solid state physics for the description of, e.g. semiconductors and polymers [290] and over the last two decades found entrance in the field of ultracold quantum gases [11, 119].

In the following, we give a brief introduction of the effective models in the literature used to describe the dressed state of an impurity in an ultracold setup. We distinguish between two cases. The first case corresponds to the homogeneous setup in the absence of any external trapping potential and in the second case we address the implications of adding an external harmonic confinement. Note in passing that beyond studying the Bose polaron, the bath-impurity Hamiltonian allows also to investigate, e.g., the transport properties of an impurity in different potential landscapes [153] such as double-well potentials [155, 194] or lattice structures [FT7, 158, 159, 179].

3.2.1 Effective Description in the Homogeneous Case

Fröhlich Hamiltonian

The Fröhlich Hamiltonian was originally devised for treating polaron problems in solid state physics and with the experimental advances in the field of ultracold physics it has found applications in bath-impurity setups. Note that the model is restricted to the homogeneous case, where the impurity and the bath atoms can move freely in space.

To arrive at the Fröhlich Hamiltonian, the bath-impurity Hamiltonian in Eq. (3.4) is first expressed in terms of bosonic and impurity field operators, $\hat{\phi}(x)$ and $\hat{\psi}(x)$, respectively, and in a next step transformed into momentum space by $\hat{\phi}_k = \frac{1}{\sqrt{2\pi}} \int \mathrm{d}x e^{ikx} \hat{\phi}(x)$. Subsequently, the bosonic field operators in momentum space $\hat{\phi}_k$ are expressed in terms of Bogoliubov phonons

$\hat{a}_k$ via the usual Bogoliubov transformation[1]. The final expression for the bath-impurity Hamiltonian in momentum representation reads [142, 144],

$$\hat{\hat{H}}^{\text{bath}-1\text{imp}} = \hat{H}^{\text{F}} + \hat{H}^{2\text{ph}} + \hat{H}^{\text{ph}-\text{ph}}, \tag{3.5}$$

where so far no additional approximation has been made. The first term corresponds to the effective Fröhlich Hamiltonian and is given by,

$$\hat{H}^{\text{F}} = \frac{\hat{p}^2}{2m_B} + \sum_k \hbar\omega_k \hat{a}^\dagger_k \hat{a}_k + g_{AB}n_0 + \sum_k V_k e^{ik\hat{x}}(\hat{a}^\dagger_k + \hat{a}_{-k}), \tag{3.6}$$

where n_0 is the density of the undisturbed homogeneous Bose gas, while $\hat{x}$ and $\hat{p}$ denote the spatial and momentum operators of the impurity, respectively. Moreover, ω_k denotes the dispersion relation stemming from the Bogoliubov transformation and V_k the scattering amplitude. They are defined as

$$\hbar\omega_k = \frac{\hbar^2 k}{2m_A\xi}\sqrt{2+k^2\xi^2} \quad \text{and} \quad V_k = \sqrt{n_0}g_{AB}\left(\frac{k^2\xi^2}{2+k^2\xi^2}\right)^{1/4},$$

where $\xi = \sqrt{\hbar^2/(2m_A n_0 g_{AA})}$ is the healing length of the bath. The second term in the sum of Eq. (3.5) accounts for two-phonon scattering processes ($\hat{H}^{2\text{ph}}$), while the last term, $\hat{H}^{\text{ph}-\text{ph}}$, describes higher-order processes beyond the Bogoliubov approximation and especially, does not depend on any impurity operators.

The Fröhlich model is represented by the Hamiltonian $\hat{H}^{\text{F}}$ and provides a mean-field description of the bath-impurity problem. Therefore, the Fröhlich model is only valid in the weak-coupling limit, i.e., when the impurity-bath interaction is sufficiently small ($g_{AB}/g_{BB} \lesssim 1$) and when the bath is appropriately described within the Bogoliubov approximation, i.e., for $\gamma \lesssim 2$ [144].

Increasing the impurity-medium coupling strength beyond the weakly-coupling regime, the mean-field approximation fails to describe the emergent physics and more elaborate models are required [85]. In order to treat regimes with strong impurity-medium couplings, the Fröhlich model can be extended by accounting for two-phonon processes ($\hat{H}^{2\text{ph}}$), see Ref. [144]. This approximation has been successfully applied to describe the self-localization of the polaron in an experiment with a dimensionless parameter of $\gamma \approx 0.4$, justifying the Bogoliubov approximation [85].

Effective One-Body Model

A property of the dressed impurity is the change in mass and energy with respect to the bare one, known as effective mass m_{eff} and self-energy ϵ [143, 144, 146]. With these quantities an one-body Hamiltonian can be devised in order to effectively describe the quasi-particle [291],

$$\hat{h}^{1\text{b,eff}}_{\text{hom.}} = \epsilon - \frac{\hbar^2}{2m^{\text{eff}}_B}\frac{\mathrm{d}^2}{\mathrm{d}x^2}. \tag{3.7}$$

---

[1] If the bosonic annihilation (creation) operators that annihilate (create) a boson with momentum k are given by $\hat{b}^{(\dagger)}$, then the Bogoliubov transformation corresponds to introducing a set of new operators $\hat{a}_k = u_k\hat{b} + v^*_{-k}\hat{b}^\dagger_{-k}$ and $\hat{a}^\dagger_k = u^*_k\hat{b}^\dagger + v_{-k}\hat{b}_{-k}$ with the demand that $|u_k|^2 - |v_{-p}|^2 = 1$ holds [40, 61]. Both sets, $\hat{b}^{(\dagger)}$ and $\hat{a}^{(\dagger)}_k$, fulfill the bosonic commutation relations. The transformation is restricted to the homogeneous case and is useful to express the single-component Hamiltonian of interacting particles in terms of non-interacting quasi-particles.

In this case, the effective mass and the effective energy depend on the impurity's momentum and the coupling to the bath. Within a Bogoliubov approximation and for weak impurity-medium couplings, an expression for the effective mass has been derived, reading as [143],

$$\frac{m_B^{\text{eff}}}{m_B} = 1 + \frac{2g_{AB}^2}{3g_{AA}^{3/2}\pi}\sqrt{\frac{m_B}{\hbar^2 n_0}}. \tag{3.8}$$

The expression for the effective mass implies that in a homogeneous setup the dressing of the impurity always results in a mass larger than the bare impurity mass m_B. In other words, the quasi-particle is always heavier than the bare impurity provided $|g_{AB}| > 0$. In fact, already for weak repulsive coupling strength the effective mass sharply increases resulting in the so-called self-localization of the polaron [143]. Note that this property has been derived in terms of an one-dimensional setup. In the three-dimensional case, the effective mass of the impurity does not increase as sharply as in the one-dimensional case so that the self-localization of the impurity occurs at comparatively large impurity-medium interaction strength [139].

3.2.2 Effective One-Body Model in the Presence of an External Potential

Next, we elaborate on the case where an additional external trapping geometry is employed. Specifically, we consider a harmonic oscillator potential for the majority species and the impurity, i.e., $V_\sigma = \frac{1}{2}m_\sigma\omega_\sigma^2 x_\sigma^2$ with $\sigma = A, B$ [292]. We remark that adding an external trapping potential significantly alters the emergent physics and can lead to phenomena such as breathing- or dipole-like oscillations [11, 152, 293] (see Section 3.1.2). However, in the following we focus on the effective description of an impurity coupled to a majority species.

In the absence of impurity-medium correlations, the many-body wave function reduces to a product state ansatz consisting of one wave function describing the impurity and one describing the medium (see Section 4.5). The impact of the majority species on the impurity is then represented in terms of a mean-field-type potential, $g_{AB}\rho_A^{(1)}(x)$. Within this approximation, the behavior of the impurity is adequately captured by an effective one-body model, where the impurity-bath interaction is treated as an external potential [11, 153, 160, 294],

$$\hat{h}^{\text{1b,effpot}} = \hat{h}^B(x) + g_{AB}\rho_A^{(1)}(x). \tag{3.9}$$

Note that we have neglected here the energy shift of the impurity as this contribution has no effect on the ground-state or dynamical behavior of the impurity. Even though the effective model neglects interspecies correlations, it can be applied in the analysis of strongly correlated many-body systems, e.g., to reveal the impact of correlations on certain one-body observables by comparing to the respective many-body results, or to yield insights into the microscopic structure of the many-body wave function by projecting it on the eigenstates of the effective model [FT1, FT8]. In this sense, the effective potential has been proven a valuable tool in yielding intuitive insights on the dynamical response of an impurity [FT1, 153, 160]. Finally, remark that this model is not necessarily restricted to systems consisting of a harmonic oscillator potential and can be applied to arbitrary potential setups, such as double-well potentials, see Refs. [FT7, FT8].

To go beyond the treatment in which the medium acts as a mean-field-type potential, a possible next step is to incorporate an effective mass (m_B^{eff}) and a renormalized trapping frequency (ω_B^{eff}) to describe the quasi-particle [291]. The respective effective Hamiltonian reads,

$$\hat{h}^{\text{1b,eff}}_{\text{harm.osc.}} = -\frac{\hbar^2}{2m_B^{\text{eff}}}\frac{\mathrm{d}^2}{\mathrm{d}x^2} + \frac{1}{2}m_B^{\text{eff}}\omega_B^{\text{eff}}x^2. \tag{3.10}$$

One possibility to specify the quantities m_B^{eff} and ω_B^{eff} is to calculate the effective mass within a local density approximation and resort to Eq. (3.8), i.e., the solution for the homogeneous case. Another way is given by tuning the effective parameters such that the effective model matches the observables of interest calculated by a many-body method [FT2, 291]. For instance, the mean position of an impurity performing a dipole-like oscillation has been fitted to the solution of a damped harmonic oscillator [FT8]. Another example denotes the case, where the impurity performs a breathing-like oscillation in an harmonic oscillator potential while being coupled to a majority species [FT3, 291]. Here, the temporal behavior of the spatial variance can be captured by the effective model presented in Eq. (3.10) when considering a time-dependent effective mass and frequency. Note that in order to determine the respective paths for the time-dependent effective parameters, a more elaborated optimization routine is required, cf. [FT3].

Comparing the values of the effective mass obtained within a harmonic setup to those of the homogeneous case, a striking difference appears at repulsive impurity-medium interaction strengths: In the trapped case, the effective mass of the impurity becomes smaller than its bare value, while in the homogeneous case the effective mass is always larger for any finite value of the interaction strength, as emphasized in Section 3.2.1. This effect can be attributed to the presence of the external harmonic trap, which leads in the repulsive case to a delocalization of the impurity, i.e, in this case the impurity probes the edges of the medium. In Ref. [FT2] we have compared the effective one-body models presented in Eqs. (3.9) and (3.10) with each other and find that for small impurity-medium couplings both approaches adequately describe the one-body behavior of the impurity. For larger impurity-medium interaction strength, the impurity is pushed out of the bath and the corresponding effective potential takes the form of a double-well potential leading to the breakdown of the quasi-particle picture [160].

3.3 Two Impurities Coupled to a Bose Gas

The impurity-medium paradigm is naturally extended by adding another impurity to the system. There are two possibilities to extend the impurity-medium Hamiltonian shown in Eq. (3.4). One possibility is to add another particle to the impurity species B, i.e.,

$$\hat{H}^{\text{bath}-2\text{imp}} = \hat{H}^A + \hat{H}^B + g_{AB} \sum_{i=1}^{N_A} \sum_{j=1}^{N_B} \delta(x_i^A - x_j^B). \tag{3.11}$$

In this case, species B consists of $N_B = 2$ particles interacting with g_{BB}, described by $\hat{H}^B$. Alternatively, one can add to the single-impurity setup an impurity of a different species C giving rise to a three-component mixture,

$$\hat{H}^{\text{bath}-\text{B}-\text{C}} = \hat{H}^A + \hat{h}^B + \hat{h}^C + g_{AB} \sum_{i=1}^{N_A} \delta(x_i^A - x^B) + g_{AC} \sum_{i=1}^{N_A} \delta(x_i^A - x^C) + g_{BC}\delta(x^B - x^C), \tag{3.12}$$

where the impurity C is described by the one-body Hamiltonian $\hat{h}^C$ and is coupled to the bath and impurity B with a contact interaction potential with strength g_{AC} and g_{BC}, respectively. These new interaction parameters introduce the flexibility to tune the impurity-medium coupling strengths g_{AB} and g_{AC} individually, which has important consequences for the effective interaction mediated by the bath, see Sections 3.3.1 and 3.3.2.

In these systems, one of the main interests lies in the study of the interplay between the impurities and, especially, in the question of how the presence of the bath influences the ground-state or dynamical properties of the impurities. In the following, we concentrate on an effective description of the two dressed impurities, similar to the single-impurity scenario (Section 3.2). The effective two-body models corresponding to $\hat{H}^{\mathrm{bath-2imp}}$ and $\hat{H}^{\mathrm{bath-B-C}}$ read,

$$\hat{H}_{BB}^{\mathrm{2b,eff}} = \sum_{i=1}^{2} \hat{h}_{B}^{\mathrm{1b,eff}}(x_i^B) + \hat{V}_{BB}^{\mathrm{eff}}(x_1^B, x_2^B), \tag{3.13}$$

$$\hat{H}_{BC}^{\mathrm{2b,eff}} = \hat{h}_{B}^{\mathrm{1b,eff}}(x^B) + \hat{h}_{C}^{\mathrm{1b,eff}}(x^C) + \hat{V}_{BC}^{\mathrm{eff}}(x^B, x^C). \tag{3.14}$$

The effective one-body terms account for the properties of the individual quasi-particles which are connected via the two-body interaction terms $\hat{V}_{BB}^{\mathrm{eff}}$ and $\hat{V}_{BC}^{\mathrm{eff}}$, which include the bare contact interaction potential, as well as, the effects stemming from an induced interaction´ [11].

3.3.1 Induced Interaction in the Homogeneous Case

The majority of the existing literature dealing with the induced interactions between impurities in one-dimensional setups is dedicated to the homogeneous scenario, where the impurities couple with the same interaction strength to the bath. By using a beyond mean-field approach, it has been shown that the mediated interaction between two static impurities takes the form a Yukawa-type of potential at small distances [168],

$$V_{BB}^{\mathrm{eff}}(r_{BB}) \approx -\frac{g_{AB}^2 m_A}{\hbar^2 \sqrt{\gamma}} \exp\left(-\frac{2r_{BB}}{\xi}\right), \tag{3.15}$$

where γ is the Lieb-Liniger parameter [see Eq. (3.3)], $r_{BB} = |x_1^B - x_2^B|$ denotes the relative distance between the impurities, and ξ corresponds to the healing length of the bath. Moreover, $r_{BB} \lesssim \xi$ has been assumed. This expression has been verified also in terms of a Bogoliubov-approximation [162], within perturbation theory [11], and for a field-theoretical approach [167]. The scaling of the induced interaction potential with $1/\sqrt{\gamma}$ implies that decreasing the interaction between the bath particles and/or increasing the density of the medium leads to a larger amplitude of V_{BB}^{eff}, i.e., to a stronger induced attraction between the impurities. The expression in Eq. (3.15) can be further approximated in terms of a contact interaction potential,

$$V_{BB}^{\mathrm{eff}}(r_{BB}) \approx -\frac{g_{AB}^2}{g_{AA}} \delta(x_1^B - x_2^B), \tag{3.16}$$

where the interaction strength is given by the net volume $\int V_{BB}^{\mathrm{eff}}(y)\mathrm{d}y \simeq -\frac{g_{AB}^2}{g_{AA}}$. This approximation for the induced interaction has been derived under the assumption of a homogeneous medium and used for the effective description of the quench dynamics of two impurities in a harmonic oscillator potential [170] (see Section 3.3.2).

At large impurity-impurity separations ($r_{BB} > \xi$) the induced interaction potential follows a Casimir-like interaction, which scales for weak-impurity medium couplings as $1/r_{BB}^3$ [167, 168, 171, 173, 177],

$$V_{BB}^{\mathrm{eff}}(r_{BB}) \approx -\frac{g_{AB}^2 m_A \xi^3}{32\pi r_{BB}^3}. \tag{3.17}$$

In general, the Casimir force is an attractive force mediated between two objects immersed in a fluctuating medium. For instance, fluctuations of the vacuum state mediate an attractive force between two neutral atoms [295]. Since ultracold quantum gases are likewise subject to quantum fluctuations, the concept of a Casimir force is applicable to impurities immersed in an ultracold bosonic medium [177]. As argued in Refs. [150, 170], this type of interaction becomes large in comparison to the Yukawa potential only at impurity-impurity separations of the order of $r_{BB} \gtrsim 6\xi$ [150] ($r_{BB} \gtrsim 5\xi$ [170]). At these distances, the effects are small on an absolute scale such that the experimental relevance of the Casimir-type interactions has not been fully resolved yet.

The above types of induced interactions feature a mediated attractive interaction between the impurities given that both impurities couple with the same interaction strength to the medium. However, when assuming two distinguishable impurities B and C the factor $-g_{AB}^2$ appearing in Eq. (3.15) can be rewritten as $-g_{AB} \cdot g_{AC}$ as suggested in Refs. [167, 177]. In such a three-component setup, each impurity couples with an individual coupling strength (g_{AB}, g_{AC}) to the bath enabling, besides an induced attraction, also an induced repulsion. Specifically, this is the case for $g_{AB} \cdot g_{AC} < 0$, that is, when one impurity attracts the medium while the other repels it. In Ref. [202], a scenario consisting of two infinitely heavy impurities coupled to a bath on a ring potential has been studied within the Born-Oppenheimer approximation. In this study, one impurity is considered to be impenetrable, i.e., it infinitely repels the medium, while the other impurity either repels or attracts the medium with a finite interaction strength. Analyzing the change of energy for varying impurity-impurity separation, the former case revealed an induced attraction while in the latter case an induced repulsion has been observed.

Finally, we would like to provide an intuitive picture which motivates the induced attractive and repulsive interaction mediated between the impurities based on mean-field arguments. For this purpose, we assume a homogeneous medium with a spatially constant density. Placing a static impurity at position x_B and letting it interact with the medium via the interaction strength g_{AB} results, for $g_{AB} > 0$, in a density-dip of the medium around x_B or in a hump at the same position for $g_{AB} < 0$. The size of the density distortion is of the order of the healing length. In the next step of the gedankenexperiment, a second impurity C is added, which interacts only with the medium with a strength of g_{AC}, implying $g_{BC} = 0$. Now we assume that impurity B is attractively coupled to the medium and the medium exhibits a density hump at position x_B. In the case where impurity C attracts the medium, it seeks the medium's density hump in order to maximize the spatial overlap with the medium and localizes around x_B. In this sense, the majority species mediates an attractive interaction between the impurities. On the other hand, for repulsive g_{AC}, the impurity C avoids the density hump at x_B giving rise to an induced repulsion between the impurities.

3.3.2 Induced Interaction in External Trapping Potentials

In the following, we discuss the implications of an external trapping potential on the induced interaction between two impurities coupled to a bosonic medium. In general, similar to the homogeneous case, we expect a mediated attraction when both impurities couple with the same sign to the medium and an induced repulsion when one impurity attracts the medium and the other repels the former. In the harmonic case, an analytical derivation of the mediated interaction potential in dependence to the impurities' relative difference is not feasible. This is due to the impossibility to decouple the effects of the external trap from the interaction potential that is mediated by the bath [165]. Still, instead of depending on the relative difference $|x_1^B - x_2^B|$, the induced interaction potential can be obtained as a function of both impurity coordinates x_1^B and x_2^B. In Ref. [165] the respective potential has been calculated to facilitate the understanding of the coalescence behavior of two impurities emerging for strong impurity-medium repulsions [165]. Similarly, an effective two-body interaction potential has been derived from an *ab initio* many-body method to account for the induced interaction mediated by interspecies entanglement [178].

However, note that a detailed derivation of the induced interaction potential in the presence of a harmonic oscillator is not always necessary. In Ref. [170] the results obtained from the homogeneous scenario have been applied to the quench dynamics in the harmonically trapped case revealing a qualitative good agreement for weak interactions and short times. In particular, the dynamics of the dressed impurities have been described in terms of an effective contact interaction potential following Eq. (3.16). In Refs. [FT2, FT3] we have studied a similar setup, where we improved the agreement between the many-body calculations and the effective two-body model by employing a contact-interaction potential with a time-dependent and optimized interaction strength.

We remark that other studies revealed an induced attractive interaction between impurities in the presence of an external lattice potential, where the clustering of the impurities [131], as well as the formation of bound states has been observed [157, 296, 297]. Moreover, it has been shown that within a harmonic potential the medium can induce impurity-impurity correlations which eventually realize Bell-states [203].

Chapter 4

Numerical Methods

This section introduces the numerical framework necessary to infer information about the ground state and dynamics of the systems that are investigated in this cumulative dissertation. In general, we presume that each considered setup is completely described by a many-body Hamiltonian $\hat{H}(t)$ which includes all system parameters and, in principle, can depend on time. The respective many-body wave function $|\Psi(t)\rangle$, which describes the ground state or dynamics of $\hat{H}(t)$, is found by solving the time-dependent Schrödinger equation, which reads in Dirac notation,

$$i\hbar\frac{\partial}{\partial t}|\Psi(t)\rangle = \hat{H}(t)|\Psi(t)\rangle. \tag{4.1}$$

In the following we set $\hbar = 1$. In order to numerically evaluate this equation, the wave function $|\Psi(t)\rangle$ is expressed in terms of a finite basis. In this way, the Hamiltonian is discretized such that the underlying Hilbert space dimension becomes finite. The equation of motion (EOMs) are derived by inserting $|\Psi(t)\rangle$ into the Dirac-Frenkel variational principle [298–300],

$$\langle\delta\Psi(t)|\hat{H}(t) - i\frac{\partial}{\partial t}|\Psi\rangle = 0, \tag{4.2}$$

which is numerically solved to determine the time-dependent solution $|\Psi(t)\rangle$. To solve the stationary problem, where the ground or excited states of $\hat{H}$ are sought, the expression in Eq. (4.1) reduces to an eigenvalue problem,

$$\hat{H}|\Psi_i\rangle = E_i|\Psi_i\rangle, \tag{4.3}$$

where $|\Psi_i\rangle$ is the i-th eigenstates of $\hat{H}$ with energy E_i.

The complexity of the numerical problem is set by the particular Hamiltonian describing the system which might correspond to a large Hilbert space. Already for a few particles, the corresponding Hilbert space dimension becomes so large that the numerical expression of of a wave function in terms of the complete basis becomes extremely challenging or even impossible. However, typically the ground state or dynamically evolved wave function does not occupy the complete Hilbert space and rather populates a fraction of it. This fact allows us to obtain numerically exact solutions even for systems with a large number of particles[1]. Therefore, the crucial task is to find for the system under consideration the appropriate basis set to reduce the numerical cost.

In this chapter we outline the methods employed in this thesis to tackle the numerical evaluation of the many-body systems of interest. In Section 4.1 we generalize the notation of the many-body Hamiltonian introduced in Section 3 to arbitrary species and particle numbers. We numerically access the spatial degree of freedom by discretizing it in terms of a primitive basis. Several types of such primitive basis sets are discussed in Section 4.2. In Section 4.3

---

[1] Within this dissertation we treat systems with a total number of particle ranging from 1 to ~ 30.

we introduce the standard approach to solve a system consisting of only a few particles and provide two examples. In Section 4.4 we discuss a more elaborated approach, which employs a time-dependent basis that moves in a variationally optimized manner through the Hilbert space, i.e., the multi-configuration time-dependent Hartree method. In Section 4.5 we introduce the multi-layered extension of the latter method and explicate the ansatzes of the many-body wave function for two- and three-component ultracold mixtures. In Section 4.6 we elaborate on the imaginary time propagation employed to relax the many-body wave function into the ground state. Finally, in Section 4.7 we give some final remarks on the convergence behavior of the many-body simulations.

4.1 Many-Body Hamiltonian

We consider a system of S different species of atoms, where each species consists of N_S indistinguishable neutral atoms that are restricted to one spatial dimension with no internal degrees of freedom (DOFs) such as a spin DOF. The interaction between atoms belonging to the same or different species is modeled with a contact interaction potential of strength $g_{\sigma\sigma}$ or $g_{\sigma\sigma'}$, respectively (see Section 2.3.3). The respective many-body Hamiltonian reads,

$$\hat{H} = \sum_{\sigma=1}^{S} \hat{H}^{\sigma}(t) + \frac{1}{2} \sum_{\substack{\sigma,\sigma'=1 \\ \sigma\neq\sigma'}}^{S} \hat{W}^{\sigma\sigma'}(t), \tag{4.4}$$

where $\hat{H}^{\sigma}(t)$ corresponds to the single-species Hamiltonian as presented in Eq. (3.1). Note that each species Hamiltonian consists of N_σ particles subject to the one-body Hamiltonian $\hat{h}^{\sigma}(t)$. In second quantization the single-species Hamiltonian reads,

$$\hat{H}^{\sigma}(t) = \int \mathrm{d}x \hat{\Psi}^{\dagger}_{\sigma}(x) \hat{h}^{\sigma}(t) \hat{\Psi}_{\sigma}(x) + \int \mathrm{d}x_1 \int \mathrm{d}x_2 \hat{\Psi}^{\dagger}_{\sigma}(x_1) \hat{\Psi}^{\dagger}_{\sigma}(x_2) W^{\sigma\sigma}(x_1, x_2; t) \hat{\Psi}_{\sigma}(x_1) \hat{\Psi}_{\sigma}(x_2) \tag{4.5}$$

where $\hat{\Psi}^{(\dagger)}_{\sigma}(x)$ denotes the bosonic field operator which annihilates (creates) a boson at position x. The interspecies interaction term $\hat{W}^{\sigma\sigma'}(t)$ in second quantization reads,

$$\hat{W}^{\sigma\sigma'}(t) = \int \mathrm{d}x_1^{\sigma} \int \mathrm{d}x_2^{\sigma'} \hat{\Psi}^{\dagger}_{\sigma}(x_1^{\sigma}) \hat{\Psi}^{\dagger}_{\sigma}(x_2^{\sigma'}) W^{\sigma\sigma'}(x_1^{\sigma}, x_2^{\sigma'}; t) \hat{\Psi}_{\sigma}(x_1^{\sigma}) \hat{\Psi}_{\sigma}(x_2^{\sigma'}). \tag{4.6}$$

In the case of a two-body contact interaction potential, $W^{\sigma\sigma'}(x_1^{\sigma}, x_2^{\sigma'}; t) = g_{\sigma\sigma'}(t)\delta(x_1^{\sigma} - x_2^{\sigma'})$ this expression can be further simplified to

$$\hat{W}^{\sigma\sigma'}(t) = g_{\sigma\sigma'}(t) \int \mathrm{d}x \hat{\Psi}^{\dagger}_{\sigma}(x) \hat{\Psi}^{\dagger}_{\sigma}(x) \hat{\Psi}_{\sigma}(x) \hat{\Psi}_{\sigma}(x). \tag{4.7}$$

4.2 Primitive Basis

In this section we introduce the primitive basis that discretizes the system and serves as a starting point for more elaborate approaches (see the following sections). In particular, the aim is to discretize the spatial dimension and provide the tools to represent the Hamiltonian in such a basis. To achieve this, we employ a discrete variable representation (DVR) [301, 302] and discuss in Sections 4.2.1 and 4.2.2 two examples corresponding to the sine and exponential DVR, respectively.

The starting point is given by an orthonormal n_{grid}-dimensional basis set $\{\phi_i(x)\}_{i=1}^{n_{\text{grid}}}$ expanded over one spatial dimension. We further consider that the matrix elements of the position operator $\hat{x}$ and the first- and second-derivative operators, $\frac{\mathrm{d}}{\mathrm{d}x}$ and $\frac{\mathrm{d}^2}{\mathrm{d}x^2}$, respectively, are known analytically. In particular, they read,

$$Q_{ij} = \langle \phi_i | \hat{x} | \phi_j \rangle, \tag{4.8}$$

$$D^{(1)}_{ij} = \langle \phi_i | \frac{\mathrm{d}}{\mathrm{d}x} | \phi_j \rangle, \tag{4.9}$$

$$D^{(2)}_{ij} = \langle \phi_i | \frac{\mathrm{d}^2}{\mathrm{d}x^2} | \phi_j \rangle. \tag{4.10}$$

This has the advantage that the evaluation of, e.g. the second derivative appearing in the kinetic term of the one-body Hamiltonian [Eq. (3.2)], can be read from the matrix $(\mathbf{D}^{(2)})_{ij}$. To represent the external potential $V(\hat{x})$ in terms of the primitive basis, an additional integration is required, i.e., $\langle \phi_i | V(\hat{x}) | \phi_j \rangle$. In order to omit such a costly integration, the position operator $\hat{x}$ can be approximated in terms of a finite basis by evaluating Eq. (4.8). This results in a $(n_{\text{grid}} \times n_{\text{grid}})$-dimensional matrix $\mathbf{Q}$ and has the consequence that the potential V depends now on the matrix $\mathbf{Q}$ instead of the operator $\hat{x}$. This approximation is known as *finite basis-set representation* (FBR). To evaluate the potential $V^{\text{FBR}}(\mathbf{Q})$, the position matrix $\mathbf{Q}$ is first diagonalized as,

$$\mathbf{Q} = \mathbf{U}\mathbf{X}\mathbf{U}^\dagger, \tag{4.11}$$

where $\mathbf{U}$ is an unitary operator constructed from the eigenstates of $\mathbf{Q}$. The matrix $\mathbf{X}$ is a diagonal matrix with entries x_α corresponding to the eigenvalues of $\mathbf{Q}$. With this on hand, the potential $V(\hat{x})$ can be approximated as,

$$V^{\text{FBR}}_{ij} = \sum_{\alpha=1}^{n_{\text{grid}}} U_{i\alpha} V(x_\alpha) U^*_{j\alpha}. \tag{4.12}$$

Even though the potential matrix $\mathbf{V}^{\text{FBR}}$ is not exactly equivalent to $V(\hat{x})$, this procedure gives a good estimate and circumvents the costly evaluation of the integrals $\langle \phi_i | V(\hat{x}) | \phi_j \rangle$.

Finally, the primitive basis states, $\phi_i(x)$, are transformed according to the unitary operator $\mathbf{U}$,

$$\chi_\alpha(x) = \sum_{i=1}^{n_{\text{grid}}} \phi_i(x) U_{i\alpha}, \tag{4.13}$$

where $\chi_\alpha(x)$ denotes the primitive basis in DVR. This has the important consequence that expressing $V(\hat{x})$ in terms of the DVR yields the convenient form,

$$V^{\text{DVR}}_{\alpha\beta} = V(x_\alpha)\delta_{\alpha\beta}, \tag{4.14}$$

which corresponds to a diagonal matrix where the elements are direct evaluations of the potential at positions x_α. Likewise, the derivative matrices are transformed into the DVR, while remaining exact. Another aspect of the DVR basis functions is their discrete δ-property,

$$\chi_\alpha(x_\beta) = w_\alpha^{-1/2}\delta_{\alpha\beta}, \tag{4.15}$$

where $w_\alpha^{-1/2}$ denotes the weight of the grid point α. This allows representing any wave function $\psi(x)$ as a vector with elements corresponding to the evaluations of $\psi(x)$, i.e., $\psi = (w_1^{1/2}\psi(x_1), \dots w_{n_{\text{grid}}}^{1/2}\psi(x_{n_{\text{grid}}}))^T$. This comes with the advantage that, for instance, scalar products reduce to simple summations, $\langle \psi | \varphi \rangle = \sum_\alpha w_\alpha \psi^*_\alpha \varphi_\alpha$ and the more costly numerical integrations are circumvented.

4.2.1 Sine DVR

A prominent example for a primitive basis set in DVR are the eigenfunctions of the one-body Hamiltonian consisting of a box potential of length L [302, 303]. The respective eigenfunctions are given by,

$$\phi_j(x) = \begin{cases} \sqrt{\frac{2}{L}} \sin\left(j\pi \frac{x-x_0}{L}\right) & \text{if } x_0 \leq x \leq x_{n_{\text{grid}}+1} \\ 0 & \text{else.} \end{cases} \tag{4.16}$$

The resulting grid points are evenly spaced with a constant weight. Since all eigenfunctions of the box potential vanish at the edges due to the imposed hard-wall boundary condition, the sine DVR implies open boundary conditions.

4.2.2 Exponential DVR

The basis functions of the exponential DVR [252, 303–305] read,

$$\phi_j(x) = \frac{1}{\sqrt{L}} \exp\left(2i\pi \frac{j(x-x_0)}{L}\right), \quad -(n_{\text{grid}}-1)/2 \leq j \leq (n_{\text{grid}}-1)/2. \tag{4.17}$$

Compared to the sine DVR, the exponential DVR imposes periodic boundary conditions, making it suitable for studying systems such as ring potentials or periodic lattices. However, if a large number of grid points is required to accurately discretize the spatial grid, i.e., for $n_{\text{grid}} > 100$, switching to momentum space can significantly reduce the numerical cost. This method is coined the *fast Fourier transform* and is equivalent to the exponential DVR [306, 307].

4.3 Exact Diagonalization Method

The exact diagonalization method is the standard method for finding the solution of a given Hamiltonian $\hat{H}(t)$. The idea is to expand $\hat{H}(t)$ in terms of a finite orthonormal basis set $\{|\kappa_i\rangle\}_{i=1}^{\mathcal{N}}$ and obtain $\hat{H}(t)$ in matrix representation,

$$\mathbf{H}(t) = \sum_{i,j=1}^{\mathcal{N}} \langle\kappa_i|\hat{H}(t)|\kappa_j\rangle. \tag{4.18}$$

The solution of $\mathbf{H}(t)$ is determined by either solving the stationary or time-dependent Schrödinger equation, see Eqs. (4.3) or (4.2), respectively.

In the stationary case $\mathbf{H}(t) = \mathbf{H}$, the problem reduces to an eigenvalue problem,

$$\mathbf{H}\,\mathbf{c}_i = E_i\,\mathbf{c}_i, \tag{4.19}$$

$$|\varphi_i\rangle = \sum_{j=1}^{\mathcal{N}} c_{ij}|\kappa_j\rangle, \tag{4.20}$$

where E_i denotes the i-th eigenenergy corresponding to the eigenfunction $|\varphi_i\rangle$. The eigenvalue problem can be numerically solved by diagonalizing the Hamiltonian in matrix representation[2]. The eigenfunctions $\{|\varphi_i\rangle\}_{i=1}^{\mathcal{N}}$ are expressed in terms of the basis states $|\kappa_j\rangle$ with expansion coefficients $c_{ij}(t)$.

---

[2] In the realm of this thesis, we use predominantly the Python routine `numpy.linalg.eigh` for the diagonalization of a hermitian matrix. This routine employs subroutines from the widely used linear algebra package (LAPACK) based on Fortran [308].

The dynamical evolution of an initial state $|\Psi_0\rangle$ is calculated by integrating over the EOMs obtained from the Dirac-Frenkel variational principle [see Eq. (4.2)]. Considering a time-dependent Hamiltonian $\hat{H}(t)$, the EOMs are given by,

$$i\frac{\partial}{\partial t}c_j(t) = \sum_{k=1}^{\mathcal{N}} H_{jk}(t)c_k(t), \tag{4.21}$$

where $H_{jk}(t) = \langle\kappa_j|\hat{H}(t)|\kappa_k\rangle$. There exist several methods designed to numerically solve such coupled ordinary differential equations, for instance, in Refs. [FT3, FT5] the python routine `scipy.integrate.ode` has been used. The latter employs Runge-Kutta- and zvode-based integrators [309–311]. Note that for each time-instance t the Hamiltonian $\hat{H}(t)$ has to be calculated and expressed in the basis $|\kappa_i\rangle$. Depending on the stiffness of the problem the employed integration routine might require a large number of intermediate integration steps during the time-propagation such that the major numerical cost lies in constructing the right-hand side of Eq. (4.21). In case the Hamiltonian is time-independent, i.e., $\hat{H}(t) = \hat{H}$, the time-evolved wave function is given by,

$$\begin{aligned} |\Psi(t)\rangle &= e^{-i\hat{H}t}|\Psi_0\rangle \qquad (4.22) \\ &= \sum_{j=1}^{\mathcal{N}} e^{-iE_jt}|\varphi_j\rangle\langle\varphi_j|\Psi_0\rangle \qquad (4.23) \end{aligned}$$

which is often the numerically cheaper alternative.

Note that the success of the exact diagonalization method crucially depends on the chosen basis set $\{|\kappa_i\rangle\}_{i=1}^{\mathcal{N}}$, which, on the one hand, has to cover the required Hilbert space to appropriately represent $|\Psi(t)\rangle$ and, on the other hand, has to remain small enough to be numerically efficient. One way to check the convergence of the exact diagonalization method is to gradually increase the basis size and check that the expectation value of an operator of interest does not change within a tolerance. Remark that there exist also techniques which can reduce the numerical cost given that the Hamiltonian corresponds to a sparse matrix [312]. In Ref. [FT5] we have used the exact diagonalization method described above to numerically evaluate the anyon-Hubbard model (see Chapter 6 and Section 7.5). Therefore, the many-body Hamiltonian has been written in a second quantization representation and expressed in terms of a complete basis set consisting of number states.

In Sections 4.3.1 and 4.3.2 we provide two examples which are treated with the exact diagonalization method, namely, the one- and two-atom Hamiltonian. Moreover, we consider that each atom is expanded in terms of a primitive DVR with n_{grid} grid points.

4.3.1 Example I: One Atom on a Spatial Grid

Here, we briefly comment on the case of a single atom confined in one dimension and trapped in an external potential $\hat{V}(x)$. The one-body Hamiltonian has the form as shown in Eq. (3.2) and can be expressed with the procedure described in Section 4.2 in terms of the DVR resulting in a matrix of size $(n_{\text{grid}} \times n_{\text{grid}})$. Since the number of grid points, which are considered in this dissertation, is typically of the order of $\sim 10^2 - 10^3$, the respective one-body Hamiltonian can be readily diagonalized. A useful application of this method is, e.g., the diagonalization of the effective one-body models presented in Eqs. (3.9) and (3.10).

4.3.2 Example II: Two Atoms on a Spatial Grid

Next, we discuss the case of two atoms in one spatial dimension. For convenience, we provide the two-body Hamiltonian for two interacting particles A and B,

$$\hat{H}^{2\mathrm{b}}(x_1, x_2; t) = \hat{h}_A^{1\mathrm{b}}(x_1; t) + \hat{h}_B^{1\mathrm{b}}(x_2; t) + \hat{W}(x_1, x_2; t), \tag{4.24}$$

which is a special case of Eq. (4.4). The term $\hat{W}(x_1, x_2; t)$ refers the two-body interaction potential. While the static one-body problem is solved by diagonalizing the one-body Hamiltonian in grid representation, a similar procedure applied to the two-body Hamiltonian is computationally very costly. For instance, considering for each atom a spatial grid with $n_{\mathrm{grid}} = 100$ grid points would correspond to a Hamiltonian in matrix representation with $(100 \cdot 100)^2 = 1 \times 10^8$ entries (cf. the one-body Hamiltonian in matrix form would correspond to a square matrix with $100^2 = 1 \times 10^4$ entries). In this sense, a more efficient basis representation is required to reduce the numerical cost. One possibility is to expand the two-body problem in terms of products constructed from the eigenfunctions $\{|\varphi_i^A\rangle\}_{i=1}^{\mathcal{M}_A}$ and $\{|\varphi_i^B\rangle\}_{i=1}^{\mathcal{M}_B}$ corresponding to the one-body Hamiltonian $\hat{h}_A^{1\mathrm{b}}$ and $\hat{h}_B^{1\mathrm{b}}$, respectively. The two-body problem is then given by,

$$\begin{aligned} H_{ijkl}^{2\mathrm{b}}(t) &= \langle\varphi_i^A|\langle\varphi_j^B|\hat{H}^{2\mathrm{b}}(t)|\varphi_k^A\rangle|\varphi_l^B\rangle \\ &= \delta_{jk}\delta_{ij}\left(E_i^A(t) + E_j^B(t)\right) + W_{ijkl}(t), \end{aligned} \tag{4.25}$$

$$|\Psi^{2\mathrm{b}}(t)\rangle = \sum_{i=1}^{\mathcal{M}_A}\sum_{j=1}^{\mathcal{M}_B} c_{ij}(t)|\varphi_i^A\rangle|\varphi_j^B\rangle, \tag{4.26}$$

where E_i^A and E_j^B are the eigenenergies of the respective one-body Hamiltonian $\hat{h}_A^{1\mathrm{b}}$ and $\hat{h}_B^{1\mathrm{b}}$, respectively, and $W_{ijkl} = \int\int \varphi_i^A(x_1)^*\varphi_j^B(x_2)^*\hat{W}(x_1, x_2)\varphi_k^A(x_1)\varphi_l^B(x_2)\mathrm{d}x_1\mathrm{d}x_2$. By contracting the indices to $I = (i, j)$ and $J = (k, l)$ the tensor given by $(H_{ijkl})_{1\leq i,k\leq\mathcal{M}_A;1\leq j,l\leq\mathcal{M}_B}$ can be expressed as a matrix $(H_{IJ})_{1\leq I,J\leq\mathcal{M}_A\mathcal{M}_B}$ of size $(\mathcal{M}_A\mathcal{M}_B, \mathcal{M}_A\mathcal{M}_B)$. Finally, the expansion coefficients $c_{ij}(t)$ of the two-body wave function $|\Psi^{2\mathrm{b}}(t)\rangle$ can be determined as described above.

Depending on the truncation parameters $\mathcal{M}_{A(B)}$ this procedure is able to significantly reduce the number of basis functions. For example, in Ref. [FT3] we have represented the effective two-body model in terms of $\mathcal{M}_{A,B} = 10 - 20$ one-body basis functions equating to roughly $\sim 10^2$ two-body basis functions, i.e., $\sim 10^4$ matrix entries. This is a significant improvement compared to the exact diagonalization in grid representation ($\sim 10^8$ matrix entries). Note, that for some special cases there exists also an exact solution for the two-body model. Namely, for two mass balanced atoms confined in a harmonic oscillator [276] or in an anisotropic trap [313, 314] (see Section 3.1.2).

4.4 The MCTDH(B) Method

In the previous Section 4.3, we have emphasized that the correct choice regarding the basis is essential for an efficient numerical treatment of the problem. However, with increasing complexity of the system the appropriate choice of the basis itself becomes a delicate matter. An early idea was to design a time-dependent basis that can be variationally steered within the Hilbert space to cover just the space that is occupied by the exact solution of the system. This space is also referred to as *active space*. A method which has realized this idea is the time-dependent Hartree method in which a single product state - the Hartree product - is varied in a self-consistent manner [298, 315]. In this method, each DOF is represented by a single time-dependent basis function, in this way, drastically decreasing the numerical cost.

A clear disadvantage of this approach is that correlation effects between individual DOFs are ignored entirely so that the Hartree method accounts only for mean-field effects.

A solution to this shortcoming is offered by the multi-configuration time-dependent Hartree method (MCTDH), where the many-body wave function is expanded in terms of several time-dependent Hartree products, allowing the formation of correlations between the DOFs [316, 317]. The corresponding many-body wave-function ansatz for N distinguishable DOFs is formulated as,

$$|\Psi\rangle = \sum_{i_1=1}^{m_1} \cdots \sum_{i_N=1}^{m_N} C_{i_1 \dots i_N}(t) |\varphi_{i_1}^{(1)}(t)\rangle \cdots |\varphi_{i_N}^{(N)}(t)\rangle, \tag{4.27}$$

where the products are weighted by time-dependent expansion coefficients $C_{i_1 \dots i_N}(t)$ and constructed from the elements of the basis sets $\{|\varphi_{i_n}^{(n)}(t)\rangle\}_{i_n=1}^{m_N}$, also referred to as *single-particle function* (SPF). The n-th set of time-dependent SPFs spans the space for the n-th DOF which are in turn expanded over a primitive (static) basis set $\{|\chi_j\rangle\}_{j=1}^{n_{\mathrm{grid}}}$ (see Section 4.2),

$$|\varphi_{i_n}^{(n)}(t)\rangle = \sum_{j=1}^{n_{\mathrm{grid}}} D_j(t) |\chi_j\rangle. \tag{4.28}$$

In the context of ultracold quantum gases, each individual DOF is interpreted as a neutral atom confined in one spatial dimension with coordinate x_i. However, note that for other system setups the DOFs might correspond to, e.g., molecular coordinates defining the vibrational and electronic motion [318–320].

The success of the MCTDH method triggered the extension to indistinguishable DOFs [321] such as fermions [322–324] and bosons [325, 326], where the latter method is abbreviated as MCTDHB. In order to treat bosonic or fermionic DOFs, the corresponding many-body wave function needs to obey the respective particle statistics, i.e., the wave function has to be symmetric or anti-symmetric under the interchange of two bosons or fermions, respectively. This is done by expanding the wave-function ansatz for bosons in terms of symmetric number states (permanents) and for fermions in terms of anti-symmetric Slater-determinants. In the following, we will focus on the description of bosons as these systems are predominantly considered in this dissertation. As mentioned above, the respective many-body wave function consists of an expansion in number states,

$$|\Psi(t)\rangle = \sum_{\vec{n}|N} C_{\vec{n}}(t) |\vec{n}(t)\rangle, \tag{4.29}$$

where $\vec{n}_i = (n_1, \dots, n_m)$ specifies the occupation number of a set of time-dependent SPFs $\{|\varphi_i(t)\rangle\}_{i=1}^{m}$. To assure particle number conservation, the sum of occupied states is required to equate the total number of atoms in the system, $\sum_i n_i = N$, denoted by $\vec{n}|N$. This condition, in combination with the size of the single-particle basis m, determines the total number of possible number states, given by $\binom{N+m-1}{m-1}$. The number states in second quantization read,

$$|\vec{n}(t)\rangle = \frac{1}{\sqrt{n_1! \cdots n_m!}} \left(\hat{b}_1^\dagger\right)^{n_1} \dots \left(\hat{b}_m^\dagger\right)^{n_m} |vac\rangle, \tag{4.30}$$

where $\hat{b}_i^\dagger$ corresponds to the creation operator acting on the vacuum state $|vac\rangle$ which creates a particle in the i-th SPF. Analog to the MCTDH method, the SPFs are expanded in a primitive basis set, see Eq. (4.28). Inserting the ansatzes given in Eqs. (4.27) and (4.29) into the Dirac-Frenkel variation principle [Eq. (4.2)], yields the EOMs for the MCTDH and MCTDHB method, respectively. For more details consult Refs. [302, 326].

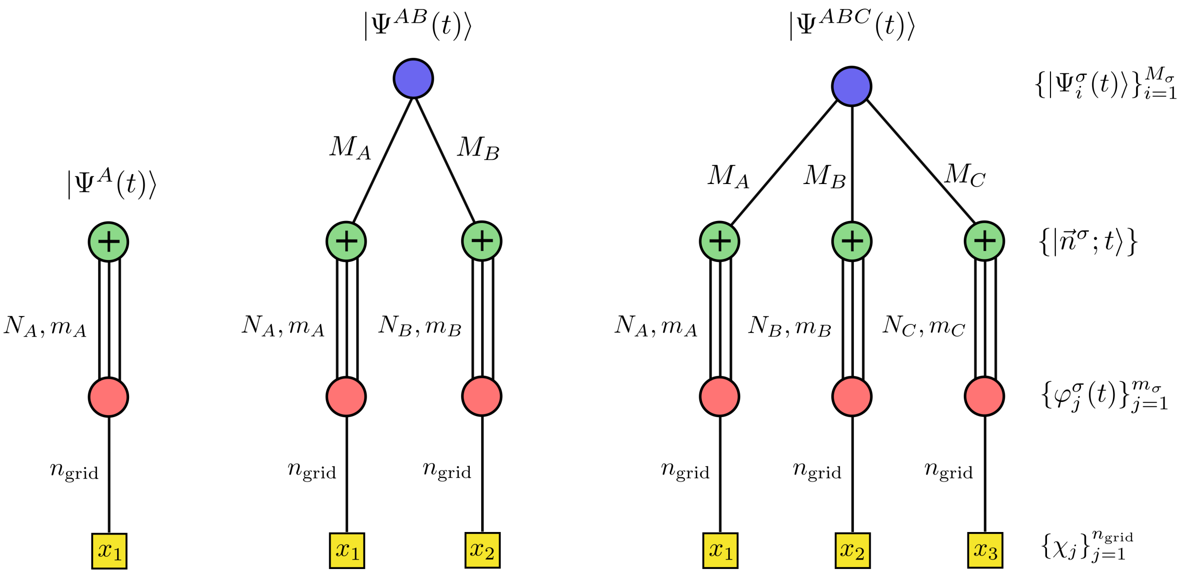

FIGURE 4.1: Tree diagram for the MCTDHB-ansatz [Eq. (4.29)] of a single-component bosonic gas consisting of N_A particles. The plus sign indicates the expansion in terms of number states $|\vec{n}_i\rangle$ constructed from m_A SPFs $(\varphi_i^A(t))$. The SPFs are expanded with respect to a primitive DOF (χ_j) which is in this case a spatial grid consisting of n_{grid} grid points. The middle and right diagram illustrate the ML-MCTDHX ansatz for a two- and three-component ultracold mixture, respectively, shown in Eqs. (4.31) and (4.33). Each species σ is expanded in terms of M_σ species functions where $\sigma = A, B, C$

Note that within this approach the only truncation parameters for a given particle number N are given by the number of grid points and the number of SPFs, which determine the number of expansion coefficients $C_{\vec{n}}(t)$. However, not all number states contribute in the same manner to the many-body wave function and for some physical setups there might be even number states with a vanishing contribution. In view of this, an idea to reduce the numerical cost is to prune such number states as explored in Ref. [327]. Finally, we remark that in this discussion we have considered SPFs that depend only on one (spatial) coordinate. Note that within this method, it is also possible to treat two- or three-dimensional systems by employing SPFs that depend on two or three spatial coordinates, respectively [328–330]. Similarly, atoms with spin can be treated by adding an extra spin-DOF [160, 331].

4.5 The ML-MCTDHX Method

The MCTDHB method outlined in Section 4.4 has been developed for the numerically accurate description of a single-component bosonic mixture. To be able to treat also multiple species of atoms, the method has been extended by adding an additional layer on top of the MCTDHB wave-function ansatz in order to connect the atomic species. This extension allows then the treatment of bosonic mixtures [204, 205]. Subsequently, this method has been generalized to mixtures consisting of bosonic and fermionic atomic species to which we refer to as *multi-layer multi-configuration time-dependent Hartree method for mixtures* (ML-MCTDHX) [206]. In the following, we present the explicit many-body wave-function ansatzes for two- and three-component ultracold mixtures, since these setups are the main subject of this thesis. The respective EOMs are derived from the Dirac-Frenkel variation principle [Eq. (4.2)] and can be found in [204–206].

The many-body wave function of a two-component mixture composed of species A and B reads,

$$|\Psi^{AB}\rangle = \sum_{i=1}^{M_A}\sum_{j=1}^{M_B} C_{ij}(t)\,|\Psi_i^A(t)\rangle\,|\Psi_j^B(t)\rangle, \tag{4.31}$$

$$= \sum_{k=1}^{\min(M_A,M_B)} \sqrt{\lambda_k(t)}\,|\tilde{\Psi}_k^A(t)\rangle\,|\tilde{\Psi}_k^B(t)\rangle. \tag{4.32}$$

In the first step, the wave-function is expanded in terms of single-species wave functions $\{|\Psi_i^\sigma\rangle\}_{i=1}^{M_\sigma}$ with $\sigma = A, B$, where each element $|\Psi_i^\sigma\rangle$ represents a specific state of the entire species σ. In a second step, in Eq. (4.32) the wave function is written in terms of a Schmidt decomposition consisting of Schmidt coefficients λ_i and natural species wave functions $|\tilde{\Psi}_i^\sigma(t)\rangle$ [206]. The squared Schmidt coefficients correspond to the population of the natural species functions and, furthermore, provide information about the interspecies entanglement (see Section 5.1). Convergence is ensured by providing a sufficient large number of species functions $M_A = M_B$ such that adding another function to the basis set does not significantly alter the observables of interest (see Section 4.7 for more details).

In some cases, it is desired to estimate the impact of correlations on certain observables. This is done, for instance, by comparing the observables calculated from different ansatzes that include or exclude correlations (see Section 5.4). In order to ignore the effects stemming from correlations between species A and B, we write the many-body wave function as a single product state, $|\Psi^{AB}\rangle = |\Psi^A(t)\rangle\,|\Psi^B(t)$, by setting $M_A = M_B = 1$. Still, correlations within the species are possible. The latter type of correlations can be additionally ignored by setting $M_A = M_B = m_A = m_B = 1$, where m_A (m_B) denotes the number of single-particle functions of species A (B). The respective two-component wave-function ansatz is then reduced to a mean-field Gross-Pitaevskii ansatz for bosons [332–334].

Analogously, the many-body wave function of a three-component mixture consisting of the components A, B and C is expanded in terms of three sets of species wave functions,

$$|\Psi^{ABC}\rangle = \sum_{i=1}^{M_A}\sum_{j=1}^{M_B}\sum_{k=1}^{M_C} C_{ijk}(t)\,|\Psi_i^A(t)\,\rangle|\Psi_j^B(t)\rangle\,|\Psi_k^C(t)\rangle. \tag{4.33}$$

Similar to the two-component case, the coefficient tensor $C_{ijk}(t)$ provides information about the interspecies entanglement. However, the particular estimation of the entanglement between the components of a three-partite system is not as straightforward as in the bipartite case, see also Chapter 5. In Figure 4.1 we present a sketch of the many-body wave-function ansatz of the MCTDHB method together with the ansatzes of a two- and three-component mixture in the form of tree diagrams to illustrate the close relationship between the methods.

A nice feature of the three-component many-body wave function ansatz is the possibility to realize different types of species mean-field ansatzes. One possibility is to suppress all interspecies correlations by writing the tripartite wave function as a simple product state,

$$|\Psi_{ABC}^{\mathrm{sMF}}\rangle = |\Psi^A(t)\rangle|\Psi^B(t)\rangle|\Psi^C(t)\rangle, \tag{4.34}$$

analogously to the two-component scenario. We refer to this ansatz as the *species mean-field* (sMF) ansatz. Again, note that correlations within a single species are still permitted. An extension beyond the sMF approach is to include correlations between two species and treat the third species as a mean-field type of potential. For instance, if we want to allow for correlations between species A and B and, at the same time, disregard correlations with species C, we can employ the wave-function ansatz,

$$|\Psi^{\text{sMFC}}_{ABC}\rangle = \sum_{i=1}^{M_A}\sum_{j=1}^{M_B} C_{ij}(t)|\Psi_i^A(t)\rangle|\Psi_j^B(t)\rangle|\Psi^C(t)\rangle, \tag{4.35}$$

where species A and B are expanded in terms of $M_{A(B)}$ species functions, while species C resides in a single species function ($M_C = 1$). This type of wave function is referred to as *species mean-field ansatz regarding species C* (sMFC). Analogously, the ansatzes *sMFA* and *sMFB* are defined. In this sense, compared to a two-component wave function, a three-component one offers three more types of species mean-field ansatzes. In Ref. [FT2] we have exploited this property in order to extract the impact of mediated interspecies correlations on the relative distance between two indistinguishable impurities, see Section 5.4 for more details regarding the used procedure.

4.6 Imaginary Time-Evolution

The MCTDHB (ML-MCTDHX) method discussed above is designed to propagate an initial state in real time according to the EOMs derived from the Dirac-Frenkel variational principle [Eq. (4.2)]. However, often the ground state of a many-body system is sought, which can serve as an initial state for a time propagation with a quenched Hamiltonian. In order to reach the ground state of a many-body system, the commonly used strategy is to construct the initial many-body wave function, $|\Psi_{\text{ini}}\rangle$, from the eigenfunctions of the one-body Hamiltonian (Section 4.3.1) and propagate this state in imaginary time, $\tau = it$ [302, 335].

The general idea of propagating in imaginary time becomes apparent when substituting τ into Eq. (4.23) leading to,

$$|\Psi(\tau)\rangle = \sum_{j=1}^{\mathcal{N}} e^{-\tau E_j}|\Psi_j\rangle\langle\Psi_j|\Psi_{\text{ini}}\rangle, \tag{4.36}$$

where $|\Psi_j\rangle$ are the eigenstates of the many-body Hamiltonian with eigenenergies E_j. Propagating the initial state $|\Psi_{\text{ini}}\rangle$ with respect to τ, we find that the overlaps between the initial state and the eigenstates, $\langle\Psi_j|\Psi_{\text{ini}}\rangle$, decay exponentially fast with rates proportional to E_j. The smallest decay rate corresponds to the ground state such that after a sufficiently long propagation time all higher eigenstates are projected out and the major contribution is given by the ground state. In this sense, the initial state relaxes into the ground state. For a successful application of the relaxation procedure, two conditions must be ideally met: A sufficiently large energy gap between the ground and excited states is required, as well as a finite overlap between the initial and the many-body ground state. Note that the imaginary time propagation given in Eq. (4.36) does not conserve the norm of the many-body wave function so that the latter has to be accordingly renormalized.

Finally, we remark that besides the relaxation into the ground state, there exists the possibility to relax into the n-th eigenstate via the improved relaxation method [336–338]. Within this method a combination of imaginary time-evolution and exact diagonalization techniques are employed which typically leads to a faster convergence compared to the energy relaxation process described above. Here, the idea is to express the Hamiltonian in the basis spanned by the species states (cf. top-layer expansion states of the many-body wave-function ansatz in Section 4.5). After diagonalizing this matrix, the wave function can be prepared in the n-th eigenstate. Subsequently, the SPFs are propagated in imaginary time for fixed top-layer coefficients after which this procedure is repeated. Remark that for the improved relaxation a necessary condition is a finite overlap between the initial and the targeted n-th eigenstate.

4.7 Comments on the Convergence of the Many-Body Simulations

In this section, we comment on the convergence properties of the ML-MCTDHX method. Before doing so, we first elaborate on the truncation parameters of this method. Consider a multi-component mixture consisting of S atomic species where each species σ consists of N_σ particles. Then the truncation parameters are given by the species expansion coefficients M_σ, the number of SPFs m_σ of each species, and the number of grid points n_{grid}. Considering that each species is expanded over the same spatial grid with n_{grid} grid points, the total number of coefficients of the many-body wave function is given by [205],

$$\prod_{\sigma=1}^{S} M_\sigma + \sum_{\sigma=1}^{S} \left(M_\sigma \mathcal{N}_\sigma + m_\sigma n_{\text{grid}}\right), \tag{4.37}$$

where $\mathcal{N}_\sigma = \binom{N_\sigma+m_\sigma-1}{m_\sigma-1}$ denotes the number of permanents of species σ. The full configuration interaction limit is reached for $m_\sigma = n_{\text{grid}}$ and $M_\sigma = m_\sigma$. However, this limit can be only reached for very small system sizes so that in general the values of M_σ and m_σ are for numerical reasons far below this limit. Nevertheless, m_σ and M_σ have to be large enough to ensure that all relevant intra- and interspecies correlations are taken into account. The optimal choice for m_σ and M_σ depends highly on the particular system on hand and the respective observables of interest. A way to determine the appropriate choice for m_σ and M_σ is to gradually increase their values and track the convergence behavior of the observables of interest.

A complementary way to judge the convergence of the ML-MCTDHX method is to investigate the natural populations of the reduced density operators $\hat{\eta}_\sigma$ of species σ and the one-body density operator $\hat{\rho}_\sigma$, which read [206],

$$\rho_\sigma^{(1),\text{spec}} = \sum_{i=1}^{M_\sigma} \lambda_i^\sigma(t) |\tilde{\Psi}_i^\sigma(t)\rangle\langle\tilde{\Psi}_i^\sigma(t)|, \tag{4.38}$$

$$\hat{\rho}_\sigma^{(1)} = \sum_{i=1}^{m_\sigma} n_i^\sigma |\Phi_i^\sigma(t)\rangle\langle\Phi_i^\sigma(t)|. \tag{4.39}$$

The eigenvalues $\lambda_i^\sigma(t)$ and $n_i^\sigma(t)$ are the natural populations of the natural species functions $|\tilde{\Psi}_i^\sigma(t)\rangle$ and natural orbitals $|\Phi_i^\sigma(t)\rangle$, respectively. The eigenvalues $\lambda_i^\sigma(t)$ and $n_i^\sigma(t)$ are considered to be hierarchically ordered and sum up to unity. An indicator for the convergence of the numerical calculation is found when the smallest natural population gets sufficiently small (typically less than 1%), i.e., the respective natural species function or natural orbital is only slightly populated and the contribution to the overall many-body wave function is suppressed. However, note that this is not a strict criterion and one has to rely additionally on the convergence behavior of the observables of interest.

Chapter 5

Entanglement and Correlation Measures

A key feature of the ML-MCTDHX method, which distinguishes itself from mean-field based approaches, is the accountability of all relevant inter- and intraspecies correlations. A natural step to characterize a system described within the ML-MCTDHX method is to make a statement about the degree of entanglement or correlation among the participating particles. The literature provides us with a plethora of entanglement measures, see e.g. Refs. [339–341]. In this chapter, we discuss only a few of these entanglement and correlation quantities and apply them to the specific case of two- or three-component ultracold mixtures treated within the ML-MCTDHX method.

In particular, this chapter is structured as follows. In Section 5.1 we introduce the von Neumann entropy and discuss its meaning, when this measure is applied to a binary pure or mixed states. In Section 5.2 we provide the logarithmic negativity, an alternative measure capable of extracting information about the entanglement of a binary mixed state. Section 5.3 is devoted to the experimentally relevant spatially resolved one-, two-, and three-body correlation functions. Finally, in Section 5.4 we discuss how to exploit different species mean-field and many-body wave-function ansatz in order to learn more about the impact of correlations on an observable of interest.

5.1 Von Neumann Entropy

The entanglement of a pure bipartite system can be conveniently estimated by the *entanglement entropy*, i.e., the von Neumann entropy. This quantity is a well-defined entanglement measure suitable for estimating the entanglement between the components of a binary pure state. This measure is directly applicable to the many-body wave-function ansatz of a two-component ultracold-mixture written in terms of a Schmidt decomposition, see Eq. (4.32). From the respective Schmidt coefficients λ_k, the von Neumann entropy is calculated as,

$$S^{\mathrm{vN}} = -\sum_{k=1}^{M} \lambda_k \ln \lambda_k. \tag{5.1}$$

This entanglement measure is maximal for an equal distribution of the natural species states, i.e., all product states $|\tilde{\Psi}_k^A\rangle\,|\tilde{\Psi}_k^B\rangle$ are equally populated with $\lambda_k = 1/M$ and vanishes if only one product state is populated, i.e., $\lambda_1 = 1$ and $\lambda_k = 0$ for $k > 1$. In ultracold setups, two components become entangled once they interact with each other and share a finite spatial overlap [FT1].

To calculate the entanglement entropy in an arbitrary multi-component mixture, one has to first group several components to ensure the required bipartition of the multi-component wave function. For instance, a many-body wave function consisting of three components A,

B and C as presented in Eq. (4.33) reads in the Schmidt-decomposed form as,

$$|\Psi^{ABC}\rangle = \sum_{i=1}^{M_A} \sum_{J=1}^{M_B \cdot M_C} C_{iJ} |\Psi_i^A\rangle |\Psi_J^{BC}\rangle \tag{5.2}$$

$$= \sum_{i=1}^{\min(M_A, M_B \cdot M_C)} \sqrt{\lambda'_k} |\tilde{\Psi}_i^A\rangle |\tilde{\Psi}_i^{BC}\rangle \tag{5.3}$$

where the indices i and j have been merged into a super-index J and the components B and C are grouped together such that the tripartite many-body wave function is interpreted as a bipartite system consisting of the subsystems A and B-C. Inserting the Schmidt coefficients λ'_k into Eq. (5.1), the resulting von Neumann entropy S^{vN}_{A-BC} quantifies the entanglement between component A and the grouped components B and C. The entanglement between B and AC as well as between C and AB can be analogously determined [FT3].

Moreover, it is also possible to calculate the von Neumann entropy for bipartite mixed states. To stay with the example of a three-component mixture, a bipartite mixed state is obtained by integrating/tracing out one component. For instance, tracing out component A leaves us with the mixed state, $\rho^{(2)}_{BC} = \mathrm{Tr}_A \left(|\Psi^{ABC}\rangle\langle\Psi^{ABC}| \right)$. In this case, the density of species B and C ($\rho^{(2),\mathrm{spec}}_{BC}$) is written as,

$$\rho^{(2),\mathrm{spec}}_{BC} = \mathrm{Tr}_A \left(|\Psi^{ABC}\rangle\langle|\Psi^{ABC}| \right) \tag{5.4}$$

$$= \sum_l \langle\Psi_l^A| \left(\sum_{ijk} \sum_{rst} C_{ijk} C^*_{rst} |\Psi_i^A\rangle |\Psi_j^B\rangle |\Psi_k^C\rangle \langle\Psi_r^A| \langle\Psi_s^B| \langle\Psi_t^C \right) |\Psi_l^A\rangle \tag{5.5}$$

$$= \sum_{ijkst} C_{ijk} C^*_{ist} |\Psi_j^B\rangle |\Psi_k^C\rangle \langle\Psi_s^B| \langle\Psi_t^C|. \tag{5.6}$$

$$\tag{5.7}$$

Reshuffling the indices and substituting $D_{jkst} = \sum_i C_{ijk} C^*_{ist}$, the expression is further simplified to

$$\rho^{(2),\mathrm{spec}}_{BC} = \sum_{ijkl} D_{ijkl} |\Psi_i^B\rangle |\Psi_j^C\rangle \langle\Psi_k^B| \langle\Psi_l^C|. \tag{5.8}$$

Grouping the indices i and j to I as well as k and l to K, the bipartite mixed state is written in terms of its eigenstates $|\tilde{\Psi}_i^{BC}\rangle$ as,

$$\rho^{(2),\mathrm{spec}}_{BC} = \sum_i \eta_i |\tilde{\Psi}_i^{BC}\rangle\langle\tilde{\Psi}_i^{BC}|. \tag{5.9}$$

Inserting the eigenvalues η_i into Eq. (5.1) results then in the von Neumann entropy S^{vN}_{BC}. However, note that this quantity has to be distinguished from the von Neumann entropy of a bipartite pure state, i.e., the entanglement entropy, since S^{vN}_{BC} can include besides bipartite entanglement also classical correlations. In Ref. [203] this measure has been used to infer information about the separability regarding the components A-B and C. An alternative way to yield information about the entanglement between the components of a bipartite mixed state, is given by the logarithmic negativity, see the next Section 5.2.

5.2 Logarithmic Negativity

As discussed in the previous section, the von Neumann entropy is a valuable entanglement measure when it comes to binary pure states (see Section 5.1). However, when applied to binary mixed states, the von Neumann entropy does not only quantify the entanglement between the components, but might also include classical correlations. This becomes an issue, when one is interested in quantifying only the quantum entanglement. Here, the logarithmic negativity offers a numerically accessible possibility to estimate the presence of entanglement in a binary mixed state [342, 343], while being an entanglement monotone [344]. This measure has been already applied on, e.g., the dynamics of two Brownian particles coupled to an environment [345–348] or in ultracold three-component setups [FT2, FT3, 194, 349]. In the following, we outline the procedure to calculate the logarithmic negativity on the example of an ultracold three-component mixture consisting of components A, B and C as we have done in Refs. [FT2, FT3]. The aim of this calculation is to obtain a statement about the entanglement between two components, here between the B and C component.

First, we trace out the DOF of the A-component which results in the bipartite mixed state $\rho_{BC}^{(2),\text{spec}}$, see Eq. (5.8). The idea is as follows, if the components B and C are not entangled, the mixed state can be written as a sum of product states,

$$\rho_{BC}^{(2),\text{spec}} = \sum_i p_i \rho_i^B \otimes \rho_i^C, \tag{5.10}$$

where p_i is the probability to find the system in $\rho_i^B \otimes \rho_i^C$. Subsequently, we perform a partially transposition regarding the component B, leading to

$$(\rho_{BC}^{(2),\text{spec}})^{T_B} = \sum_i p_i (\rho_i^B)^T \otimes \rho_i^C. \tag{5.11}$$

For a non-entangled mixed state this operation leaves the spectrum of the partially transposed density matrix $(\rho_{BC}^{(2),\text{spec}})^{T_B}$ unchanged and the eigenvalues remain positive semi-definite, which is referred to as positive partial transpose (PPT) criterion [339, 350]. Note that the inverse case of this criterion holds only when the Hilbert space dimension of the combined subsystems B and C is smaller than six.

In other words, the PPT criterion predicts the presence of entanglement between two subsystems if there exists any negative eigenvalues in the spectrum of the partially transposed density matrix [351, 352]. To convert this criterion into a single quantity, the general form of the bipartite mixed state $\rho_{BC}^{(2),\text{spec}}$ [Eq. (5.8)] is considered and a partial transposition is performed, leading to,

$$\left(\rho_{BC}^{(2),\text{spec}}(t)|_{ijkl}\right)^{T_B} = \rho_{BC}^{(2),\text{spec}}(t)|_{kjil}. \tag{5.12}$$

From this matrix, we extract the negativity $\mathcal{N}$ by diagonalizing it and summing up all negative eigenvalues. Additionally, the sum is multiplied by -1. Remark that the $\mathcal{N}$ is independent of the choice to which species the partial transposition is applied. Finally, we calculate the logarithmic negativity $\mathcal{E}_{BC}$ as

$$\mathcal{E}_{BC} = \log_2(1 + 2\mathcal{N}). \tag{5.13}$$

In this sense, the PPT criterion has been merged into a single quantity that provides us with information about the entanglement of a bipartite mixed state.

5.3 Spatial Correlation Measures

In Sections 5.1 and 5.2 we have discussed binary entanglement measures which are calculated from the coefficients of the respective many-body wave functions. In the following, we provide with the spatial correlation measures a valuable analysis tool accessible also in experiments. In particular, we describe the procedure for calculating the two- and three-body correlation function on the example of a tripartite ultracold mixture consisting of the components A, B and C, as it was done in Refs. [FT2, FT3]. Remark that the employed ML-MCTDHX method introduced in Section 4.5 provides us access to the complete many-body wave function and, therefore, enables the access to any N-body observable.

We begin with giving the definition of the reduced one-, two- and three-body densities [353],

$$\begin{aligned}
\rho^{(1)}_{\sigma}(x^{\sigma}) =&\langle \Psi^{ABC}|\hat{\psi}^{\dagger}_{\sigma}(x^{\sigma})\hat{\psi}_{\sigma}(x^{\sigma})|\Psi^{ABC}\rangle, && (5.14)\\
\rho^{(2)}_{\sigma\mu}(x^{\sigma}_1,x^{\mu}_2) =&\langle \Psi^{ABC}|\hat{\psi}^{\dagger}_{\sigma}(x^{\sigma}_1)\hat{\psi}^{\dagger}_{\mu}(x^{\mu}_2)\hat{\psi}_{\mu}(x^{\mu}_2)\hat{\psi}_{\sigma}(x^{\sigma}_1)|\Psi^{ABC}\rangle, && (5.15)\\
\rho^{(3)}_{\sigma\mu\nu}(x^{\sigma}_1,x^{\mu}_2,x^{\nu}_3) =&\langle \Psi^{ABC}|\hat{\psi}^{\dagger}_{\sigma}(x^{\sigma}_1)\hat{\psi}^{\dagger}_{\mu}(x^{\mu}_2)\hat{\psi}^{\dagger}_{\nu}(x^{\nu}_3)\hat{\psi}_{\nu}(x^{\nu}_3)\hat{\psi}_{\mu}(x^{\mu}_2)\hat{\psi}_{\sigma}(x^{\sigma}_1)|\Psi^{ABC}\rangle, && (5.16)
\end{aligned}$$

where $\sigma,\mu,\nu \in \{A,B,C\}$ and $\hat{\psi}^{(\dagger)}_{\sigma}(x^{\sigma})$ denotes the field operator that annihilates (creates) a particle of species σ at position x^{σ}. The one-body density $\rho^{(1)}_{\sigma}(x^{\sigma})$ provides information about the probability of finding a particle of species σ at the position x^{σ}, while the two-body density $\rho^{(2)}_{\sigma\mu}(x^{\sigma}_1,x^{\mu}_2)$ denotes the probability of measuring at the same time one particle of species σ at position x^{σ}_1 and another particle of species μ at position x^{μ}_2. Analogously is the three-body density $\rho^{(3)}_{\sigma\mu\nu}(x^{\sigma}_1,x^{\mu}_2,x^{\nu}_3)$ defined. The particles can stem from the same or different species.

Following the principles of the cluster expansion approach, the two- and three-body densities can be decomposed with respect to the uncorrelated density and the contribution of two- and three-body correlations [354, 355],

$$\begin{aligned}
\rho^{(2)}_{\sigma\mu} =&\rho^{(1)}_{\sigma}\rho^{(1)}_{\mu} + \mathcal{C}^{(2)}_{\sigma\mu}, && (5.17)\\
\rho^{(3)}_{\sigma\mu\nu} =&\rho^{(1)}_{\sigma}\rho^{(1)}_{\mu}\rho^{(1)}_{\nu} + \left(\mathcal{C}^{(2)}_{\sigma\mu}\rho^{(1)}_{\nu} + \mathcal{C}^{(2)}_{\sigma\nu}\rho^{(1)}_{\mu} + \mathcal{C}^{(2)}_{\mu\nu}\rho^{(1)}_{\sigma}\right) + \mathcal{C}^{(3)}_{\sigma\mu\nu}, && (5.18)
\end{aligned}$$

where $\mathcal{C}^{(2)}_{\sigma\mu}$ inherits information about the two-body correlation between one particle of species σ and another particle of species μ, while $\mathcal{C}^{(3)}_{\sigma\mu\nu}$ accounts for three-body correlations. For simplicity, we have dropped the spatial coordinates x^{σ}_1, x^{μ}_2 and x^{ν}_3. Note that the scheme presented above can be readily extended towards the N-body correlation function. In Refs. [FT2, FT3] we have calculated the two-body correlation function $\mathcal{C}^{(2)}_{BC}$ to extract information about the induced correlation between two non-interacting impurities B and C coupled to a bosonic medium. An alternative expression for the two-body correlation function is obtained by dividing the two-body density with the product of the one-body densities, $g^{(2)}_{\sigma\mu} = \rho^{(2)}_{\sigma\mu}/(\rho^{(1)}_{\sigma}\rho^{(1)}_{\mu})$ [353, 356, 357]. In this way, $g^{(2)}_{\sigma\mu}$ provides information about the relative impact of two-body correlations. This method comes with the caveat that for the numerical estimation a cutoff is required to handle those spatial regions where the one-body densities vanish.

Experimentally, there exists a multifaceted toolbox which allows the detection of multi-body observables [60, 329, 358–361]. For instance, by recording the absorption images after a time-of-flight measurement, it is possible to extract the phase correlation up to the tenth order between two coupled superfluids in a double-well potential [361]. For partially condensed ^{4}He atoms the correlation functions up to the sixth order has been measured by using a single-atom detector [360]. Another technique involves the measurement of polarization phase-contrast images to extract the spatially resolved two-body correlation function of an elongated ^{7}Li BEC [329]. In case of systems a small number of participating particles, as it is the case in

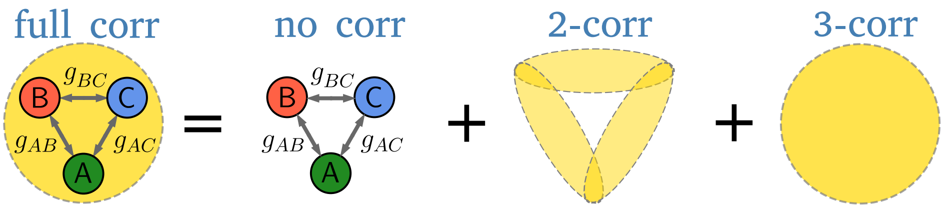

FIGURE 5.1: Schematic diagram to illustrate the decomposition of a three-component system into components with different degrees of correlations. The expectation value of any observable of interest obtained with the full many-body ansatz can be decomposed according to Eq. (5.20) into an uncorrelated part as well as the parts corresponding to second- and third-order correlations.

this dissertation, a larger sample of single-shot images might be necessary to reproduce the density [356, 362]. Yet another method developed more recently consists of a protocol where a deep optical lattice is suddenly ramped up to freeze out the spatial motion of the atoms followed by a fluorescence measurement [363].

5.4 Determining the Impact of Interspecies Correlations on Observables

A feature of the ML-MCTDHX method outlined in Section 4.5 is the ability to calculate the ground state or dynamics of a given system, not only taking into account all relevant correlations, but also using wave function approaches that explicitly exclude certain types of correlations. We can make use of this feature by calculating the expectation value of an observable of interest using different types of wave-function ansatzes that permit or ignore the presence of correlations. Comparing the respective expectation values with each other, we can estimate the impact of correlations on this observable.

In the following, we elaborate further on the example of a three-component mixture consisting of species A, B and C. For these kind of systems, we can suppress the interspecies correlations in various ways with the corresponding wave-function ansatz. For instance, employing the full many-body wave-function ansatz (MB) all interspecies correlations are taken into account, while for the species mean-field ansatz (sMF) all interspecies correlations are suppressed. On the other hand, employing the sMFA (sMFB, sMFC) ansatz only correlations regarding species A (B, C) are suppressed.

With these tools on hand, we are now in the position to determine the impact of correlations between, e.g. species A and B, on any observable $\hat{O}$. For this purpose, we calculate,

$$\Delta_{AB} = \langle \hat{O} \rangle_{\mathrm{sMFC}} - \langle \hat{O} \rangle_{\mathrm{sMF}}, \tag{5.19}$$

where $\langle \hat{O} \rangle_X$ denotes the expectation value of $\hat{O}$ obtained with the wave-function ansatz X. In this sense, Δ_{AB} denotes the difference between the expectation values obtained with a wave function that either facilitates or suppresses correlations between species A and C. In a similar way, the impact of the correlation between A and C as well as B and C on the observable $\hat{O}$ can be determined.

Following a similar line of thought as described in Section 5.3, where the three-body density has been written as a sum of two- and three-body correlation terms, we write also the expectation value $\langle \hat{O} \rangle_{\mathrm{MB}}$ in such a decomposition, i.e.,

$$\langle \hat{O} \rangle_{\mathrm{MB}} = \langle \hat{O} \rangle_{\mathrm{sMF}} + (\Delta_{AB} + \Delta_{AC} + \Delta_{BC}) + \Delta_{ABC}, \tag{5.20}$$

where $\langle \hat{O} \rangle_{\mathrm{MB}}$ denotes the expectation value obtained from the many-body wave function which facilitates any interspecies correlations. This expectation value is further decomposed into a species mean-field part $\langle \hat{O} \rangle_{\mathrm{sMF}}$, the contribution of correlations between two species $(\Delta_{AB}+\Delta_{AC}+\Delta_{BC})$ and a third-order correlation term Δ_{ABC} (see Fig. 5.1 for an illustration). In Ref. [FT2, FT4] we have performed such a decomposition with respect to the relative difference of two distinguishable impurities coupled to a bath. Since the two impurities have been considered to be non-interacting, the third-order correlation contribution can be grasped as a mediated effect. In terms of the relative difference, this mediated effect has be then interpreted as an induced attraction and repulsion.

Chapter 6

One-Dimensional Anyon-Hubbard Model

In this chapter, we give a brief introduction to the anyon-Hubbard model studied in Ref. [FT5]. In quantum mechanics exchanging two indistinguishable particles does not alter the physical state, but can lead to an additional phase factor $e^{i\theta}$. In three dimensions this phase factor is either $+1$ or -1 corresponding to bosons ($\theta = 0$) or fermions ($\theta = \pi$), respectively. However, restricting the motion of the particles to one or two dimensions the phase factor is not only limited to ± 1 and the statistical angle θ can interpolate between bosons and fermions giving rise to anyons [214, 216]. Particles with such an exchange statistic are referred to as abelian anyons which have to be distinguished from non-abelian anyons. A key difference is that adiabatically interchanging two particles with non-abelian statistics leads, instead of a global phase factor, to a nontrivial unitary transformation, a property, which might even find applications in quantum computing [364, 365].

This chapter is divided in two parts. In Section 6.1 we introduce the anyon-Hubbard model and the mapping to the Bose-Hubbard model. In Section 6.2 follows a brief discussion of an experimental realization.

6.1 Mapping to the Bose-Hubbard Model

In the following, we consider N anyons distributed on a lattice potential with L sites. The respective anyon-Hubbard Hamiltonian reads [237, 366],

$$\hat{H}^{\mathrm{AHM,a}} = -J \sum_{j=1}^{L-1} \left(\hat{a}_j^{\dagger} \hat{a}_{j+1} + \mathrm{H.c.} \right) + \frac{U}{2} \sum_{j=1}^{L} \hat{n}_j \left(\hat{n}_j - 1 \right) + \sum_{j=1}^{L} \mu_j \hat{n}_j, \tag{6.1}$$

where $\hat{a}_j^{(\dagger)}$ denotes the annihilation (creation) operator that creates (annihilates) a particle at site j and $\hat{n}_j = \hat{a}_j^{\dagger} \hat{a}_j$ denotes the number operator acting on site j. The parameter J refers to the hopping amplitude between two neighboring sites, while U represents the on-site interaction potential and μ specifies the site-dependent potential. The anyonic exchange statistics can be formulated as [231],

$$\hat{a}_j \hat{a}_k - l e^{-i\theta \mathrm{sgn}(j-k)} \hat{a}_k \hat{a}_j = 0 \tag{6.2}$$

$$\hat{a}_j^{\dagger} \hat{a}_k^{\dagger} - l e^{-i\theta \mathrm{sgn}(j-k)} \hat{a}_k^{\dagger} \hat{a}_j^{\dagger} = 0 \tag{6.3}$$

$$\hat{a}_j \hat{a}_k^{\dagger} - l e^{-i\theta \mathrm{sgn}(j-k)} \hat{a}_k^{\dagger} \hat{a}_j = \delta_{j,k}, \tag{6.4}$$

where $l = \pm 1$ and with $\mathrm{sgn}(j - k) = \pm 1$ for $j \gtrless k$ and $\mathrm{sgn}(0) = 0$. In the case of $l = +1$, for $\theta = 0$ the bosonic exchange statistics is restored while for $\theta = \pi$ the particles behave like pseudo-fermions, i.e., they obey a fermionic exchange statistics with respect to different sites ($j \neq k$) and a bosonic one regarding same sites. The main difference between fermions and pseudo-fermions is that pseudo-fermions can occupy the same site, which is forbidden for spinless fermions due to the Pauli exclusion principle. The situation changes for $l = -1$. In this case, $\theta = 0$ leads to $\hat{a}_j \hat{a}_k^\dagger + \hat{a}_k^\dagger \hat{a}_j = \delta_{j,k}$ which implies a fermionic exchange statistics, while $\theta = \pi$ corresponds to pseudo-bosons. However, in the following, we consider $l = +1$.

Since the atoms occurring in nature follow either a bosonic or fermionic exchange statistics, it is convenient for an experimental realization to express the Hamiltonian in Eq. (6.1) in terms of bosonic or fermionic creation and annihilation operators. To stay in line with Ref. [FT5], we choose bosons as the parent particles for the anyon-Hubbard implementation. The Jordan-Wigner transformation that transforms anyonic operators to bosonic ones reads [366],

$$\hat{a}_j = e^{i\theta \sum_{k<j} \hat{n}_k} \hat{b}_j \tag{6.5}$$

where $\hat{b}_j^{(\dagger)}$ denotes the bosonic annihilation (creation) operator. Applying this transformation to Eq. (6.1), the anyon-Hubbard Hamiltonian becomes,

$$\hat{H}^{\mathrm{AHM,b}} = -J \sum_{j=1}^{L-1} \left(\hat{b}_j^\dagger e^{i\theta \hat{n}_j} \hat{b}_{j+1} + \mathrm{H.c.} \right) + \frac{U}{2} \sum_{j=1}^{L} \hat{n}_j \left(\hat{n}_j - 1 \right) + \sum_{j=1}^{L} \mu_j \hat{n}_j, \tag{6.6}$$

with $\hat{n}_j = \hat{a}_j^\dagger \hat{a}_j = \hat{b}_j^\dagger \hat{b}_j$. In this model the anyonic exchange statistics appears as a density dependent phase in the hopping terms, while the potential terms are independent of the statistical angle θ. Similar to the two-dimensional case, where an additional phase is picked up upon physically exchanging the positions of two particles, in the one-dimensional case, the additional phase is picked up once the system evolves around a closed loop in the Fock space [213]. Moreover, the phase acquired due to hopping processes leads to a breaking of the spatial inversion as well as the time reversal symmetry provided that θ is neither 0 nor a multiple of π, i.e., bosonic nor pseudo-fermionic, respectively. This asymmetry can be observed, e.g. in the expansion dynamics of initially localized anyons and controlled by tuning θ or U [233].

In the above introduction of the anyon-Hubbard model we have implicitly considered open boundary conditions. Alternatively, one can impose periodic boundary conditions. Two possible ways to realize them are given by adding to the open-boundary Hamiltonians $\hat{H}^{\mathrm{AHM,a}}$ and $\hat{H}^{\mathrm{AHM,b}}$ the respective hopping terms to the which connect the first and last lattice site [367], i.e.,

$$H^{\mathrm{AHM,a}}_{\mathrm{periodic}} = \hat{H}^{\mathrm{AHM,a}} - J \left(\hat{a}_L^\dagger \hat{a}_1 + \mathrm{H.c.} \right), \tag{6.7}$$

$$H^{\mathrm{AHM,b}}_{\mathrm{periodic}} = \hat{H}^{\mathrm{AHM,b}} - J \left(\hat{b}_L^\dagger e^{i\theta \hat{n}_L} \hat{b}_1 + \mathrm{H.c.} \right). \tag{6.8}$$

$$\tag{6.9}$$

Note that these two realizations are not equivalent. This becomes evident when mapping the anyonic operators appearing in $H^{\mathrm{AHM,a}}_{\mathrm{periodic}}$ to bosonic ones. In this case, the additional phase $e^{-i\theta N}$ emerges corresponding to a twist at the boundary [367],

$$H^{\mathrm{AHM,b}}_{\mathrm{twisted}} = \hat{H}^{\mathrm{AHM,b}} - J \left(\hat{b}_L^\dagger e^{i\theta \hat{n}_L} \hat{b}_1 e^{-i\theta N} + \mathrm{H.c.} \right). \tag{6.10}$$

The additional twist has the consequence that $H^{\mathrm{AHM,b}}_{\mathrm{twisted}}$ loses the property of being translational invariant. This symmetry can be restored by multiplying each hopping term in $H^{\mathrm{AHM,b}}_{\mathrm{periodic}}$ with the phase $e^{\pm i\theta N/L}$.

In Ref. [FT5] we treat the Hamiltonian in Eq. (6.6) in terms of an exact diagonalization

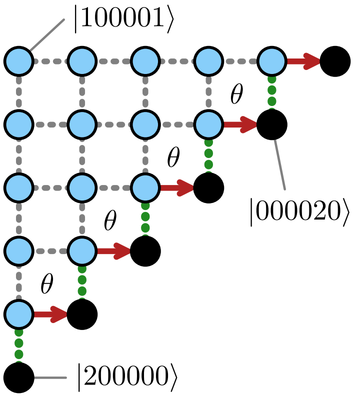

FIGURE 6.1: Configuration space of the anyon-Hubbard model for $L = 6$ and $N = 2$. Each dot represents a bosonic number state, where the black dots denote a double occupation, while the remaining dots denote a single occupation. The edges represent hopping processes with different amplitudes: $-J$ (gray thin), $-\sqrt{2}J$ (green thick) and $-\sqrt{2}Je^{i\theta}$ (red arrow). Figure adapted from Ref. [FT5].

method, see Section 4.3, where we employ a number state basis in order to express $\hat{H}$. The static and dynamical properties are determined as outlined in Section 4.3, i.e., by explicitly solving the stationary and time-depending Schrödinger equation.

6.2 Experimental Implementation

In the following, we discuss the experimental realization of the one-dimensional anyon-Hubbard model. There exists numerous proposals to experimentally realize the anyon-Hubbard model in one dimension, including the implementation in photonic systems [368] or in ultracold atomic platforms, where the atoms are confined by optical lattices [227, 229, 366]. However, only recently the anyon-Hubbard model has been realized in an ultracold setup. In Ref. [213] the anyon-Hubbard model, as expressed in Eq. (6.6), has been realized for the case of two atoms with tunable on-site interactions U and statistical angle θ. Shortly after this, in Ref. [238] the implementation of the hard-core anyon-Hubbard model ($U \to \infty$) has been reported, where the underlying platform consists of a strongly-interacting quantum gas.

Next, we elaborate in more detail on the experiment presented in Ref. [213] as this realization of the anyon-Hubbard model comes closest to the model we have considered in Ref. [FT5]. The experiment in Ref. [213] is conducted with two ^{87}Rb atoms that are loaded into a tilted optical lattice potential. The tilt is required in order to suppress the naturally occurring tunneling processes between the lattice sites. The nearest neighbor tunneling is artificially reintroduced upon applying a Floquet scheme consisting of three modulation frequencies [369]. Therefore, three hopping processes need to be reintroduced. In Figure 6.1 we sketch the possible hopping processes needed for a system consisting of $N = 2$ particles on the basis of $L = 6$ lattice sites. In particular, we show the configuration space where each node corresponds to a specific number state which are connected via edges that represent the nearest-neighbor hopping. The three hopping processes are: (I) A particle hops from a single occupied to an empty site leading to a factor of $-J$ (gray dotted lines in Figure 6.1); (II) a particle hops to an occupied site corresponding to a factor of $-\sqrt{2}Je^{i\theta}$ (red arrows in Figure 6.1); and (III) a particle hops from a doubly-occupied to an empty site resulting in a factor of $-\sqrt{2}J$ (see green dotted lines in Figure 6.1). Each experimental sequence starts with initializing two atoms in neighboring sites of an optical lattice via a postselection process. Subsequently, a tilt is applied and the system is evolved in time using the three-tone Floquet scheme. After the time-evolution, the system is projected on a number state by measuring the atoms at the lattice sites via fluorescence imaging [370]. Averaging over many such snapshots results then in the time-dependent density-density correlation function. When tuning the statistical parameter θ from bosons to fermions, the corresponding dynamics of the anyons reveal the expected fermionization process. The latter appears as an anti-bunching behavior in the density-density correlator. Moreover, considering a finite U the characteristic asymmetric transport process of the anyons for a finite $\theta \neq 0, \pi$ has been observed, in agreement with Ref. [233].

Chapter 7

Outline of the scientific contributions

In this chapter, we provide a summary for the scientific contributions which form the basis of this cumulative dissertation. The respective manuscripts can be found in Chapter 8.

7.1 Counterflow Dynamics of Two Correlated Impurities Immersed in a Bosonic Gas

Impurities in ultracold quantum gases have become a well-established field in ultracold physics enabling the opportunity to study fundamental quantum processes such as the formation of quasi-particles [119], induced interaction [173] or the dynamical response followed by a parameter quench [11]. In Ref. [FT1] we combine several of these aspects into a one-dimensional setup, i.e., we investigate the counterflow dynamics of two impurities immersed in a bosonic medium for different trapping geometries. Since most of the existing literature has been focusing on the counterflow of two large ensembles of atoms [180, 181, 185], we focus in Ref. [FT1] on the counterflow dynamics of two impurities coupled to a bosonic medium. Upon preparing the impurities in a double-well potential, the dynamics is triggered by ramping down the central barrier of the double-well [see Figures 7.1(a) and (b)]. The numerical calculations are obtained within the ML-MCTDHX method, see Section 4.5.

The analysis begins with categorizing the ground state properties of the system with respect to the two-body densities for variations of the impurity-impurity, as well as the impurity-medium interaction strengths, g_{BB} and g_{AB}, respectively[1]. In case the medium is trapped in a box potential, we distinguish four different regimes. These regimes range from a bunching of the impurities for strong attractive or repulsive impurity-medium interactions [regimes (I) and (IV) in Figure 7.1(c)] to an anti-bunching behavior for weak interspecies couplings and strong impurity-impurity repulsions [regime (III)], and an intermediate regime [regime (II)]. The bunching of the impurities emerges as density maxima along the diagonal of the two-body density, reflecting the enhanced probability of finding the impurities at the same position [see insets of Figure 7.1(c)]. This behavior is also referred to as the coalescence of the impurities and has its origin from an induced attraction which is mediated by the bath [166]. On the other hand, for weak g_{AB}, i.e. for weak induced attraction, and comparatively strong internal repulsion, g_{BB}, the impurities anti-bunch, as indicated by the exclusive population of the off-diagonal parts of the respective two-body density. The crossover region can be defined as the interaction region, where the induced attractive interaction strength is comparable to the internal impurity-impurity repulsion, i.e., where $g_{BB} \approx -\frac{g_{AB}^2}{g_{AA}}$ [see Eq. (3.16) and black line in Figure 7.1(c)].

Turning to the case of a harmonically trapped bosonic medium, the impurities show a similar bunching and anti-bunching behavior as in the previous case of a box confined medium, but at altered interaction regions. Here, the relation $g_{BB} \approx -\frac{g_{AB}^2}{g_{AA}}$ cannot be used to determine

---

[1] Note that in [FT1] we refer to the impurity-impurity and impurity-medium interaction strengths as g_{II} and g_{BI}, respectively, but in this dissertation we use the expressions g_{BB} and g_{AB} for consistency reasons.

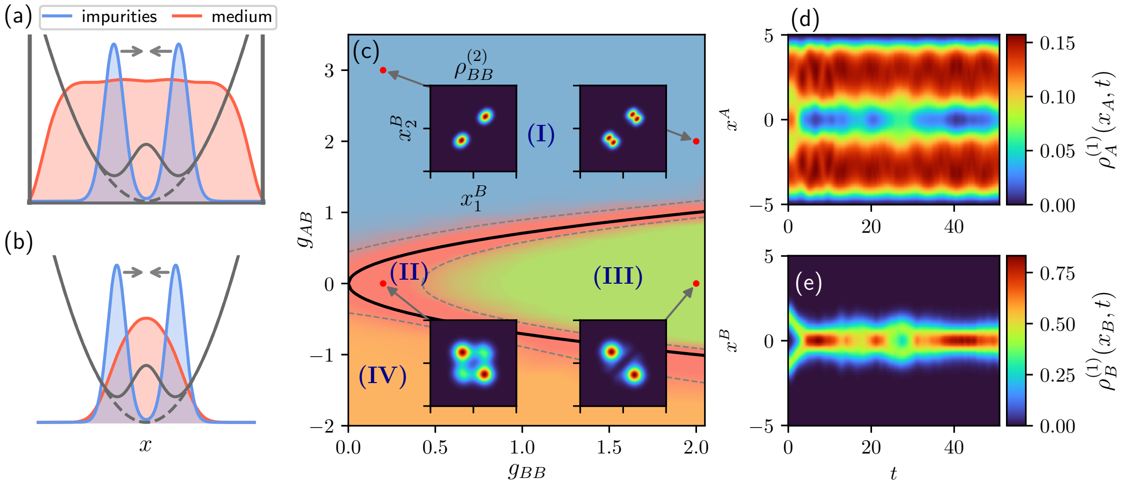

FIGURE 7.1: Sketch of the quench protocol applied in Ref. [FT1], where two impurities are coupled to a medium confined in (a) a box or (b) harmonic oscillator potential. (c) Ground state phase diagram categorized with respect to the two-body densities of the impurities (see insets) and the medium. Dynamical evolution of the one-body density of (d) the medium and (e) the impurities for weak impurity-impurity and strong impurity-medium repulsions ($g_{BB} = 0.2$ and $g_{AB} = 1.5$). Figure adapted from Ref. [FT1].

crossover regime between bunched and anti-bunched impurities in this sense, revealing the strong impact of the underlying trapping potential of the medium on the impurities' interplay. Moreover, for strong attractive g_{AB} the impurities and the bath particles localize at the same spatial position and show a bunching behavior. This clustering is accompanied by a negative bipolaron energy indicating the formation of a bound state, i.e., a bipolaron [166, 169, 193].

In a second step, the dynamics is induced by ramping down the potential barrier of the impurities' double-well potential, in this way, triggering the counterflow of the impurities. For weak impurity-medium interaction strengths, the impurities perform a breathing like motion, regardless of the underlying trapping potential of the medium. For larger repulsive g_{AB} and for a bosonic medium confined in a box potential, the impurities collide at the trap center, where they remain localized in the course of the time-propagation. This property is reminiscent for the presence of an induced attractive behavior [see Figures 7.1(d) and (e)]. In the case of a harmonically confined medium, the breathing-like dynamics of the impurities observed in the temporal evolution of the one-body density turns out to be a projection of an oscillation between a bunching and an anti-bunching tendency. This becomes apparent when inspecting the temporal evolution of the two-body density function. A deeper insight into the participating states is obtained by devising an effective two-body model consisting of two one-body terms of the form of Eq. (3.9) and a contact interaction potential with strength g_{BB}. By projecting the respective many-body wave function on the eigenfunctions of this two-body Hamiltonian, we identify the participating two-body states. Finally, for strong g_{AB}, i.e., in the immiscible regime, the impurities are not able to penetrate the medium and remain at the edges of the latter where they perform small oscillations.

7.2 Crossover from Attractive to Repulsive Induced Interactions and Bound States of Two Distinguishable Bose Polarons

In the case where two or more impurities couple to an ultracold gas, intriguing phenomena emerge that are beyond the single-impurity paradigm. Analogous to the case of a single

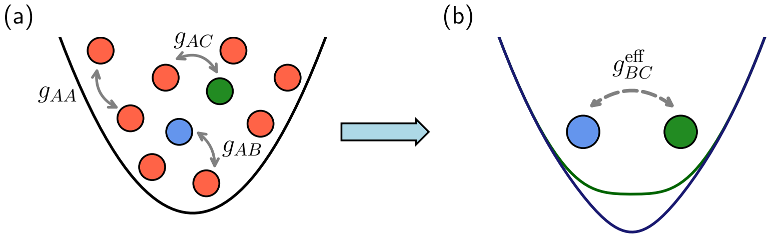

FIGURE 7.2: (a) Sketch of the three-component setup analyzed in Ref. [FT2]. We consider two non-interacting impurities coupled to a bosonic medium confined in a one-dimensional harmonic oscillator potential. (b) The behavior of each impurity is effectively captured by an effective one-body model. The induced interaction between the impurities is modeled by an effective contact interaction potential of strength g_{BC}^{eff}.

impurity coupled to a bath, also multiple impurities can become dressed by the excitations of the medium giving rise to quasi-particles. Depending on the coupling strength between the host and the impurity atoms, the former can mediate a strong or weak effective interaction between the impurities. For an one-dimensional Bose gas and two indistinguishable impurities it has been shown that the character of the induced interaction is always attractive [165–171]. However, distinguishable impurities offer the flexibility of coupling each impurity individually to the bath, opening up the scenario, where one impurity is attractively coupled, and the other repulsively coupled to the bath. In this case the mediated interaction is expected to be repulsive [167, 168, 177, 202]. In Ref. [FT2] we consider a harmonically confined majority species A coupled to two distinguishable impurities B and C in one dimension [see Figure 7.2(a)]. Furthermore, to facilitate the observation of a mediated interaction, we set the interaction strength among the impurities to zero, $g_{BC} = 0$, and vary only the impurity-medium coupling parameters g_{AB} and g_{AC}.

In a first step, we calculate the one-body densities of the three species using the many-body wave-function ansatz of the ML-MCTDHX method for various interaction configurations. The behavior of the impurities' one-body density is interpreted in terms of an effective one-body picture in which the medium acts as a mean-field potential [see Eq. (3.9)]. Adding this mean-field contribution to the harmonic oscillator potential leads to an effective potential which has, i.e., for repulsive impurity-medium interaction strengths, the form of a double-well potential. In this sense, the effective potential reflects the dephasing process between the impurities and the medium occurring at these interactions. In the attractive case, the impurities localize at the center and the effective potential takes the form of a dipped harmonic oscillator potential. Solving the effective one-body model shown in Eq. (3.9), we find good agreement with the many-body approach in terms of the one-body density.

In a second step, the two-body correlation behavior of the impurities and the medium is analyzed. For this purpose we calculate the spatially resolved two-body correlation function [see Eq. (5.17)]. If the impurities couple both attractively or repulsively to the bath, their correlation function is positive along the diagonal and negative at the off-diagonal parts, indicating an induced bunching tendency between the impurities [see Figure 7.3(a2)]. We observe the inverse behavior when the impurities couple to the bath with opposite signs, i.e., one impurity attracts the bath while the other repels it. In this case, the two-body correlation function exhibits an anti-correlated pattern indicating an anti-bunching tendency between the impurities [see Figure 7.3(a1)]. By integrating over a certain part of the spatial correlation function the (anti-)bunching tendency is extracted and captured by a scalar value [see dashed lines in Figures 7.3(a1) and (a2)]. This reduced quantity is used to draw a phase diagram shown in Figure 7.3(b) as a function of the impurity-medium interaction strengths g_{AB} and g_{AC}.

Next, we conduct a more direct approach to quantify the induced interaction by devising

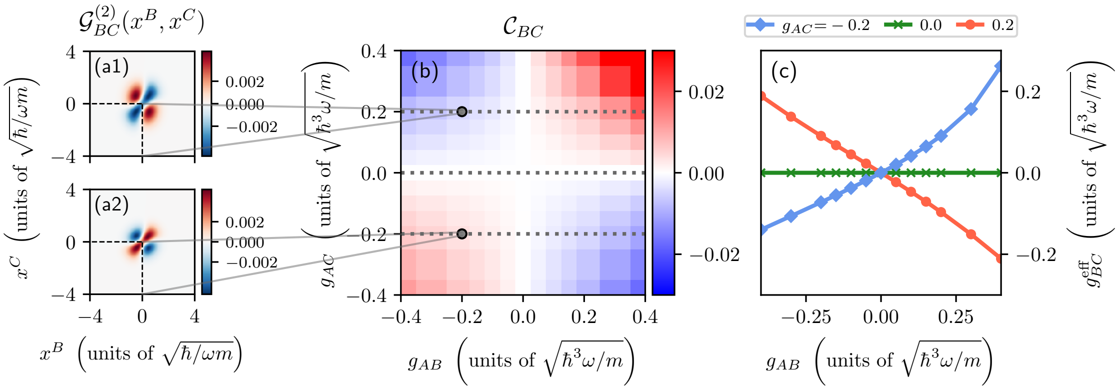

FIGURE 7.3: Depending on the impurity-medium interaction strength the impurities' two-body correlation function exhibits either an induced (a1) anti-bunching or (a2) bunching behavior. Integrating over the left side of the spatial grid [dashed lines in panels (a1) and (a2)], the induced correlation behavior is merged into a single quantity from which a phase diagram can be constructed, see panel (b). (c) By devising an effective two-body model the induced bunching (anti-bunching) behavior can be associated with an induced attraction (repulsion). Figure adapted from Ref. [FT2].

an effective two-body model. This model consists of two effective one-body models coupled via a contact interaction potential, see for a sketch Figure 7.2(b). The respective effective interaction strength (g^{eff}_{BC}) is determined by varying its value such that the two-body correlation function obtained from the effective two-body model matches that one obtained from the full many-body ansatz. By doing so, we ensure that the effective interaction strength can be directly related to the two-body correlation behavior of the impurity. Fixing one interaction strength to, e.g., attractive values and vary the other interaction parameter from attractive to repulsive values, we observe the crossover from an induced attraction to an induced repulsion, following the relation $g^{\mathrm{eff}}_{BC} \sim -g_{AB} \cdot g_{AC}$. In particular, we find that in regimes where the impurities are correlated (anti-correlated), the mediated interaction is attractive (repulsive) [see Figure 7.3(c)]. To infer information about the effect of the interspecies correlations on the induced interaction, the impurities' relative difference is decomposed in terms of a species mean-field, a two-body and a three-body correlation part, see Eq. (5.20). We find that the contribution of the three-body correlation term, i.e., the contribution associated with the mediated interaction, behaves as $\sim -g_{AB} \cdot g_{AC}$. In particular, the mediated correlation between the impurities causes either a reduction of the impurities' relative difference for $g_{AB} \cdot g_{AC} > 0$ (associated with an induced attraction) or an increase for $g_{AB} \cdot g_{AC} < 0$ (corresponding to an induced repulsion).

Finally, we investigate the formation of bound states which emerge for attractive impurity-medium interaction strengths. In these regimes the mediated interaction between the impurities can reach sufficiently strong values and facilitate the formation of a bound state, also known as bipolaron [150, 174–176]. We demonstrate the formation of a bipolaron in our setup by verifying that the respective bipolaron energy is negative for sufficiently strong impurity-medium attractions. Moreover, we assure that the size of the dimer state, captured by the impurities' squared relative difference, shrinks with increasing attraction in agreement with Ref. [175]. In addition, when both interaction parameters g_{AB} and g_{AC} are equally tuned towards large attractive values, the impurities' two-body density obtains an ellipse-like shape indicating the bunching of the impurities. We calculate the respective eccentricity of the ellipse and observe its saturation at moderate attractive values. The dimer state keeps shrinking when further increasing the impurity medium attractions. A similar analysis is performed with respect to the three-body density calculated for one bath particle and the impurities. Varying g_{AB} and g_{AC} equally towards attractive values, the three-body density evolves into the form of an ellipsoid exhibiting three eccentricities. Analog to the behavior of the two-body density, also the shape of the ellipsoid does not significantly change after moderate attractive values which is reflected in a saturation of the eccentricities. This analysis suggests that the formation of a bipolaron is additionally accompanied by the formation of a trimer state consisting of the impurities and one bath particle.

7.3 Effective Approaches to the Dynamical Properties of Two Distinguishable Bose Polarons

In the previous Section 7.2 we have elaborated on a three-component ultracold setup consisting of a harmonically confined bath A coupled to two distinguishable impurities B and C [FT2]. In this course, we have revealed the presence of an effective attractive and repulsive interaction potential mediated between the impurities due to the coupling to the majority. In particular, we have quantified the effective interaction employing an effective two-body model. However, this study has exclusively focused on the static properties of the induced interplay, which urges the question how the mediated interaction between the impurities is affected when tuning the coupling parameters in time, e.g., when the impurity-medium coupling strengths vary between regimes corresponding to different induced effective interactions. In Ref. [FT3] we pursue this question and study the dynamical response upon linearly ramping the interaction parameters $g_{AB}(t)$ and $g_{AC}(t)$ in time from either attractive to repulsive values or vice versa, while $g_{BC} = 0$. Here, the aim is to understand the dynamical behavior of the impurities coupled to a majority species in the framework of effective one- and two-body models [see Figures 7.4(a) and (b)]. For this purpose, we apply several approaches and reveal their quality and limitation in terms of the ability to capture the behavior of observables obtained with a many-body approach.

We begin with exploring the dynamical response of the one-body densities for different linear interaction ramps. Depending on the slope of the applied ramps the impurities reveal a weak or strong breathing-like dynamics. For instance, when tuning both interaction parameters $g_{AB}(t)$ and $g_{AC}(t)$ equally from attractive to repulsive values, the impurities, which are initially localized at the trap center, expand and subsequently contract again, which is repeated in a periodic fashion. Ramping instead from attractive to large repulsive values, which are larger than the internal repulsion between the bath particles g_{AA}, we observe a temporal phase-separation of the impurities and the majority species. In this dynamical regime, the impurities probe the edges of the bath for finite periods of time.

To construct an effective two-body model, we first develop an effective one-body model which is able to capture the dynamical behavior of a single impurity. In particular, we consider only correlations between the first impurity and the medium and neglecting correlations with the second impurity. This scenario is realized by employing a sMFB or sMFC ansatz (see Section 4.5). In this way, the effective model is compared only to results that neglect third-order effects on the species level, i.e., effects that stem from an induced correlation. We employ three different one-body models constructed from time-dependent effective parameters and judge their quality by comparing their spatial variance to the ones obtained with an sMFB or sMFC ansatz. The first one-body model follows the idea presented in Eq. (3.9), i.e., the effects of the bath are treated in a mean-field type of manner by adding to the undisturbed one-body Hamiltonian a time-dependent effective potential. This mean-field potential consists of the medium's one-body density weighted by the respective impurity-medium interaction strength. The second and third models follow the ansatz presented in Eq. (3.10), where the impurity is interpreted as a quasi-particle with a time-dependent effective mass, $m_\sigma^{\mathrm{eff}}(t)$, and effective trapping frequency, $\omega_\sigma^{\mathrm{eff}}(t)$, where $\sigma = B, C$. In the second model, the effective mass and frequency are ramped in time according to their adiabatic solution, while the third

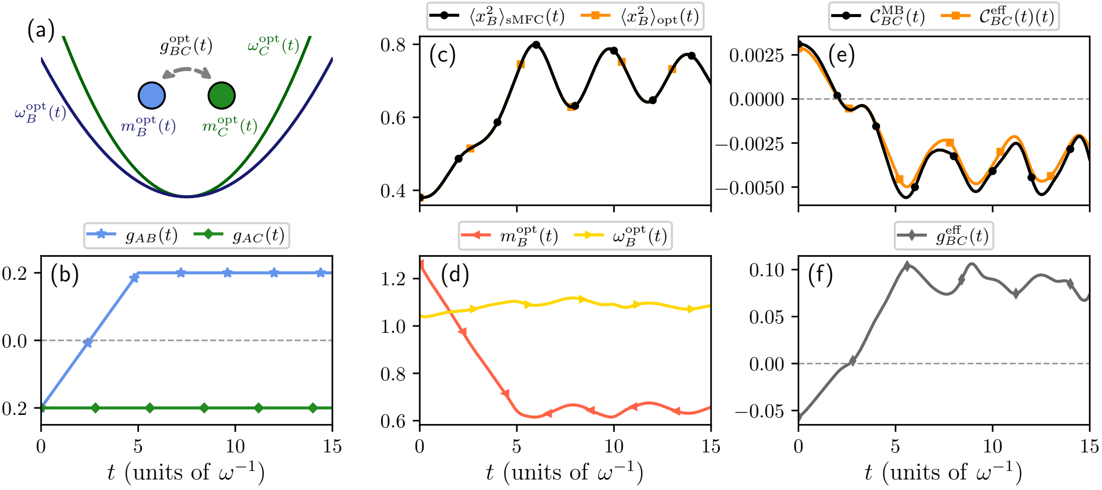

FIGURE 7.4: We consider two distinguishable impurities coupled to a bosonic medium. (a) Sketch of the effective two-body model devised to capture the impurity dynamics triggered by ramping the impurity-medium interaction strength. Employing the interaction ramp shown in panel (b), the spatial variance of impurity B obtained within the sMFC ansatz is accurately captured by the effective one-body model that consists of an optimized effective mass and frequency, shown in (d). (e) Time-evolution of the integrated correlation function. The crossover from an induced anti-bunching to bunching behavior can be described by a time-dependent effective contact interaction potential with strength $g_{BC}^{\rm eff}(t)$, see panel (f). Figure partially adapted from Ref. [FT3].

model employs effective parameters that are fitted to the one-body density and the spatial variance obtained from the sMFB or sMFC ansatz. This fitting process leads to an optimized effective mass, $m_\sigma^{\rm opt}(t)$, and frequency, $\omega_\sigma^{\rm opt}(t)$. Compared to the former two methods, the last one captures best the target behavior of the spatial variance [cf. Figures 7.4(c) and (d)]. Importantly, the optimized effective mass and frequency give insights into the change of the dressed impurities during the dynamics. For example, we find that as $g_{AB}(t)$ ramps from weakly attractive to weakly repulsive values and for constant weakly attractive g_{AC}, the effective mass of impurity B decreases from a value above the bare mass to a value below, indicating the transition from a heavy to a light dressed impurity. This behavior can be attributed to the presence of a harmonic oscillator potential, which is known to lead to smaller effective masses in the repulsive regime [FT2, FT8, 291]. The procedure applied in this work provides an alternative approach for treating the dynamical response of dressed impurities in an effective picture. So far, the existing literature has focused on describing the dynamical response of an impurity in terms of static effective models with constant effective parameters. An example is given by [153], where a constant effective mass has been extracted by fitting the time-evolved mean position of an impurity to a damped harmonic oscillator. In contrast to these kind of approaches, we show that the application of time-dependent effective models consisting of optimized effective parameters can be a complementary powerful tool, when it comes to accurately describing the complex dynamics of dressed impurities.

To construct the effective two-body model, we couple two effective one-body models via a time-dependent effective interaction potential. As one-body models we take the ones, which capture best the one-body dynamics of the quasi-particles, namely, the ones consisting of optimized effective parameters. For the effective interaction potential, we consider three different types of potentials and judge their ability to capture the induced interplay between the impurities by comparing the impurities' relative difference and integrated two-body correlation function to the ones obtained by the full many-body approach. The first ansatz for the effective interaction potential has the form of a Yukawa-type potential [see Eq. (3.15)] with a time-dependent factor proportional to $-g_{AB}(t) \cdot g_{AC}(t)$. The other two approaches approximate the induced interactions by a contact interaction potential with a time-dependent effective interaction strength $g_{BC}^{\text{eff}}(t)$. In the first case, the effective interaction strength evolves in time according to the adiabatic solution, i.e., for each time-instance t the effective interaction strength is obtained from the ground-state solution corresponding to the interaction values $g_{AB}(t)$ and $g_{AC}(t)$. In the second case, the path of the interaction strength is varied such that the overlap between the spatially resolved two-body correlation function obtained by the effective model and the correlation function calculated from the many-body ansatz is minimized. As it turns out, the adiabatic model as well as the model that includes the Yukawa-type potential are only qualitatively able to capture the impurities' two-body correlation behavior and deviate significantly from the target behavior at time scales larger than the ramp time. The best approximation is found regarding the optimized effective interaction strength, $g_{BC}^{\text{opt}}(t)$ [see Figure 7.4(e)][2]. In this course, we find that, e.g., by ramping $g_{AB}(t)$ from attractive to repulsive values and fixing $g_{AC}(t)$ to an attractive value, the mediated interaction varies from an initial attraction ($g_{BC}^{\text{opt}}(t) < 0$) to a mediated repulsion ($g_{BC}^{\text{opt}}(t) > 0$), see Figure 7.4(f). Importantly, the optimized interaction strength captures the correlated two-body behavior of the impurities also for times longer than the ramp time. Finally, we use the effective two-body model to estimate the entanglement between the impurities and compare the results to the logarithmic negativity and to the von-Neumann entropy (see Sections 5.1 and 5.2).

7.4 Effective Two- and Three-Body Interactions between Dressed Impurities in a Tilted Double-Well Potential

In the works [FT2, FT3] we have investigated the interplay between two distinguishable impurities mediated by a bosonic majority species and devised an effective two-body model that relied on fitting to the two-body correlation function obtained by a many-body method. In Ref. [FT4] we provide an alternative approach for determining the induced interaction mediated between impurities and reveal the impact of an effective two- and three-body interaction strength on the one-body density.

The setup significantly differs from the ones considered in Refs. [FT2, FT3]. In particular, we consider a homogeneous bosonic gas A confined on a ring potential with periodic boundary conditions which is coupled to up to three impurities trapped in a tilted double-well potential [see Figures 7.5(a)-(c)]. The idea of the applied tilt is to break the spatial inversion symmetry of the system and bring it close to a tipping point, where slight variations can have significant effects [87]. Specifically, the tilt leads to a population imbalance of the impurities with respect to the two double-well sites. We quantify the population imbalance by integrating over the one-body density at the energetically elevated site. We begin with assuming two weakly-interacting bosonic impurities of species B. When increasing or decreasing the impurity-medium coupling strength g_{AB} away from the non-interacting case ($g_{AB} = 0$), the impurities begin to localize at the energetically lower site, which is accompanied by a decrease of the integrated density. We capture this behavior in terms of an effective two-body model of the form of Eq. (3.13), where the mediated interaction potential is approximated by a contact interaction potential. The effective interaction strength is found by matching the energy of the effective model to the polaron and bipolaron energies obtained by many-body

---

[2] Note that this optimization routine is computationally highly demanding. We tackle this by representing the time-dependent path of $g_{BC}^{\text{opt}}(t)$ in terms of interpolation points. The respective amplitudes are varied according to an optimization algorithm. During the optimization process, each iteration corresponds to a separate time-evolution of the effective two-body Hamiltonian with time-dependent effective parameters. The two-body dynamics are calculated following the procedure outlined in Section 4.3.2.

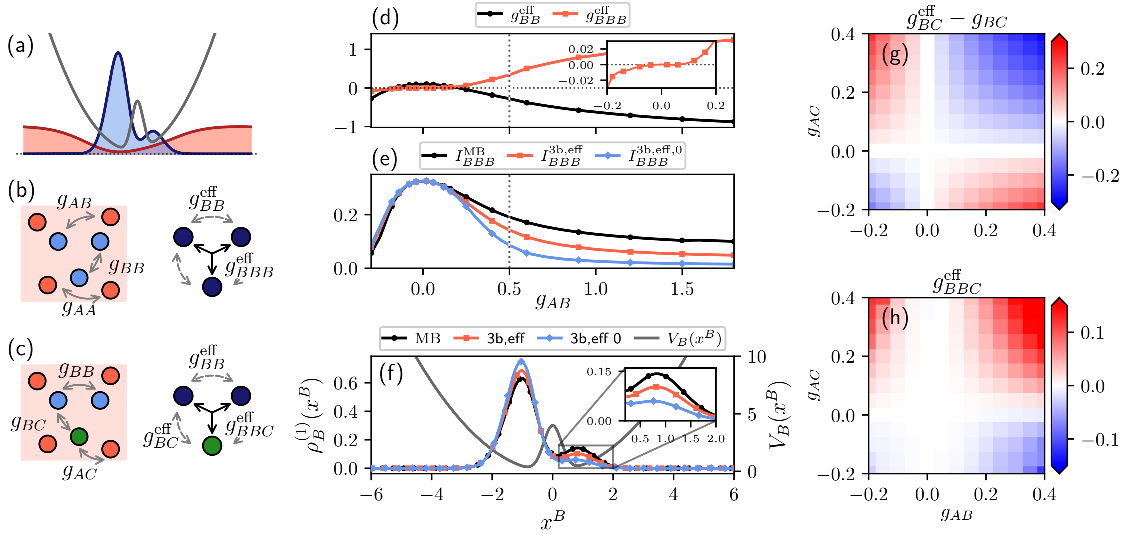

Figure 7.5: We consider up to three interacting impurities belonging to the same or different species which are trapped in a tilted double-well potential and coupled to a bosonic medium A that is confined on a ring potential. (a) Illustration of the one-body density of the medium (red shaded area) and the impurities (blue shaded area) together with the tilted double-well potential (gray line). (b) Sketch of the setup consisting of (b) three bosonic impurities belonging species B and (c) two bosonic and one distinguishable impurity belonging to species B and C, respectively. The impurities' behavior is effectively captured by two- and three-body models consisting of effective two- and three-body contact interaction potentials, see right side of panels (b) and (c). (d) Effective two- and three-body interaction strengths mediated among three bosonic impurities. (e) The quality of the three-body model is judged by comparing the impurities' density integrated over the right double-well site ($I_{BBB}^{\mathrm{3b,eff}}$) to the many-body results (I_{BBB}^{MB}). $I_{BBB}^{\mathrm{3b,eff,0}}$ denotes the results of the effective model, where $g_{BBB}^{\mathrm{eff}} = 0$. (f) One-body densities at $g_{AB} = 0.5$ obtained by different approaches (see legend). Effective (g) two- and (h) three-body interaction strengths for two distinguishable impurities as well as two indistinguishable and one distinguishable impurity, respectively, in dependence of the impurity-medium coupling parameters g_{AB} and g_{AC}. Figure partially adapted from Ref. [FT4].

calculations [166, 207, 297, 371]. We find an overall mediated attractive interaction between the impurities that obeys the relation $g_{BB}^{\mathrm{eff}} - g_{BB} \sim -g_{AB}^2$, where g_{BB} is the bare impurity-impurity interaction strength [cf. Figure 7.5(d)]. Comparing the integrated one-body density of the effective model with the results obtained by a many-body calculation, i.e., by the ML-MCTDHX method (see Section 4.5), we find good agreement.

The setup is further extended to the case of three bosonic impurities. Their effective behavior is captured by an effective three-body model that approximates the mediated forces in terms of an effective two-body interaction potential and, additionally, by a three-body contact interaction potential. Similar to the two-impurity scenario, the three-body interaction strength (g_{BBB}^{eff}) is determined by fitting the ground state energy of the effective model to the polaron, bipolaron and three-polaron energies. For small impurity-medium interaction strengths, we find a cubed behavior, i.e., $g_{BBB}^{\mathrm{eff}} \sim g_{AB}^3$, see Figure 7.5(d) and its inset. In particular, for positive g_{AB} the effective three-body interaction strength is repulsive and counteracts the induced attractive two-body forces. The impact of the three-body interaction strength on the integrated one-body density can be judged by comparing the results obtained with and without the three-body interaction term [Figure 7.5(e)]. When increasing g_{AB} from 0 to repulsive values, the effect of excluding the three-body interaction term manifests in a faster localization of the impurities compared to the results obtained with a three-body term, see also the spatially resolved one-body densities for $g_{AB} = 0.5$ in Figure 7.5(f). This effect is more pronounced for larger values of g_{AB}, where the mediated three-body interaction strength g_{BBB}^{eff} becomes larger.

We extend the analysis further by considering two distinguishable impurities B and C that interact with a majority species A. This setup presumes a three-component ultracold mixture and is similar to the scenarios considered in Refs. [FT2, FT3]. The three-impurity scenario is realized by adding a second impurity to species B. We construct the respective two- and three-body models and apply an analogous fitting procedure as done in the case of indistinguishable impurities. In particular, we find a scaling for the effective two-body interaction strength which behaves like $g_{BC}^{\mathrm{eff}} - g_{BC} \sim -g_{AB} \cdot g_{AC}$, as well as a scaling for the effective three-body interaction strength of the form of $g_{BBC}^{\mathrm{eff}} \sim g_{AB}^2 \cdot g_{AC}$, see Figures 7.5(g) and (h), respectively. Additionally, we compare the many-body simulations with a pure mean-field calculation, which shows a good agreement in terms of the energy and a qualitative agreement regarding the one-body density. Finally, we discuss the implications for the one-body results when including an effective mass in the effective two-body model.

7.5 Chirally-Protected State Manipulation by Tuning One-Dimensional Statistics

Before delving into the details of Ref. [FT5], we would like to give a brief overview of the history of this project and how this work is related to the previous projects outlined above. The project has been inspired by an earlier work (see Ref. [FT8]), where we have studied the collisional aspects of an impurity injected into a Bose gas confined in a double-well potential. Since this work has been done employing the ML-MCTDHX method, the idea was to combine this method with the anyon-Hubbard model in the continuum limit [231] and study the collision dynamics of two or more anyons. However, we realized that this idea could not be easily adapted to the ML-MCTDHX implementation and continued with investigating the collision of anyons in the framework of the anyon-Hubbard model (see Chapter 6). The project took another turn, when we found some unexpected degeneracies in the energy spectrum of the ground state with intriguing properties so that we have based the work [FT5] on these observations.

The starting point is given by N atoms with an anyonic exchange statistics that are distributed over a lattice with L sites. Furthermore, we neglect on-site interactions and allow only hopping between nearest-neighbors. Such a system is described by the anyon-Hubbard model presented in Eq. (6.1) with $U = 0$ and $J = 1$ so that the Hamiltonian consists only of bosonic hopping terms multiplied by a density-dependent Peierls phase with a statistical angle θ. The energy spectrum is calculated by employing an exact diagonalization method. We find that certain combinations of (L, N) lead to a degeneracy of the eigenvalues with zero energy [see Figure 7.6(a)]. Importantly, the degree of the degeneracy d_0 appears to be independent of the statistical parameter θ, for $\theta \neq 0$. Note that only the dimension of the zero energy subspace $\mathcal{H}_0$ remains invariant under variations of θ, whereas the space spanned by the respective eigenvectors can rotate in the Hilbert space. We found that the minimal number of degenerate states is inherently connected to the underlying chiral symmetry of the model. In particular, the chiral operator $\hat{S}$ subdivides the Hilbert space in terms of chiral eigenspaces, i.e., $\mathcal{H} = \mathcal{H}_+ \otimes \mathcal{H}_-$ with eigenvalues $\chi = \pm 1$ and dimensions $\dim\mathcal{H}_\pm = d_\pm$. The minimal dimension of the zero-energy eigenspace is given by $d_0 \geq |d_+ - d_-|$. We refer to d_0 as the *minimal* degeneracy, since for $\theta = 0$, i.e., in the case of non-interacting bosons, there can exist additional states with zero energy due to specific trigonometric relations of the analytical solutions, e.g. for systems with $L = 8$ and $N \geq 3$. Note that these findings are not unique to the anyon-Hubbard model, but hold for any correlated hopping models with only nearest-neighbor hopping and in the absence of classical on-site interactions. Another property of the

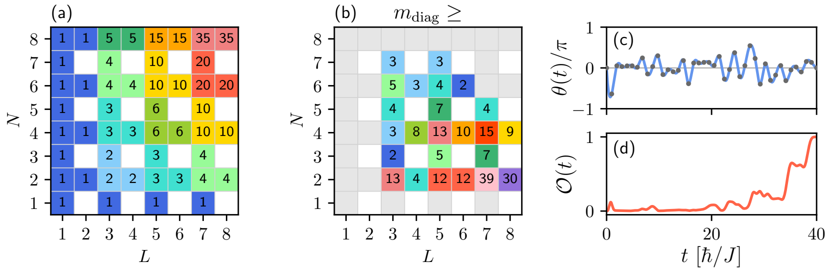

(a)

N	1	2	3	4	5	6	7	8
8	1	1	5	5	15	15	35	35
7	1		4		10		20	
6	1	1	4	4	10	10	20	20
5	1		3		6		10	
4	1	1	3	3	6	6	10	10
3	1		2		3		4	
2	1	1	2	2	3	3	4	4
1	1		1		1		1	

(b) $m_{\text{diag}} \geq$

N	1	2	3	4	5	6	7	8
8								
7			3		3			
6			5	3	4	2		
5			4		7		4	
4			3	8	13	10	15	9
3			2		5		7	
2			13	4	12	12	39	30
1								

FIGURE 7.6: (a) Minimal dimension of the zero-energy subspace d_0 for different lattice sites L and atom numbers N. (b) Minimum number of multiplications until the nontrivial holonomy matrix becomes trivial within a given error. (c) Time-dependent path of the statistical angle $\theta(t)$ which steers the number state $|001100\rangle$ to an eigenstate with zero energy. (d) Time-dependent overlap of the propagated and target state. Figure adapted from Ref. [FT5].

zero-energy subspace is the emergence of a checkerboard pattern in the one-body density or in the N-body density given that $L > N$.

Next, we investigate the behavior of the zero-energy space $\mathcal{H}_0$ when the statistical angle is adiabatically tuned along a closed loop in the parameter space. The starting point denotes the subspace $\mathcal{H}_0$ at $\theta = 0$. Subsequently, this subspace is adiabatically propagated from $\theta = 0$ to 2π by projecting the initial subspace onto a series of zero-energy subspaces with incrementally increasing values of θ. This procedure is known as Kato's adiabatic theorem [372, 373],

$$\hat{G} = \lim_{N_\theta \to \infty} \prod_{j=1}^{n_\theta} \hat{P}_j, \tag{7.1}$$

where $\hat{P}_j = \sum_{i=1}^{d_0} |\psi_\mu(\theta_j)\rangle\langle\psi_\mu(\theta_j)|$ is the projector of the d_0-dimensional zero-energy subspace corresponding to θ_j. During the adiabatic propagation, the subspace $\mathcal{H}_0$ rotates inside the Hilbert space while keeping its dimension fixed. Finally, when $\theta = 2\pi$ is reached, the propagated subspace is projected back on the initial one. The overlap matrix $(\mathbf{G})_{\mu\nu} = \langle\psi_\mu(0)|\hat{G}|\psi_\nu(2\pi)\rangle$, also called the holonomy matrix, describes a unitary transformation of the initial subspace and encapsulates the effects of the cyclic adiabatic propagation. In the case of a trivial rotation, where the adiabatic evolution has no effect, the initial and propagated subspace are identical and the holonomy matrix corresponds to the unitary matrix. Interestingly, we find for all considered systems with $L, N \leq 8$ and $d_0 \geq 3$ a nontrivial holonomy matrix indicating that adiabatically evolving the zero-energy subspace along a closed loop in parameter space corresponds to a nontrivial unitary transformation. Moreover, we estimate the integer number m_{diag} of how many times the unitary transformation can be applied ($\hat{G}^m_{\text{diag}}$) until the final state returns back to the initial one. We find that this number is in most of the considered cases larger than four within a given error, see Figure 7.6(b).

Finally, motivated by the recent experimental progress reported in Ref. [213], we develop a protocol in order to steer an initial number state into the zero-energy subspace. The optimization scheme relies only on the time-dependent variation of θ and is able to achieve an overlap of the propagated state with the target state of the order of $1-10^{-4}$ [see Figures 7.6(c) and (d)]. The success of the state preparation can experimentally observed by checking the emergence of a checkerboard pattern in the two-site density.

Chapter 8

Scientific Contributions

PHYSICAL REVIEW A **105**, 053314 (2022)

Counterflow dynamics of two correlated impurities immersed in a bosonic gas

Friethjof Theel,[1] Simeon I. Mistakidis,[2,3] Kevin Keiler,[1] and Peter Schmelcher[1,4]
[1]*Center for Optical Quantum Technologies, Department of Physics,*
University of Hamburg, Luruper Chaussee 149, D-22761 Hamburg, Germany
[2]*ITAMP, Center for Astrophysics | Harvard & Smithsonian Cambridge, Massachusetts 02138, USA*
[3]*Department of Physics, Harvard University, Cambridge, Massachusetts 02138, USA*
[4]*The Hamburg Centre for Ultrafast Imaging, University of Hamburg, Luruper Chaussee 149, D-22761 Hamburg, Germany*

(Received 16 December 2021; revised 26 April 2022; accepted 12 May 2022; published 31 May 2022)

The counterflow dynamics of two correlated impurities in a double well coupled to a one-dimensional bosonic medium is explored. We determine the ground-state phase diagram of the system according to the impurity-medium entanglement and the impurities' two-body correlations. Specifically, bound impurity structures reminiscent of bipolarons for strong attractive couplings as well as configurations with two clustered or separated impurities in the repulsive case are identified. The interval of existence of these phases depends strongly on the impurity-impurity interactions and external confinement of the medium. Accordingly the impurities' dynamical response, triggered by suddenly ramping down the central potential barrier, is affected by the medium's trapping geometry. In particular, for a box-confined medium, repulsive impurity-medium couplings lead, due to attractive induced interactions, to the localization of the impurities around the trap center. In contrast, for a harmonically trapped medium the impurities perform a periodic collision and expansion dynamics further interpreted in terms of a two-body effective model. Our findings elucidate the correlation aspects of the collisional physics of impurities which should be accessible in recent cold-atom experiments.

DOI: 10.1103/PhysRevA.105.053314

I. INTRODUCTION

Ultracold quantum gases provide an exceptional playground for the investigation of fundamental quantum many-body phenomena since they feature an exquisite experimental control [1]. For instance, it is possible to control the shape and dimensionality of the external potential [2–4], design species-selective potentials [5–8], and, most importantly, tune the interparticle interactions to an almost arbitrary extent via Feshbach resonances [1,9,10]. A particular research focus has been set on strongly particle-imbalanced mixtures, which allow to emulate impurity systems interacting with a bath. The key mechanism is that the bare impurity becomes dressed by the excitations of the bath and, thus, can be considered as a quasiparticle, the so-called polaron [11]. In this regard, several works have been devoted to exemplify the fundamental stationary properties of both Fermi [12–18] and Bose polarons [19–27], such as their effective mass [13,24,26], energy [20,21], and residue [12,14].

Recently, more attention has been placed on the interplay between several impurities immersed in a quantum gas [28–31]. Among others, the coalescence of two bosonic impurities coupled to a harmonically trapped bosonic medium has been predicted [32] as well as the existence of their induced interactions [33–35]. In the strongly attractive interaction regime, the formation of bipolarons referring to impurity bound states was also unraveled [36,37]. Beyond these studies the nonequilibrium dynamics of quasiparticles following an interaction quench [38–40] has been examined, unveiling, in particular, energy redistribution processes, temporal orthogonality catastrophe phenomena, and the effective temperature of the impurities [39], e.g., by emulating pump-probe and Ramsey spectroscopy.

Another branch in the field of ultracold quantum gases concerns the collisional aspects of atomic ensembles. Counterflow dynamics can be triggered, e.g., by employing a magnetic field gradient separating two atomic hyperfine states [41] or releasing an ultracold quantum gas from a double-well potential into a harmonic oscillator [42]. For a single atomic species these protocols result in the oscillation of the formed dark solitons [42] or in the case of a two-component mixture in the spontaneous generation of dark-bright soliton trains [41]. Another technique to initiate atomic collisions constitutes two counterpropagating harmonic oscillator potentials [43], which has been experimentally realized with ^{40}K and ^{87}Rb clouds utilizing two optical tweezers [44,45].

In this sense, it is intriguing to explore the counterflow correlated dynamics of impurities in combination with a superimposed superfluid background. A similar question was addressed for fermions [46,47], e.g., showing the formation of shock waves. Thereby, of immediate interest is the influence of the background on the collisional response and the associated emergent induced interactions between the impurities [47]. The impact of the bath on the impurity dynamics is expected to depend on the confining potential of the bath, and the impurities' coupling strength as well as the interaction between the impurities and the bath particles [48]. To tackle these open questions, herein we consider a minimal model of two bosonic impurities trapped in a double well and immersed

©2022 American Physical Society

in a bosonic bath. The counterflow dynamics between the impurities is induced by suddenly ramping down the potential barrier of their double well and, subsequently, letting the system evolve in time for different interaction configurations.

Specifically, it is shown that already the ground-state configurations depend on the chosen impurity-medium and impurity-impurity interaction strength and, importantly, on the type of the underlying trapping potential of the medium. For instance, in the case of a box-confined medium the impurities coalesce for intermediate repulsive impurity-medium couplings independently of the impurity-impurity repulsion. On the other hand, for a harmonically trapped bath the impurities separate from each other for strong impurity-impurity and impurity-medium repulsions [32]. Moreover, we find indications of bipolaron formation [36] for strong impurity-medium attractions.

The dynamical response of the impurities appears to be strongly affected by the combination of the involved interaction strengths as well as by the external confinement of the bath. More precisely, in the case of a box-confined medium and intermediate repulsive impurity-medium couplings the impurities' induced interactions lead to their localization at the trap center after their first collision. However, increasing the impurity-medium interaction strength, the impurities experience a periodic collisional response characterized by a damped amplitude: a behavior that is argued to be governed by finite size effects determined by the size of the box potential. Employing a harmonically trapped medium, the impurities localize at the trap center for attractive impurity-medium coupling strengths, while for intermediate and strong repulsions they phase separate with the medium [49,50] and thus their dressing is suppressed. Considering weakly repulsive impurity-impurity interactions, a state transfer manifests from two separated to two coalesced impurities. Importantly, this process is absent in the decoupled case, elucidating the role of the coupling with the bath and thus of the interspecies correlations (entanglement).

A microscopic analysis provides insights into the single-particle excitation processes and the two-body states participating in the dynamics and the aforementioned state transfer. To describe the stationary and dynamical properties of the composite impurity-medium system we employ the multilayer multiconfiguration time-dependent Hartree method for atomic mixtures (ML-MCTDHX) [51–54]. This *ab initio* approach allows us to efficiently track the relevant inter- and intraspecies correlations which are anticipated to be enhanced, especially during the dynamics. This is in part due to the few-body impurity subsystem as well as the spatial inhomogeneity caused by the external potential.

This work is structured as follows. In Secs. II and III we present the impurity model under consideration and introduce the ingredients of the variational method, respectively. We proceed in Sec. IV with an analysis of the system's ground state and draw a phase diagram with respect to variations of the impurity-impurity and impurity-medium interaction strengths. This analysis is based on the two-body densities quantifying the correlations of the bath particles and the impurities. Next, in Secs. V and VI the dynamical response of the system following a sudden reduction of the double-well barrier is discussed. In particular, Sec. V elaborates on the case of a box-confined medium in which we explicate, e.g., the localization of the impurities at intermediate repulsive impurity-medium coupling strengths and the emergence of finite size effects. The case of a harmonically trapped medium is investigated in Sec. VI, where the focus is set on the impurities' excitation processes and their dependence on the impurity-medium couplings. Our results are summarized in Sec. VII together with an outlook regarding further research directions. Appendix A elaborates on the behavior of the impurities' relative distance in their ground state and in Appendix B the impact of the impurities' mass on their collisions is exposed. In Appendix C we discuss the persistence of the impurities' collisional features when a linear ramp is applied to the barrier height of the double-well potential.

II. IMPURITY-MEDIUM SETTINGS

The system consists of two different bosonic species B and I at ultracold temperatures. In particular, we consider $N_I = 2$ impurities of mass m_I and a bosonic bath of $N_B = 20$ particles with mass m_B. The corresponding Hamiltonian reads

$$\hat{\mathcal{H}} = \hat{\mathcal{H}}_B + \hat{\mathcal{H}}_I + \hat{\mathcal{H}}_{BI}, \tag{1}$$

where $\hat{\mathcal{H}}_\sigma = \sum_{i=1}^{N_\sigma} (- \frac{\hbar^2}{2m_\sigma} \frac{\partial^2}{(\partial x_i^\sigma)^2} + V_\sigma(x_i^\sigma) + g_{\sigma\sigma} \sum_{i<j} \delta(x_i^\sigma - x_j^\sigma))$ is the interaction Hamiltonian of species $\sigma \in \{B, I\}$. Each component is subject to a different external potential $V_\sigma(x_i^\sigma)$, a scenario that can be achieved via species-selective optical potentials [55,56]. It is also restricted to one spatial dimension [57] that can be realized experimentally, e.g., by freezing out the transverse degrees of freedom using a strong harmonic confinement [58,59].

Since we are operating in the ultracold regime it is sufficient to take into account only s-wave scattering processes and thus the interaction between two particles of the same species is modeled with a contact interaction potential [9] determined by the one-dimensional effective coupling strength parameter $g_{\sigma\sigma}$. Analogously, the coupling between the impurities and the bath is described through a contact interaction potential $\hat{\mathcal{H}}_{BI} = g_{BI} \sum_{i=1}^{N_B} \sum_{j=1}^{N_I} \delta(x_i^B - x_j^I)$, where g_{BI} denotes the impurity-medium interaction strength. Due to the fact that $g_{\sigma\sigma'}$ with $\sigma, \sigma' \in \{B, I\}$ depends, among others, on the three-dimensional s-wave scattering length it can be experimentally adjusted, e.g., via Feshbach resonances utilizing either magnetic or optical fields [1,10,60,61]. Below, we consider a bosonic medium of ^{87}Rb atoms and ^{133}Cs impurities. Thus, the mass ratio is $m_I/m_B = 133/87$ [5,55,62,63].

At $t = 0$ the system is prepared in its ground state with a specific combination of interaction strengths ($g_{\sigma\sigma'}$). The impurities are initially confined in a double well $V_I^{\mathrm{dw}}(x) = \frac{1}{2} m_I \omega_I^2 x^2 + \frac{h_I}{w_I \sqrt{2\pi}} \exp(\frac{-x^2}{2w_I^2})$ which is the superposition of a harmonic oscillator potential with frequency ω_I and a Gaussian of width w_I and height h_I [64,65]. For the external potential of the bosonic medium we consider two cases: a box potential of size $L_B = 1$ with $V_B(x) = 0$ for $-L_B/2 < x < L_B/2$ and $V_B(x) = \infty$ elsewhere, and a harmonic oscillator $V_B(x) = \frac{1}{2} m_B \omega_B^2 x^2$. In the former scenario we consider $\tilde{x}_{\mathrm{box}} = L_B/10$ and $\tilde{E}_{\mathrm{box}} = \frac{\hbar^2}{m_B \tilde{x}_{\mathrm{box}}^2}$ as characteristic length and energy scales, respectively [66]. Thus, the time

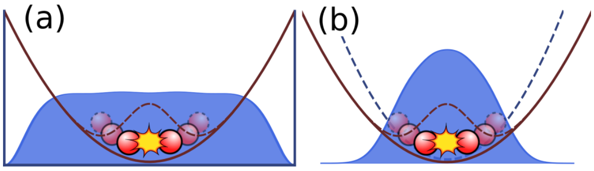

FIG. 1. Schematic representation of the considered setup and the quench protocol. Two bosons (red circles) are coupled to a bosonic medium (blue shaded area) which is either confined in (a) a box potential or (b) a harmonic oscillator. First, the two impurities are loaded into the double well and the equilibrium state of the system is obtained for a specific set of inter- and intraspecies interaction parameters (g_{BB}, g_{II}, g_{BI}). Subsequently, a counterflow dynamics between the two impurities is induced by suddenly ramping down the barrier of the double-well potential.

and interaction strength are expressed in units of $\tilde{t}_{\rm box} = \frac{m_B \tilde{x}_{\rm box}^2}{\hbar}$ and $\tilde{g}_{\rm box} = \frac{\hbar^2}{m_B \tilde{x}_{\rm box}}$, respectively. However, in the case of a harmonically trapped medium it is more convenient to express the energy in units of the medium's harmonic oscillator, $\tilde{E}_{\rm ho} = \hbar\tilde{\omega}_{\rm ho}$, where $\omega_B/\tilde{\omega}_{\rm ho} = 1$. It follows that the length, interaction strength, and timescales are given in terms of $\tilde{x}_{\rm ho} = \sqrt{\frac{\hbar}{m_B\omega_B}}$, $\tilde{g}_{\rm ho} = \sqrt{\frac{\hbar^3\omega_B}{m_B}}$, and $\tilde{t}_{\rm ho} = \omega_B^{-1}$, respectively. To construct the impurities' double well we employ $\omega_I/\tilde{\omega}_{\rm box,ho} = 0.6$, $h_I/\tilde{E}_{\rm box,ho}\tilde{x}^{-1}_{\rm box,ho} = 3.0$, and $w_I/\tilde{x}_{\rm box,ho} = 0.7$.

The ground state of the composite system is acquired for a set of values of interaction strengths (g_{BB}, g_{II}, g_{BI}). In the case of a box-confined medium the impurities always exhibit a finite spatial overlap with the bath particles for the considered interaction strengths. However, for a harmonically trapped bath the impurity-medium overlap vanishes as long as $g_{BI} > g_{BB}$ (see also the discussion below). Subsequently, the dynamics is triggered by suddenly reducing (at $t = 0$) the barrier of the impurities' double-well potential (see Fig. 1). Consequently, in the course of the time evolution the impurities collide and experience a harmonic oscillator potential $V_I^{\rm ho}(x)$ with frequency ω_I. As we argue below, the emerging collisional correlated dynamics depends strongly on the initial phase of the system determined by the interaction parameters (g_{BB}, g_{II}, g_{BI}).

III. VARIATIONAL APPROACH AND WAVE-FUNCTION ANSATZ

To determine the time-dependent solution of the problem described by the Hamiltonian of Eq. (1) we invoke the ML-MCTDHX method [51–54]. This approach is an *ab initio* one and optimizes a chosen basis, e.g., in terms of the Dirac-Frenkel variational principle [67]. In particular, the basis set which underlies the many-body wave function $|\Psi^{\rm MB}(t)\rangle$ is characterized by a time-dependent and multilayered structure with individual truncation parameters [68]. First, the many-body wave function is expanded into distinct sets of species functions $\{|\Psi_i^\sigma(t)\rangle\}_{i=1}^{D_\sigma}$ with D_σ denoting the number of the latter for species $\sigma \in \{B, I\}$. Since here we consider a two-component mixture, $|\Psi^{\rm MB}(t)\rangle$ is first expressed in two such basis sets and, thus, can be written in the form a truncated Schmidt decomposition [69–71]:

$$|\Psi^{\rm MB}(t)\rangle = \sum_{i=1}^{D} \sqrt{\lambda_i(t)}\, |\Psi_i^B(t)\rangle\, |\Psi_i^I(t)\rangle\,, \tag{2}$$

where $D = D_B = D_I$ and $|\Psi_i^\sigma(t)\rangle$ are the so-called natural species functions [53]. The time-dependent Schmidt coefficients $\lambda_i(t)$ determine the population of the ith natural species function and provide information about the interspecies entanglement [71,72]. For instance, in the case that only a single Schmidt coefficient $\lambda_i(t)$ is nonzero, the system is described by a direct product ansatz of species functions indicating the absence of entanglement. On the other hand, the two species are considered to be entangled when more than one Schmidt coefficient is nonzero.

In the next step of the many-body wave function $|\Psi^{\rm MB}(t)\rangle$ truncation, each species function is expanded into time-dependent permanents,

$$|\Psi_i^\sigma(t)\rangle = \sum_{\vec{n}|N_\sigma} C^\sigma_{i,\vec{n}}(t)|\vec{n}(t)\rangle. \tag{3}$$

Here, each permanent represents one of the $\binom{N_\sigma + d_\sigma - 1}{N_\sigma}$ possible configurations to distribute N_σ particles on d_σ single-particle functions $|\varphi_j^\sigma(t)\rangle$. A further imposed condition is that the number of occupied single-particle functions for each permanent has to be equal to N_σ (indicated by $\vec{n}|N_\sigma$). This expansion enables us to account for intraspecies correlations. Finally, the time-dependent single-particle functions $|\varphi_j^\sigma(t)\rangle$ are expanded into a time-independent discrete variable representation [73], which we choose here to consist of 300 grid points in an interval $\{-5, 5\}$ in units of $\tilde{x}_{\rm box,ho}$. Additionally, in this work we employ $D = 6$ species functions and $d_A = 4$, $d_B = 6$ single-particle functions for the accurate calculation of the considered systems.

In particular, the multilayered architecture and the time-dependent basis of the many-body wave function mainly contribute to the high degree of flexibility of the method which enables $|\Psi^{\rm MB}(t)\rangle$ to approach the accurate solution for each time instant with a high fidelity even for systems containing a mesoscopic particle number. In this way, the ML-MCTDHX method keeps the number of required wave-function coefficients within a computationally feasible limit and, at the same time, accounts for the relevant inter- and intraspecies correlations.

IV. CHARACTERIZATION OF THE GROUND STATE

In the following we provide an overview of the ground-state characteristics of two impurities trapped in a double well and coupled to a bosonic bath confined either in a box potential or a harmonic oscillator. These ground states will subsequently serve as a starting point for examining the counterflow impurity dynamics immersed in a medium which will be discussed below in Sec. V. Unless stated otherwise, the interaction strength between the bath particles is kept fixed to $g_{BB}/\tilde{g}_{\rm box} = g_{BB}/\tilde{g}_{\rm ho} = 0.5$.

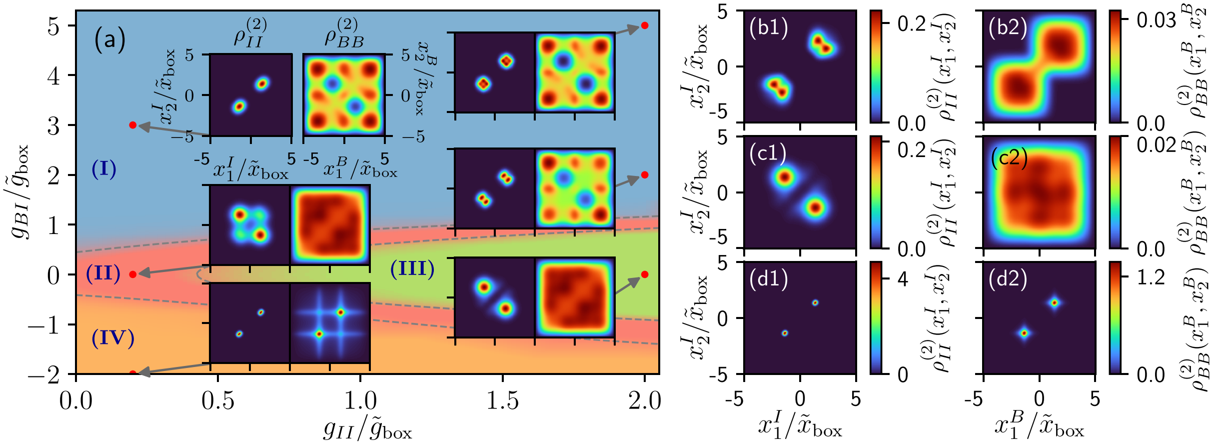

FIG. 2. (a) Phase diagram of the impurities-bath ground state with respect to the impurity-medium (g_{BI}) and impurity-impurity (g_{II}) interaction strengths for constant interactions of the medium ($g_{BB}/\tilde{g}_{\mathrm{box}} = 0.5$). The impurities are confined in a double well and the medium is trapped in a box potential. The respective ground-state configurations are characterized in terms of the two-body densities of the bath, $\rho^{(2)}_{BB}(x_1^B, x_2^B)$, and the impurities, $\rho^{(2)}_{II}(x_1^I, x_2^I)$. All crossovers among the involved phases are smooth. For each inset the range of the color map is optimally chosen and maximally extends from 0 to 2 [0.2] for $\rho^{(2)}_{II}(x_1^I, x_2^I)$ [$\rho^{(2)}_{BB}(x_1^B, x_2^B)$]. In (b1)–(d2) the ground-state two-body densities of the bath and the impurities are presented in terms of a weakly interacting bath ($g_{BB}/\tilde{g}_{\mathrm{box}} = 0.1$) and strongly interacting impurities ($g_{II}/\tilde{g}_{\mathrm{box}} = 2.0$). The interspecies interaction strengths from the top to the bottom row are $g_{BI}/\tilde{g}_{\mathrm{box}} = 5.0$, 0.2, and −2.0, respectively.

A. Main observables of interest

Let us first introduce the quantities that will be employed for the identification of the ground-state phases and the quench dynamics of the two interacting impurities in the cases of a box-confined and a harmonically trapped medium. The distinction between the emergent ground-state configurations is performed with respect to the two-body density distributions of the impurities and the bath particles at $t = 0$. The reduced two-body density of two particles of the same species is given by

$$\rho^{(2)}_{\sigma\sigma}(x_1^\sigma, x_2^\sigma, t) = \langle \Psi^{\mathrm{MB}}(t) |\, \hat{\Psi}^\dagger_\sigma(x_1^\sigma) \hat{\Psi}^\dagger_\sigma(x_2^\sigma) \times \hat{\Psi}_\sigma(x_1^\sigma) \hat{\Psi}_\sigma(x_2^\sigma) \,| \Psi^{\mathrm{MB}}(t) \rangle, \quad (4)$$

where $\hat{\Psi}^{(\dagger)}_\sigma(x_1^\sigma)$ denotes the bosonic field operator which annihilates (creates) a particle of species $\sigma \in \{B, I\}$ at position x_1^σ. In fact, $\rho^{(2)}_{\sigma\sigma}(x_1^\sigma, x_2^\sigma)$ is the probability of finding one particle at x_1^σ and, simultaneously, another particle of the same species at x_2^σ. In the following, we will drop the time parameter since for the ground state $t = 0$.

In both considered external confinements of the medium, an increase of the repulsive impurity-medium coupling strength leads to the development of interspecies correlations (entanglement) which eventually impact the ground-state configurations [74]. A common measure for quantifying entanglement in a bipartite system is the von Neumann entropy [71,75], defined as

$$S^{\mathrm{vN}} = -\sum_{i=1}^{D} \lambda_i \ln \lambda_i. \quad (5)$$

Recall that D denotes the number of the employed species functions and λ_i are the Schmidt coefficients [cf. Eq. (2)]. For a maximally entangled mixture the von Neumann entropy obtains its maximum value, $S^{\mathrm{vN}}_{\mathrm{max}} = \ln D$ and $\lambda_i = 1/D$. This value corresponds to $S^{\mathrm{vN}}_{\mathrm{max}} = 1.79$ in our case. In contrast, a vanishing von Neumann entropy indicates a decoupled (i.e., nonentangled) mixture such that the total many-body wave function can be written as a direct product state of the two individual species wave functions.

Moreover, in order to judge the degree of miscibility among the impurity and medium clouds we calculate the interspecies spatial overlap [76,77] which is quantified through

$$\Lambda_{BI} = \frac{\left[\int dx \rho_B^{(1)}(x) \rho_I^{(1)}(x)\right]^2}{\int dx \left[\rho_B^{(1)}(x)\right]^2 \int dx \left[\rho_I^{(1)}(x)\right]^2}. \quad (6)$$

Here, $\rho_\sigma^{(1)}(x) = \langle \Psi^{\mathrm{MB}} |\, \hat{\Psi}^\dagger_\sigma(x) \hat{\Psi}_\sigma(x) \,| \Psi^{\mathrm{MB}} \rangle$ is the one-body density of $\sigma \in \{B, I\}$ species [78].

B. Decoupled case $g_{BI} = 0$

Before addressing the ground-state properties of the coupled mixture, we focus on the simpler scenario where the bath and the impurities are decoupled from each other ($g_{BI} = 0$) and thus they can be treated individually. Accordingly, the impurity-bath entanglement is vanishing, i.e., $S^{\mathrm{vN}} = 0$. Then, the system reduces to two interacting bosons in a double well [79–81] with the bath being homogeneous or harmonically trapped [cf. Figs. 2(a) and 3(a) for $g_{BI} = 0$]. Here, we distinguish between weakly and strongly coupled impurities. In the former case, the two impurities are delocalized over the two sites of the double well; see the dominant population of the off-diagonal compared to the diagonal elements of $\rho^{(2)}_{II}(x_1^I, x_2^I)$ [cf. insets of Figs. 2(a) and 3(a) corresponding to regime (II)].

On the other hand, for larger impurity-impurity repulsion g_{II} the density maxima along the diagonal vanish and only density peaks at the off-diagonal remain [cf. inset of Fig. 2(a)

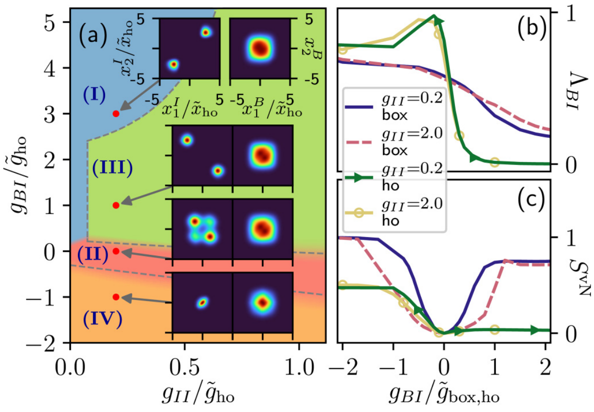

FIG. 3. (a) Ground-state phase diagram of the impurities inside a harmonically trapped medium. The crossover from region (I) to region (III) is abrupt, marked by the dashed line, while all others are smooth. (b) Spatial overlap Λ_{BI} and (c) von Neumann entropy $S^{\rm vN}$ between the bath and the impurities for varying impurity-medium interaction strength and different fixed impurity-impurity couplings (in units of $\tilde{g}_{\rm box,ho}$) as well as for distinct external potentials of the bath (see legend). The interaction strength among the bath particles is fixed to $g_{BB}/\tilde{g}_{\rm box} = g_{BB}/\tilde{g}_{\rm ho} = 0.5$.

belonging to regime (III)]. This configuration of $\rho_{II}^{(2)}(x_1^I, x_2^I)$ is described by the conditional probability of finding one impurity at the left and one impurity at the right site of the double well or vice versa. In this sense, the impurities tend to separate from each other and are anticorrelated within the same site of the double well. Thus, they reside in a Mott-type state. Notice that for a decoupled mixture the above-described impurity configurations corresponding to regimes (II) and (III) occur independently of the particular trapping geometry of the bath [cf. $g_{BI} = 0$ in Figs. 2(a) and 3(a)]. Thereby, the medium extends almost homogeneously over the box potential as also reflected by the shape of its two-body density [see inset of Fig. 2(a)], while in the harmonically trapped scenario it exhibits a Gaussian profile [cf. inset of Fig. 3(a)].

C. Finite interspecies interactions with the medium confined in a box potential

Having analyzed the spatial configurations of the interacting impurities for a suppressed impurity-bath coupling we then discuss the ground-state properties of the composite system when the bath is confined in a box potential and the interspecies interaction strength g_{BI} becomes finite. The respective ground-state phase diagram is mapped out and presented in Fig. 2(a) based on the underlying two-body configurations identified in $\rho_{BB}^{(2)}(x_1^B, x_2^B)$ and $\rho_{II}^{(2)}(x_1^I, x_2^I)$. Overall, we find that upon varying g_{BI} and g_{II}, the system deforms smoothly across the different phases, which are analyzed in detail in the following (see also Ref. [82]).

In the case of strong repulsive g_{BI}, the mixture enters regime (I) [see Fig. 2(a)] [83]. Here, the impurities' two-body density exhibits two peaks along its diagonal meaning that the two impurities occupy simultaneously a single site of the double well. Such a behavior is referred to as the coalescence of the impurities and has been observed also for the case where the impurities and bath particles are both harmonically confined [32]. Intuitively, we explain this behavior as follows. One impurity lying at a specific site of the double well repels the bath particles and, thereby, creates an effective hole which attracts the other impurity [84,85]. On the other hand, the impurities impact accordingly the bath. This back-action manifests, for instance, in the off-diagonal parts of the medium's two-body density which exhibits strongly suppressed spatial regions at the location of the impurities [see inset in regime (I) of Fig. 2(a)]. Indeed, the probability to find two bath particles at positions corresponding to opposite double-well sites is vanishing. This is due to the fact that the impurities lie both either at the left or at the right double-well site as it becomes apparent from their reduced two-body density. However, a configuration where two bath particles reside simultaneously at the same double-well site is still conceivable, assuming that the impurities are at the opposite site, thereby avoiding the bath particles [note the nonvanishing density at the diagonal of $\rho_{BB}^{(2)}(x_1^B, x_2^B)$ in the inset of Fig. 2(a)].

Increasing the impurity-medium interaction strength within regime (I) for a fixed $g_{II}/\tilde{g}_{\rm box} \in [0, 2]$ we observe two prominent features appearing in terms of $\rho_{BB}^{(2)}(x_1^B, x_2^B)$. First, the two-body density holes at the off diagonal of $\rho_{BB}^{(2)}(x_1^B, x_2^B)$ become more pronounced for increasing g_{BI} and, second, for a $g_{BI}/\tilde{g}_{\rm box} \gtrsim 2.5$ two bath particles are correlated at the most right and most left or at opposite sites of the bath cloud [see the outermost density peaks at the diagonal and off-diagonal elements of $\rho_{BB}^{(2)}(x_1^B, x_2^B)$ in the inset of Fig. 2(a)]. From this latter behavior we can conclude that the bath particles exhibit two-body long-distance correlations. Moreover, we note that in the case of strong impurity-impurity repulsions, e.g., for $g_{II}/\tilde{g}_{\rm box} = 2.0$, the two-body state of the impurities begins to fermionize and the diagonal peaks of $\rho_{II}^{(2)}(x_1^I, x_2^I)$ broaden and, eventually, fragment [86] [see corresponding inset of Fig. 2(a)].

Similarly to the coalescence of the impurities in the repulsive case [regime (I)], also in the attractive scenario the two impurities simultaneously occupy either the left or right site of the double well, as it can be deduced from their diagonal and highly localized two-body density configuration $\rho_{II}^{(2)}(x_1^I, x_2^I)$ [see the inset of Fig. 2(a)]. In both the repulsive and the attractive cases, the bath mediates an induced attractive interaction between the impurities such that the latter coalesce and tend to occupy the same double-well site. For a more detailed discussion regarding the presence of the attractive induced interactions between the impurities via their relative distance, see Appendix A. Furthermore, due to the attractive interactions the bath particles localize in the vicinity of the impurities such that also the two-body density of the medium exhibits two dominant peaks along the diagonal [Fig. 2(a)]. Also, we remark that regime (II) in Fig. 2(a) includes ground states corresponding to delocalized impurities, i.e., where the diagonal and off-diagonal elements of $\rho_{II}^{(2)}(x_1^I, x_2^I)$ are simultaneously populated. However, with varying g_{II} and g_{BI} the particular density peaks are deformed compared to the depicted insets of regime (II) in Fig. 2(a). For instance, in the case of $g_{II}/\tilde{g}_{\rm box} = 2.0$ and $g_{BI}/\tilde{g}_{\rm box} = 1.0$ corresponding to regime (II) in Fig. 2(a), the two-body density of the impurities exhibits peaks at its off-diagonal elements [similar to regime

(III)] and fragmented density humps at its diagonal [as observed in regime (I)].

Moreover, increasing (decreasing) the interspecies interaction to large repulsive (attractive) values leads to a noticeable growth of the von Neumann entropy. Namely, the impurities become highly entangled with the bath [cf. Fig. 3(b)]. At the same time the impurities and the bath share a finite spatial overlap with each other for all the considered values of g_{BI} and g_{II} [Fig. 3(c)]. Therefore, since these two features constitute a basic requirement for the formation of quasiparticles, e.g., as discussed in Refs. [24,39,50,87], in principle, the impurities can be dressed by the excitations of the bath and, thus, form Bose polarons.

Additionally, we investigated the ground state of the system for a weakly interacting bath, e.g., for $g_{BB}/\tilde{g}_{\text{box}} = 0.1$. As we will argue, the enhanced compressibility of the bath can alter the ground-state configurations and this is evident, among other observables, in terms of the two-body density. In Figs. 2(b1)–2(d2) we exemplarily present the two-body densities of the impurities and the bath particles for $g_{BB}/\tilde{g}_{\text{box}} = 0.1$ and $g_{II}/\tilde{g}_{\text{box}} = 2.0$. Here, the impurities' two-body densities exhibit a qualitatively similar structure with the ones corresponding to a moderately interacting bath [Fig. 2(a)]. For instance, a localization at the sites of the double well is observed for strongly attractive g_{BI} [Fig. 2(d1)] as well as an anticorrelated behavior for weak impurity-medium couplings [Fig. 2(c1)] and the coalescence of the impurities for strong g_{BI} [Fig. 2(b1)]. Similarly, the two-body density of the weakly interacting medium resembles the one of a moderately interacting bath in the cases of weak attractive and repulsive as well as strong attractive g_{BI} [Figs. 2(c2) and 2(d2)]. However, for strong repulsive g_{BI} the medium's two-body density is modified for weak g_{BB}; i.e., the off-diagonal parts of $\rho^{(2)}_{BB}(x^B_1, x^B_2)$ are depopulated and only the diagonal ones are occupied [Fig. 2(b2)]. We attribute this behavior to the increased compressibility of the bath which suppresses correlations between two bath particles residing at longer distances, e.g., the opposite edges of the cloud as observed in Fig. 2(a). Additionally, this behavior is accompanied by strong anticorrelations between the impurities and the bath particles; i.e., the respective two-body density $\rho^{(2)}_{BI}(x^B_1, x^I_2)$ exhibits only peaks at its off diagonal (not shown).

Furthermore, we have found that in the corresponding ground-state phase diagram of a weakly interacting medium ($g_{BB}/\tilde{g}_{\text{box}} = 0.1$) with $N_B = 20$, regimes (II) and (III) shrink as compared to the $g_{BB}/\tilde{g}_{\text{box}} = 0.5$ case shown in Fig. 2(a). Specifically, their phase boundaries are shifted towards the line corresponding to $g_{BI} = 0$. A similar, but less pronounced, shift of the phase boundaries is observed when increasing the number of bath particles to $N_B = 30$ but keeping g_{BB} fixed. Summarizing, both decreasing g_{BB} or increasing N_B while considering fixed all other parameters leads to an enhancement of the magnitude of the attractive induced interactions between the impurities when g_{BI} is switched on towards finite attractive or repulsive values.

D. Harmonically trapped medium

We then proceed to analyze in more detail the system consisting of a harmonically trapped medium. This change of the external confinement reduces the mobility of the bath particles which are then naturally bounded by the harmonic oscillator around the trap center. The respective phases presented in Fig. 3(a) feature smooth crossovers among them besides the one between regimes (I) and (III), which is abrupt. To testify to the "smoothness" of the underlying crossover regions, we track, as in the box-confined scenario, the behavior of the impurities' two-body densities (cf. Ref. [82]).

An increasing impurity-medium repulsion such that $g_{BI} > g_{BB}$ leads to a phase separation between the impurities and the bath particles as it is captured by the diminishing spatial overlap depicted in Fig. 3(b). In this case the impurities are no longer dressed by the excitations of the bath and, thus, the quasiparticle notion is essentially lost [39,49,50]. Thereby, we distinguish between two cases according to the impurity-impurity interaction strength. In the case of weak g_{II} and strong g_{BI} corresponding to regime (I) in Fig. 3(a) the impurities coalesce in a similar manner as described above (see also Ref. [32]). However, as the impurity-impurity interaction strength becomes large enough or the impurity-medium repulsion sufficiently small, regime (III) is accessed in which the impurities spatially separate. This is identified by the exclusive population of the off diagonals of $\rho^{(2)}_{II}(x^I_1, x^I_2)$ [cf. corresponding inset of Fig. 3(a)]. Turning to strongly attractive impurity-medium interaction strengths assigned as regime (IV) in Fig. 3(a), a localization of the impurities in the barrier of the double well is observed [see in particular the elongation of $\rho^{(2)}_{II}(x^I_1, x^I_2)$ along its diagonal]. This property is related to the formation of a bipolaron, referring to a dimer bound state consisting of two polarons [35,36,39]. We base our argument of bipolaron formation on the following observations which have also been used in Ref. [36] to expose the existence of such states in three dimensions. The continuous decrease of the so-called bipolaron energy $E_{\text{BP}} = E_2 - E_1 + E_0$ has been verified for increasing impurity-medium attraction, where E_i denotes the total energy of the bosonic gas containing $i = 0, 1, 2$ impurities. In the same manner, also the size of the dimer state quantified in our case by $1/\sqrt{\langle \hat{r}^2_{II} \rangle}$ increases for larger g_{BI} (not shown here).

Concluding, let us mention in passing that similarly to the case of a box-confined medium, the main requirements for the formation of Bose polarons are also fulfilled in the presence of a harmonic trap. The only exception consists of the region of phase separation among the impurities and the medium at $g_{BI} > g_{BB}$. Thus, the impurities' response, to be presented below, can be interpreted as the counterflow-correlated dynamics of two quasiparticles, here Bose polarons.

V. COLLISIONAL MANY-BODY DYNAMICS FOR A BOX-CONFINED MEDIUM

Next, we investigate the time evolution of the composite system upon suddenly ramping down the central barrier of the impurities' double-well potential such that they are henceforth externally confined in a harmonic oscillator and, thus, their counterflow dynamics is triggered. In a decoupled mixture ($g_{BI} = 0$) this quench results in an undamped periodic impurities motion where they collide and subsequently expand repeatedly. Turning to finite impurity-medium couplings the

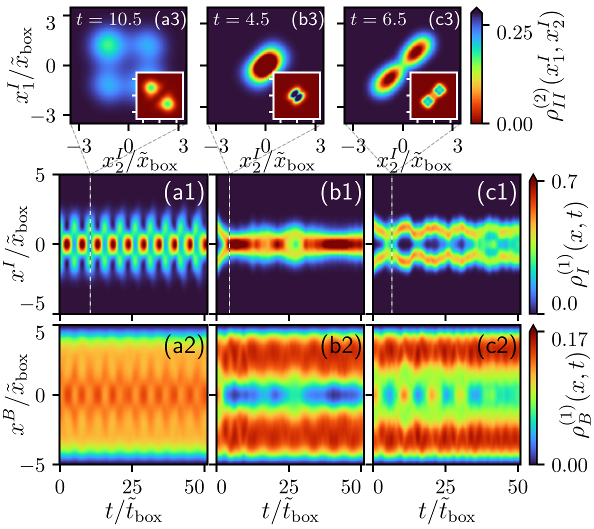

FIG. 4. Time evolution of the one-body density of [(a1)–(c1)] the harmonically trapped impurities and [(a2)–(c2)] the bath particles confined in a box potential. Each column represents the dynamics for a fixed impurity-medium interaction strength which is from left to right: $g_{BI}/\tilde{g}_{\mathrm{box}} = -0.2, 1.5, 5.0$. In all cases, the impurity-impurity coupling is $g_{II}/\tilde{g}_{\mathrm{box}} = 0.2$. [(a3)–(c3)] Snapshots of the impurities' two-body density at different time instants (see legends). The insets depict the two-body densities at the same time instants and scales, but for two strongly interacting impurities, i.e., $g_{II}/\tilde{g}_{\mathrm{box}} = 2.0$. At those time instants, the one-body densities for two weakly and strongly interacting impurities reveal similar features, thus allowing the comparison on the two-body density level.

response is substantially altered and depends strongly on the trapping potential of the medium, as we will argue below.

A. Response through the time evolution of the density

We monitor the counterflow dynamics of two impurities coupled via g_{BI} to a bosonic medium trapped in a box potential. After ramping down the potential barrier of the double well, the impurities are left to evolve in the resulting harmonic trap. As a first step, we categorize the emergent dynamical response regimes by inspecting the one-body densities $\rho_I^{(1)}(x,t)$ and $\rho_B^{(1)}(x,t)$ depicted in Figs. 4(a1)–4(c1) and 4(a2)–4(c2), respectively. The impurity-impurity coupling is kept fixed at $g_{II}/\tilde{g}_{\mathrm{box}} = 0.2$ and only the impurity-medium interaction is varied. We are able to identify four distinct dynamical response regimes taking place at strongly attractive ($g_{BI}/\tilde{g}_{\mathrm{box}} < -0.8$), weakly attractive and repulsive ($-0.8 \lesssim g_{BI}/\tilde{g}_{\mathrm{box}} < 0.8$), intermediate repulsive ($0.8 \lesssim g_{BI}/\tilde{g}_{\mathrm{box}} \lesssim 2.0$), and strongly repulsive ($2 < g_{BI}/\tilde{g}_{\mathrm{box}}$) values of g_{BI}. These dynamical regimes are, of course, inherently related to the corresponding phases unraveled in the ground state of the system [see Fig. 2(a)]. Note that the behaviors of the one-body densities in the respective regions do not qualitatively alter for varying g_{II} from small to large repulsive values at least in the range of $0 \leqslant g_{II}/\tilde{g}_{\mathrm{box}} \leqslant 2.0$ considered herein. Only inspecting higher-body observables, such as the reduced two-body density, reveals significant alterations of the impurities' response regarding variations of g_{II}.

B. Dynamics for weakly attractive and repulsive impurity-medium couplings

In the case of either weakly attractive or repulsive g_{BI} the impurities' one-body densities feature a periodic motion consisting of a collision and an expansion of their cloud [cf. Fig. 4(a1) for $g_{BI}/\tilde{g}_{\mathrm{box}} = -0.2$]. As a consequence, the bath is only weakly perturbed from its initial homogeneous profile showing small amplitude distortions at the instantaneous location of the impurities [see Fig. 4(a2)]. This response emerges when considering initial configurations corresponding to the interaction regimes (II) and (III) discussed in Fig. 2(a). Interestingly, the time evolution of the one-body density does not depend strongly on variations of the impurity-impurity interaction strength [88]. Therefore, one has to rely on two-body observables, such as the two-body density $\rho_{II}^{(2)}(x_1^I, x_2^I)$, e.g., presented in Fig. 4(a3) for $g_{BI}/\tilde{g}_{\mathrm{box}} = -0.2$ and $g_{II}/\tilde{g}_{\mathrm{box}} = 0.2$ at $t/\tilde{t}_{\mathrm{box}} = 10.5$ and in the respective inset for two strongly interacting impurities with $g_{II}/\tilde{g}_{\mathrm{box}} = 2.0$. In the former case, the two weakly interacting impurities are initially and throughout the evolution delocalized over both sites of the double well since both the diagonal and the off-diagonal elements of $\rho_{II}^{(2)}(x_1^I, x_2^I)$ are nonvanishing.

However, for strongly interacting impurities we find that in the course of the evolution a pronounced correlation hole occurs [39]; i.e., solely the off diagonal of $\rho_{II}^{(2)}(x_1^I, x_2^I)$ is populated [cf. inset of Fig. 4(a3)]. In other words, due to the strong repulsion the impurities reside at spatially opposite positions and avoid each other during the dynamical evolution. The respective dynamics of the impurities is characterized by the periodic expansion and contraction of their cloud around the trap center while avoiding residing at the same location [see the correlation hole of $\rho_{II}^{(2)}(x_1^I, x_2^I)$]. However, independently of g_{II} the impurities remain within the medium, thus forming a polaron due to the finite g_{BI}.

C. Time evolution for intermediate interspecies repulsions

Increasing the impurity-medium repulsion to intermediate values ($g_{BI}/\tilde{g} \lesssim 2.0$) and, thereby, entering regime (I) in Fig. 2(a), a comparatively altered response is realized. Indeed, once the two impurities collide at the trap center, they remain localized [89] [see Fig. 4(b1) for $g_{BI}/\tilde{g}_{\mathrm{box}} = 1.5$]. Consequently, because of the repulsive character of the employed g_{BI}, the bath is pushed towards the edges of the box with each density branch undergoing weak amplitude oscillations due to its reflection from the walls of the confining box [Fig. 4(b2)]. Simultaneously, the bosonic medium becomes highly depleted, meaning that higher-lying natural orbitals [being the eigenvalues of the reduced one-body density matrix $\rho_B^{(1)}(x, x', t)$] are macroscopically populated. Accordingly, the bosonic gas is correlated and deviates from a perfect Bose-Einstein condensate. This behavior is in contrast to the case of $g_{BI}/\tilde{g}_{\mathrm{box}} < 0.8$ where the first orbital is dominantly occupied.

However, the corresponding two-body density $\rho_{II}^{(2)}(x_1^I, x_2^I)$ when the impurities collide at the trap center at $t/\tilde{t}_{\mathrm{box}} = 4.5$ is shown in Fig. 4(b3). The elongated shape of $\rho_{II}^{(2)}(x_1^I, x_2^I)$

along the diagonal indicates the presence of an attractive interaction between the impurities induced by the coupling with the bath [32,39,50]. Apparently the strength of this induced attraction is larger than for $g_{BI}/\tilde{g}_{\text{box}} = 0.2$. Moreover, by comparing this case to the one of strongly interacting impurities ($g_{II}/\tilde{g}_{\text{box}} = 2.0$), we find once again significant differences only in the behavior of their two-body density. At $t = 0$, the shape of $\rho^{(2)}_{II}(x^I_1, x^I_2)$ corresponds to two coalesced impurities whose density peaks lay on its diagonal and are fragmented [cf. inset of Fig. 2(a)]. In the course of the dynamics the impurities collide at the center where they remain in the course of the evolution [see inset of Fig. 4(b3)]. Thereby, the strong repulsion between the impurities hinders a population at the exact diagonal of the two-body density. Notice their small spatial overlap with the bath hinting towards their suppressed dressing [90].

D. Dynamical response for strong impurity-medium repulsions

For even stronger impurity-medium repulsions ($g_{BI}/\tilde{g} > 2.0$), once the impurities collide around $x = 0$ they drift apart from each other and collide again [see Fig. 4(c1) for $g_{BI}/\tilde{g}_{\text{box}} = 5.0$]. This behavior is repeated in the course of time with a damped collision amplitude. Thereby, the population on the diagonal of $\rho^{(2)}_{II}(x^I_1, x^I_2)$ becomes narrower as compared to the case of intermediate repulsive g_{BI}, indicating the presence of an even stronger strength of induced interactions [cf. Fig. 4(c3)]. Again two strongly repulsive impurities fragment along the diagonal of $\rho^{(2)}_{II}(x^I_1, x^I_2)$ [see the inset of Fig. 4(c3)] with the two respective density fragments exhibiting each four faint maxima which persist until an evolution time of $t/\tilde{t}_{\text{box}} = 8$. During the evolution the one-body density of the bath allocates at the edges of the box when the impurities collide and reoccupies the trap center when the latter drift apart (see also below for a more detailed discussion).

We attribute the impurities' density splitting for large g_{BI}, even though the induced attractive interaction is higher in this case than for intermediate repulsive couplings, to the finite size of the considered box potential. In order to elucidate the underlying mechanism, we show in Fig. 5(a) the time-dependent spatial variance of the medium, $\langle \hat{X}^2_B \rangle(t)$, which serves as a measure for the instantaneous spatial extension of the medium's cloud [19,91]. At $t = 0$ and for sufficiently strongly repulsive g_{BI} the impurities reside both either at the right or at the left site of the double well while the bath particles avoid these pairs [cf. regime (I) in Fig. 2(a)], leading for larger g_{BI} to an increased $\langle \hat{X}^2_B \rangle(t = 0)$ [see Fig. 5(a)].

Subsequently, after ramping down the barrier of the double well, the impurities collide around $x = 0$, enforcing the medium to depopulate the trap center, a process that results in the increase of $\langle \hat{X}^2_B \rangle(t)$. To facilitate further our discussion, we provide specific profiles of the impurities' one-body density and their effective potential [24,39,92]. The effective potential is constructed from the superposition of the impurities' (postquench) harmonic oscillator and the one-body density of the bath weighted by the impurity-medium coupling strength. It reads

$$V^{\text{eff}}(x^I, t) = V^{\text{dw}}_I(x^I) + N_B g_{BI} \rho^{(1)}_B(x^I, t). \qquad (7)$$

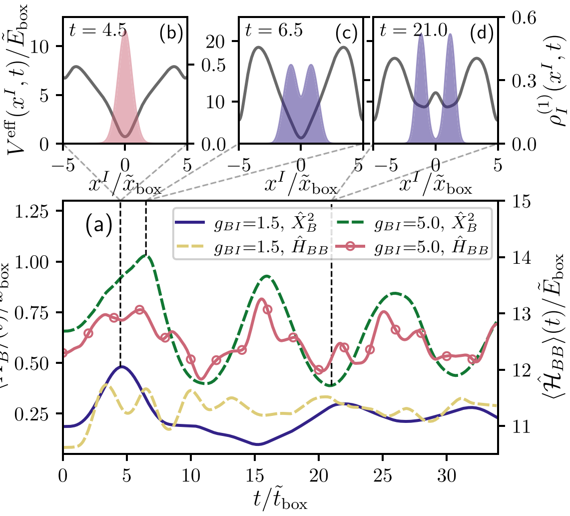

FIG. 5. (a) Dynamics of the width of the medium cloud [captured by the spatial variance $\langle \hat{X}^2_B \rangle(t)$] and internal interaction energy of the bath particles $\langle \hat{\mathcal{H}}_{BB} \rangle$ for different impurity-medium couplings (see legend) and fixed impurity-impurity interaction strength $g_{II}/\tilde{g}_{\text{box}} = 0.2$. [(b)–(d)] Profiles of the impurities' one-body density $\rho^{(1)}_I(x^I, t)$ are shown together with their effective potential (gray lines) for specific time instants (see legends). In (b) $g_{II}/\tilde{g}_{\text{box}} = 1.5$ while in (c) and (d) $g_{II}/\tilde{g}_{\text{box}} = 5.0$. The time and interaction are expressed in units of $\tilde{t}_{\text{box}}$ and $\tilde{g}_{\text{box}}$, respectively.

A maximum of $\langle \hat{X}^2_B \rangle(t)$ is reached, i.e., the spatial extent of the medium is largest, when the impurities allocate at the trap center [see Figs. 5(b) and 5(c)]. Thereby, the impurities transfer energy to the medium, leading to an increased interaction energy between the particles of the latter; i.e., $\langle \hat{\mathcal{H}}_{BB} \rangle = \langle g_{BB} \sum_{i<j} \delta(x^B_i - x^B_j) \rangle$ is maximized [cf. Fig. 5(a)]. After reaching a maximum of $\langle \hat{\mathcal{H}}_{BB} \rangle$ the bath reoccupies the trap center as indicated by the reduction of $\langle \hat{X}^2_B \rangle(t)$ and the impurities' density splits again, a behavior that is repeated in the course of time. As argued below, this dynamical response can be attributed to finite size effects stemming from the size of the medium's box potential.

E. Impact of the barrier height, atom number, and box size on the impurity dynamics

In order to check the robustness of the observed dynamical response regimes of the impurities against the system parameters we have additionally varied the height of the double well, h_I, the size of the box potential, L_B, and the number of bath particles, N_B. For small g_{BI} and fixed $g_{II}/\tilde{g}_{\text{box}} = 0.2$, increasing the height of the double well from $h_I/\tilde{E}_{\text{box}}\tilde{x}^{-1}_{\text{box}} = 2$ to 7 leads to a crossover of the impurities, i.e., from a superfluid to a Mott-insulating phase. The former phase corresponds to a two-body density $\rho^{(2)}_{II}(x^I_1, x^I_2)$ where in all quarters prominent density peaks are present. In the latter case only the off diagonal of $\rho^{(2)}_{II}(x^I_1, x^I_2)$ is populated [compare with the ground-state configurations in regime (III) of Fig. 2(a)]. Further increasing the impurity-medium coupling to intermediate repulsive values the impurities coalesce again independently of the barrier height of the double well. Thereby, the impurities' ground state corresponds to the one of regime (I) depicted in Fig. 2(a). Regarding the dynamical response of the above-described system, we did not find a qualitatively different behavior when h_I is varied but rather a shifting of the identified regimes towards a larger value of g_{BI}.

In Sec. IV C it was mentioned that the ground-state phase diagram is altered with respect to variations of g_{BB} and N_B. As such, also the dynamical response of the system is affected upon tuning these parameters by means that the specific dynamical features are realized for smaller values of g_{BI}. This is attributed to the fact that the impurities feature an enhanced magnitude of attractive induced interactions for either a decreased g_{BB} (e.g., $g_{BB}/\tilde{g}_{\text{box}} = 0.1$ and especially in the interval $|g_{BI}| < g_{BB}$) or an increased N_B (for instance at $N_B = 30$). Consequently, they localize around the trap center after their first collision for a smaller g_{BI} than for $g_{BB}/\tilde{g}_{\text{box}} = 0.5$ or a larger N_B such as $N_B = 30$. This effect is arguably more prominent in the former scenario and during the dynamics manifests by the enhanced impurities localization at the trap center.

An opposite behavior is observed for varying only the size of the medium's box potential L_B. In this case, an increasing L_B broadens the medium such that the impurities are less affected by the presence of bath particles which, eventually, for intermediate repulsive g_{BI} increases the relative distance between the impurities for a larger L_B (not shown here). However, when the box size is of the order of the distance of the double-well minima, the bath particles localize at the trap center (between the two double-well sites) for intermediate repulsive impurity-medium interaction strengths. Additionally, for strongly repulsive g_{BI} an increasing box size leads to the localization of the impurities around $x = 0$ and a dynamical response similar to the one observed in Fig. 4(c1) is absent. This holds also when we simultaneously increase the number of bath particles and the size of the box potential while keeping the ratio N_B/L_B fixed [93].

VI. IMPURITY DYNAMICS FOR THE HARMONICALLY TRAPPED BATH

Next, we examine the counterflow dynamics (induced by the same quench protocol) of the two impurities coupled to a harmonically confined bath. Since in this case the medium tends to localize at the trap center a phase separation between the two species is facilitated for intermediate to strongly repulsive impurity-medium interaction strengths which eventually prohibits a subsequent dynamical mixing of the species. Indeed, we find that for values larger than $g_{BI}/\tilde{g}_{\text{ho}} = 0.6 > g_{BB}/\tilde{g}_{\text{ho}}$, corresponding to a vanishing spatial overlap at $t = 0$ [cf. Fig. 3(b)], the initial phase separation between the impurities and the medium persists also in the course of the propagation. However, for $g_{BI}/\tilde{g} < 0.6$ an intriguing response is observed.

A. Collision features in terms of the one-body density

Figure 6 illustrates the time evolution of $\rho^{(1)}_B(x,t)$ and $\rho^{(1)}_I(x,t)$ for weak impurity-impurity couplings, i.e., $g_{II}/\tilde{g}_{\text{ho}} = 0.2$, and for varying impurity-medium interaction strength. As it can be exemplarily inferred from Figs. 6(a1) and 6(b1) for weakly attractive or repulsive g_{BI} the impurities perform a periodic motion within the harmonic trap and induce only small deformations to the bath density associated with sound-wave emission of the latter [Figs. 6(a2) and 6(b2)]. In the former case, a persisting breathing dynamics of the initially localized impurities takes place being somewhat similar to the one which has been previously discussed for a medium confined in a box potential [Fig. 4(a1)]. In the latter scenario corresponding to Fig. 6(b2), the originally spatially separated impurities collide around $x = 0$ and then split in a periodic fashion (see also the discussion below).

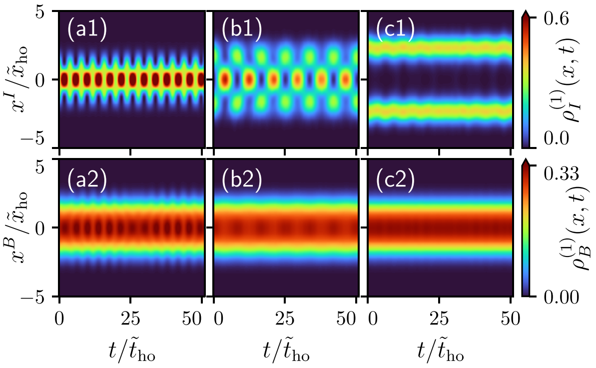

FIG. 6. Spatiotemporal evolution of the one-body densities for two weakly interacting impurities ($g_{II}/\tilde{g}_{\text{ho}} = 0.2$) and a weakly interacting bath ($g_{BB}/\tilde{g}_{\text{ho}} = 0.5$) trapped in a harmonic oscillator. The dynamics is induced by ramping down the barrier of the double well in which the impurities initially reside. In each column a different impurity-medium interaction strength is considered, which is from left to right $g_{BI}/\tilde{g}_{\text{ho}} = -0.2, 0.2, 0.6$.

Moreover, we show the respective density evolution in the phase-separation regime, i.e., for $g_{BI}/\tilde{g}_{\text{ho}} = 0.6 > g_{BB}/\tilde{g}_{\text{ho}}$ [Figs. 6(c1) and 6(c2)]. It can be readily deduced that here the impurities are already initially phase separated with the bath and remain in this state also in the course of the evolution while performing small amplitude oscillations due to their collisions with the bath edges [94]. In particular, for $g_{BI}/\tilde{g}_{\text{ho}} > 0.6$ the impurities remain in the coalescence regime if the initial chosen values for g_{BI} and g_{II} coincide with regime (I) [Fig. 3(a)] and are spatially separated if the values for g_{BI} and g_{II} correspond to regime (III) [Fig. 3(a)]. Furthermore, for very strong attractive g_{BI} the impurities and the medium localize together at the trap center where they remain throughout the time evolution (not shown) (see also Ref. [95] for a similar dynamics). We finally remark that, as in the case of a box-confined medium, increasing the number of bath atoms, e.g., to $N_B = 30$, does not lead to significant alterations of the observed dynamical response.

B. Two-body density evolution for weak impurity-medium repulsions

Let us now focus on the dynamical properties of two impurities which are weakly repulsively coupled to the medium, e.g., via $g_{BI}/\tilde{g}_{\text{ho}} = 0.2$ and interacting among each other with $g_{II}/\tilde{g}_{\text{ho}} = 0.2$ [Fig. 6(b1)]. Specifically, we are interested in

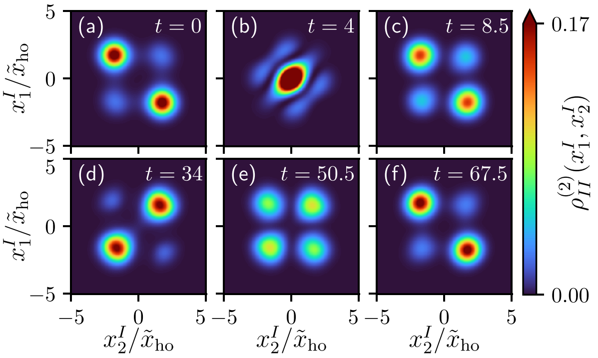

FIG. 7. Dynamical evolution of the impurities' two-body density $\rho_{II}^{(2)}(x_1^I, x_2^I)$ for $g_{BI}/\tilde{g}_{\mathrm{ho}} = 0.2$ and $g_{II}/\tilde{g}_{\mathrm{ho}} = 0.2$ at specific time instants (see legends) in units of $\tilde{t}_{\mathrm{ho}}$. Following the quench the impurities perform a periodic motion consisting of their collision at the trap center and a subsequent expansion. Panel (b) corresponds to a collision event of the impurities, while the other panels refer to time instants at which the impurities expand [cf. Fig. 6(b1)].

the dynamical evolution of the impurities' reduced two-body density $\rho_{II}^{(2)}(x_1^I, x_2^I)$ depicted in Fig. 7. At $t = 0$, corresponding to the ground state in which the two impurities are confined in a double well, their two-body density exhibits two dominant density peaks across its off-diagonal and two suppressed peaks at its diagonal elements [see Fig. 7(a)]. Considering the two diagonal peaks as sufficiently small, this two-body configuration can be interpreted as the probability for the impurities to occupy opposite double-well sites. Following the quench, the impurities collide at the trap center and their cloud starts to contract and expand with a frequency corresponding to the periodic motion of the one-body density [Fig. 6(b1)]. In the course of this periodic motion the two-body configuration alters from a two-body superposition state where both diagonals and off-diagonal elements are populated [Fig. 7(c)] upon expansion of the cloud to a diagonal structure when featuring contraction [see Fig. 7(d)] and vice versa [Fig. 7(f)]. Notice that this dynamical response is inherently related to a process which is hidden on the one-body level [cf. Fig. 6(b1)].

C. Single-particle dynamical excitation processes

To obtain insights into the underlying microscopic processes in the course of the impurity dynamics we project the many-body wave function onto basis functions consisting of the generalized Wannier functions $\phi_i^I(x^I)$ of the initially considered (prequenched) double-well potential [96,97]. In this way we can retrieve the probabilities for the impurities to occupy certain localized states of this basis and distinguish between the left and right double-well sites. The Wannier functions are constructed as a superposition from the six energetically lowest eigenfunctions of the one-body Hamiltonian $\hat{H}^{(1),\mathrm{dw}} = -\frac{\hbar^2}{2m_I}\frac{\partial^2}{(\partial x^I)^2} + V_I^{\mathrm{dw}}(x^I)$ and are provided in Fig. 8(a) together with their associated eigenenergies ϵ_i. In particular, the Wannier state corresponding to $i = 1$ ($i = 2$) is the energetically lowest one at the left (right) site. Analogously, $i = 3, 5$ ($i = 4, 6$) signify the first and second excited Wannier states at the left (right) site. Note that, even though for the analysis a basis of a double-well potential is utilized, the impurities' dynamics still takes place within a harmonic oscillator. The respective two-body probabilities for the impurities to simultaneously occupy the ith and jth Wannier state are given by

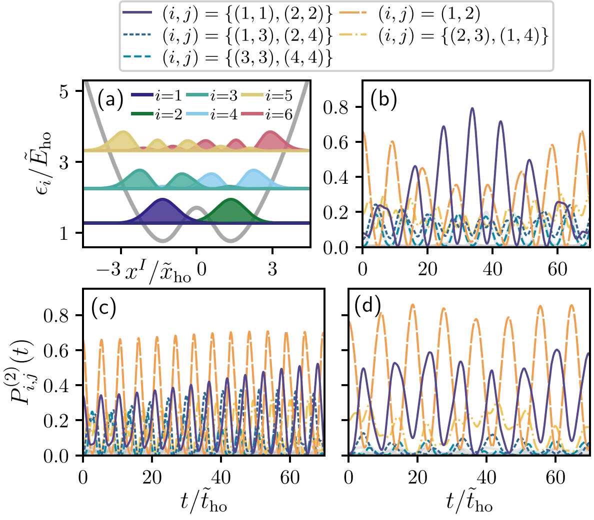

FIG. 8. (a) Wannier states corresponding to the first six energetically lowest eigenfunctions of the one-body Hamiltonian consisting of the double-well potential. [(b)–(d)] Temporal evolution of the two-body probabilities $P_{i,j}^{(2)}(t)$ for the impurities to simultaneously occupy the ith and jth Wannier states for different sets of interaction strengths (g_{BI}, g_{II}), which are (b) (0.2, 0.2), (c) (0.0, 0.2), and (d) (0.2, 2.0), expressed in units of $\tilde{g}_{\mathrm{ho}}$. Probabilities involving either the fifth or the sixth Wannier states are suppressed, having at most an amplitude of 0.05, and are shown in gray. The dynamics is induced by ramping down the barrier of the impurities' double-well potential.

$$P_{i,j}^{(2)}(t) = \langle \Psi^{\mathrm{MB}}(t) | \mathbb{1}_B \otimes |\phi_i^I\rangle\langle\phi_i^I| \otimes |\phi_j^I\rangle\langle\phi_j^I| \, \Psi^{\mathrm{MB}}(t)\rangle. \quad (8)$$

Here $\mathbb{1}_B$ is the unit operator defined in the subspace of the bath and $|\phi_i^I\rangle\langle\phi_i^I|$ are the one-body projectors of the ith Wannier state acting on a single impurity. The quality of the basis is tested by summing up all probabilities $P_{i,j}^{(2)}(t)$ for each time instant and verifying that $\sum_{i,j} P_{i,j}^{(2)}(t) > 0.97$ holds until $t/\tilde{t}_{\mathrm{ho}} = 70$.

The above-described two-body probabilities for $g_{BI}/\tilde{g}_{\mathrm{ho}} = 0.2$ and $g_{II}/\tilde{g}_{\mathrm{ho}} = 0.2$ are presented in Fig. 8(b). All probabilities show an oscillatory behavior stemming from the periodic collision and expansion of the impurities [cf. Fig. 6(b)]. Beyond this rapid motion, a decay and revival of $P_{1,2}^{(2)}(t)$ takes place at longer time scales, where $P_{1,2}^{(2)}(t)$ corresponds to the probability of finding one impurity in the energetically lowest left-site Wannier state while the other one occupies the right-site Wannier state. On the other hand, when the envelope of $P_{1,2}^{(2)}(t)$ reaches a minimum the probability of finding two impurities both in the left $P_{1,1}^{(2)}(t)$ [right $P_{2,2}^{(2)}(t)$] Wannier state is maximized as demonstrated in Fig. 6(b). This observation implies that a single-particle intraband excitation process takes place. Moreover, also energetically higher-lying Wannier states contribute to the ground-state configuration of the impurities as well as to their dynamical response. For

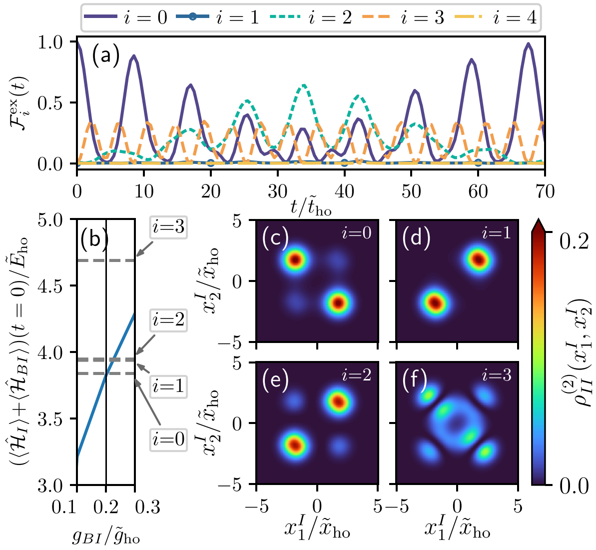

FIG. 9. (a) Time evolution of the fidelity between the many-body wave function for $g_{BI}/\tilde{g}_{\text{ho}} = 0.2$ and $g_{II}/\tilde{g}_{\text{ho}} = 0.2$ and the excited states of the effective two-body Hamiltonian $\hat{H}^{(2),\text{eff}}$ [see also Eq. (7)]. (b) Sum of the impurity-medium interaction energy $\langle\hat{\mathcal{H}}_{BI}\rangle$ and the energy of the impurities $\langle\hat{\mathcal{H}}_I\rangle$ in the many-body approach for the ground state as a function of the impurity-medium coupling (blue line) depicted together with the eigenenergies of $\hat{H}^{(2),\text{eff}}$ (grey horizontal dashed lines). The two-body density of the ground state and the first three excited eigenstates are provided in (c)–(f).

instance, the second and third (first and fourth) Wannier states contribute with $P_{2,3}(0) = P_{1,4}(0) = 19\%$ to the ground-state configuration. Therefore, the initial state is a superposition of different single-particle states. This is to be contrasted with the discussion below (see Fig. 9) where a two-body basis is employed, accounting in a more natural way for effects stemming from impurity-impurity interactions and the coupling to the bath.

For comparison the case of two weakly interacting impurities $g_{II}/\tilde{g}_{\text{ho}} = 0.2$ which are decoupled from the bath ($g_{BI} = 0$) is showcased in Fig. 8(c). It can be readily seen that the impurities do not perform a state transfer similar to the one depicted in Fig. 8(b) but rather retain their delocalized configuration. In particular, at time instants corresponding to an expansion of the impurities cloud the two-body probabilities associated with the energetically lowest Wannier states lying at opposite and the same sites significantly contribute to the impurities' many-body wave function, thus confirming the former statement. Otherwise, the impurities' response is characterized by excitations to energetically higher-lying states. Next, we inspect the case of strongly interacting impurities ($g_{II}/\tilde{g}_{\text{ho}} = 2.0$) which are weakly coupled to the bath ($g_{BI}/\tilde{g} = 0.2$) [Fig. 8(d)]. The dynamics begins with initially separated impurities, viz., $P^{(2)}_{1,2}(t)$ obtains a maximum at $t = 0$, and continues with the collision of the impurities at the trap center where they both dominantly populate the same energetically lowest left or right Wannier state [cf. $P^{(2)}_{1,1}(t) = P^{(2)}_{2,2}(t)$]. Subsequently, the strong impurity-impurity repulsion enforces the impurities to occupy again opposite double-well sites. This scheme repeats itself during the evolution and, in particular, lasts until $T/\tilde{t}_{\text{ho}} = 200$. Again a state transfer process occurs as it can be seen from the competition of $P^{(2)}_{1,2}(t)$ and $P^{(2)}_{1,1}(t)$. However, in this case the transfer is less transparent and not as dominant as for $g_{II}/\tilde{g}_{\text{ho}} = 0.2$, implying that an increasing $g_{II}/\tilde{g}_{\text{ho}}$ results in the suppression of this process.

Therefore, the intraband excitation process observed for $g_{BI}/\tilde{g}_{\text{ho}} = 0.2$ and $g_{II}/\tilde{g}_{\text{ho}} = 0.2$ proves to be sensitive to the impurity-impurity interaction strength and, most importantly, requires a finite impurity-medium coupling. In this manner, we can conclude that this state transfer of the impurities is induced by the presence of the bath. Moreover, we have verified the absence of this mechanism for a species mean-field ansatz [$D = 1$ in Eq. (2)], i.e., when the entanglement is not taken into account. Thus, we can deduce that many-body effects and, in particular, the impurity-medium entanglement play a crucial role for the realization of such processes.

D. Effective two-body impurity mechanisms

To further understand the participating excitation processes we consider a projection of the many-body wave function onto a two-body basis set. In particular, we choose for this investigation the ground state and the first four energetically lowest excited states of an effective Hamiltonian. This effective Hamiltonian $\hat{H}^{(2),\text{eff}}$ describes two weakly interacting impurities ($g_{II}/\tilde{g}_{\text{ho}} = 0.2$) trapped in the effective potential defined in Eq. (7) with $g_{BI}/\tilde{g}_{\text{ho}} = 0.2$. In this manner, we take the back-action induced by the medium into account. In Figs. 9(c)–9(f) we present the impurities' two-body density for the ground state as well as the first three excited states $|\Phi_i^I\rangle$ of $\hat{H}^{(2),\text{eff}}$. As such, we associate the ground state ($i = 0$) with the two-body state $(|LR\rangle + |RL\rangle)/\sqrt{2}$ where $|L\rangle$ ($|R\rangle$) represents a single-particle state corresponding to the left (right) site of the double well. Analogously, we refer to the first ($i = 1$) and second ($i = 2$) excited states as the configurations $(|LL\rangle - |RR\rangle)/\sqrt{2}$ and $(|LL\rangle + |RR\rangle)/\sqrt{2}$, respectively. The corresponding eigenenergies are shown in Fig. 9(b). Note that the first ($i = 1$) and second ($i = 2$) excited eigenstates are approximately degenerate. In order to support the validity of this two-body approach for two impurities coupled to a larger medium, we additionally provide the sum of the impurity energy and the interaction energy $(\langle\hat{\mathcal{H}}_I\rangle + \langle\hat{\mathcal{H}}_{BI}\rangle)$ at $t = 0$ as predicted within the many-body approach, namely, when the impurities are still trapped in a double-well potential. Since this energy matches at $g_{BI}/\tilde{g}_{\text{ho}} = 0.2$ the ground-state energy of the effective approach [cf. intersection of $\langle\hat{\mathcal{H}}_I\rangle + \langle\hat{\mathcal{H}}_{BI}\rangle$ with $i = 0$ in Fig. 9(b)] we conclude that the effective potential adequately accounts for the presence of the medium at $t = 0$.

As a next step, we calculate the fidelity of the two-body eigenstates $|\Phi_i^I\rangle$ with the time-dependent species functions of the impurities being coupled to the medium. In this way, the probabilities of the contributing two-body configurations are revealed. Therefore, we estimate the absolute square of the projection of $\sum_{j=1}^{D} |\Psi_j^B(t)\rangle \otimes |\Phi_i^I\rangle$ on the many-body wave function $|\Psi^{\mathrm{MB}}(t)\rangle$ defined in Eq. (2), which reads as

$$\mathcal{F}_i^{\mathrm{ex}}(t) = \left| \sum_{j=1}^{D} \sqrt{\lambda_j(t)} \langle \Phi_i^I | \Psi_j^I(t) \rangle \right|^2. \tag{9}$$

The dynamics of the fidelity with respect to the ground state and the first four excited eigenstates of $\hat{H}^{(2),\mathrm{eff}}$ is provided in Fig. 9(a). Analogously with the analysis regarding the Wannier states, we observe besides a fast periodic motion a slower decay and revival of the ground state $|\Phi_0^I\rangle$ associated with two separated impurities. This behavior is accompanied by a complementary increase of the second excited state $|\Phi_2^I\rangle = (|LL\rangle + |RR\rangle)/\sqrt{2}$ associated with the coalescence of the impurities. Since the first excited state, corresponding to the antisymmetric configuration $(|LL\rangle - |RR\rangle)/\sqrt{2}$, is strongly suppressed we conclude that the impurities undergo the two-body state transfer from $(|LR\rangle + |RL\rangle)/\sqrt{2}$ to $(|LL\rangle + |RR\rangle)/\sqrt{2}$. Moreover, we note that during the impurities' collision an appreciable amount of higher excited states need to be taken into account as indicated, for instance, by the non-negligible occupation of the third exited state $|\Phi_3^I\rangle$.

Concluding, we have explicated the microscopic mechanisms on both the one- and the two-body level taking place during the collision dynamics of interacting impurities coupled to a harmonically confined bath. For instance, the single-particle intraband excitation process appears to be sensitive with respect to the impurity-impurity interaction strength and requires a finite coupling to the bath. Moreover, an analysis with respect to a two-body basis deciphered the transitions among particular two-body configurations.

VII. CONCLUSIONS AND OUTLOOK

We have investigated the ground state and correlated dynamics of two interacting bosonic impurities confined in a double well and immersed in a bosonic medium. The latter either experiences a box potential or it is confined in a harmonic trap. We establish the phase diagram of the ground state for varying impurity-impurity and impurity-medium coupling strengths. Thereby, the emergent ground states have been characterized with the aid of the two-body densities and impurity-medium entanglement. An analysis of the impact of different trapping geometries on the formation of these phases has been performed. For instance, we explicate that the coalescence of the impurities at strong (repulsive or attractive) impurity-medium interaction strengths is preserved for different impurity-impurity repulsions when the bath is in a box. However, in the case of a harmonically trapped bath the impurities separate from each other for strong impurity-impurity repulsion residing in a Mott-type configuration. Moreover, in the latter scenario, we observe at strong impurity-medium attractions indications for the formation of a bipolaron.

Focusing on a specific interaction-dependent ground-state configuration we trigger the dynamics by suddenly ramping down the potential barrier of the impurities' double well. First, the dynamical response regimes of the impurities coupled to a box-confined medium are unraveled with respect to their associated one- and two-body densities. In particular, for intermediate impurity-medium repulsions a localization of the impurities at the trap center after the original collision is realized. The impurities' two-body density features an elongated shape along the diagonal for weak impurity-impurity repulsion which suggests the presence of attractive induced interactions mediated by the bath. This induced localization of the impurities persists also when the coupling strength between the impurities is further increased. This observation together with the existence of a spatial overlap for finite impurity-medium interaction strengths support the formation of quasiparticles, i.e., two interacting polarons. We have attested the robustness of the above phenomena with respect to variations of the number of bath particles and the size of the box potential. However, for strong repulsions finite size effects of the medium's box potential come into play and govern the dynamical response of the system. Essentially, after the impurities' collision at the trap center they drift apart and then the medium reoccupies the center.

By considering a harmonically confined bath the impurities' response is qualitatively altered. Due to the spatial localization of the bath at the trap center the impurities and the medium undergo a phase separation already for intermediate impurity-medium repulsions as it was also observed on the ground-state level. The response becomes especially intriguing for weak impurity-medium couplings where the impurities are able to perform a breathing motion within the bath. Specifically, for weak impurity-medium repulsions we observe a state transfer of the impurities starting with two spatially separated ones located at different double-well sites and evolving into a coalesced configuration, i.e., the impurities cluster. Interestingly, this state transfer process does not emerge for strongly interacting impurities and, most importantly, requires a finite impurity-medium interaction strength; viz., it is induced by the coupling to the bath. Moreover, it is shown that this mechanism can be well understood in terms of a single-particle Wannier basis of the double well. Additionally, we reveal the participating two-body states in this process using an analysis in terms of a two-body basis which consists of the low-lying excited states of a corresponding effective two-body Hamiltonian.

There are several possible extensions of our results. An immediate one will be to investigate the collision features of the impurities immersed in a spatially extended bosonic gas with the aim to unveil their possible damping mechanisms and appreciate the corresponding drag force. In another context, it would be worth including a spin degree of freedom for the impurities. Here, the dynamics of the emergent spin-spin correlations is of interest especially when the impurities localize around the trap center. Moreover, it would be intriguing to consider two impurities with different masses, e.g., a light and heavy one, coupled to a background. This way it would be feasible to investigate the influence of the mass on the emergent collisional aspects of the impurities and their induced interactions as well as trigger specific population transfer channels by considering a Rabi coupling term.

ACKNOWLEDGMENTS

This work has been funded by the Deutsche Forschungsgemeinschaft (DFG, Germany Research Foundation), SFB 925, project 170620586. S.I.M. gratefully acknowledges financial

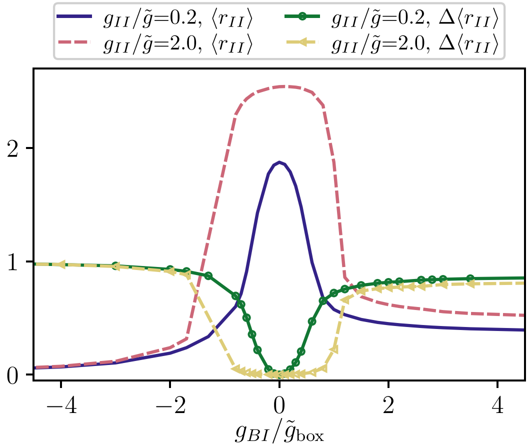

FIG. 10. Ground-state relative distance between the impurities $\langle r_{II}\rangle$ (in units of $\tilde{x}_{\rm ho}$) with respect to the impurity-medium interaction strength g_{BI} for different impurity-impurity couplings (see legend). The relative difference $\Delta\langle r_{II}\rangle$ between the impurity-impurity distance predicted within the many-body approach ($\langle r_{II}\rangle$) and the effective Hamiltonian of Eq. (7) with $V_I^{\rm dw}(x^I)=0$ ($\langle r_{II}^{\rm eff}\rangle$) is also provided (see main text).

support from the NSF through a grant for ITAMP at Harvard University. The authors acknowledge fruitful discussions with G. M. Koutentakis.

APPENDIX A: BATH CONFINED IN A BOX POTENTIAL: RELATIVE DISTANCE BETWEEN THE IMPURITIES

In the following, we examine the impurities' relative distance $\langle r_{II}\rangle$ which can serve as an indicator for the existence of their induced interactions mediated by the bath [38,39,98]. This quantity, which is accessible through *in situ* spin-resolved single-shot measurements on the impurities state [99], reads

$$\langle r_{II}\rangle(t)=\frac{1}{N_I(N_I-1)}\int dx_1^I dx_2^I |x_1^I-x_2^I|\rho_{II}^{(2)}(x_1^I,x_2^I). \quad \text{(A1)}$$

The impurities' relative distance is presented in Fig. 10 for the ground state of the system ($t=0$) for varying impurity-medium interaction strength and different impurity-impurity couplings. In the case of two weakly interacting impurities as well as for two strongly interacting ones we observe that with an increasing absolute value of g_{BI} the relative distance between the impurities reduces. This behavior implies an induced attraction mediated by the coupling to the bath. Furthermore, it is evident that for larger impurity-impurity interactions $\langle r_{II}\rangle$ is enhanced when compared to the one of weakly interacting impurities. This behavior is caused by the increased intraspecies impurities' direct repulsion compensating their induced attraction.

To further justify the presence of induced interactions, we compare the resulting impurities' relative distance as obtained using the many-body approach ($\langle r_{II}\rangle$) with the one ($\langle r_{II}^{\rm eff}\rangle$) predicted within the effective two-body Hamiltonian $\bar{H}^{(2),\rm eff}$. The latter was introduced in Sec. VI for a harmonically confined medium. Notice that here this effective Hamiltonian describes the interplay between two interacting particles confined in an effective potential constructed by the one-body density of a box-trapped medium [see Eq. (7)]. As such, the entanglement between the impurities and the medium is neglected while effects stemming from the back-action to the bath are taken into account. By comparing $\langle r_{II}\rangle$ between these two methods we can determine whether the decrease of $\langle r_{II}\rangle$ for increasing $|g_{BI}|$ (see Fig. 10) originates from an entanglement-assisted induced interaction or if it is due to an alteration of the effective potential.

Inspecting $\Delta\langle r_{II}\rangle=(\langle r_{II}^{\rm eff}\rangle-\langle r_{II}\rangle)/\langle r_{II}^{\rm eff}\rangle$ depicted in Fig. 10, a large deviation among $\langle r_{II}\rangle$ and $\langle r_{II}^{\rm eff}\rangle$ becomes evident for increasing $|g_{BI}|$. This confirms the presence of attractive induced interactions between the impurities. The fact that $\Delta\langle r_{II}\rangle$ is finite can be traced back to the shape of the impurities' two-body densities as obtained within the aforementioned approaches for large g_{BI} [corresponding to regime (I) in Fig. 2(a)]. While in the many-body scenario the impurities coalesce [namely, only the diagonal of $\rho_{II}^{(2)}(x_1^I,x_2^I)$ is occupied], in the effective potential case both the diagonal and the off-diagonal elements of $\rho_{II}^{(2)}(x_1^I,x_2^I)$ are equally populated. This naturally leads to a larger relative distance. Concluding, the comparison with the effective model underlies the importance of considering correlations in the system and reveals the presence of attractive induced interactions between the impurities (see more details in Refs. [39,100]).

APPENDIX B: COLLISIONAL PROPERTIES OF TWO HEAVY IMPURITIES

Throughout this work we have considered a system consisting of ^{87}Rb bath particles and ^{133}Cs impurities corresponding to a mass ratio of $m_I=133/87m_B$. Below, we employ a mixture characterized by a mass ratio $m_I'=5m_B$ in order to elaborate on the dynamical response of two heavy impurities [38] immersed in a bath confined in a box potential [101]. The time evolution of the corresponding one- and two-body densities of the impurities and the bath particles is depicted in Figs. 11(a1)–11(c1) and 11(a2)–11(c2) for interaction parameters as the ones employed in the main text (Fig. 4). In particular, we assume two weakly interacting impurities ($g_{II}/\tilde{g}_{\rm box}=0.2$) and vary the impurity-medium interaction strength g_{BI}. Regarding the one-body density evolution we do observe a qualitatively similar behavior as compared to the case of lighter impurities. Only in the case of weak attractive g_{BI} [Fig. 11(a1)] do the heavy impurities perform a more pronounced breathing oscillation with a larger oscillation period. Inspecting a two-body density snapshot reveals that the impurities are spatially separated from each other and oscillate along the off diagonal of $\rho_{II}^{(2)}(x_1^I,x_2^I)$ [cf. Fig. 11(a3)]. Therefore, they are not delocalized as their lighter counterparts [Fig. 4(a3)], and this behavior persists for two strongly interacting impurities [cf. inset of Fig. 11(a3)].

Additionally, for intermediate impurity-medium repulsions, i.e., $g_{BI}/\tilde{g}_{\rm box}=1.5$, the one-body densities of the impurities and the medium [Figs. 11(b1) and 11(b2)] as well as the impurities' two-body density [Fig. 11(b3) and its inset] do not reveal a qualitatively different response with respect to the case of lighter impurities [cf. Figs. 4(b1)–4(b3)]. Indeed the impurities remain very close throughout the time evolu-

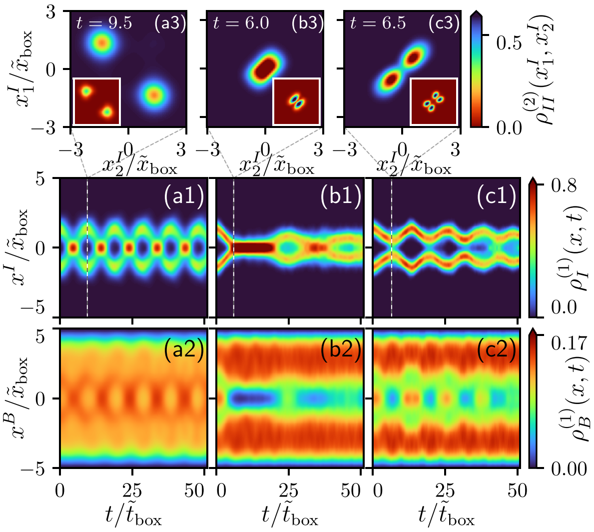

FIG. 11. Time evolution of the one-body density of [(a1)–(c1)] two heavy impurities and [(a2)–(c2)] a box-confined bosonic bath. Each column represents the dynamics for a fixed impurity-medium interaction strength which is from left to right $g_{BI}/\tilde{g}_{\rm box} = -0.2, 1.5, 5.0$. The impurity-impurity coupling remains constant, being $g_{II}/\tilde{g}_{\rm box} = 0.2$. [(a3)–(c3)] Snapshots of the impurities' two-body density. The insets show the two-body densities at the same time instants, but for two strongly interacting impurities, i.e., $g_{II}/\tilde{g}_{\rm box} = 2.0$.

tion, exhibiting a more pronounced localization trend around the trap center as compared to lighter ones. The same holds also for the case of strong impurity-medium interactions [see Figs. 11(c1)–11(c3) for $g_{BI}/\tilde{g}_{\rm box} = 5.0$] where the impurities feature multiple collisions with a dissipative amplitude. Only, the fragmentation in terms of the diagonal of the two-body density for $g_{II}/\tilde{g}_{\rm box} = 2.0$ is more prominent in the case of heavy impurities than for lighter ones [cf. inset of Fig. 11(c3)] and becomes visible even on the one-body density level (not shown here).

APPENDIX C: IMPURITY DYNAMICS AFTER A LINEAR RAMP OF THEIR DOUBLE-WELL POTENTIAL

In the following we address the robustness of the impurities' dynamical response when ramping down their barrier height h_I in a time-dependent manner and not suddenly as in the main text. Specifically, we apply the following linear protocol: $\tilde{h}_I(t) = h_I - h_I t/\tau$ if $0 \leqslant t \leqslant \tau$ while $\tilde{h}_I(t) = 0$ as long as $\tau < t$. The ramp time τ is defined as the one at which the barrier height vanishes, i.e., when $\tilde{h}_I(\tau) = 0$. For our purposes, we restrict our study to finite values of τ which deviate from the instantaneous quench but also do not refer to an adiabatic linear ramping.

To visualize the impact of the time-dependent protocol on the impurities' collision process we present in Fig. 12 the time evolution of the von Neumann entanglement entropy [Eq. (5)] and the impurities' one-body density. We follow a linear ramp of the impurities' barrier height characterized by a finite ramp time $\tau/\tilde{t}_{\rm box} = 30$. Notice that the latter appreciably deviates from the quench scenario ($\tau/\tilde{t}_{\rm box} = 0$). Moreover, we exemplarily invoke the system where the medium is confined in a box potential while the relevant interactions are $g_{BB}/\tilde{g}_{\rm box} = 0.5$, $g_{II}/\tilde{g}_{\rm box} = 0.2$, and $g_{BI}/\tilde{g}_{\rm box} = 1.5$. Recall that in the main text it has been shown that in this regime the impurities localize at the trap center after their first collision event [see also Fig. 4(b1)]. As it can be readily seen [Fig. 12(b)], the impurities' dynamical response in terms of $\rho^{(1)}_I(x,t)$ remains qualitatively unchanged as compared to the quench [Fig. 4(b1)]. The most prominent difference regards the timescale at which the impurities collide and subsequently localize at the trap center. As expected the initial collision can be delayed for an increasing ramp time. Turning to the evolution of the respective von Neumann entropies for varying ramp times we observe an interesting behavior. At short timescales the impurities and the medium are highly entangled [Fig. 12(a)]. The magnitude of the entanglement is maintained in the course of the evolution until the impurities collide and then localize at the trap center, where it suddenly decreases. This drop of the entanglement depends strongly on the ramp time and in particular it takes place faster for smaller τ since in this case the collision event is accelerated.

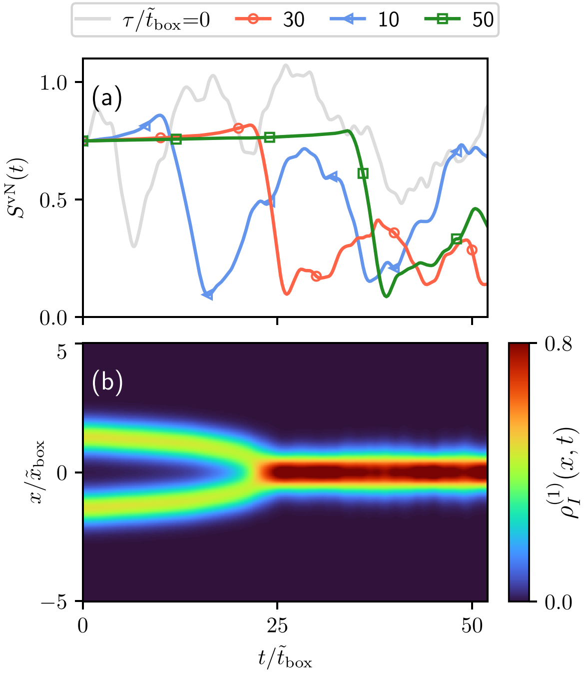

FIG. 12. (a) Time evolution of the von Neumann entropy upon linearly ramping down the barrier height h_I of the double well for different ramp times τ (see legend). The impurities are weakly interacting with $g_{II}/\tilde{g}_{\rm box} = 0.2$ and are coupled to a box-confined medium with an interspecies coupling $g_{BI}/\tilde{g}_{\rm box} = 1.5$. An increasing ramp time maintains an almost constant magnitude of entanglement until the impurities' collision. (b) The corresponding one-body density evolution of the impurities for $\tau/\tilde{t}_{\rm box} = 30$. As it can be seen the linear ramp delays the impurities' first collision event when compared to Fig. 4(b1), referring to the corresponding quench dynamics.

Concluding, we remark that the linear protocol affects the remaining response regimes, occurring for other interspecies interaction strengths, in a similar vein. Namely, the main features as described in Sec. V are not substantially altered but rather the underlying timescales change. For instance, considering weak attractive or repulsive g_{BI} referring to the impurities' breathing motion [Fig. 4(a1)], we find a decreasing tendency of the breathing amplitude and frequency for larger τ (not shown). This is attributed to the fact that for increasing τ the collision of the impurities is less violent, thus producing a less pronounced breathing. Analogous effects are observed for a harmonically trapped medium where, for instance, also in this case the amplitude and frequency of the underlying breathing motion depend strongly on the ramp time τ.

[1] C. Chin, R. Grimm, P. Julienne, and E. Tiesinga, Rev. Mod. Phys. **82**, 1225 (2010).

[2] R. Grimm, M. Weidemüller, and Y. B. Ovchinnikov, Adv. At. Mol. Opt. Phys. **42**, 95 (2000).

[3] K. Henderson, C. Ryu, C. MacCormick, and M. G. Boshier, New J. Phys. **11**, 043030 (2009).

[4] A. L. Gaunt, T. F. Schmidutz, I. Gotlibovych, R. P. Smith, and Z. Hadzibabic, Phys. Rev. Lett. **110**, 200406 (2013).

[5] M. Haas, V. Leung, D. Frese, D. Haubrich, S. John, C. Weber, A. Rauschenbeutel, and D. Meschede, New J. Phys. **9**, 147 (2007).

[6] J. Catani, G. Lamporesi, D. Naik, M. Gring, M. Inguscio, F. Minardi, A. Kantian, and T. Giamarchi, Phys. Rev. A **85**, 023623 (2012).

[7] A. J. Barker, S. Sunami, D. Garrick, A. Beregi, K. Luksch, E. Bentine, and C. J. Foot, New J. Phys. **22**, 103040 (2020).

[8] A. J. Barker, S. Sunami, D. Garrick, A. Beregi, K. Luksch, E. Bentine, and C. J. Foot, J. Phys. B: At. Mol. Opt. Phys. **53**, 155001 (2020).

[9] M. Olshanii, Phys. Rev. Lett. **81**, 938 (1998).

[10] T. Köhler, K. Góral, and P. S. Julienne, Rev. Mod. Phys. **78**, 1311 (2006).

[11] L. D. Landau, Phys. Z. Sowjetunion **3**, 644 (1933).

[12] A. Schirotzek, C.-H. Wu, A. Sommer, and M. W. Zwierlein, Phys. Rev. Lett. **102**, 230402 (2009).

[13] S. Nascimbène, N. Navon, K. J. Jiang, L. Tarruell, M. Teichmann, J. McKeever, F. Chevy, and C. Salomon, Phys. Rev. Lett. **103**, 170402 (2009).

[14] C. Kohstall, M. Zaccanti, M. Jag, A. Trenkwalder, P. Massignan, G. M. Bruun, F. Schreck, and R. Grimm, Nature (London) **485**, 615 (2012).

[15] V. Ngampruetikorn, J. Levinsen, and M. M. Parish, Europhys. Lett. **98**, 30005 (2012).

[16] P. Massignan, M. Zaccanti, and G. M. Bruun, Rep. Prog. Phys. **77**, 034401 (2014).

[17] R. Schmidt, M. Knap, D. A. Ivanov, J.-S. You, M. Cetina, and E. Demler, Rep. Prog. Phys. **81**, 024401 (2018).

[18] H. Tajima, J. Takahashi, S. I. Mistakidis, E. Nakano, and K. Iida, Atoms **9**, 18 (2021).

[19] T. Fukuhara, A. Kantian, M. Endres, M. Cheneau, P. Schauß, S. Hild, D. Bellem, U. Schollwöck, T. Giamarchi, C. Gross, I. Bloch, and S. Kuhr, Nat. Phys. **9**, 235 (2013).

[20] N. B. Jørgensen, L. Wacker, K. T. Skalmstang, M. M. Parish, J. Levinsen, R. S. Christensen, G. M. Bruun, and J. J. Arlt, Phys. Rev. Lett. **117**, 055302 (2016).

[21] M.-G. Hu, M. J. Van de Graaff, D. Kedar, J. P. Corson, E. A. Cornell, and D. S. Jin, Phys. Rev. Lett. **117**, 055301 (2016).

[22] A. G. Volosniev and H.-W. Hammer, Phys. Rev. A **96**, 031601(R) (2017).

[23] F. Grusdt, R. Schmidt, Y. E. Shchadilova, and E. Demler, Phys. Rev. A **96**, 013607 (2017).

[24] S. I. Mistakidis, G. C. Katsimiga, G. M. Koutentakis, T. Busch, and P. Schmelcher, Phys. Rev. Lett. **122**, 183001 (2019).

[25] L. A. Peña Ardila, N. B. Jörgensen, T. Pohl, S. Giorgini, G. M. Bruun, and J. J. Arlt, Phys. Rev. A **99**, 063607 (2019).

[26] L. A. Peña Ardila, G. E. Astrakharchik, and S. Giorgini, Phys. Rev. Research **2**, 023405 (2020).

[27] M. G. Skou, T. G. Skov, N. B. Jørgensen, K. K. Nielsen, A. Camacho-Guardian, T. Pohl, G. M. Bruun, and J. J. Arlt, Nat. Phys. **17**, 731 (2021).

[28] F. Grusdt, G. E. Astrakharchik, and E. Demler, New J. Phys. **19**, 103035 (2017).

[29] A. Camacho-Guardian and G. M. Bruun, Phys. Rev. X **8**, 031042 (2018).

[30] D. Huber, H.-W. Hammer, and A. G. Volosniev, Phys. Rev. Research **1**, 033177 (2019).

[31] F. Brauneis, H.-W. Hammer, M. Lemeshko, and A. Volosniev, SciPost Phys. **11**, 008 (2021).

[32] A. S. Dehkharghani, A. G. Volosniev, and N. T. Zinner, Phys. Rev. Lett. **121**, 080405 (2018).

[33] C. Charalambous, M. A. Garcia-March, A. Lampo, M. Mehboud, and M. Lewenstein, SciPost Phys. **6**, 010 (2019).

[34] B. Reichert, Z. Ristivojevic, and A. Petković, New J. Phys. **21**, 053024 (2019).

[35] K. Keiler, S. I. Mistakidis, and P. Schmelcher, Phys. Rev. A **104**, L031301 (2021).

[36] A. Camacho-Guardian, L. A. Peña Ardila, T. Pohl, and G. M. Bruun, Phys. Rev. Lett. **121**, 013401 (2018).

[37] M. Will, G. E. Astrakharchik, and M. Fleischhauer, Phys. Rev. Lett. **127**, 103401 (2021).

[38] K. Mukherjee, S. I. Mistakidis, S. Majumder, and P. Schmelcher, Phys. Rev. A **102**, 053317 (2020).

[39] S. I. Mistakidis, G. M. Koutentakis, G. C. Katsimiga, T. Busch, and P. Schmelcher, New J. Phys. **22**, 043007 (2020).

[40] G. Bougas, S. I. Mistakidis, and P. Schmelcher, Phys. Rev. A **103**, 023313 (2021).

[41] C. Hamner, J. J. Chang, P. Engels, and M. A. Hoefer, Phys. Rev. Lett. **106**, 065302 (2011).

[42] A. Weller, J. P. Ronzheimer, C. Gross, J. Esteve, M. K. Oberthaler, D. J. Frantzeskakis, G. Theocharis, and P. G. Kevrekidis, Phys. Rev. Lett. **101**, 130401 (2008).

[43] F. Köhler and P. Schmelcher, Phys. Rev. A **103**, 043326 (2021).

[44] R. Thomas, M. Chilcott, C. Chisholm, A. B. Deb, M. Horvath, B. J. Sawyer, and N. Kjærgaard, J. Phys.: Conf. Ser. **875**, 012007 (2017).

[45] R. Thomas, M. Chilcott, E. Tiesinga, A. B. Deb, and N. Kjærgaard, Nat. Commun. **9**, 4895 (2018).

[46] H. Tajima, J. Takahashi, E. Nakano, and K. Iida, Phys. Rev. A **102**, 051302(R) (2020).

[47] J. Kwasniok, S. I. Mistakidis, and P. Schmelcher, Phys. Rev. A **101**, 053619 (2020).

[48] F. Theel, K. Keiler, S. I. Mistakidis, and P. Schmelcher, Phys. Rev. Research **3**, 023068 (2021).

[49] J. Goold, T. Fogarty, N. Lo Gullo, M. Paternostro, and T. Busch, Phys. Rev. A **84**, 063632 (2011).

[50] S. I. Mistakidis, G. C. Katsimiga, G. M. Koutentakis, and P. Schmelcher, New J. Phys. **21**, 043032 (2019).

[51] S. Krönke, L. Cao, O. Vendrell, and P. Schmelcher, New J. Phys. **15**, 063018 (2013).

[52] L. Cao, S. Krönke, O. Vendrell, and P. Schmelcher, J. Chem. Phys. **139**, 134103 (2013).

[53] L. Cao, V. Bolsinger, S. I. Mistakidis, G. M. Koutentakis, S. Krönke, J. M. Schurer, and P. Schmelcher, J. Chem. Phys. **147**, 044106 (2017).

[54] F. Köhler, K. Keiler, S. I. Mistakidis, H.-D. Meyer, and P. Schmelcher, J. Chem. Phys. **151**, 054108 (2019).

[55] L. J. LeBlanc and J. H. Thywissen, Phys. Rev. A **75**, 053612 (2007).

[56] A. D. Lercher, T. Takekoshi, M. Debatin, B. Schuster, R. Rameshan, F. Ferlaino, R. Grimm, and H. C. Nägerl, Eur. Phys. J. D **65**, 3 (2011).

[57] M. A. Cazalilla, R. Citro, T. Giamarchi, E. Orignac, and M. Rigol, Rev. Mod. Phys. **83**, 1405 (2011).

[58] W. Ketterle and N. J. van Druten, Phys. Rev. A **54**, 656 (1996).

[59] A. Görlitz, J. M. Vogels, A. E. Leanhardt, C. Raman, T. L. Gustavson, J. R. Abo-Shaeer, A. P. Chikkatur, S. Gupta, S. Inouye, T. Rosenband, and W. Ketterle, Phys. Rev. Lett. **87**, 130402 (2001).

[60] S. Inouye, M. R. Andrews, J. Stenger, H.-J. Miesner, D. M. Stamper-Kurn, and W. Ketterle, Nature (London) **392**, 151 (1998).

[61] P. O. Fedichev, Y. Kagan, G. V. Shlyapnikov, and J. T. M. Walraven, Phys. Rev. Lett. **77**, 2913 (1996).

[62] Q. Bouton, J. Nettersheim, D. Adam, F. Schmidt, D. Mayer, T. Lausch, E. Tiemann, and A. Widera, Phys. Rev. X **10**, 011018 (2020).

[63] D. Adam, Q. Bouton, J. Nettersheim, S. Burgardt, and A. Widera, arXiv:2105.03331.

[64] M. Albiez, R. Gati, J. Fölling, S. Hunsmann, M. Cristiani, and M. K. Oberthaler, Phys. Rev. Lett. **95**, 010402 (2005).

[65] S. Zöllner, H.-D. Meyer, and P. Schmelcher, Phys. Rev. Lett. **100**, 040401 (2008).

[66] The characteristic length of the box potential is set such that the resulting interaction scales are comparable with the ones used in the case of a harmonically trapped medium.

[67] A. Raab, Chem. Phys. Lett. **319**, 674 (2000).

[68] Throughout this work the characterization "many-body" refers to the applied treatment for addressing the properties of the binary mixture. Indeed, the *ab initio* ML-MCTDHX method provides access to both intra- and intercomponent correlations by considering an expansion of the system's wave function as a superposition of many-particle configurations with variationally optimized single-particle functions.

[69] E. Schmidt, Math. Ann. **63**, 433 (1907).

[70] A. Ekert and P. L. Knight, Am. J. Phys. **63**, 415 (1995).

[71] R. Horodecki, P. Horodecki, M. Horodecki, and K. Horodecki, Rev. Mod. Phys. **81**, 865 (2009).

[72] H. Li and F. D. M. Haldane, Phys. Rev. Lett. **101**, 010504 (2008).

[73] J. C. Light, I. P. Hamilton, and J. V. Lill, J. Chem. Phys. **82**, 1400 (1985).

[74] M. A. García-March, B. Juliá-Díaz, G. E. Astrakharchik, T. Busch, J. Boronat, and A. Polls, New J. Phys. **16**, 103004 (2014).

[75] R. Paškauskas and L. You, Phys. Rev. A **64**, 042310 (2001).

[76] P. Jain and M. Boninsegni, Phys. Rev. A **83**, 023602 (2011).

[77] S. Bandyopadhyay, A. Roy, and D. Angom, Phys. Rev. A **96**, 043603 (2017).

[78] E. J. Mueller, T.-L. Ho, M. Ueda, and G. Baym, Phys. Rev. A **74**, 033612 (2006).

[79] S. Zöllner, H.-D. Meyer, and P. Schmelcher, Phys. Rev. A **74**, 053612 (2006).

[80] S. Zöllner, H.-D. Meyer, and P. Schmelcher, Phys. Rev. A **74**, 063611 (2006).

[81] D. S. Murphy, J. F. McCann, J. Goold, and T. Busch, Phys. Rev. A **76**, 053616 (2007).

[82] To discern among the different phases we rely on the integrated two-body density of the impurities $\int_{-\infty}^{0} dx_1^I dx_2^I \rho_{II}^{(2)}(x_1^I, x_2^I)$. It immediately distinguishes the cases of two separated (coalesced) impurities where it acquires the value 0.0 (0.5). Furthermore, it allows to also identify intermediate regimes where both the diagonal and the off-diagonal elements of $\rho_{II}^{(2)}(x_1^I, x_2^I)$ are populated. Notice that for a box-confined medium we additionally weight the integrated density by $\mathrm{sgn}(g_{BI})$ in order to distinguish between regimes (I) and (III) appearing at strongly repulsive and attractive g_{BI}, respectively.

[83] Throughout this work we refer to weakly (strongly) interacting impurities when $g_{II} < g_{BB}$ ($g_{II} > g_{BB}$). Similarly, we use the term weak (intermediate, strong) impurity-medium interaction strength if $g_{BI} < g_{BB}$ ($g_{BI} > g_{BB}, g_{BI} \gg g_{BB}$).

[84] A. C. Pflanzer, S. Zöllner, and P. Schmelcher, J. Phys. B: At. Mol. Opt. Phys. **42**, 231002 (2009).

[85] A. C. Pflanzer, S. Zöllner, and P. Schmelcher, Phys. Rev. A **81**, 023612 (2010).

[86] Y. Liu and Y. Zhang, Phys. Rev. A **91**, 053610 (2015).

[87] S. P. Rath and R. Schmidt, Phys. Rev. A **88**, 053632 (2013).

[88] We have verified that varying from $g_{II}/\tilde{g}_{\mathrm{box}} = 0.0$ to 2.0 the overall shape of the one-body density of both species does not qualitatively alter for fixed g_{BI}. However, quantitative deviations are in play, for example, for strong g_{II} for which the periodic motion consisting of the impurities' collision and expansion is more pronounced than for weak g_{II}.

[89] A similar localization behavior of the impurities is also observed for the dynamical evolution at intermediate and strong attractive g_{BI} (not shown here). However, in this case also the medium localizes around the trap center.

[90] However, we remark that for an adequate description of the quasiparticle notion more elaborated measures need to be con-

sidered such as the residue, which goes beyond the present scope.

[91] J. P. Ronzheimer, M. Schreiber, S. Braun, S. S. Hodgman, S. Langer, I. P. McCulloch, F. Heidrich-Meisner, I. Bloch, and U. Schneider, Phys. Rev. Lett. **110**, 205301 (2013).

[92] F. Theel, K. Keiler, S. I. Mistakidis, and P. Schmelcher, New J. Phys. **22**, 023027 (2020).

[93] Since in this scenario the size of the impurities' double-well potential is not altered, the absence of the dynamical response corresponding to Fig. 4(c1) provides further evidence for the involvement of finite size effects in this latter case.

[94] We remark that such a diminishing response for these values of g_{BI} is observed besides the one-body density level also for the corresponding two-body densities which preserve their initial diagonal or off-diagonal shape depending on the species (not shown here).

[95] S. I. Mistakidis, A. G. Volosniev, and P. Schmelcher, Phys. Rev. Research **2**, 023154 (2020).

[96] S. Kivelson, Phys. Rev. B **26**, 4269 (1982).

[97] S. Kivelson and J. R. Schrieffer, Phys. Rev. B **25**, 6447 (1982).

[98] S. I. Mistakidis, L. Hilbig, and P. Schmelcher, Phys. Rev. A **100**, 023620 (2019).

[99] A. Bergschneider, V. M. Klinkhamer, J. H. Becher, R. Klemt, G. Zürn, P. M. Preiss, and S. Jochim, Phys. Rev. A **97**, 063613 (2018).

[100] J. Chen, J. M. Schurer, and P. Schmelcher, Phys. Rev. Lett. **121**, 043401 (2018).

[101] Additionally, the trap frequency of the harmonic confinement has been adjusted according to $\omega_I' = \omega_I \sqrt{\frac{m_I}{m_I'}}$ in order to preserve the initial shape of the double-well potential.

SciPost | SciPost Phys. 16, 023 (2024)

Crossover from attractive to repulsive induced interactions and bound states of two distinguishable Bose polarons

Friethjof Theel[1], **Simeon I. Mistakidis**[2,3] and **Peter Schmelcher**[4]

1 Center for Optical Quantum Technologies, University of Hamburg,
Department of Physics, Luruper Chaussee 149, D-22761, Hamburg, Germany
2 ITAMP, Center for Astrophysics | Harvard & Smithsonian, Cambridge, MA 02138 USA
3 Department of Physics, Harvard University, Cambridge, Massachusetts 02138, USA
4 The Hamburg Centre for Ultrafast Imaging, University of Hamburg,
Luruper Chaussee 149, D-22761, Hamburg, Germany

Abstract

We study the impact of induced correlations and quasiparticle properties by immersing two distinguishable impurities in a harmonically trapped bosonic medium. It is found that when the impurities couple both either repulsively or attractively to their host, the latter mediates a two-body correlated behavior between them. In the reverse case, namely the impurities interact oppositely with the host, they feature anti-bunching. Monitoring the impurities relative distance and constructing an effective two-body model to be compared with the full many-body calculations, we are able to associate the induced (anti-) correlated behavior of the impurities with the presence of attractive (repulsive) induced interactions. Furthermore, we capture the formation of a bipolaron and a trimer state in the strongly attractive regime. The trimer refers to the correlated behavior of two impurities and a representative atom of the bosonic medium and it is characterized by an ellipsoidal shape of the three-body correlation function. Our results open the way for controlling polaron induced correlations and creating relevant bound states.

Copyright F. Theel *et al*.
This work is licensed under the Creative Commons
Attribution 4.0 International License.
Published by the SciPost Foundation.

Received 09-03-2023
Accepted 28-12-2023
Published 23-01-2024
doi:10.21468/SciPostPhys.16.1.023

Check for updates

Contents

---

1 Introduction

Impurities embedded in a many-body medium, e.g. a Bose-Einstein condensate (BEC), are dressed by its excitations and generate quasiparticles [1, 2]. In the case of a structureless host these refer to polarons [3], while for instance, utilizing a magnetic environment or in the presence of a cavity, magnetic polarons [4–6] and polaritons [7, 8] are formed respectively. Polarons, which we will investigate herein, have been widely studied in cold-atom settings owing to the enormous flexibility, e.g., in terms of controlling the spatial dimension [9–11], the interparticle interactions [12–14], as well as the trapping geometry and the number of species [15–19] and atoms [20,21]. Depending on the statistics of the medium both Bose [11,22–26] and Fermi [1,27,28] polarons have been experimentally realized. Theoretically fundamental properties of these type of quasiparticles including effective mass [29–31], residue [1, 2], and bound state formation [1, 2, 32] emerging in two-component systems have been discussed. Interestingly, by immersing at least two impurities into a quantum gas the latter mediates interactions between the former [33–36], a phenomenon that has been interpreted in terms of a Casimir-type interaction describing the induced interaction between two objects in a fluctuating medium [37–39]. In particular, induced interactions between two impurities are solely attractive as long as they couple in the same way (i.e. in terms of sign and strength) to the fluctuating medium [38–46]. The magnitude of this induced attraction, in general, increases for larger impurity-medium coupling strength and specifically for sufficiently strong attractive ones the impurities assemble in a bound state that can be a bipolaron [32, 43, 45, 47–49] or a trimeron [50]. Notice that besides the above-discussed studies in a homogeneous BEC environment, the attractive nature of induced interactions has been unveiled also for a harmonically confined [42,51,52] or a lattice trapped [53] medium. Moreover, in the context of open quantum systems where, e.g., two non-interacting particles are coupled to a heat bath, a mediated induced entanglement between the particles has been predicted and its interplay with the inherent decoherence effects has been analyzed for instance in terms of the interatomic distance and temperature [54–62].

Interestingly, it was predicted [37, 39] that there is also the possibility of mediating repulsive impurity-impurity interactions when two impurities are coupled with different signs to a bosonic bath. In this sense, the underlying experimentally relevant three-component system [16, 18] allows to unravel additional polaronic properties as it has been also argued by immersing impurities into a two-component pseudospinor mixture [4–6, 63–66] in order to create, for instance, spin-wave excitations and magnetic polarons [4, 5], impurities diffusive response [64] or to facilitate the detection of the dressing cloud via interferometry [4]. However, quasiparticle formation in three-component systems is largely unexplored, besides the few above-mentioned recent studies. An interesting direction is to exploit the tunability of such mixtures, e.g. in terms of different intercomponent couplings, for devising the ground state quasiparticle properties such as the impurities effective mass and induced interactions. Here, it is important to understand the interplay of the latter properties and the underlying impurities' correlations. Also, the formation of relevant bound states either solely among the impurities (bipolarons) or between the impurities and the host atoms (trimers) remains elusive. To address these questions, we consider two distinguishable and non-interacting impurities that are embedded into an one-dimensional bosonic gas. The impurities' couplings with the host are individually tuned spanning the regime from attractive to repulsive interactions. Here, the effective interactions between the impurities can be only mediated in the presence of impurity-medium entanglement and bound states require the involvement of strong correlations. As such, to account for the relevant inter and intra-component correlations we employ the variational multilayer multiconfiguration time-dependent Hartree method for atomic mixtures (ML-MCTDHX) approach [67–69] which is well established for investigating impurity physics [36].

Inspecting the spatial two-body correlations between the two impurities we reveal that, in general, they are correlated (anti-correlated) when the two impurity-medium coupling strengths posses the same (opposite) sign. To shed more light on the impact of induced impurities' correlations we carefully monitor their relative distance [70], excluding all mean-field type contributions, for varying coupling strengths. A central result of our work is that the impurities' correlated (anti-correlated) behavior is related to a decrease (increase) of their relative distance, thus, indicating the presence of an induced attraction (repulsion) between them. This observation is additionally confirmed by constructing an effective two-body model in the weak impurity-medium coupling regime inspired from the case of indistinguishable impurities [36, 52]. It specifically allows to assign the impurities' induced interaction strength and sign but also other quasiparticle related properties such as their effective mass and trap frequency.

For strong impurity-medium attractions, we identify the formation of a bipolaron state involving the two distinguishable impurities. This bound quasi-particle state is characterized by the so-called bipolaron energy [32], and the size of the impurities' dimer state featuring an exponential decrease for larger attractions. Proceeding a step further, we find that for such strong attractive impurity-medium interactions the three-body correlation function features an ellipsoidal shape indicating bunching and revealing the creation of a trimer state among the two impurities and a corresponding bath atom. To further testify the existence of this trimer state we employ the Jacobi relative distances of the three distinguishable atoms [71] showing an exponentially decreasing trend for increasing impurity-medium attractions.

This work is organized as follows. In section 2, the three-component setup under consideration is introduced and in Section 3 we explain the variational method used to obtain the ground state properties of the many-body system. Section 4 elaborates on the possible ground state density configurations upon varying the impurity-medium couplings. The emergence of induced impurity-impurity correlation patterns is explicated in Section 5. The interrelation of the aforementioned induced correlations with the induced attractive and repulsive impurity interactions is provided in Section 6 through monitoring their relative distance and constructing an effective two-body model. Delving into the strongly attractive impurity-medium interaction regime, we demonstrate the formation of a bipolaron state among the two distinguishable impurities in Section 7 and the generation of a trimer state among the impurities and a bath atom in Section 8. We summarize our findings and discuss future perspectives in Section 9. The behavior of the logarithmic negativity in order to quantify the bipartite intercomponent entanglement is discussed in Appendix A. Appendices B and C provide supplemental information regarding the polaron characteristics and induced effective interactions. In Appendix D we comment on the impact of the impurity mass and the number of bath particles on the ground state properties of the system. Finally, in Appendix E we elaborate on the microscopic excitation processes of the system via a number state analysis.

2 Two distinguishable impurities in a bosonic gas

We consider a one-dimensional harmonically trapped three component mixture. It contains a bosonic medium A with $N_A = 15$ atoms of mass m_A and two distinguishable impurities B and C, i.e., $N_B = N_C = 1$, having masses m_B and m_C, respectively. The many-body Hamiltonian of this system reads

$$\hat{H} = \sum_{\sigma} \hat{H}_{\sigma} + \sum_{\sigma \neq \sigma'} \hat{H}_{\sigma\sigma'} \,, \tag{1}$$

where $\hat{H}_{\sigma}$ denotes the Hamiltonian of each component σ and $\hat{H}_{\sigma\sigma'}$ represents the intercomponent interaction contribution with $\sigma, \sigma' \in \{A, B, C\}$. Specifically,

$$\hat{H}_{\sigma} = \sum_{i=1}^{N_{\sigma}} \left(-\frac{\hbar^2}{2m_{\sigma}} \frac{\partial^2}{(\partial x_i^{\sigma})^2} + \frac{1}{2} m_{\sigma} \omega_{\sigma}^2 (x_i^{\sigma})^2 + g_{\sigma\sigma} \sum_{i<j} \delta(x_i^{\sigma} - x_j^{\sigma}) \right), \tag{2}$$

$$\hat{H}_{\sigma\sigma'} = g_{\sigma\sigma'} \sum_{i=1}^{N_{\sigma}} \sum_{j=1}^{N_{\sigma'}} \delta(x_i^{\sigma} - x_j^{\sigma'}) \,. \tag{3}$$

Assuming that the system is at ultracold temperatures it dominantly experiences s-wave scattering processes that can be described by two-body contact interactions between particles of the same as well as of different species characterized by the generic strength $g_{\sigma\sigma'}$ [14]. The latter depends on the respective three-dimensional scattering lengths $a^{3D}_{\sigma\sigma'}$ and the transversal confinement frequency $\omega_{\perp}$ that are experimentally tunable via Feshbach resonances [13, 14] and confinement induced resonances respectively [12]. The latter would allow the tuning of interactions even in the absence of a Feshbach resonance.

For simplicity, we focus on the mass-balanced case $m_{\sigma} \equiv m$ (unless stated otherwise) and thus $\omega_{\sigma} \equiv \omega$. Moreover, we rescale our Hamiltonian in harmonic oscillator units $\hbar\omega$ which means that the length and interaction scales are given in $\sqrt{\hbar/m\omega}$ and $\sqrt{\hbar^3\omega/m}$, respectively. Such a three-component system could be experimentally realized [16, 18] e.g., by trapping three different hyperfine states of ^{87}Rb which can feature various Feshbach resonances. An alternative candidate may be two isotopes of Rubidium atoms with ^{85}Rb emulating the medium and two-hyperfine states of ^{87}Rb [72, 73] representing the impurities. Since our main findings persist also for mass-imbalanced mixtures, see the discussion in Section D, corresponding heteronuclear mixtures of different isotopes could also be used. We also note that the experimental realization of three-component mixtures was reported in Refs. [16, 18] and a proposal for a corresponding impurity system was recently made in Ref. [74]. Since our aim is to understand the role of induced interactions between the impurities mediated by the medium, in the ground state of the system, it is natural to consider two non-interacting impurities setting $g_{BC} = 0$, which could be realized, for instance, via magnetic Feshbach resonances [75].

3 Variational wave function approach

The ground state of the three-component mixture, described by the Hamiltonian of Eq. (1), is determined within the ML-MCTDHX method [67–69, 76]. A central aspect of this *ab-initio* approach is based on the expansion of the many-body wave function on different layers using a variationally optimized time-dependent many-body basis. This leads to an efficient truncation of the underlying Hilbert space tailored to capture the relevant inter- and intracomponent correlations. Specifically, the many-body wave function is first expressed in terms of three different sets of D_σ species functions as follows

$$|\Psi^{\mathrm{MB}}(t)\rangle = \sum_{i=1}^{D_A}\sum_{j=1}^{D_B}\sum_{k=1}^{D_C} C_{ijk}(t)\,|\Psi_i^A(t)\rangle\,|\Psi_j^B(t)\rangle\,|\Psi_k^C(t)\rangle\ . \tag{4}$$

The time-dependent coefficients $C_{ijk}(t)$ bare information about the entanglement between the involved components. For instance, the bipartite entanglement between two components can be analyzed by tracing out the degrees of freedom of the third one and then apply the positive partial transpose criterion on the resulting mixed state [77] (see also Appendix A). Next, the intracomponent correlations are included into the wave function ansatz by expanding each species function as a superposition of permanents $|\vec{n}(t)\rangle$ weighted by time-dependent expansion coefficients $C^\sigma_{i,\vec{n}}(t)$. In this notation, $\vec{n} = (n_1^\sigma, \dots, n_{d_\sigma}^\sigma)$ represents the occupation distribution of N_σ particles on d_σ time-dependent single-particle functions. Additionally, the single-particle functions are expanded into a time-independent discrete variable representation [78] consisting in our case of $\mathcal{M}_r = 300$ evenly spaced grid points.

The number of utilized species functions D_σ dictates the degree of intercomponent entanglement. For instance, by providing only one species function for each component, i.e., by setting $D_A = D_B = D_C = 1$, the many-body wave function reduces on its top layer to a product state, thereby, prohibiting any interspecies entanglement. Such a treatment is commonly referred to as a species mean-field ansatz (sMF) [67]. For two-component mixtures the sMF ansatz is unique, however, in three-component systems there are various sMF that could be constructed. As an example, setting $D_\sigma = 1$ and $D_{\sigma'}, D_{\sigma''} > 1$, we allow for entanglement generation only between the species σ' and σ'', whilst intercomponent correlations with species σ are suppressed. To clearly distinguish among the different possible sMF ansatzes, in the following, we abbreviate as sMFσ where $\sigma \in \{A, B, C\}$ the ansatz that ignores intercomponent correlations between species σ and the remaining ones. In this sense, the sMFC is written as

$$|\Psi^{\mathrm{sMFC}}(t)\rangle = \sum_{i=1}^{D_A}\sum_{j=1}^{D_B} C_{ij1}(t)\,|\Psi_i^A(t)\rangle\,|\Psi_j^B(t)\rangle\,|\Psi_1^C(t)\rangle\ , \tag{5}$$

where only species A and B can become entangled while species C remains uncorrelated with the other species.

The ground state of the three component mixture is obtained through the imaginary time propagation method. The time-dependent coefficients of each layer, namely the species and single-particle layers, are optimally adapted to the system, e.g. by following the Dirac-Frenkel variational principle [79] in order to determine the underlying ML-MCTDHX equations of motion. The latter correspond to $D_A D_B D_C$ linear differential equations of motion for the $C_{ijk}(t)$ coefficients coupled to $\sum_{\sigma=A,B,C} D_\sigma \binom{N_\sigma + d_\sigma - 1}{d_\sigma - 1}$ nonlinear integrodifferential equations for the species functions and $d_A+d_B+d_C$ nonlinear integrodifferential equations for the single-particle functions. This co-moving basis concept minimizes the number of required states for achieving numerical convergence. In this sense, it reduces the computational cost as compared to methods relying on time-independent basis sets, while simultaneously allows to account for all relevant correlations. The truncation of the Hilbert space is determined by the number of employed species- and single-particle functions defining the numerical configuration space (D_A, D_B, D_C; d_A, d_B, d_C). Utilizing this method, it is in principle possible to describe mixtures with mesoscopic particle numbers and strong interactions. However, as the number of particles increases and correlations become enhanced a larger number of orbitals should be taken into account in order to reach numerical convergence. The latter is carefully checked by systematically increasing the numerical configuration space and ensuring that the observables of interest remain unchanged within a desired level of accuracy. As expected, this process is accompanied by a significant computational cost and in particular it is the interplay of intra- and intercomponent correlations with the components atom number that limits the applicability of the method due to numerical feasibility. Elaborated discussions on the ingredients, applicability and benchmarks of this variational method to different multicomponent settings can be found in the recent reviews [36, 80].

For our system, the degree of correlations in the bosonic bath, e.g. as captured by its depletion [81] $1-n_0^A$ with n_0^A representing the largest eigenvalue of the bath's one-body reduced density matrix is negligible within the considered interaction strength intervals. This allows us to use only a few orbitals for the medium in order to ensure convergence. On the other hand, the impurities depletion is in general larger, especially for strongly repulsive interactions, and thus we need to use more orbitals. Herewith, we have checked that employing an orbital configuration (6, 6, 6; 4, 6, 6) results in the convergence of the observables of interest, such as the species densities and intercomponent two-body correlation functions, while the amount of equations of motion are tractable. For completeness, let us note that stronger intercomponent interactions than the ones to be reported below e.g. $|g_{AC}| < 10$ require a larger number of species functions and impurities orbitals which is still numerically feasible. Similarly, in order to tackle systems with stronger intracomponent bath interactions the number of the respective d_A orbitals should be increased. This naturally entails more difficult convergence issues than increasing the impurities orbitals (and thus considering stronger impurity-medium interactions) since the number of the underlying equations of motion becomes larger in the former case.

4 One-body density configurations of the three-component mixture

To investigate the emergent spatial configurations of the three-component impurity setting arising due to different combinations of the involved interactions, we initially employ the σ-component one-body density being normalized to unity. Namely, $\rho_\sigma^{(1)}(x) = \langle \Psi^{\mathrm{MB}} | \hat{\Psi}_\sigma^\dagger(x) \hat{\Psi}_\sigma(x) | \Psi^{\mathrm{MB}} \rangle$ where $\hat{\Psi}_\sigma^{(\dagger)}$ denotes the bosonic field operator which annihilates (creates) a σ-species atom at position x. In an experiment, the density is routinely detected through *in-situ* absorption imaging [82–84]. Our understanding on the mixture spatial distributions at different interactions is also corroborated by an effective potential picture, which has been proven thus far successful in order to qualitative explicate various aspects of impurity physics in two-component settings [70, 85, 86]. According to this, each σ component is subjected to an effective potential stemming from the superposition of its external harmonic trap and the density of the complementary components σ' weighted by the respective intercomponent interactions,

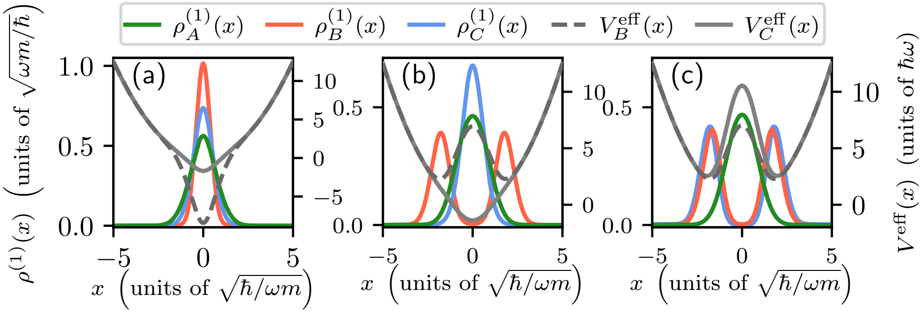

Figure 1: One-body σ-species density, $\rho_\sigma^{(1)}(x)$, shown together with the effective potentials [Eq. (6)] of the impurities (see legend). Two distinguishable non-interacting impurities (B, C) are considered which are individually coupled to a bosonic medium A with $g_{AA} = 0.2$. The impurity-medium coupling strengths from left to right panels refer to $(g_{AB}, g_{AC}) = (-1.0, -0.2)$, $(1.0, -0.2)$ and $(1.0, 1.5)$. For attractive interactions the medium atoms accumulate in the vicinity of the impurities and their effective potential is attractive. Turning to repulsive couplings a tendency for impurity-medium phase-separation occurs for $g_{A\sigma} > g_{AA}$ with $\sigma = B, C$.

i.e.,

$$V_\sigma^{\mathrm{eff}}(x) = V_\sigma(x) + \sum_{\sigma' \neq \sigma} N_{\sigma'} g_{\sigma\sigma'} \rho_{\sigma'}^{(1)}(x)\,. \tag{6}$$

Naturally, this is a sMF framework since it ignores intercomponent correlations. Moreover, it is more meaningful for the impurity subsystem since the impact of the impurity densities is suppressed for the medium. Density profiles of all three components and the impurity effective potentials are provided in Fig. 1 for characteristic impurity-medium interaction configurations, namely $(g_{AB}, g_{AC}) = (-1.0, -0.2)$, $(1.0, -0.2)$ and $(1.0, 1.5)$. The impurities are considered to be non-interacting among each other, i.e., $g_{BC} = 0$, and the medium bosons feature throughout $g_{AA} = 0.2$.

As it can be seen, for an overall attractive impurity-medium coupling the bosons of the medium are placed in the vicinity of the impurities which are naturally localized at the trap center [cf. Figure 1(a)]. This distribution of the medium atoms can also be understood in terms of the respective attractive impurity-medium interaction energy $E_{A\sigma}^{\mathrm{int}} = \langle \Psi^{\mathrm{MB}} | \mathcal{H}_{A\sigma} | \Psi^{\mathrm{MB}} \rangle$ for $g_{A\sigma} < 0$ with $\sigma = B, C$. Also, for both $g_{AB} < 0$ and $g_{AC} < 0$ the effective potential of each impurity corresponds to a dipped harmonic trap enforcing its localization whose degree is, of course, enhanced for stronger attractions [cf. Figure 1(a)]. The value of the attractive interaction determines the degree of spatial localization, i.e., the B impurity with $g_{AB} = -1.0$ is more localized than the C impurity experiencing $g_{AC} = -0.2$. For sufficiently large attractive impurity-medium couplings ($|g_{A\sigma}| \gg g_{AA}$) the impurities form a bipolaron, see for details the discussion in Section 7.

On the other hand, tuning at least one of the impurity-medium couplings towards the repulsive regime such that $g_{A\sigma} > g_{AA}$ is satisfied leads to the phase-separation among these components since $E_{A\sigma}^{\mathrm{int}} > 0$. In this case, the impurity forms a shell around the edges of the bath residing around the trap center [65]. Such configurations can be readily observed, for instance, in Figure 1(b) where solely the B impurity is strongly repulsively coupled with the bath ($g_{AB} > g_{AA}$) and also in Figure 1(c) where both impurities phase separate with the bath due to $g_{AB} > g_{AA}$ and $g_{AC} > g_{AA}$. Notice that for strong repulsive impurity-medium couplings the underlying effective potential of the impurity has the form of a double-well potential which

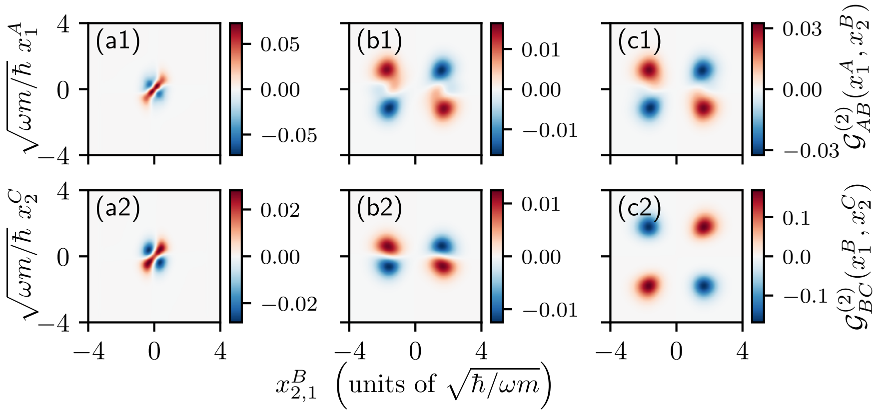

Figure 2: Two-body correlation function (in units of $m\omega/\hbar$) between (a1)-(c1) one bath particle and the B impurity as well as (a2)-(c2) among the two non-interacting impurities [see Eq. (7)]. Each column corresponds to the same interaction configuration which is from left to right $(g_{AB}, g_{AC}) = (-1.0, -0.2)$, $(1.0, -0.2)$ and $(1.0, 1.5)$. We consider two distinguishable non-interacting impurities and an interacting medium with $g_{AA} = 0.2$. Impurity B is correlated (anti-correlated) with a bath particle at the same location in the case of attractive (repulsive) g_{AB}, see panel (a1) [(b1), (c1)]. The impurities experience induced correlations when they both couple either repulsively or attractively to the bath [panels (a2), (c2)], while they are anti-correlated when each impurity couples with an opposite sign to the majority species [panel (b2)].

favors the phase-separation among the bath and the corresponding impurity [cf. Figures 1(b) and (c)].

Another interesting phenomenon reflecting the richness of three-component systems arises upon considering distinct interactions between each impurity and the bath. Indeed, varying the impurity-medium coupling for a specific impurity affects the shape of the bath accordingly and, in turn, impacts the distribution of the other impurity. This is visualized in Figures 1(a) and (b) where g_{AC} is the same while g_{AB} is modified from attractive to repulsive values ultimately altering the spatial localization of impurity C, see in particular the peak of $\rho_C^{(1)}(x)$. Therefore, it is possible to implicitly manipulate the distribution of one impurity by adjusting the coupling of the other impurity with the bath and importantly in the absence of direct impurity-impurity interaction. This property, as it will be discussed below, can be proved crucial for controlling impurity-impurity induced interactions.

5 Intercomponent (induced) correlations and entanglement

Next, we shed light on the associated intercomponent correlation patterns with a particular emphasis on the existence of induced correlations between the impurities mediated by the bosonic gas. The intercomponent two-body spatial correlations, or two-body coherence, can be quantified through [84],

$$\mathcal{G}^{(2)}_{\sigma\sigma'}(x_1^{\sigma}, x_2^{\sigma'}) = \rho^{(2)}_{\sigma\sigma'}(x_1^{\sigma}, x_2^{\sigma'}) - \rho^{(1)}_{\sigma}(x_1^{\sigma})\rho^{(1)}_{\sigma'}(x_2^{\sigma'}). \tag{7}$$

Here, we subtract the probability of independently detecting a σ and a σ' atom at positions x_1^{σ} and $x_2^{\sigma'}$ from the probability to simultaneously measure one at x_1^{σ} and the other at $x_2^{\sigma'}$.

The latter is provided by the reduced two-body density

$$\rho^{(2)}_{\sigma\sigma'}(x_1^{\sigma}, x_2^{\sigma'}) = \langle \Psi^{\mathrm{MB}} | \,\hat{\Psi}^{\dagger}_{\sigma}(x_1^{\sigma})\hat{\Psi}^{\dagger}_{\sigma'}(x_2^{\sigma'})\hat{\Psi}_{\sigma'}(x_2^{\sigma'})\hat{\Psi}_{\sigma}(x_1^{\sigma})\, |\Psi^{\mathrm{MB}}\rangle \,, \tag{8}$$

which is normalized to unity. In this sense, the two particles are correlated or bunched (anti-correlated or antibunched) if $\mathcal{G}^{(2)}_{\sigma\sigma'}(x_1^{\sigma}, x_2^{\sigma'})$ is positive (negative); otherwise, they are referred to as two-body un-correlated [84, 87]. Experimentally the two-body correlation function is accessible through analyzing the respective single-shot images, see e.g. Refs. [88–92].

5.1 Characteristic correlation patterns

First, we study the emergent two-body correlation patterns between the B impurity and the medium for different intercomponent interactions [Figures 2(a1)-(c1)]. For attractive $g_{AB} < 0$ and $g_{AC} < 0$ the B impurity is correlated with a bath atom at the same position, see the diagonal of $\mathcal{G}^{(2)}_{AB}(x_1^A, x_2^B) > 0$, while these two particles are anti-correlated when symmetrically placed with respect to the trap center as it is shown from the anti-diagonal of $\mathcal{G}^{(2)}_{AB}(x_1^A, x_2^B) < 0$ [Figure 2(a1)]. In this sense, the B impurity prefers to occupy the same spatial region with the bath. Turning to repulsive $g_{AB} > 0$ and independently of $g_{AC} \lesseqgtr 0$, the above-discussed two-body correlation distributions are inverted and the B impurity features an anti-bunched (bunched) behavior at the same (different) location with a bath particle as can be deduced by the diagonal (anti-diagonal) of $\mathcal{G}^{(2)}_{AB}(x_1^A, x_2^B)$ [cf. Figures 2(b1) and (c1)]. This trend reflects the impurity-medium phase-separation identified on the density level [Figures 1(b) and (c)].

Let us now discuss the induced correlations among the non-interacting impurities. When both impurities are attractively coupled to the bath they exhibit a bunching tendency which is, of course, mediated by the bosonic gas, see the diagonal of $\mathcal{G}^{(2)}_{BC}(x_1^B, x_2^C)$ depicted in Figure 2(a2). Otherwise, the impurities are anti-bunched when residing at different locations with respect to $x = 0$. This two-body configuration of the impurities manifests the presence of their attractive induced interactions regulated by the impurity-medium attractive interactions as we will discuss in Section 6. Note also that a further increase of the impurity-bath attraction can result in the formation of a bipolaron state which we analyze in detail within Section 7. A similar two-body impurities correlation pattern occurs when they both repulsively couple with their bath [Figure 2(c2)]. However, in this case the impurities cluster either at the left or the right side of the bath, while the probability to reside at opposite sides is suppressed [cf. Figure 2(c2)]. This trend which is inherently related to the impurity-medium phase-separation has also been observed for two indistinguishable impurities and it is known as their coalescence [42]. In sharp contrast, if one impurity couples repulsively and the other attractively to the bath the reverse to the above-described correlation behavior is observed. Namely, the impurities anti-bunch (bunch) at the same (different) location in terms of the trap center, see Figure 2(b2). This scenario manifests the flexibility offered by three component mixtures and it is connected to the emergence of repulsive impurity-impurity induced interactions, a phenomenon that can not occur in two-component systems and we analyze in Section 6.

5.2 Emergent correlation regimes

To provide an overview of the two-body correlation behavior stemming from the interplay of the distinct impurity-medium couplings, we inspect the spatially integrated over $[-\infty, 0\,]$ (due to symmetry) correlation function

$$\mathcal{C}_{\sigma\sigma'} = \int_{-\infty}^{0} dx_1^{\sigma} \int_{-\infty}^{0} dx_2^{\sigma'} \mathcal{G}^{(2)}_{\sigma\sigma'}(x_1^{\sigma}, x_2^{\sigma'})\,. \tag{9}$$

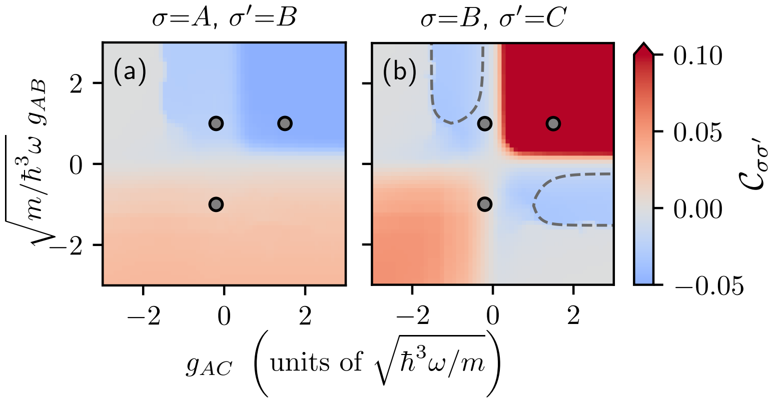

Figure 3: (a)-(b) Phase diagram of the intercomponent (see legends) spatially integrated correlation functions $\mathcal{C}_{\sigma\sigma'}$ [Eq. (9)] in the parametric plane of the impurity-medium interaction strengths (g_{AB}, g_{AC}). A value of $\mathcal{C}_{\sigma\sigma'} < 0$ ($\mathcal{C}_{\sigma\sigma'} > 0$) indicates an anti-correlated (correlated) behavior between the atoms of species σ and σ', while $\mathcal{C}_{\sigma\sigma'} = 0$ denotes the absence of two-body correlations (see also main text). The gray circles correspond to the interaction combinations (g_{AB}, g_{AC}) depicted in Figures 1 and 2. The regions enclosed by the dashed lines in panel (b) indicate the interaction regions where the impurities do not overlap but are still two-body anti-correlated. The harmonically trapped three component system consists of two non-interacting but distinguishable impurities immersed in a bosonic gas of $N_A = 15$ atoms with $g_{AA} = 0.2$.

It quantifies the amount of intercomponent correlations or anti-correlations by means that it is positive (negative) when the particles prefer (avoid) to occupy the same region with respect to the trap center.[1] The phase diagrams of the impurity-medium $\mathcal{C}_{AB}$ and impurity-impurity $\mathcal{C}_{BC}$ integrated correlations as a function of g_{AB} and g_{AC} are depicted in Figure 3(a) and (b) respectively. Recall that since $g_{BC} = 0$ all emerging impurity correlations are induced by their coupling to the bath.

An anti-correlated (correlated) behavior between the B impurity and the bath occurs for $g_{AB} > 0$ ($g_{AB} < 0$) and varying g_{AC}, see also Figures 2(a1)-(c1). Notice also the un-correlated tendency for strongly attractive g_{AC} and repulsive g_{AB} [Figures 3(a), (b)]. Indeed, due to the large $g_{AC} < 0$ both the bath A and the C impurity localize at the trap center minimizing their spatial overlap with the B impurity since $g_{AB} > 0$ and thus $\mathcal{C}_{AB}$ is suppressed. Naturally, a less attractive g_{AC} enhances the overlap between impurity B and the bath leading to an anti-correlated behavior. The largest degree of anti-correlation as captured by $\mathcal{C}_{AB}$ is reached when $g_{AB} > g_{AA}$ and $g_{AC} > g_{AA}$ where both impurities form a shell around the bath and coalesce [cf. corresponding region in Figure 3(a)].

Turning to the impurities' correlations, we observe that as long as they both couple either repulsively or attractively to the bath it holds that $\mathcal{C}_{BC} > 0$, implying that they are correlated [see also Figures 2(a1) and (c1)]. However, when the couplings g_{AB} and g_{AC} have opposite signs, with one lying in the weak and the other in the strong interaction regime, then mostly $\mathcal{C}_{BC} < 0$, i.e., the impurities are anti-correlated [cf. Figure 2(b1)]. A notable exception takes place if one of the impurities couples strongly repulsively to the bath (e.g. $g_{AB} > g_{AA}$) and the other strongly attractively (e.g. $|g_{AC}| > g_{AA}$). This leads to a suppressed spatial overlap among

---

[1] Due to parity symmetry the maximum (minimum) value of $\mathcal{C}_{\sigma\sigma'}$ is 0.25 (-0.25) denoting strong bunching (anti-bunching).

the bath and the repulsively interacting impurity[2] and thus the bath is only correlated with the attractively coupled impurity, see also the discussion above. Together with the fact that the impurities are spatially separated in this interaction region, if mediated impurity correlations occur they have to be nonlocal. This is indeed the case since the impurities are found to be anti-correlated, $\mathcal{C}_{BC} < 0$, see the two parameter regimes in Figure 3(b) enclosed by the dashed lines.

6 Quantification of impurities induced interactions

Below, we examine how the mediated correlations among the distinguishable impurities alter their relative distance and, subsequently, relate the induced impurity-impurity correlation patterns with an effective induced interaction strength. The latter as it will be argued can be either attractive or repulsive due to the genuine three-component nature of the system and it is further quantified via an effective two-body model.

6.1 Effect of the induced impurity-impurity correlations on their relative distance

A reliable measure for this purpose, that has also been utilized in two-component settings [70, 87] and can be experimentally monitored via *in-situ* spin-resolved single-shot measurements [93], is the relative distance between the impurities

$$\langle r_{BC} \rangle = \frac{1}{N_B N_C} \int \mathrm{d}x_1^B \mathrm{d}x_2^C \left| x_1^B - x_2^C \right| \rho_{BC}^{(2)}(x_1^B, x_2^C) \,. \tag{10}$$

Specifically, in order to extract the contribution stemming from genuine impurity-medium correlations we estimate the modified relative distance at different correlation levels as dictated by the respective truncation of the many-body (MB) wave function (see also Section 3), namely

$$\Delta\langle r_{BC} \rangle = \langle r_{BC}^{\mathrm{MB}} \rangle - \left[\langle r_{BC}^{\mathrm{sMF}} \rangle + \left(\langle r_{BC}^{\mathrm{sMFB}} \rangle - \langle r_{BC}^{\mathrm{sMF}} \rangle \right) + \left(\langle r_{BC}^{\mathrm{sMFC}} \rangle - \langle r_{BC}^{\mathrm{sMF}} \rangle \right) \right] . \tag{11}$$

Here, sMF stands for the general species mean-field case where all intercomponent correlations are neglected, while sMFB (sMFC) refers to the case at which only intercomponent correlations between the B (C) impurity and the medium are ignored [36, 65]. Excluding the sMF contribution as well as the ones corresponding to the entanglement between the bath and impurity C or B [cf. last four terms of Eq. (11)] from the relative distance where all correlations are included, i.e., $\langle r_{BC}^{\mathrm{MB}} \rangle$, we are able to distill the effects originating from the mutual correlation among the impurities and the bosonic gas by tracking $\Delta\langle r_{BC} \rangle$. As such, $\Delta\langle r_{BC} \rangle$ captures the genuine effects of the induced correlations as described by $\mathcal{C}_{BC}$ [Figure 3(b)]. We interpret a value of $\Delta\langle r_{BC} \rangle$ which is positive (negative) as the signal of emergent repulsive (attractive) impurities' induced interactions.

The modified relative distance, $\Delta\langle r_{BC} \rangle$, is presented in Figure 4(a) with respect to the g_{AC} coupling and for characteristic fixed g_{AB} values. In general, we find an induced attraction between the impurities when they both couple either attractively or repulsively to the medium, while they feature a mediated repulsion if one of them couples attractively and the other repulsively to the bosonic gas. Since $\Delta\langle r_{BC} \rangle$ is closely related to $\mathcal{C}_{BC}$, an induced correlation (anti-correlation) between the impurities can be associated to their attractive (repulsive)

---

[2] Notice here that since the impurity B is neither entangled with the bath nor with the impurity C, it is sufficient to consider the sMFB ansatz. We have checked that $|\langle \Psi^{\mathrm{sMFB}} | \Psi^{\mathrm{MB}} \rangle|^2 \approx 1$ holds, see also Appendix E for a detailed number state analysis of the many-body wave function.

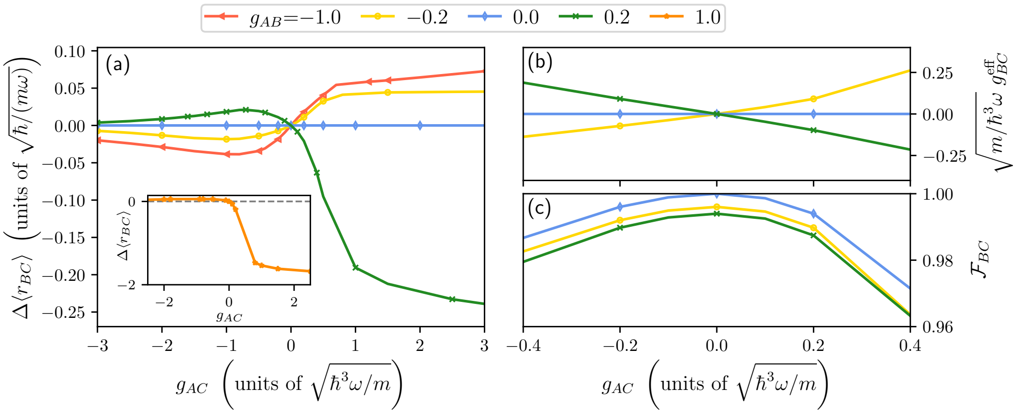

Figure 4: (a) and its inset: Modified relative distance [Eq. (11)] reflecting the effects on $\langle r_{BC}^{\rm MB}\rangle$ which are exclusively caused by the induced impurities correlation as a function of g_{AC} and for different fixed g_{AB}. (b) Induced interaction strength between the two Bose polarons estimated by maximizing the overlap between the two-body correlation functions $\mathcal{G}_{BC}^{(2),\rm eff}$ obtained from the effective two-body model and $\mathcal{G}_{BC}^{(2)}$ predicted within the many-body approach (see main text). (c) Fidelity $\mathcal{F}_{BC}$ of the impurities wave function as found in the many-body method and the effective two-body model with respect to the impurity-medium couplings g_{AB} and g_{AC}. We consider two non-interacting but distinguishable impurities immersed in a bosonic gas of $N_A = 15$ atoms with $g_{AA} = 0.2$.

induced interaction and vice versa [cf. Figures 3(b) and 4(a)]. For instance, considering repulsive g_{AB} and tuning g_{AC} to weak attractions, $\Delta\langle r_{BC}\rangle$ becomes positive denoting an induced repulsion between the impurities. However, for stronger repulsive g_{AC} $\Delta\langle r_{BC}\rangle$ is negative and thus attractive induced interactions occur maximizing in the coalescence regime where g_{AB} and g_{AC} are both strongly repulsive, see also the inset of Figure 3(a). Furthermore, in the case of suppressed mediated correlations between the impurities ($\mathcal{C}_{BC} \approx 0$), i.e., in the trivial case where $g_{AB} = 0$ or for strong attractive g_{AC} and repulsive g_{AB} [cf. Figure 3(b)], also $\Delta\langle r_{BC}\rangle$ vanishes (see Figure 4(a) for strong attractive g_{AC} and $g_{AB} = 0.2, 1.0$). In the last scenario, the gradually increasing g_{AC} attraction leads to a reduction (enhancement) of the correlation between the bath and the B (C) impurity whose interplay impedes the development of mediated impurity correlations and therefore induced interactions.

In the case of an attractively coupled impurity B, e.g. $g_{AB} = -1.0, -0.2$, $\Delta\langle r_{BC}\rangle$ decreases when g_{AB} is tuned to strong attractive values, a phenomenon also occurring for $\mathcal{C}_{BC}$ [Figure 3(b)]. Here, increasing the attraction between impurity C and the bath enhances their correlation, while at sufficiently strong attractive g_{AC} the correlation between the bath and the impurity B begins to slightly decrease for constant attractive g_{AB} (cf. Figure 3). This competition between the different impurity-medium correlations suggests an interesting interplay between the individual intercomponent correlations and could in principle hinder the bath to mediate correlations between the impurities leading eventually to the observed reduction of the induced impurity-impurity correlation/interaction. Such an interplay of intercomponent correlations is indicative of a more intricate and generic correlation transfer process among the species [36], that is an exciting future perspective but lies beyond the focus of our study. However, note that for decreasing $g_{AB} = g_{AC}$ results in a saturation of the impurity-impurity correlation, a fact that will also become important later in the discussion regarding the bipolaron formation in Section 7.

Finally, notice that a similar qualitative behavior of the intercomponent correlations and thus also of $\Delta\langle r_{BC}\rangle$ takes place for either increasing the number of atoms of the bosonic medium or the bare mass of one of the impurities, see Appendix D. In fact, both scenarios lead for repulsive g_{AB} and g_{AC} to an amplified impurities entanglement and to a stronger attractive induced interaction.

6.2 Effective two-body model

To determine the strength of induced impurity-impurity interactions, we reduce the three-component many-body system to an effective two-body model consisting of two interacting quasi-particles. This is a common approach to identify polaron properties from many-body simulations and has been successfully applied to two indistinguishable impurities [52] but not to distinguishable ones. Here, the effective two-body model employs the effective potential $V^{\text{eff}}_{\sigma}(x^{\sigma})$ [defined in Eq. (6)] for each impurity and thus neglects impurity-medium correlations. Also, the underlying impurities induced interactions are represented by a contact potential of strength g^{eff}_{BC} (a treatment with finite range interactions leads to similar results as it is demonstrated in Appendix C). Specifically, the corresponding effective two-body Hamiltonian reads

$$H^{(2),\text{eff}} = \sum_{\sigma=B,C}\left(-\frac{\hbar^2}{2m_\sigma}\frac{\partial^2}{(\partial x^\sigma)^2} + V^{\text{eff}}_{\sigma}(x^\sigma)\right) + g^{\text{eff}}_{BC}\,\delta(x^B - x^C)\,. \tag{12}$$

The effective potential accounts for the effective mass and frequency of each impurity [94]. These effective parameters originate from the polaron picture where the impurity becomes dressed by the excitations of the bath, see Appendix B for a more detailed discussion.

In order to deduce the effective interaction strength g^{eff}_{BC}, we minimize $\Delta\mathcal{G}^{(2)}_{BC} = \int \mathrm{d}x_B \mathrm{d}x_C \left|\mathcal{G}^{(2)}_{BC} - \mathcal{G}^{(2),\text{eff}}_{BC}\right|^2$, where $\mathcal{G}^{(2)}_{BC}$ and $\mathcal{G}^{(2),\text{eff}}_{BC}$ are the impurities' two-body correlation functions calculated from the many-body three-component mixture and the effective two-body model, respectively.[3] By estimating the value of g^{eff}_{BC} which minimizes $\Delta\mathcal{G}^{(2)}_{BC}$, we are able to associate the emergent induced correlation pattern between the impurities described in Fig. 3(b) with a corresponding induced interaction strength g^{eff}_{BC}. The resultant behavior of g^{eff}_{BC} provided in Figure 4(b) for fixed g_{AB} and varying g_{AC} agrees qualitatively with the observations made for $\Delta\langle r_{BC}\rangle$. The impurities experience an induced attraction when they both couple either attractively or repulsively to the bath, corresponding to an induced correlation, otherwise they feature an induced repulsion related to their anti-correlated tendency.[4] To testify the validity range of the effective two-body model [Eq. (12)] for describing the impurities, we calculate the fidelity $\mathcal{F}_{BC}$ of their ground state wave function as obtained from $H^{(2),\text{eff}}$ ($|\Phi^{BC}_{\text{eff}}\rangle$) and the full three-component mixture ($|\tilde{\Psi}^{BC}_{i}\rangle$).[5] The fidelity is provided in Figure 4(c) as a function of g_{AC} and for different fixed values of g_{AB}. It becomes apparent that $H^{(2),\text{eff}}$ is not valid for $g_{AA} < g_{A\sigma}$ where the respective impurity phase separates with the bath. We further note that especially in the regime where the impurities are anti-correlated and share no significant spatial overlap, an effective treatment considering a contact interaction potential fails to describe the full many-body calculations. Instead, in this interaction regime, due to the presence of non-local correlations, a more appropriate choice to model effective impurity-impurity interactions would be a long-range interaction potential, such as the one used in Appendix C.

---

[3] We find $\Delta\mathcal{G}^{(2)}_{BC} \lesssim 10^{-5}$ for all considered interaction strengths g_{AB} and g_{AC}.

[4] Note that $g^{\text{eff}}_{BC} = 0$ if one of the impurities does not interact with the bath which further confirms the validity of the effective model predictions since in this case no correlations are mediated.

[5] For this reason we use the Schmidt decomposition $|\Psi^{\text{MB}}\rangle = \sum_i \sqrt{\lambda_i}\,|\tilde{\Psi}^{A}_{i}\rangle \otimes |\tilde{\Psi}^{BC}_{i}\rangle$ where the λ_i correspond to the Schmidt coefficients [95,96]. As such the fidelity is expressed as $\mathcal{F}_{BC} = \sum_i \lambda_i \left|\langle\tilde{\Psi}^{BC}_{i}|\Phi^{BC}_{\text{eff}}\rangle\right|^2$.

Still, within this effective two-body model different observables for the impurities such as their residue and correlation functions can be extracted and shown to exhibit a qualitative correct behavior. Deviations from the full many-body results are mostly traced back to the absence of intracomponent correlations of the bath and impurity-medium ones.

7 Bipolaron formation

Strong attractive induced interactions between two dressed impurities, commonly occurring for strong attractive impurity-medium direct interactions, eventually lead to the formation of a bound dimer quasi-particle state, the so-called bipolaron [32, 45]. In order to probe the presence of such a dimer impurity bound state in our setup, we study the bipolaron energy,

$$E_{\text{bip}}(g_{AB}, g_{AC}) = E(g_{AB}, g_{AC}) - E_1(g_{AB}) - E_1(g_{AC}) + E_0 \,. \tag{13}$$

Here, $E(g_{AB}, g_{AC})$ denotes the total energy of the system including the two distinguishable impurities, E_0 is the energy of the bosonic gas in the absence of impurities and $E_1(g_{AB})$, $E_1(g_{AC})$ is the energy of one impurity coupled to the bath. The bipolaron energy is presented in Figure 5(a) covering a wide range of attractive and repulsive impurity-medium interactions, g_{AB} and g_{AC}. It features a rapid decrease when both impurities couple attractively to the medium, thereby, evincing the formation of a bound state.[6]

A complementary observable used for the identification of the bipolaron is the spatial size of this dimer state. This is naturally captured by $\sigma \sim \sqrt{\langle r_{BC}^2 \rangle}$, where $\langle r_{BC}^2 \rangle$ is the squared relative distance [cf. Eq. (10)] between the impurities B and C [32]. Specifically, in the following, we track $\sqrt{\sigma/\sigma_0}$ with σ_0 being the distance in the uncoupled scenario, i.e., at $g_{AB} = g_{AC} = 0$, such that we explicitly estimate the impact of the impurity-medium interactions on the dimer size. This is depicted in Figure 5(a) as contour dashed lines along which $\sqrt{\sigma/\sigma_0}$ is constant in the g_{AB}-g_{AC} plane on top of the bipolaron energy. It can be readily seen that for increasing magnitude of the attractive impurity-medium couplings, i.e., g_{AB} and g_{AC}, the size of the dimer state shrinks further, see in particular the dashed lines in Figure 5 which from bottom left to top right correspond to $\sqrt{\sigma/\sigma_0} \approx 0.18, 0.29, 0.65$.

The bipolaron dimer state refers to the bunching behavior of the impurities at the same spatial region which manifests in the elongated shape of their two-body density $\rho^{(2)}_{BC}(x_1^B, x_2^C)$ along the diagonal. In the non-interacting case, i.e., $g_{AB} = g_{AC} = 0$, $\rho^{(2)}_{BC}(x_1^B, x_2^C)$ is circularly symmetric in the $x_1^B - x_2^C$ plane and becomes gradually elongated for larger attractions due to the mediated attraction between the impurities, see e.g. Figures 5(b) and (c) for the cases $(g_{AB}, g_{AC}) = (-0.5, -0.5)$ and $(-1.5, -1.5)$, respectively, also marked as gray dots in Figure 5(a). To quantify the degree of the aforementioned elongation, we fit the half maximum of the impurities' two-body density,[7] i.e. $\rho^{(2)}_{BC}(0,0)/2$ to a rotated ellipse [see white dotted lines in Figures 5(b) and (c)] and determine the corresponding eccentricity $e = \sqrt{1 - b^2/a^2}$ where a (b) denotes the semi-major (semi-minor) axis marked by the black lines of the ellipse.[8] Apparently for $e = 0$, $\rho^{(2)}_{BC}(x_1^B, x_2^C)$ is circularly symmetric while in the case of $e < 1$ it is elongated having the shape of an ellipse.

The eccentricity of the impurities' two-body density is depicted in Figure 5(d) for $g_{AB} = g_{AC}$. By tuning the impurity-medium coupling from the non-interacting limit towards strong attrac-

---

[6] The bipolaron energy decreases exponentially if both impurity-medium couplings (g_{AB}, g_{AC}) are equally varied from the non-interacting limit to the strongly attractive regime, i.e., along the diagonal in Figure 5(a).

[7] We remark that choosing $\rho^{(2)}_{BC}(0,0)/2$ for the fitting is employed for convenience. Indeed, also other density values were used, e.g. $\rho^{(2)}_{BC}(0,0)/4$, verifying the same behavior of the eccentricity.

[8] For the fitting we use the general ellipse equation $\alpha x_1^2 + \beta x_1 x_2 + \gamma x_2^2 + \delta x_1 + \epsilon x_2 + \phi = 0$, which in the frame of the ellipse reduces to $\tilde{x_1}^2/a^2 + \tilde{x_2}^2/b^2 = 1$.

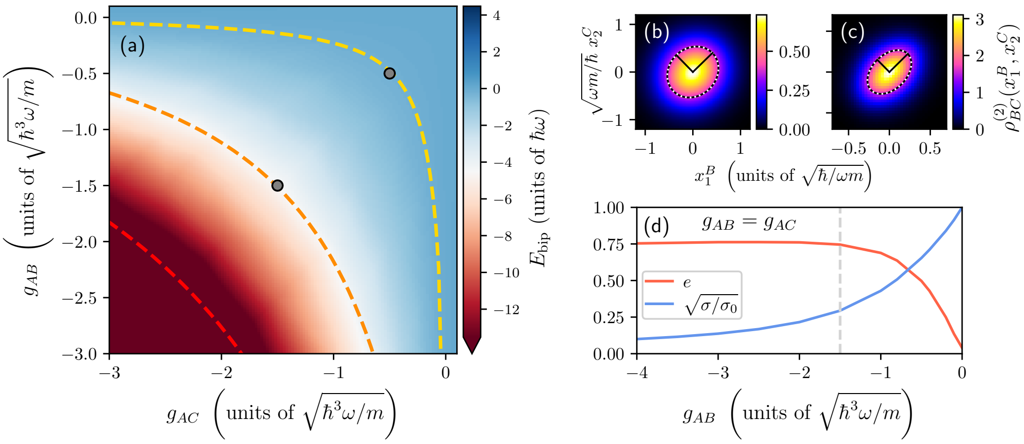

Figure 5: (a) Bipolaron energy, E_{bip}, as a function of the intercomponent coupling strengths g_{AB} and g_{AC}. The dashed lines represent contours along which the size of the dimer state σ remains fixed and in particular from bottom left to top right correspond to $\sqrt{\sigma/\sigma_0} \approx 0.18, 0.29, 0.65$. (b), (c) Reduced two-body impurities' density $\rho^{(2)}_{BC}(x_1^B, x_2^C)$ for $(g_{AB}, g_{AC}) = (-0.5, -0.5)$ and $(-1.5, -1.5)$, respectively, in units of $m\omega/\hbar$ [see also corresponding gray dots in panel (a)]. The region where $\rho^{(2)}_{BC}(x_1^B, x_2^C) = \rho^{(2)}_{\sigma\sigma'}(0,0)/2$ is fitted to an ellipse (white dotted line) and shown together with the semi-minor and semi-major axis (black lines). The corresponding eccentricity is depicted in panel (d) assuming $g_{AB} = g_{AC}$. The transition to a bipolaron state where the eccentricity saturates for increasing impurity-medium attractions and the size of the dimer state is $\sqrt{\sigma/\sigma_0} \approx 0.29$ occurs at $g_{AC} = -1.5$ (gray dashed line). We consider two non-interacting but distinguishable impurities immersed in a bosonic gas of $N_A = 15$ atoms with $g_{AA} = 0.2$.

tions, e increases from $e \approx 0$ at $g_{AB} = g_{AC} = 0$ to finite positive values until it saturates at around $g_{AB} \approx -1.5$. A larger attraction leads only to an additional shrinking of the dimer size, see in particular the exponential decrease of $\sqrt{\sigma/\sigma_0}$ in Figure 5(d), leaving the shape of $\rho^{(2)}_{BC}(x_1^B, x_2^C)$ almost unchanged. In this sense, we deduce that the bipolaron state is formed at $g_{AB} = g_{AC} \approx -1.5$ corresponding to $\sqrt{\sigma/\sigma_0} \approx 0.29$ [vertical gray dashed line in Figure 5(d)]. This observation allows us to generalize our conclusions for the bipolaron formation also in the case of $g_{AB} \neq g_{AC}$ from the critical size of the dimer state being $\sqrt{\sigma/\sigma_0} \lesssim 0.29$, which corresponds to the central contour dashed line in Figure 5(a).

We remark that the above-described behavior of both $E_{\mathrm{bip}}(g_{AB}, g_{AC})$ and σ/σ_0 is in accordance with previously studied two-component systems containing two indistinguishable bosonic impurities that form a bipolaron[9] in the strongly attractive coupling regime [32]. However, our results generalize these findings demonstrating the existence of a bipolaron in the case of two distinguishable impurities and suggesting that this bound state is robust to individual variations of g_{AB} or g_{AC} as indicated by the contour lines in Figure 5. Another aspect that we have addressed is that increasing the mass of one impurity, e.g. considering $m_B = 2$, leads to a faster reduction of the dimer state size as well as the bipolaron energy for decreasing $g_{AB} = g_{AC}$ while the eccentricity saturates at smaller impurity-medium attractions as compared to the mass-balanced case. This suggests, as expected, that a heavier impurity facilitates bipolaron formation.

---

[9] We have also verified that upon considering two indistinguishable bosonic impurities our results regarding the bipolaron energy, dimer size and eccentricity coincide with those of the three-component setup with $g_{AB} = g_{AC}$.

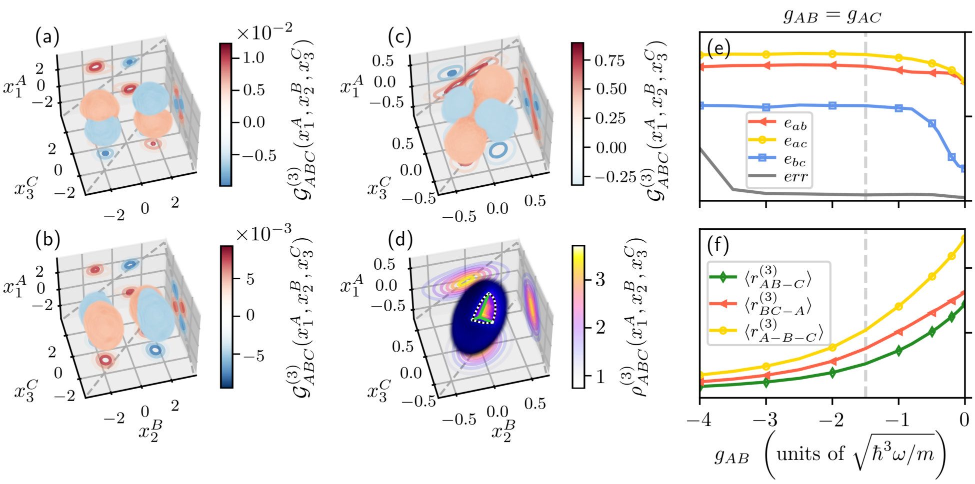

Figure 6: (a)-(c) Reduced three-body correlation function $\mathcal{G}^{(3)}_{ABC}(x_1^A,x_2^B,x_3^C)$ for $(g_{AB},g_{AC})=(1.0,-0.2)$, $(1.0,0.2)$ and $(-1.5,-1.5)$, respectively and (d) reduced three-body density $\rho^{(3)}_{ABC}(x_1^A,x_2^B,x_3^C)$ for $(g_{AB},g_{AC})=(-1.5,-1.5)$. In each panel, the contours of either (a)-(c) the two-body correlation functions, i.e., $\mathcal{G}^{(2)}_{AB}$, $\mathcal{G}^{(2)}_{AC}$, $\mathcal{G}^{(2)}_{BC}$, or (d) the two-body density functions, i.e., $\rho^{(2)}_{AB}$, $\rho^{(2)}_{AC}$, $\rho^{(2)}_{BC}$, are provided in the $x_1^A-x_2^B$-, $x_1^A-x_3^C$-, $x_2^B-x_3^C$-planes. The spatial coordinates x^σ are expressed in units of $\sqrt{\hbar/m\omega}$, whereas $\rho^{(3)}_{ABC}$ and $\mathcal{G}^{(3)}_{ABC}$ are presented in units of $(m\omega/\hbar)^{3/2}$. For visualization purposes we only show the data whose correlation or density value is larger than 0.2 of the respective maximum value. The region corresponding to $\rho^{(3)}_{ABC}(x_1^A,x_2^B,x_3^C)=\rho^{(3)}_{ABC}(0,0,0)/2$ is fitted to an ellipsoid rotated in space (part of the fitted ellipsoid is marked by the white dashed lines). The three semi-axis are denoted by the green lines in panel (d). (e) Eccentricities calculated from the semi-axis (see main text) for attractive $g_{AB}=g_{AC}$. (f) Jacobi relative distances $\langle r^{(3)}_{AB-C}\rangle$ and $\langle r^{(3)}_{BC-A}\rangle$ [Eq. (17)] as well as the hyperspherical radius $\langle r^{(3)}_{A-B-C}\rangle$ [Eq. (16)] for $g_{AB}=g_{AC}$. We mark the transition to a trimer state at $g_{AC}=-1.5$ [gray dashed line in panels (e) and (f)]. For the three-component setup two non-interacting but distinguishable impurities immersed in a bosonic gas of $N_A=15$ atoms with $g_{AA}=0.2$ are considered.

8 Three-body correlations and trimer state

In the following, we aim to shed light on the existence of three-body correlations appearing in the ground state of the two distinguishable impurities embedded into the bosonic gas. For this purpose, we construct as a first step the normalized reduced three-body density

$$\rho^{(3)}_{ABC}(x_1^A,x_2^B,x_3^C)=\langle\Psi^{\mathrm{MB}}|\,\hat{\Psi}_A^\dagger(x_1^A)\hat{\Psi}_B^\dagger(x_2^B)\hat{\Psi}_C^\dagger(x_3^C)\hat{\Psi}_C(x_3^C)\hat{\Psi}_B(x_2^B)\hat{\Psi}_A(x_1^A)\,|\Psi^{\mathrm{MB}}\rangle\,, \tag{14}$$

which represents the spatially resolved probability of finding at the same time a representative atom of the medium at position x_1^A and the impurities B and C at positions x_2^B and x_3^C [97, 98]. Experimentally, the three-body density could be obtained by detecting simultaneously the positions of the three particles of interest, here, the two impurities and one bath atom, and then average over a sample of experimental absorption images [99]. Having defined the three-body density, we construct the spatially resolved three-body correlation function as a straightforward extension of the two-body one defined in Eq. (7), i.e.,

$$\mathcal{G}^{(3)}_{ABC}(x^A_1, x^B_2, x^C_3) = \rho^{(3)}_{ABC}(x^A_1, x^B_2, x^C_3) - \rho^{(1)}_A(x^A_1)\rho^{(1)}_B(x^B_2)\rho^{(1)}_C(x^C_3). \tag{15}$$

According to this measure, the three participating particles are correlated (anti-correlated) if $\mathcal{G}^{(3)}_{ABC}(x^A_1, x^B_2, x^C_3) > 0$ ($\mathcal{G}^{(3)}_{ABC}(x^A_1, x^B_2, x^C_3) < 0$), whilst a vanishing $\mathcal{G}^{(3)}_{ABC}(x^A_1, x^B_2, x^C_3) = 0$ implies that they are uncorrelated. Note, that this measure still contains two-body correlation effects since only the product of one-body densities has been subtracted from the three-body density.

The three-body correlation function is depicted in Figures 6(a) and (b) for the case of strong repulsions between impurity B and the bath ($g_{AB} = 1$) and either weak attractive or repulsive couplings between the bath and the C impurity, namely $g_{AC} = -0.2$ and 0.2, respectively. Moreover, for visualization and completeness issues, we additionally showcase within the x^A_1-x^B_2, x^A_1-x^C_3 and x^B_2-x^C_3 planes the underlying two-body correlation functions $\mathcal{G}^{(2)}_{AB}(x^A_1, x^B_2)$, $\mathcal{G}^{(2)}_{AC}(x^A_1, x^C_3)$ and $\mathcal{G}^{(2)}_{BC}(x^B_2, x^C_3)$, respectively.[10] Focusing on $g_{AC} = -0.2$, it becomes evident that $\mathcal{G}^{(3)}_{ABC}(x^A_1, x^B_2, x^C_3)$ fragments into two correlated and two anti-correlated parts. The correlated segments indicate that it is likely for one bath atom and the C impurity to reside at the same side with respect to the trap center while the repulsively coupled impurity B favors to be on the opposite side. On the other hand, the anti-correlated fragments suggest that a configuration where the impurities and a bath atom are at the same location is not favorable. The spatial arrangement of these fragments is altered in the three-dimensional space if the sign of g_{AC} is inverted, in a sense that the correlated and anti-correlated regions are rotated by roughly 90° around the x^B_2 direction. In such a configuration the impurities are located at the same side in terms of the trap center and a bath atom lies on the opposite side. The corresponding two-body correlation functions $\mathcal{G}^{(2)}_{AC}(x^A_1, x^C_3)$ and $\mathcal{G}^{(2)}_{BC}(x^B_2, x^C_3)$ become inverted, whereas $\mathcal{G}^{(2)}_{AB}(x^A_1, x^B_2)$ preserves its pattern, see the contours in Figures 6(a) and (b).

Subsequently, we turn to strongly attractive impurity-medium interactions with $g_{AB} = g_{AC}$. Here, the three-body density $\rho^{(3)}_{ABC}(x^A_1, x^B_2, x^C_3)$ becomes elongated exhibiting an ellipsoidal shape, see e.g. Figure 6(d) for $(g_{AB}, g_{AC}) = (-1.5, -1.5)$. Thereby, the three-body density is stretched along the (x^A_1, x^B_2, x^C_3)-direction, i.e., the diagonal of the coordinate system, demonstrating a bunching behavior of the two impurities and a representative atom of the bath species. In particular, the corresponding three-body correlation function, presented in Figure 6(c), features a correlated pattern along the diagonal around which a shell-like structure consisting of anti-correlated fragments is formed.

To quantify the deformation of the three-body density, we fit its half maximum, i.e., $\rho^{(3)}_{ABC}(0, 0, 0)/2$, to a rotated ellipsoid (see white dashed lines in Figure 6(d) corresponding to a profile of the ellipsoid). Specifically, we fit the ellipsoid equation $\tilde{x}^2_1/a^2 + \tilde{x}^2_2/b^2 + \tilde{x}^2_3/c^2 = 1$, where $\tilde{x}_i$ refers to the coordinate system of the ellipsoid spanned by its semi-axis with lengths a, b and c [green lines in Figure 6(d)]. From the semi-axis we determine three eccentricities, namely $e_{ab} = \sqrt{1 - b^2/a^2}$, $e_{ac} = \sqrt{1 - c^2/a^2}$ and $e_{bc} = \sqrt{1 - c^2/b^2}$ with $a \geq b \geq c$. These eccentricities are depicted in Figure 6(e) together with the relative deviation, err, from the ellipsoid function for varying g_{AB} and assuming $g_{AB} = g_{AC}$. In the non-interacting case, i.e., $g_{AB} = g_{AC} = 0$, the eccentricities are already finite indicating a deviation from a spherical shape, which is in contrast to the bipolaron [cf. Figure 5(d)]. This is attributed to the presence of finite intraspecies interactions among the bath particles causing the observed spatial deformation. Importantly, the eccentricities show an increasing tendency for stronger attractive values of $g_{AB} = g_{AC}$, meaning that the elongation of the ellipsoid is enhanced until it saturates at around $g_{AB} = g_{AC} \approx -1.5$.

---

[10] As an example, notice that the contours in the x^A_1-x^B_2 and x^B_2-x^C_3 planes of Figure 6(c) correspond to the $\mathcal{G}^{(2)}_{AB}(x^A_1, x^B_2)$ and $\mathcal{G}^{(2)}_{AB}(x^B_1, x^C_2)$ illustrated in Figures 2(b1) and (b2), respectively.

A further characterization of the size of the three-body cluster at strong attractions is achieved by inspecting the hyperspherical radius $\langle r^{(3)}_{\sigma-\sigma'-\sigma''}\rangle$ and the Jacobi relative distance $\langle r^{(3)}_{\sigma'\sigma''-\sigma}\rangle$. The latter denotes the distance between the atom σ and the center-of-mass of the particles σ' and σ'' [71, 100, 101]. These observables are defined as

$$\langle r^{(3)}_{A-B-C}\rangle = \frac{1}{N_A N_B N_C}\int \mathrm{d}x_1^A \mathrm{d}x_2^B \mathrm{d}x_3^C \sqrt{(x_1^A)^2+(x_2^B)^2+(x_3^C)^2}\,\rho^{(3)}_{ABC}(x_1^A,x_2^B,x_3^C)\,, \tag{16}$$

$$\langle r^{(3)}_{\sigma'\sigma''-\sigma}\rangle = \frac{1}{N_A N_B N_C}\int \mathrm{d}x_1^A \mathrm{d}x_2^B \mathrm{d}x_3^C \left| x^{\sigma} - \frac{1}{2}\left(x^{\sigma'} + x^{\sigma''}\right)\right| \rho^{(3)}_{ABC}(x_1^A,x_2^B,x_3^C)\,, \tag{17}$$

with $\sigma,\sigma',\sigma'' \in \{A,B,C\}$ and $\sigma \neq \sigma'$, $\sigma \neq \sigma''$, $\sigma' \neq \sigma''$. Note that in the present case $\langle r^{(3)}_{AB-C}\rangle = \langle r^{(3)}_{AC-B}\rangle$, since impurity B and C have identical mass and are coupled with the same strength to the bath. Figure 6(f) reveals that for stronger impurity-medium attractions the hyperspherical radius decreases exponentially implying an exponential shrinking of the size of the three-body cluster. The same exponential decrease is also captured by the expectation values of the Jacobi relative distances where we find $\langle r^{(3)}_{BC-A}\rangle < \langle r^{(3)}_{AB-C}\rangle$ reflecting the fact that the bath atoms extend over a larger spatial region than the impurities due to the repulsive g_{AA}. The above properties imply the formation of a bound trimer state for couplings $g_{AB} = g_{AC} \leq -1.5$ corresponding to values where the ellipsoidal structure of the three-body density saturates. In this sense, the formation of a bipolaron is accompanied by the development of a bound trimer state.

9 Conclusions and perspectives

We have studied the correlation properties in the ground state of two non-interacting distinguishable impurities immersed in a bosonic bath with the entire three-component system being harmonically trapped. The impurities become dressed by the excitations of the bosonic gas generating quasiparticle states, herein Bose polarons, having characteristic properties such as effective mass and featuring induced correlations. In order to appreciate the impact of inter- and intracomponent correlations we rely on the variational ML-MCTDHX method whose flexible wave function truncation ansatz allows to operate at different correlation orders. An emphasis is placed on the high tunability of the three-component setting unveiling rich density and correlation patterns, the manipulation of both the sign and the strength of impurities induced interactions as well as the formation of bound impurity states.

Specifically, we demonstrate that upon varying the involved impurity-medium couplings, both impurities can either localize at the trap center (attractive intercomponent interactions), form a shell around the bosonic gas (repulsive interactions), i.e., phase-separate, or one of them localize and the other phase-separate (alternating signs of impurity-medium couplings). These density configurations can be understood at least qualitatively in terms of an effective potential picture for the impurities which refers to a dipped harmonic oscillator (double-well) for attractive (repulsive) intercomponent interactions.

A detailed characterization of the induced correlations is provided in a wide range of impurity-medium interactions aiming to expose their intricate role. Inspecting the two-body intercomponent correlation functions we find that the bosonic gas mediates anti-correlations among the impurities if one of them couples repulsively and the other attractively to it. In contrast, induced two-body correlations occur as long as both impurities couple either attractively or repulsively to their medium. The origin of the aforementioned correlation patterns is traced back to the spatial configurations of each component. This means that if the impurities have a finite spatial overlap with the bath the latter mediates two-body correlations between them. Interestingly, there is also the possibility that the impurities are not overlapping but can be still correlated implying that non-local correlations are in play. To quantify the strength and sign of the induced interactions we employ the relative two-body distance among the impurities extracting all contributions stemming from mean-field effects. In this sense, it is demonstrated that induced two-body correlations (anti-correlations) are related to mediated attractive (repulsive) impurity interactions. These findings are further supported by an effective two-body model containing the impurities effective trapping potential and their induced interactions. Importantly, this approach allows to determine the strength and sign of the effective interactions mediated between the impurities through a comparison with the full many-body results. Moreover, by constructing an effective one-body Hamiltonian enables us to estimate the effective mass and trapping frequency of each distinguishable impurity (polaron), see Appendix B.

Evidences regarding bipolaron formation are provided, when both impurities are strongly attractively coupled to the bosonic gas, by means that the bipolaron energy and the size of the underlying dimer state rapidly decrease for stronger attractions. Interestingly, we determine the intercomponent three-body correlation function according to which overall weak three-body correlations exist and become enhanced for strongly attractive impurity-medium interactions signaling the formation of trimers among the impurities and an atom of the medium.

In this investigation we have restricted ourselves to the ground state of the three-component mixture. Further understanding on the character of the impurities induced interactions and in particular their nonlocal character and their dependence on the statistics of the medium are interesting perspectives. In this context, a systematic finite size scaling analysis with respect to the number of bath particles in order to infer the persistence of our findings e.g. in terms of the crossover of the impurities induced interactions (see also Appendix D) and in general the build-up of intercomponent correlations would be desirable as well. Also, the emulation of spectroscopic schemes that will allow the identification of the ensuing polaron states and excitations [24, 102] constitutes an intriguing direction. Furthermore, studying the behavior of impurities induced interactions and bound states in different external trapping potentials is also an interesting direction. Here, a setup of immediate interest would be to load the bath atoms in a ring potential and investigate the formation of impurities bound states in both the attractive and the repulsive impurities-medium interaction regimes. Another straightforward extension would be to explore the nonequilibrium impurities dynamics in order to understand the build-up of induced correlations. An additional fruitful research direction is to understand the Bose polaron formation when indistinguishable impurities are immersed in an attractive two-component gas forming a droplet. Certainly, studying correlation effects in particle-balanced three component settings with an emphasis on the few- to many-body crossover and in particular close to the pair immiscibility threshold is worth to be pursued.

Acknowledgments

Funding information This work has been funded by the Deutsche Forschungsgemeinschaft (DFG, Germany Research Foundation) — SFB 925 — project 170620586. S.I.M. gratefully acknowledges financial support from the NSF through a grant for ITAMP at Harvard University.

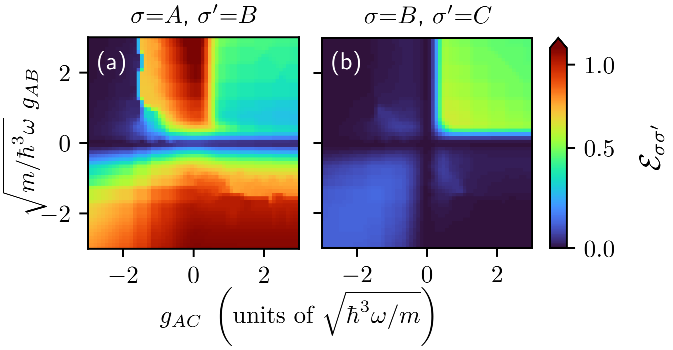

Figure 7: (a)-(b) Diagram of the intercomponent (see legends) logarithmic negativity $\mathcal{E}_{\sigma\sigma'}$ [Eq. (A.1)] as a function of the impurity-medium couplings (g_{AB}, g_{AC}). The harmonically trapped three component system consists of two non-interacting but distinguishable impurities immersed in a bosonic gas of $N = 15$ atoms with $g_{AA} = 0.2$.

A Behavior of the bipartite entanglement

A standard measure to estimate the bipartite entanglement of mixed states that exist in a multi-component system[11] is encapsulated in the logarithmic negativity [56–59, 62, 104, 105]. It is based on the partial transpose of the two-body species reduced density matrix,[12] which, e.g. referring to species σ and σ', is obtained by integrating out the degrees of freedom of species σ'' leading to $\rho^{(2),\text{spec}}_{\sigma\sigma'} = \text{Tr}_{\sigma''}\left(|\Psi^{\text{MB}}\rangle\langle\Psi^{\text{MB}}|\right) = \sum_{ijlm}\sum_k C_{ijk}C^*_{lmk}|\Psi^{\sigma}_i\rangle|\Psi^{\sigma'}_j\rangle\langle\Psi^{\sigma}_l|\langle\Psi^{\sigma'}_m|$ [54, 55, 77].

Its partial transpose T_σ with respect to species σ is calculated by exchanging the indices i and l associated with species σ, i.e., $\left(\rho^{(2),\text{spec}}_{\sigma\sigma'}|_{ijlm}\right)^{T_\sigma} = \rho^{(2),\text{spec}}_{\sigma\sigma'}|_{ljim}$. Calculating the eigenvalues of $\left(\rho^{(2),\text{spec}}_{\sigma\sigma'}\right)^{T_\sigma}$ and in particular summing up its negative eigenvalues μ_i yields the so-called negativity, $\mathcal{N}_{\sigma\sigma'} = \sum_i |\mu_i|$. Subsequently, the logarithmic negativity reads

$$\mathcal{E}_{\sigma\sigma'} = \log_2\left(1 + 2\mathcal{N}_{\sigma\sigma'}\right) . \tag{A.1}$$

This measure exploits the fact that for a separable mixture, e.g. $\rho^{(2),\text{spec}}_{\sigma\sigma'} = \sum_i p_i \tilde{\rho}^{(1),\text{spec}}_{\sigma,i} \otimes \tilde{\rho}^{(1),\text{spec}}_{\sigma',i}$, the partial transpose does not alter the spectrum of $\rho^{(2),\text{spec}}_{\sigma\sigma'}$ and, hence, all eigenvalues remain positive. In this sense, the presence of negative eigenvalues guarantees the existence of entanglement. However, this statement can not be inverted, i.e., even if the logarithmic negativity is zero the species σ and σ' can still be entangled [103].

The logarithmic negativity between the bath and the B impurity, $\mathcal{E}_{AB}$, as well as among the impurities, $\mathcal{E}_{BC}$, is illustrated in Figures 7(a) and (b) respectively within the g_{AB}-g_{AC} plane. As expected it overall captures the main features of the integrated correlation functions shown in Figures 3(a) and (b). For instance, $\mathcal{E}_{AB}$ vanishes for strongly attractive g_{AC} and strongly repulsive g_{AB} [Figure 7(a)], while the parameter region referring to the impurities coalescence is in a similar way pronounced in $\mathcal{E}_{BC}$ as it has been observed for $\mathcal{C}_{BC}$, compare Figures 3(a) and (b) for repulsive g_{AB} and g_{AC}. Recall that while $\mathcal{E}_{\sigma\sigma'}$ provides only a quantitative diagnostic for the bipartite entanglement and does not describe the correlated or anti-correlated behavior as $\mathcal{C}_{\sigma\sigma'}$ it still gives insight into the entanglement content of the many-body system. As such, for large $g_{AB} < 0$ the logarithmic negativity uncovers that the bath and the B impurity are strongly

---

[11] Notice that, for instance, the von-Neumann entropy as an entanglement measure is well-defined in a two species but it is not applicable in multi-component ones [103].

[12] This is completely different from the two-body density matrix of two particles given by Eq. (8).

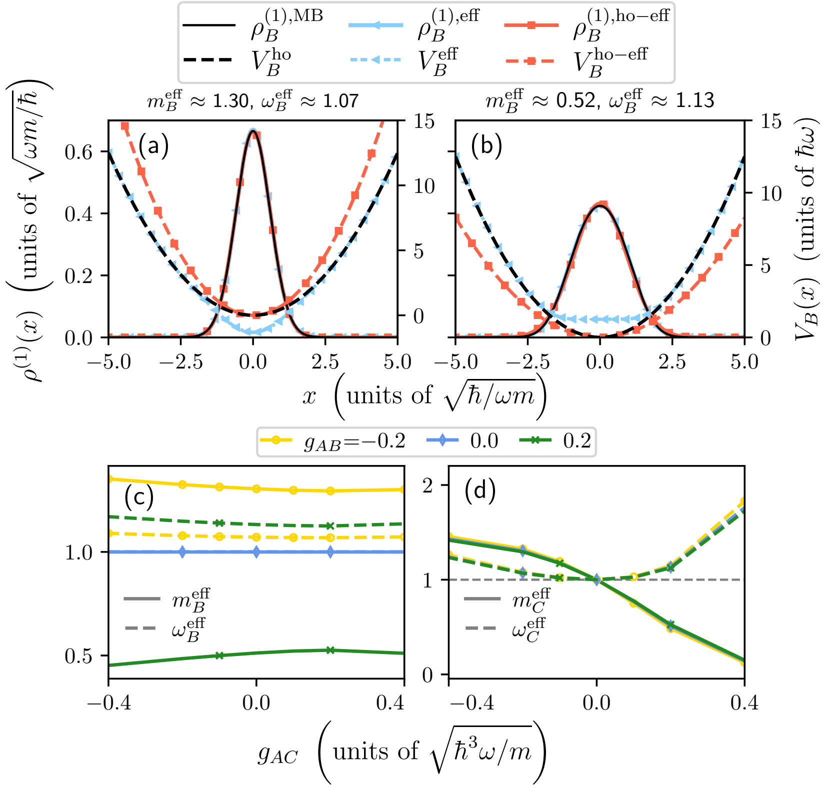

Figure 8: One-body density of the B impurity obtained within different approaches (see legend) for the interaction configurations (a) $(g_{AB}, g_{AC}) = (-0.2, 0.1)$ and (b) $(0.2, 0.1)$. Specifically, $\rho_{\mathrm{MB}}^{(1)}$ denotes the one-body distribution of the full three-component many-body system, whereas $\rho_B^{(1),\mathrm{eff}}$ and $\rho_B^{(1),\mathrm{ho-eff}}$ are calculated using the effective one-body Hamiltonians composed of either an effective harmonic oscillator with an effective mass and frequency [cf. Eq. (B.1)] or the effective potential defined in Eq. (6), respectively. Effective mass and trapping frequency of the dressed (b) B and (c) C impurity, respectively, as deduced from the effective polaron model defined of Eq. (B.1).

entangled especially so in the repulsive $g_{AC} > 0$ region, while varying g_{AB} towards the weakly attractive regime and for $|g_{AC}| > 1$ entanglement is reduced [Figure 7(a)]. This is attributed to the simultaneous increase of $\mathcal{E}_{AC}$,[13] unveiling a competition between the intercomponent entanglement of individual impurities with the medium. Finally, in line with the predictions of $\mathcal{C}_{BC}$, $\mathcal{E}_{BC}$ demonstrates that entanglement is finite when both impurities are either weakly attractive or strongly repulsively coupled to the medium, see Figure 3(d).

B Effective mass and trap frequency of a single impurity

In the following, we approach the three-component impurity setting as a polaron problem since each individual impurity via its coupling to the bosonic gas is dressed by the excitations

---

[13] Since the impurities are in this case physically identical, i.e., $m_A = m_B \equiv m$ and $\omega_A = \omega_B \equiv \omega$, the phase diagram of $\mathcal{E}_{AC}$ corresponds to the one of $\mathcal{E}_{AB}$ but reflected along the diagonal $g_{AB} = g_{AC}$.

of the latter. In this sense, we aim to capture the effective behavior of the B and C impurity with the effective one-body model [94],

$$\hat{H}_{\sigma}^{(1),\text{ho}-\text{eff}} = -\frac{\hbar^2}{2m_{\sigma}^{\text{eff}}}\frac{\partial^2}{(\partial x^{\sigma})^2} + \frac{1}{2}m_{\sigma}^{\text{eff}}(\omega_{\sigma}^{\text{eff}})^2 x^2\,, \tag{B.1}$$

where m_{σ}^{eff} and $\omega_{\sigma}^{\text{eff}}$ denote the polaron effective mass and trapping frequency with $\sigma \in \{B, C\}$.[14] To identify the values of the effective mass and frequency, we minimize the cost function

$$\mathcal{L}_{\sigma} = \Delta\rho_{\sigma}^{(1)} + \Delta E_{\sigma}\,. \tag{B.2}$$

In this expression, the first term refers to $\Delta\rho_{\sigma}^{(1)} = \int \mathrm{d}x_{\sigma} \left|\rho_{\sigma}^{(1),\text{MB}}(x_{\sigma}) - \rho_{\sigma}^{(1),\text{ho}-\text{eff}}(x_{\sigma})\right|^2$ with $\rho_{\sigma}^{(1),\text{MB}}$ and $\rho_{\sigma}^{(1),\text{ho}-\text{eff}}$ being the one-body density as predicted from the full three-component system and the effective one-body model, respectively. The second contribution of the right-hand side in Eq. (B.2) designates the energy difference $\Delta E_{\sigma} = \left|E_{\sigma}^{\text{MB}} - E_{\sigma}^{\text{ho}-\text{eff}}\right|^2$, where $E_{\sigma}^{\text{MB}} = \langle\Psi^{\text{MB}}|\hat{H}_{\sigma}|\Psi^{\text{MB}}\rangle$ is the σ impurity energy and $E_{\sigma}^{\text{ho}-\text{eff}} = \langle\phi|\hat{H}_{\sigma}^{(1),\text{ho}-\text{eff}}|\phi\rangle = \frac{1}{2}\omega_{\sigma}^{\text{eff}}$ is the energy of the effective one-body model and $|\phi\rangle$ the corresponding ground state. Note that in order to uniquely estimate m_{σ}^{eff} and $\omega_{\sigma}^{\text{eff}}$ one needs to adequately describe both the density and the energy of the impurity.

Figures 8(a) and (b) showcase the one-body densities $\rho_B^{(1),\text{MB}}$ and $\rho_B^{(1)\text{ho}-\text{eff}}$ for the characteristic interaction configurations $(g_{AB}, g_{AC}) = (-0.2, 0.1)$ and $(0.2, 0.1)$, respectively. For comparison we additionally provide the one-body density $\rho_B^{(1),\text{eff}}$ obtained from $\hat{H}_B^{(1),\text{eff}} = -\frac{\hbar^2}{2m_B}\frac{\partial^2}{(\partial x^B)^2} + V_B^{\text{eff}}$. As it can be readily seen, the one-body densities predicted by the two effective one-body models are in excellent agreement with the one corresponding to the full three-component many-body system. Deviations start to become evident for strong repulsive impurity-medium couplings (not shown) where the impurity and the medium phase separate [36, 94]. Recall that the effective model is by definition valid for weak intercomponent repulsions where the impurity does not probe the edges of the bosonic cloud.

The effective masses and frequencies of the B and C impurities after minimization of the cost function given by Eq. (B.2) are represented in Figures 8(c) and (d) with respect to the impurity-medium couplings. It is important to point out that both the effective mass and frequency of a specific impurity, e.g. the B one, primarily depend on its coupling with the bath g_{AB}. The interaction strength of the other impurity (C) with the bath, e.g. g_{AC}, has almost no impact on the effective parameters of impurity B. For instance, this conclusion can be drawn from the nearly constant behavior of m_B^{eff} and ω_B^{eff} for varying g_{AC} shown in Figure 8(c), or the fact that m_C^{eff} and ω_C^{eff} remain almost intact for fixed g_{AC} and different g_{AB}, see Figure 8(d).

For an attractively coupled impurity with the bosonic gas, the effective mass and frequency become larger than their bare values [gray dashed lines in Figures 8(c) and (d)], see in particular m_B^{eff}, ω_B^{eff} when $g_{AB} = -0.2$ in Figure 8(c) and m_C^{eff}, ω_C^{eff} for $g_{AC} < 0$ in Figure 8(d). As such, the emergent Bose polaron experiences a narrower trapping potential, thereby, reflecting the localization of the impurity at the trap center [cf. $\rho_B^{(1),\text{ho}-\text{eff}}$ and $V_B^{\text{ho}-\text{eff}}$ in Figure 8(a)]. On the other hand, in the case of a repulsively coupled impurity the effective trapping frequency is still tighter than the original value, but the effective mass becomes smaller than its bare value [cf. m_B^{eff}, ω_B^{eff} for $g_{AB} = 0.2$ in Figure 8(c) as well as m_C^{eff}, ω_C^{eff} for $g_{AC} > 0$ in Figure 8(d)]. In particular, the effective mass is small enough to compensate the increased effective frequency meaning that the underlying harmonic trap is eventually broadened [cf. $V_B^{\text{ho}-\text{eff}}$ in Figure 8(b)]. Additionally, the comparatively smaller effective mass is related to

---

[14] Recall that within the effective two-body model described by Eq. (12) we implicitly account for the effective mass and frequency via the effective potential $V_{B,C}^{\text{eff}}$ Eq. (6). Indeed, beyond mean-field corrections imprinted on $\rho_A^{(1)}$ and, thus appearing in $V_{B,C}^{\text{eff}}$, affect the effective mass and frequency [94].

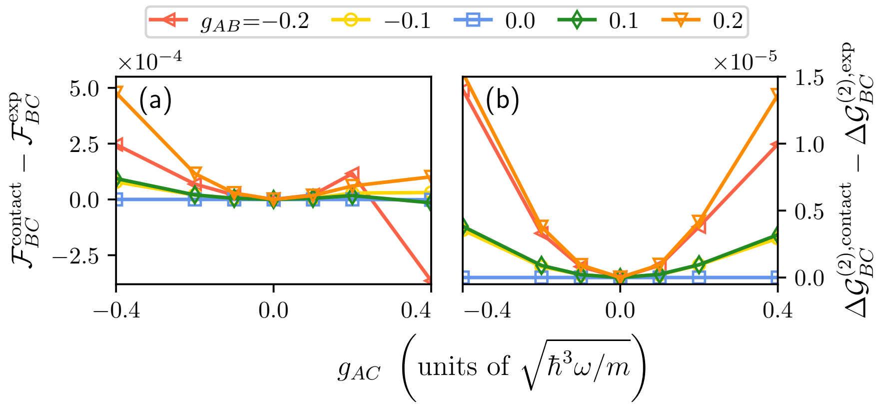

Figure 9: (a) Relative deviation between the fidelities $\mathcal{F}_{BC}^{\text{exp}}$ and $\mathcal{F}_{BC}^{\text{contact}}$, which correspond to the overlap of the impurities two-body wave function obtained from the full many-body approach and the effective model of Eq. (12) containing either an exponential or a contact-type interaction potential, respectively. (b) Difference between $\Delta\mathcal{G}_{BC}^{(2),\text{exp}}$ and $\Delta\mathcal{G}_{BC}^{(2),\text{contact}}$, referring to the variance of the two-body correlation function calculated within the effective two-body model using either the contact or the exponential interaction potential with respect to the full three-component system. For both quantities the relative deviations are minor, testifying the validity of both effective interaction potentials.

a spatial delocalization of the impurity cloud.[15] In this way, the effective one-body model captures the effects imprinted on the impurity in the three-component system.

C Modelling the effective impurity interactions with an exponential potential

To verify the validity of the contact interaction potential for describing the induced interactions between the impurities [Eq. (12)], we next exemplify that our results do not change if one instead uses an exponential potential. The latter has been derived in Refs. [38, 39] and holds in the homogeneous case and for immobile impurities residing at distances satisfying $l = |x^B - x^C| \ll \xi_A$, with $\xi_A \approx 1/\sqrt{2m_A g_{AA} N_A \rho_A^{(1)}(0)} \approx 0.6$ being the healing length of the bath. In particular, we replace the interaction term in Eq. (12) with

$$U(l) = -\frac{g_{AB}\, g_{AC}\, m_A}{\sqrt{\gamma}} e^{-2l/\xi_A}\,, \tag{C.1}$$

where $\gamma = \frac{m_A g_{AA}}{N_A \rho_A^{(1)}(0)}$.[16] As discussed in Section 6.2, we judge the quality of the effective two-body model by estimating the fidelity, $\mathcal{F}_{BC}$, between the impurities two-body wave function as extracted from the full many-body system and the effective two-body model containing either a contact or an exponential interaction potential. Subsequently, we determine the difference $\mathcal{F}_{BC}^{\text{exp}} - \mathcal{F}_{BC}^{\text{contact}}$ which as shown in Figure 9(a) testifies deviations at most of the order 10^{-4}.

Proceeding one step further, we determine the overlap between the respective two-body correlation functions of the impurities determined within the full three-component system

---

[15] Indeed, the kinetic energy of, e.g., the impurity C increases for increasing g_{AC} while the potential energy remains nearly constant.

[16] We model the exponential potential with the so-called POTFIT method [106, 107].

and the effective two-body model. Namely, we track $\Delta\mathcal{G}_{BC}^{(2),\text{exp}} = \int \mathrm{d}x_B \mathrm{d}x_C \left|\mathcal{G}_{BC}^{(2)} - \mathcal{G}_{BC}^{(2),\text{exp}}\right|^2$, where $\mathcal{G}_{BC}^{(2),\text{exp}}$ denotes the two-body correlation function obtained within the effective two-body model (see also Section 6.2) with an exponential interaction. To infer the deviations among the exponential and contact effective interactions at the two-body correlation level, we calculate the difference $\Delta\mathcal{G}_{BC}^{(2),\text{exp}} - \Delta\mathcal{G}_{BC}^{(2),\text{contact}}$, see Figure 9(b). Also here, only small deviations of the order 10^{-5} are identified.

Therefore, the contact and exponential effective interaction potentials lead essentially to the same description regarding the impurities properties. This outcome was not *a-priori* expected since the exponential potential is originally derived in the homogeneous case.

D Impact of mass-imbalanced impurities and the atom number of the bosonic gas

Let us demonstrate the generalization of our results in the main text when the impurities are mass-imbalanced or the bosonic medium contains a larger number of particles. For this purpose, we focus on the behavior of the intercomponent correlations which can be quantified through the integrated correlation function [Eq. (9)] presented in Figure 10 for different system parameters.

In general, increasing the mass of an impurity disturbs the cloud of the bosonic gas to a larger degree which should eventually lead to an enhanced impurity-medium correlation. This is indeed evident in Figure 10(a) where the integrated correlation function, $\mathcal{C}_{AB}$, is increased as compared to the mass-balanced case, thus testifying an overall larger degree of entanglement. Furthermore, since the correlation between the C impurity and the bath is not affected by the change of m_B [Figure 10(b)], the larger $\mathcal{C}_{AB}$ leads to a stronger mediated correlation between the impurities, see e.g. $\mathcal{C}_{BC}$ in Figure 10(c). The latter naturally leads to an amplified impurities' induced interaction for increasing m_B. In particular, for $g_{AB} = 0.2$ and strong repulsive g_{AC}, where $\mathcal{C}_{BC}$ features the largest increase.

Next, we concentrate on the mass-balanced system but consider a larger number of bath particles and in particular $N_A = 30$, while maintaining the same mean-field interaction, i.e., $N_A g_{AA} = \text{const}$. As it can be seen, the impurity-medium correlations, as captured by $\mathcal{C}_{AB}$ and $\mathcal{C}_{AC}$, are reduced compared to the reference case $N_A = 15$, $g_{AA} = 0.2$ [Figure 10(a), (b)]. This is attributed to the smaller intra-species coupling strength $g_{AA} = 0.1$ resulting in a decrease of the respective intra-species correlations among the bath particles. However, the mediated correlations among the impurities B and C are clearly enhanced when g_{AB} and g_{AC} are both repulsive, see Figure 10(c). In this sense, a larger number of bath particles featuring a decreasing intraspecies interaction is associated to a reduction of intraspecies correlations of the bath and impurity-medium ones but enhances to a certain degree the mediated correlation between the impurities. This behavior hints towards a complicated correlation transfer mechanism to the impurity-impurity subsystem which deserves further future investigations. Nevertheless, a systematic finite size scaling analysis in terms of the atom number in the bath is required in order to deduce the robustness of our findings. However, we expect that the main features of the impurities dressing, e.g. the crossover from a correlated to an anti-correlated behavior (associated to attractive and repulsive induced interactions as discussed in Sections 5 and 6), and the existence of the impurities bound states for attractive interactions are retained for larger number of bath atoms.

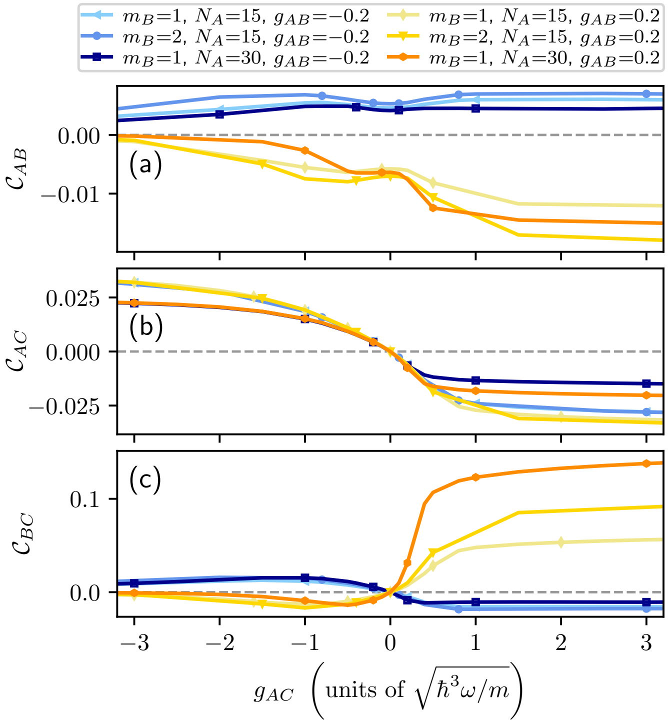

Figure 10: Integrated two-body correlation function [Eq. (9)] among (a) the B impurity and the medium, (b) the C impurity and the medium and (c) between the impurities as a function of the intercomponent interaction strength g_{AC}. In all panels, we consider fixed $g_{AB} = -0.2, 0.2$ as well different masses of the B impurity (simultaneously setting $\omega_B = \sqrt{m_A/m_B}$) and atom numbers of the medium (see legend), while keeping constant the mean-field interaction $N_A g_{AA}$. The gray dashed line in panel (c) marks $\Delta \langle r_{BC} \rangle = 0$.

E Estimating the importance of correlations on the many-body wave function

To expose the impact of intercomponent correlations at different interaction regimes on the level of the many-body wave function we analyze the fidelity $\left|\langle \Psi^{\text{sMF}} | \Psi^{\text{MB}} \rangle\right|^2$, see Figure 11(a). Here, $|\Psi^{\text{MB}}\rangle$ denotes the full many-body wave function where all emergent inter- and intracomponent correlations are taken into account, while $|\Psi^{\text{sMF}}\rangle$ refers to the species mean-field wave function which ignores all intercomponent correlations. Naturally, the fidelity is unity when the species are non-interacting, i.e., $g_{AB} = g_{AC} = 0$, since in this scenario intercomponent correlations are *a-priori* prohibited. However, the fidelity decays for increasing impurity-medium coupling strengths as intercomponent correlations are triggered in this case. The largest deviation between the many-body and species mean-field wave functions occurs in the parameter region corresponding to the coalescence of the impurities, i.e., for strongly repulsive g_{AB} and g_{AC}.

Further understanding of the respective correlation mechanisms can be delivered by identifying the participating microscopic configurations. For this reason we construct the species function eigenbasis $|\psi_i^A\rangle|\psi_j^B\rangle|\psi_k^C\rangle$ obtained by calculating the eigenfunctions of an effective

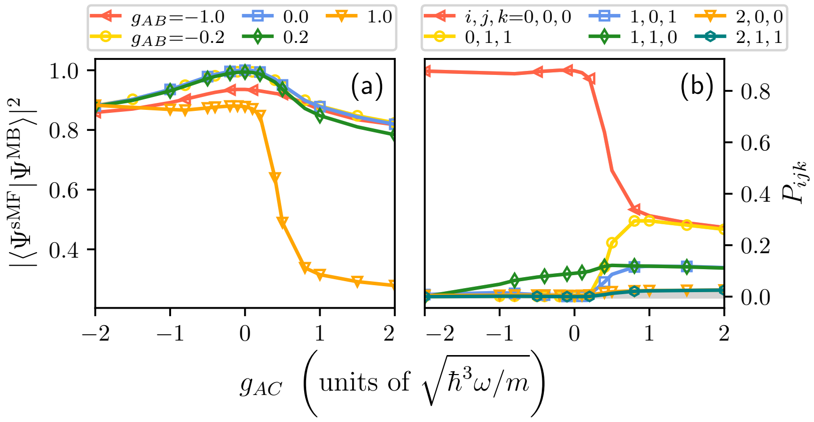

Figure 11: (a) Fidelity between the many-body wave function, $|\Psi^{\mathrm{MB}}\rangle$ (including all emerging intra- and intercomponent correlations) and the species mean-field wave function $|\Psi^{\mathrm{sMF}}\rangle$ where intercomponent correlations are neglected. The reduction of the overlap from unity for finite interactions evinces the participation of intercomponent correlations. (b) Probability amplitude P_{ijk} denoting the overlap of a three-component time-independent basis $|\psi_i^A\rangle|\psi_j^B\rangle|\psi_k^C\rangle$, constructed from the eigenstates of an effective species Hamiltonian (see main text), with the many-body wave function $|\Psi^{\mathrm{MB}}\rangle$. Apparently, energetically higher-lying excited states possess substantial contribution. Probability amplitudes which remain below 0.02 within the interaction range $-2.0 \leq g_{AC} \leq 2.0$ are shown as gray lines. The harmonically trapped three component system consists of two non-interacting but distinguishable impurities immersed in a bosonic gas of $N_A = 15$ atoms with $g_{AA} = 0.2$.

species Hamiltonian [cf. Eq. (2)] characterized by the effective potential defined in Eq. (6).[17] As basis for the bath we take the ground and the energetically two lowest excited states of the effective potential into account, while for the two impurities we consider the corresponding energetically lowest six eigenstates leading to a total number of 108 three-component basis states $|\psi_i^A\rangle|\psi_j^B\rangle|\psi_k^C\rangle$.

The respective probability amplitudes $P_{ijk} = \left|\left(\langle\psi_i^A|\langle\psi_j^B|\langle\psi_k^C|\right)\Psi^{\mathrm{MB}}\rangle\right|^2$, with $|\Psi^{\mathrm{MB}}\rangle$ being the full many-body wave function, are presented in Figure 11(b) for $g_{AB} = 1.0$ and varying g_{AC}. Notice that the state $|\psi_0^A\rangle|\psi_0^B\rangle|\psi_0^C\rangle$, denoting the case in which each species occupies the ground state of the effective species Hamiltonian, represents the three-body ground state obtained with a sMF ansatz. Consequently, $P_{000} = \left|\langle\Psi^{\mathrm{sMF}}|\Psi^{\mathrm{MB}}\rangle\right|^2$ (cf. Figures 11(a) and (b) for $g_{AB} = 1.0$). In general, it is observed that finite interactions yield a non-negligible population of energetically higher-lying excited states. Importantly, this behavior becomes enhanced in the coalescence regime, i.e., for strong repulsive g_{AB} and g_{AC}. This means that there are several macroscopically occupied basis states reflecting the significant intercompoment entanglement (cf. Figures 2 and 7).

---

[17] The impurities eigenstates are found by solving the corresponding one-body Hamiltonian, while the eigenstates of the effective bath Hamiltonian, consisting of N_A particles, are determined via improved relaxation [108].

References

[1] P. Massignan, M. Zaccanti and G. M. Bruun, *Polarons, dressed molecules and itinerant ferromagnetism in ultracold Fermi gases*, Rep. Prog. Phys. **77**, 034401 (2014), doi:10.1088/0034-4885/77/3/034401.

[2] R. Schmidt, M. Knap, D. A. Ivanov, J.-S. You, M. Cetina and E. Demler, *Universal many-body response of heavy impurities coupled to a Fermi sea: A review of recent progress*, Rep. Prog. Phys. **81**, 024401 (2018), doi:10.1088/1361-6633/aa9593.

[3] L. D. Landau, *Über die Bewegung der Elektronen in Kristallgitter*, Phys. Z. Sowjetunion **3**, 644 (1933).

[4] Y. Ashida, R. Schmidt, L. Tarruell and E. Demler, *Many-body interferometry of magnetic polaron dynamics*, Phys. Rev. B **97**, 060302 (2018), doi:10.1103/PhysRevB.97.060302.

[5] S. I. Mistakidis, G. M. Koutentakis, F. Grusdt, P. Schmelcher and H. R. Sadeghpour, *Inducing spin-order with an impurity: Phase diagram of the magnetic Bose polaron*, New J. Phys. **24**, 083030 (2022), doi:10.1088/1367-2630/ac836c.

[6] L. Rammelmüller, D. Huber, M. Čufar, J. Brand, H.-W. Hammer and A. G. Volosniev, *Magnetic impurity in a one-dimensional few-fermion system*, SciPost Phys. **14**, 006 (2023), doi:10.21468/SciPostPhys.14.1.006.

[7] F. Grusdt and M. Fleischhauer, *Tunable polarons of slow-light polaritons in a two-dimensional Bose-Einstein condensate*, Phys. Rev. Lett. **116**, 053602 (2016), doi:10.1103/PhysRevLett.116.053602.

[8] A. Frisk Kockum, A. Miranowicz, S. De Liberato, S. Savasta and F. Nori, *Ultrastrong coupling between light and matter*, Nat. Rev. Phys. **1**, 19 (2019), doi:10.1038/s42254-018-0006-2.

[9] R. Grimm, M. Weidemüller and Y. B. Ovchinnikov, *Optical dipole traps for neutral atoms*, in *Advances in atomic, molecular, and optical physics, volume 42*, Elsevier, Amsterdam, Netherlands, ISBN 9780120038428 (2000), doi:10.1016/S1049-250X(08)60186-X.

[10] I. Bloch, J. Dalibard and W. Zwerger, *Many-body physics with ultracold gases*, Rev. Mod. Phys. **80**, 885 (2008), doi:10.1103/RevModPhys.80.885.

[11] J. Catani, G. Lamporesi, D. Naik, M. Gring, M. Inguscio, F. Minardi, A. Kantian and T. Giamarchi, *Quantum dynamics of impurities in a one-dimensional Bose gas*, Phys. Rev. A **85**, 023623 (2012), doi:10.1103/PhysRevA.85.023623.

[12] M. Olshanii, *Atomic scattering in the presence of an external confinement and a gas of impenetrable bosons*, Phys. Rev. Lett. **81**, 938 (1998), doi:10.1103/PhysRevLett.81.938.

[13] T. Köhler, K. Góral and P. S. Julienne, *Production of cold molecules via magnetically tunable Feshbach resonances*, Rev. Mod. Phys. **78**, 1311 (2006), doi:10.1103/RevModPhys.78.1311.

[14] C. Chin, R. Grimm, P. Julienne and E. Tiesinga, *Feshbach resonances in ultracold gases*, Rev. Mod. Phys. **82**, 1225 (2010), doi:10.1103/RevModPhys.82.1225.

[15] M. Haas, V. Leung, D. Frese, D. Haubrich, S. John, C. Weber, A. Rauschenbeutel and D. Meschede, *Species-selective microwave cooling of a mixture of rubidium and caesium atoms*, New J. Phys. **9**, 147 (2007), doi:10.1088/1367-2630/9/5/147.

[16] M. Taglieber, A.-C. Voigt, T. Aoki, T. W. Hänsch and K. Dieckmann, *Quantum degenerate two-species Fermi-Fermi mixture coexisting with a Bose-Einstein condensate*, Phys. Rev. Lett. **100**, 010401 (2008), doi:10.1103/PhysRevLett.100.010401.

[17] S. B. Papp, J. M. Pino and C. E. Wieman, *Tunable miscibility in a dual-species Bose-Einstein condensate*, Phys. Rev. Lett. **101**, 040402 (2008), doi:10.1103/PhysRevLett.101.040402.

[18] C.-H. Wu, I. Santiago, J. W. Park, P. Ahmadi and M. W. Zwierlein, *Strongly interacting isotopic Bose-Fermi mixture immersed in a Fermi sea*, Phys. Rev. A **84**, 011601 (2011), doi:10.1103/PhysRevA.84.011601.

[19] A. J. Barker, S. Sunami, D. Garrick, A. Beregi, K. Luksch, E. Bentine and C. J. Foot, *Realising a species-selective double well with multiple-radiofrequency-dressed potentials*, J. Phys. B: At. Mol. Opt. Phys. **53**, 155001 (2020), doi:10.1088/1361-6455/ab9152.

[20] F. Serwane, G. Zürn, T. Lompe, T. B. Ottenstein, A. N. Wenz and S. Jochim, *Deterministic preparation of a tunable few-Fermion system*, Science **332**, 336 (2011), doi:10.1126/science.1201351.

[21] B. J. Lester, Y. Lin, M. O. Brown, A. M. Kaufman, R. J. Ball, E. Knill, A. M. Rey and C. A. Regal, *Measurement-based entanglement of noninteracting bosonic atoms*, Phys. Rev. Lett. **120**, 193602 (2018), doi:10.1103/PhysRevLett.120.193602.

[22] T. Fukuhara et al., *Quantum dynamics of a mobile spin impurity*, Nat. Phys. **9**, 235 (2013), doi:10.1038/nphys2561.

[23] M.-G. Hu, M. J. Van de Graaff, D. Kedar, J. P. Corson, E. A. Cornell and D. S. Jin, *Bose polarons in the strongly interacting regime*, Phys. Rev. Lett. **117**, 055301 (2016), doi:10.1103/PhysRevLett.117.055301.

[24] N. B. Jørgensen, L. Wacker, K. T. Skalmstang, M. M. Parish, J. Levinsen, R. S. Christensen, G. M. Bruun and J. J. Arlt, *Observation of attractive and repulsive polarons in a Bose-Einstein condensate*, Phys. Rev. Lett. **117**, 055302 (2016), doi:10.1103/PhysRevLett.117.055302.

[25] F. Meinert, M. Knap, E. Kirilov, K. Jag-Lauber, M. B. Zvonarev, E. Demler and H.-C. Nägerl, *Bloch oscillations in the absence of a lattice*, Science **356**, 945 (2017), doi:10.1126/science.aah6616.

[26] M. G. Skou, T. G. Skov, N. B. Jørgensen, K. K. Nielsen, A. Camacho-Guardian, T. Pohl, G. M. Bruun and J. J. Arlt, *Non-equilibrium quantum dynamics and formation of the Bose polaron*, Nat. Phys. **17**, 731 (2021), doi:10.1038/s41567-021-01184-5.

[27] A. Schirotzek, C.-H. Wu, A. Sommer and M. W. Zwierlein, *Observation of Fermi polarons in a tunable Fermi liquid of ultracold atoms*, Phys. Rev. Lett. **102**, 230402 (2009), doi:10.1103/PhysRevLett.102.230402.

[28] C. Kohstall, M. Zaccanti, M. Jag, A. Trenkwalder, P. Massignan, G. M. Bruun, F. Schreck and R. Grimm, *Metastability and coherence of repulsive polarons in a strongly interacting Fermi mixture*, Nature **485**, 615 (2012), doi:10.1038/nature11065.

[29] L. A. Peña Ardila and S. Giorgini, *Impurity in a Bose-Einstein condensate: Study of the attractive and repulsive branch using quantum Monte Carlo methods*, Phys. Rev. A **92**, 033612 (2015), doi:10.1103/PhysRevA.92.033612.

[30] F. Grusdt, G. E. Astrakharchik and E. Demler, *Bose polarons in ultracold atoms in one dimension: Beyond the Fröhlich paradigm*, New J. Phys. **19**, 103035 (2017), doi:10.1088/1367-2630/aa8a2e.

[31] J. Jager, R. Barnett, M. Will and M. Fleischhauer, *Strong-coupling Bose polarons in one dimension: Condensate deformation and modified Bogoliubov phonons*, Phys. Rev. Res. **2**, 033142 (2020), doi:10.1103/PhysRevResearch.2.033142.

[32] A. Camacho-Guardian, L. A. Peña Ardila, T. Pohl and G. M. Bruun, *Bipolarons in a Bose-Einstein condensate*, Phys. Rev. Lett. **121**, 013401 (2018), doi:10.1103/PhysRevLett.121.013401.

[33] A. Klein and M. Fleischhauer, *Interaction of impurity atoms in Bose-Einstein condensates*, Phys. Rev. A **71**, 033605 (2005), doi:10.1103/PhysRevA.71.033605.

[34] F. Brauneis, H.-W. Hammer, M. Lemeshko and A. Volosniev, *Impurities in a one-dimensional Bose gas: The flow equation approach*, SciPost Phys. **11**, 008 (2021), doi:10.21468/SciPostPhys.11.1.008.

[35] A. Petković and Z. Ristivojevic, *Mediated interaction between polarons in a one-dimensional Bose gas*, Phys. Rev. A **105**, L021303 (2022), doi:10.1103/PhysRevA.105.L021303.

[36] S. I. Mistakidis, A. G. Volosniev, R. E. Barfknecht, T. Fogarty, T. Busch, A. Foerster, P. Schmelcher and N. T. Zinner, *Cold atoms in low dimensions – a laboratory for quantum dynamics*, Phys. Rep. **1042**, 1 (2023), doi:10.1016/j.physrep.2023.10.004.

[37] M. Schecter and A. Kamenev, *Phonon-mediated Casimir interaction between mobile impurities in one-dimensional quantum liquids*, Phys. Rev. Lett. **112**, 155301 (2014), doi:10.1103/PhysRevLett.112.155301.

[38] B. Reichert, Z. Ristivojevic and A. Petković, *The Casimir-like effect in a one-dimensional Bose gas*, New J. Phys. **21**, 053024 (2019), doi:10.1088/1367-2630/ab1b8e.

[39] B. Reichert, A. Petković and Z. Ristivojevic, *Field-theoretical approach to the Casimir-like interaction in a one-dimensional Bose gas*, Phys. Rev. B **99**, 205414 (2019), doi:10.1103/PhysRevB.99.205414.

[40] A. Recati, J. N. Fuchs, C. S. Peça and W. Zwerger, *Casimir forces between defects in one-dimensional quantum liquids*, Phys. Rev. A **72**, 023616 (2005), doi:10.1103/PhysRevA.72.023616.

[41] A. I. Pavlov, J. van den Brink and D. V. Efremov, *Phonon-mediated Casimir interaction between finite-mass impurities*, Phys. Rev. B **98**, 161410 (2018), doi:10.1103/PhysRevB.98.161410.

[42] A. S. Dehkharghani, A. G. Volosniev and N. T. Zinner, *Coalescence of two impurities in a trapped one-dimensional Bose gas*, Phys. Rev. Lett. **121**, 080405 (2018), doi:10.1103/PhysRevLett.121.080405.

[43] A. Camacho-Guardian and G. M. Bruun, *Landau effective interaction between quasiparticles in a Bose-Einstein condensate*, Phys. Rev. X **8**, 031042 (2018), doi:10.1103/PhysRevX.8.031042.

[44] M. Pasek and G. Orso, *Induced pairing of fermionic impurities in a one-dimensional strongly correlated Bose gas*, Phys. Rev. B **100**, 245419 (2019), doi:10.1103/PhysRevB.100.245419.

[45] M. Will, G. E. Astrakharchik and M. Fleischhauer, *Polaron interactions and bipolarons in one-dimensional Bose gases in the strong coupling regime*, Phys. Rev. Lett. **127**, 103401 (2021), doi:10.1103/PhysRevLett.127.103401.

[46] G. E. Astrakharchik, L. A. Peña Ardila, K. Jachymski and A. Negretti, *Many-body bound states and induced interactions of charged impurities in a bosonic bath*, Nat. Commun. **14**, 1647 (2023), doi:10.1038/s41467-023-37153-0.

[47] W. Casteels, J. Tempere and J. T. Devreese, *Bipolarons and multipolarons consisting of impurity atoms in a Bose-Einstein condensate*, Phys. Rev. A **88**, 013613 (2013), doi:10.1103/PhysRevA.88.013613.

[48] P. Naidon, *Two impurities in a Bose-Einstein condensate: From Yukawa to Efimov attracted polarons*, J. Phys. Soc. Jpn. **87**, 043002 (2018), doi:10.7566/JPSJ.87.043002.

[49] J. Jager and R. Barnett, *The effect of boson-boson interaction on the bipolaron formation*, New J. Phys. **24**, 103032 (2022), doi:10.1088/1367-2630/ac9804.

[50] Y. Nishida, *Polaronic atom-trimer continuity in three-component Fermi gases*, Phys. Rev. Lett. **114**, 115302 (2015), doi:10.1103/PhysRevLett.114.115302.

[51] F. Theel, S. I. Mistakidis, K. Keiler and P. Schmelcher, *Counterflow dynamics of two correlated impurities immersed in a bosonic gas*, Phys. Rev. A **105**, 053314 (2022), doi:10.1103/PhysRevA.105.053314.

[52] S. I. Mistakidis, A. G. Volosniev and P. Schmelcher, *Induced correlations between impurities in a one-dimensional quenched Bose gas*, Phys. Rev. Res. **2**, 023154 (2020), doi:10.1103/PhysRevResearch.2.023154.

[53] V. R. Yordanov and F. Isaule, *Mobile impurities interacting with a few one-dimensional lattice bosons*, J. Phys. B: At. Mol. Opt. Phys. **56**, 045301 (2023), doi:10.1088/1361-6455/acb51b.

[54] D. Braun, *Creation of entanglement by interaction with a common heat bath*, Phys. Rev. Lett. **89**, 277901 (2002), doi:10.1103/PhysRevLett.89.277901.

[55] F. Benatti, R. Floreanini and M. Piani, *Environment induced entanglement in Markovian dissipative dynamics*, Phys. Rev. Lett. **91**, 070402 (2003), doi:10.1103/PhysRevLett.91.070402.

[56] C. Hörhammer and H. Büttner, *Environment-induced two-mode entanglement in quantum Brownian motion*, Phys. Rev. A **77**, 042305 (2008), doi:10.1103/PhysRevA.77.042305.

[57] O. S. Duarte and A. O. Caldeira, *Effective quantum dynamics of two Brownian particles*, Phys. Rev. A **80**, 032110 (2009), doi:10.1103/PhysRevA.80.032110.

[58] T. Zell, F. Queisser and R. Klesse, *Distance dependence of entanglement generation via a bosonic heat bath*, Phys. Rev. Lett. **102**, 160501 (2009), doi:10.1103/PhysRevLett.102.160501.

[59] K. Shiokawa, *Non-Markovian dynamics, nonlocality, and entanglement in quantum Brownian motion*, Phys. Rev. A **79**, 012308 (2009), doi:10.1103/PhysRevA.79.012308.

[60] F. Benatti, R. Floreanini and U. Marzolino, *Entangling two unequal atoms through a common bath*, Phys. Rev. A **81**, 012105 (2010), doi:10.1103/PhysRevA.81.012105.

[61] C. H. Fleming, N. I. Cummings, C. Anastopoulos and B. L. Hu, *Non-Markovian dynamics and entanglement of two-level atoms in a common field*, J. Phys. A: Math. Theor. **45**, 065301 (2012), doi:10.1088/1751-8113/45/6/065301.

[62] C. Charalambous, M. A. Garcia-March, A. Lampo, M. Mehboud and M. Lewenstein, *Two distinguishable impurities in BEC: Squeezing and entanglement of two Bose polarons*, SciPost Phys. **6**, 010 (2019), doi:10.21468/SciPostPhys.6.1.010.

[63] E. Compagno, G. De Chiara, D. G. Angelakis and G. M. Palma, *Tunable polarons in Bose-Einstein condensates*, Sci. Rep. **7**, 2355 (2017), doi:10.1038/s41598-017-02398-5.

[64] C. Charalambous, M. Á. García-March, G. Muñoz-Gil, P. R. Grzybowski and M. Lewenstein, *Control of anomalous diffusion of a Bose polaron*, Quantum **4**, 232 (2020), doi:10.22331/q-2020-02-20-232.

[65] K. Keiler, S. I. Mistakidis and P. Schmelcher, *Polarons and their induced interactions in highly imbalanced triple mixtures*, Phys. Rev. A **104**, L031301 (2021), doi:10.1103/PhysRevA.104.L031301.

[66] M. Stefanini, M. Capone and A. Silva, *Full view on the dynamics of an impurity coupled to two one-dimensional baths*, Phys. Rev. B **107**, 184316 (2023), doi:10.1103/PhysRevB.107.184316.

[67] S. Krönke, L. Cao, O. Vendrell and P. Schmelcher, *Non-equilibrium quantum dynamics of ultra-cold atomic mixtures: The multi-layer multi-configuration time-dependent Hartree method for bosons*, New J. Phys. **15**, 063018 (2013), doi:10.1088/1367-2630/15/6/063018.

[68] L. Cao, S. Krönke, O. Vendrell and P. Schmelcher, *The multi-layer multi-configuration time-dependent Hartree method for bosons: Theory, implementation, and applications*, J. Chem. Phys. **139**, 134103 (2013), doi:10.1063/1.4821350.

[69] L. Cao, V. Bolsinger, S. I. Mistakidis, G. M. Koutentakis, S. Krönke, J. M. Schurer and P. Schmelcher, *A unified ab initio approach to the correlated quantum dynamics of ultracold fermionic and bosonic mixtures*, J. Chem. Phys. **147**, 044106 (2017), doi:10.1063/1.4993512.

[70] S. I. Mistakidis, G. M. Koutentakis, G. C. Katsimiga, T. Busch and P. Schmelcher, *Many-body quantum dynamics and induced correlations of Bose polarons*, New J. Phys. **22**, 043007 (2020), doi:10.1088/1367-2630/ab7599.

[71] C. H. Greene, P. Giannakeas and J. Pérez-Ríos, *Universal few-body physics and cluster formation*, Rev. Mod. Phys. **89**, 035006 (2017), doi:10.1103/RevModPhys.89.035006.

[72] M. Egorov, B. Opanchuk, P. Drummond, B. V. Hall, P. Hannaford and A. I. Sidorov, *Measurement of s-wave scattering lengths in a two-component Bose-Einstein condensate*, Phys. Rev. A **87**, 053614 (2013), doi:10.1103/PhysRevA.87.053614.

[73] A. Álvarez, J. Cuevas, F. R. Romero, C. Hamner, J. J. Chang, P. Engels, P. G. Kevrekidis and D. J. Frantzeskakis, *Scattering of atomic dark-bright solitons from narrow impurities*, J. Phys. B: At. Mol. Opt. Phys. **46**, 065302 (2013), doi:10.1088/0953-4075/46/6/065302.

[74] G. Bighin, A. Burchianti, F. Minardi and T. Macrì, *Impurity in a heteronuclear two-component Bose mixture*, Phys. Rev. A **106**, 023301 (2022), doi:10.1103/PhysRevA.106.023301.

[75] G. Roati, C. D'Errico, L. Fallani, M. Fattori, C. Fort, M. Zaccanti, G. Modugno, M. Modugno and M. Inguscio, *Anderson localization of a non-interacting Bose-Einstein condensate*, Nature **453**, 895 (2008), doi:10.1038/nature07071.

[76] F. Köhler, K. Keiler, S. I. Mistakidis, H.-D. Meyer and P. Schmelcher, *Dynamical pruning of the non-equilibrium quantum dynamics of trapped ultracold bosons*, J. Chem. Phys. **151**, 054108 (2019), doi:10.1063/1.5104344.

[77] K. Życzkowski, P. Horodecki, A. Sanpera and M. Lewenstein, *Volume of the set of separable states*, Phys. Rev. A **58**, 883 (1998), doi:10.1103/PhysRevA.58.883.

[78] J. C. Light, I. P. Hamilton and J. V. Lill, *Generalized discrete variable approximation in quantum mechanics*, J. Chem. Phys. **82**, 1400 (1985), doi:10.1063/1.448462.

[79] A. Raab, *On the Dirac-Frenkel/McLachlan variational principle*, Chem. Phys. Lett. **319**, 674 (2000), doi:10.1016/S0009-2614(00)00200-1.

[80] A. U. J. Lode, C. Lévêque, L. B. Madsen, A. I. Streltsov and O. E. Alon, *Colloquium: Multiconfigurational time-dependent Hartree approaches for indistinguishable particles*, Rev. Mod. Phys. **92**, 011001 (2020), doi:10.1103/RevModPhys.92.011001.

[81] O. Penrose and L. Onsager, *Bose-Einstein condensation and liquid helium*, Phys. Rev. **104**, 576 (1956), doi:10.1103/PhysRev.104.576.

[82] J. Catani, G. Barontini, G. Lamporesi, F. Rabatti, G. Thalhammer, F. Minardi, S. Stringari and M. Inguscio, *Entropy exchange in a mixture of ultracold atoms*, Phys. Rev. Lett. **103**, 140401 (2009), doi:10.1103/PhysRevLett.103.140401.

[83] P. Cheiney, C. R. Cabrera, J. Sanz, B. Naylor, L. Tanzi and L. Tarruell, *Bright soliton to quantum droplet transition in a mixture of Bose-Einstein condensates*, Phys. Rev. Lett. **120**, 135301 (2018), doi:10.1103/PhysRevLett.120.135301.

[84] S. I. Mistakidis, G. C. Katsimiga, P. G. Kevrekidis and P. Schmelcher, *Correlation effects in the quench-induced phase separation dynamics of a two species ultracold quantum gas*, New J. Phys. **20**, 043052 (2018), doi:10.1088/1367-2630/aabc6a.

[85] S. I. Mistakidis, G. C. Katsimiga, G. M. Koutentakis, T. Busch and P. Schmelcher, *Quench dynamics and orthogonality catastrophe of Bose polarons*, Phys. Rev. Lett. **122**, 183001 (2019), doi:10.1103/PhysRevLett.122.183001.

[86] F. Theel, K. Keiler, S. I. Mistakidis and P. Schmelcher, *Many-body collisional dynamics of impurities injected into a double-well trapped Bose-Einstein condensate*, Phys. Rev. Res. **3**, 023068 (2021), doi:10.1103/PhysRevResearch.3.023068.

[87] K. Keiler, S. I. Mistakidis and P. Schmelcher, *Doping a lattice-trapped bosonic species with impurities: From ground state properties to correlated tunneling dynamics*, New J. Phys. **22**, 083003 (2020), doi:10.1088/1367-2630/ab9e34.

[88] S. S. Hodgman, R. G. Dall, A. G. Manning, K. G. H. Baldwin and A. G. Truscott, *Direct measurement of long-range third-order coherence in Bose-Einstein condensates*, Science **331**, 1046 (2011), doi:10.1126/science.1198481.

[89] R. G. Dall, A. G. Manning, S. S. Hodgman, W. RuGway, K. V. Kheruntsyan and A. G. Truscott, *Ideal n-body correlations with massive particles*, Nat. Phys. **9**, 341 (2013), doi:10.1038/nphys2632.

[90] J. H. V. Nguyen, M. C. Tsatsos, D. Luo, A. U. J. Lode, G. D. Telles, V. S. Bagnato and R. G. Hulet, *Parametric excitation of a Bose-Einstein condensate: From Faraday waves to granulation*, Phys. Rev. X **9**, 011052 (2019), doi:10.1103/PhysRevX.9.011052.

[91] F. Borselli et al., *Two-particle interference with double twin-atom beams*, Phys. Rev. Lett. **126**, 083603 (2021), doi:10.1103/PhysRevLett.126.083603.

[92] S. Hofferberth, I. Lesanovsky, T. Schumm, A. Imambekov, V. Gritsev, E. Demler and J. Schmiedmayer, *Probing quantum and thermal noise in an interacting many-body system*, Nat. Phys. **4**, 489 (2008), doi:10.1038/nphys941.

[93] A. Bergschneider, V. M. Klinkhamer, J. H. Becher, R. Klemt, G. Zürn, P. M. Preiss and S. Jochim, *Spin-resolved single-atom imaging of ^{6}Li in free space*, Phys. Rev. A **97**, 063613 (2018), doi:10.1103/PhysRevA.97.063613.

[94] S. I. Mistakidis, A. G. Volosniev, N. T. Zinner and P. Schmelcher, *Effective approach to impurity dynamics in one-dimensional trapped Bose gases*, Phys. Rev. A **100**, 013619 (2019), doi:10.1103/PhysRevA.100.013619.

[95] E. Schmidt, *Zur Theorie der linearen und nichtlinearen Integralgleichungen*, Math. Ann. **63**, 433 (1907), doi:10.1007/BF01449770.

[96] A. Ekert and P. L. Knight, *Entangled quantum systems and the Schmidt decomposition*, Am. J. Phys. **63**, 415 (1995), doi:10.1119/1.17904.

[97] K. Sakmann, A. I. Streltsov, O. E. Alon and L. S. Cederbaum, *Reduced density matrices and coherence of trapped interacting bosons*, Phys. Rev. A **78**, 023615 (2008), doi:10.1103/PhysRevA.78.023615.

[98] C. Lévêque, F. Diorico, J. Schmiedmayer and A. U. J. Lode, *Many-body density and coherence of trapped cold bosons*, (arXiv preprint) doi:10.48550/arXiv.2006.10755.

[99] T. Schweigler, V. Kasper, S. Erne, I. Mazets, B. Rauer, F. Cataldini, T. Langen, T. Gasenzer, J. Berges and J. Schmiedmayer, *Experimental characterization of a quantum many-body system via higher-order correlations*, Nature **545**, 323 (2017), doi:10.1038/nature22310.

[100] R. C. Whitten and F. T. Smith, *Symmetric representation for three-body problems. II. Motion in space*, J. Math. Phys. **9**, 1103 (1968), doi:10.1063/1.1664683.

[101] G. Bougas, S. I. Mistakidis, P. Giannakeas and P. Schmelcher, *Few-body correlations in two-dimensional Bose and Fermi ultracold mixtures*, New J. Phys. **23**, 093022 (2021), doi:10.1088/1367-2630/ac0e56.

[102] S. I. Mistakidis, G. C. Katsimiga, G. M. Koutentakis, T. Busch and P. Schmelcher, *Pump-probe spectroscopy of Bose polarons: Dynamical formation and coherence*, Phys. Rev. Res. **2**, 033380 (2020), doi:10.1103/PhysRevResearch.2.033380.

[103] R. Horodecki, P. Horodecki, M. Horodecki and K. Horodecki, *Quantum entanglement*, Rev. Mod. Phys. **81**, 865 (2009), doi:10.1103/RevModPhys.81.865.

[104] G. Vidal and R. F. Werner, *Computable measure of entanglement*, Phys. Rev. A **65**, 032314 (2002), doi:10.1103/PhysRevA.65.032314.

[105] J. Becker, M. Pyzh and P. Schmelcher, *Interaction-controlled impurity transport in trapped mixtures of ultracold bosons*, Phys. Rev. A **106**, 053314 (2022), doi:10.1103/PhysRevA.106.053314.

[106] A. Jäckle and H.-D. Meyer, *Product representation of potential energy surfaces*, J. Chem. Phys. **104**, 7974 (1996), doi:10.1063/1.471513.

[107] A. Jäckle and H.-D. Meyer, *Product representation of potential energy surfaces. II*, J. Chem. Phys. **109**, 3772 (1998), doi:10.1063/1.476977.

[108] H.-D. Meyer and G. A. Worth, *Quantum molecular dynamics: Propagating wavepackets and density operators using the multiconfiguration time-dependent Hartree method*, Theor. Chem. Acc. **109**, 251 (2003), doi:10.1007/s00214-003-0439-1.

PHYSICAL REVIEW A **111**, 013306 (2025)

Effective approaches to the dynamical properties of two distinguishable Bose polarons

F. Theel,[1] S. I. Mistakidis,[2] and P. Schmelcher[1,3]
[1]*Center for Optical Quantum Technologies, Department of Physics, University of Hamburg, Luruper Chaussee 149, D-22761 Hamburg, Germany*
[2]*Department of Physics, Missouri University of Science and Technology, Rolla, Missouri 65409, USA*
[3]*The Hamburg Centre for Ultrafast Imaging, University of Hamburg, Luruper Chaussee 149, D-22761 Hamburg, Germany*

(Received 24 September 2024; accepted 17 December 2024; published 8 January 2025)

We explore effective approaches for describing the dynamics of induced interactions among two noninteracting distinguishable impurities (Bose polarons) when their couplings to the host species are switched on. First, we evaluate the time-dependent characteristics of each polaron through reduced single-particle models. Their validity is ultimately judged by comparing them to observables obtained within a many-body variational approach. We argue that utilizing a time-dependent optimization process with the effective mass and frequency being fitting parameters leads to an accurate matching on the level of one-body observables with the prediction of the many-body method. Next, we construct two-body effective models, which, in addition to the effective parameters of the single polaron, include a contact interaction potential modeling the induced interactions. It is shown that the instantaneous coupling strength obtained with a time-dependent optimization process allows for an accurate description of the impurities two-body correlation dynamics when compared to the many-body calculations. In this sense, it is possible to describe the dynamical crossover from correlated to anticorrelated impurity patterns related to the transition from attractive to repulsive induced interactions. Our results should facilitate the description of strongly particle-imbalanced mixtures via reduced models and hence their experimental understanding.

DOI: 10.1103/PhysRevA.111.013306

I. INTRODUCTION

Multicomponent ultracold quantum gases are versatile platforms to explore complex many-body states of matter [1–3] since they exhibit an exquisite tunability in terms of system parameters such as species selective external potentials [4–6], interactions [7–9], and atom number [10–12]. In the case of strongly particle imbalanced two-component mixtures the minority species, called an impurity, is coupled to a majority gas and becomes dressed by its excitations forming a quasiparticle [13–15] dubbed the Bose [16–21] or Fermi [22,23] polaron depending on the statistics of the host. Polaron properties are usually spectroscopically probed in the experiment [24,25].

The large population imbalance naturally motivates reductions of the original many-body problem. These involve effective single-particle models [15,26–29] aiming to capture quasiparticle characteristics such as their effective mass and residue [14,29–31], or effective two-body approaches [32–35] to describe induced impurity-impurity interactions mediated by the host. Specifically, the presence of attractive induced interaction has been identified when the impurities couple either both attractively or repulsively to their medium [21,34–43]. This eventually leads for strong impurity-medium attractions to the generation of bound states, named bipolarons [44–47]. However, another intriguing possibility is to consider a three-component setting where distinguishable impurities can couple with opposite signs to their bosonic host suggesting the existence of a mediated repulsive interaction potential [40,48–50]. In Ref. [50] the existence of mediated attractive and repulsive interactions was unveiled being accompanied by a two-body correlated and anticorrelated behavior of the impurities, respectively. A similar behavior has also been predicted for a fermionic host where the induced interaction can be approximated by a contact interaction potential [51].

Apparently, to reveal such processes three-component mixtures are required. Relevant experimental realizations consist of isotopes including ^{41}K, ^{40}K, and ^{6}Li [8] or ^{87}Rb, ^{40}K, and ^{6}Li [52] as well as the three hyperfine states of spin-1 ^{87}Rb condensates [53,54]. Notable investigations with three-component mixtures revolve from soliton creation and their interactions [53,54], the formation of droplet-like configurations [55–57] to enriched lattice phases beyond the common superfluid to Mott-insulator transition [58,59]. Other relevant studies investigated the impact of impurities on a binary mixture [60–65], thereby, focusing on either polaronic properties in a harmonic trap [62,63], or transport mechanisms within a double-well potential [64] as well as the interplay between a disordered external potential and the interspecies interactions in the emergent dynamical response [65].

The aim of the present work is to utilize the richness of three-component cold atom platforms to study the validity of effective approaches to capture dynamical properties of ensuing quasiparticles. Quasiparticles in our case are generated through embedding two noninteracting distinguishable impurities to a bosonic environment. Notice here also that the dynamical response of three-component systems is largely unexplored especially so for strongly imbalanced settings. Initially, we identify the ground-state impurity-impurity induced correlation patterns with respect

©2025 American Physical Society

to the distinct impurity-medium interactions. As in Ref. [50], we showcase the existence of a crossover from attractive to repulsive induced interactions when the product of the different impurity-medium couplings changes sign.

Next, linear ramps of the impurity-medium interactions are performed across the distinct induced interaction regimes or remaining within the same. This process leads to a time-dependent effective mass and frequency of the polarons as well as induced correlations [35,66]. To estimate these effective parameters we first construct different single-particle reduced models describing the composite system when solely one of the impurities interacts with the medium. To testify the applicability of these reduced approaches their predictions are directly compared with the ones of the correlated many-body simulations at the level of one-body observables. We find that the best agreement occurs for the model based on a time-dependent optimization using the effective mass and frequency as time-dependent fitting parameters for matching one-body observables within the many-body method. Other reductions, e.g., assuming adiabatic ramping of the interaction or that the host acts as an effective time-independent potential for the impurity, appear to be less accurate, e.g., due to neglecting the backaction of the impurities to the host.

Subsequently, we develop two-body reduced models for quantifying the presence of induced correlations in the course of the evolution. These approaches inherit the information of the appropriate optimized one-body models and additionally contain an effective two-body interaction potential for the impurities. Their validity is confirmed by minimizing the deviation of the impurities two-body correlation function between the effective picture and the many-body simulations [35]. Once again, we showcase that a time-dependent optimization procedure on the impurities effective coupling provides the most accurate description as compared to the many-body results. Interestingly, adequate (but less) agreement is observed by deploying an exponentially decaying interaction potential. Finally, we quantify the presence of impurities-medium and impurity-impurity entanglement in the dynamics of the von Neumann entropy and the logarithmic negativity, respectively.

The present work is structured as follows. In Sec. II we introduce the many-body Hamiltonian of the three-component mixture and describe the applied linear ramp of the impurity-medium coupling. The main facets of the employed many-body variational method are explicated in Sec. III. The ground-state impurity-impurity induced correlation patterns are classified in Sec. IV. The impurity dynamics triggered via linear ramps of the impurity-medium interactions is analyzed in detail in Sec. V along with the respective single- and two-particle reduced models used to quantify the time-dependent effective mass and frequency of the polaron. We monitor the impurities-medium and impurities entanglement in Sec. VI. We summarize our results and discuss possible future extensions in Sec. VII. In Appendix A we showcase the impact of the quench ramp rate. Appendix B elaborates on the reduced methods used to determine the ground-state effective parameters, while in Appendix C the convergence behavior of the optimization technique is explicated. The applicability of the effective two-body model for various ramp protocols is demonstrated in Appendix D. We estimate the dominant expansion coefficients of the impurities' correlation function in Appendix E.

II. THREE-COMPONENT BOSONIC MIXTURE

We deploy an ultracold three-component atomic mixture in the presence of an external one-dimensional (1D) harmonic oscillator potential with $\omega_A = \omega_B = \omega_C \equiv \omega = 1$. Species A consists of $N_A = 10$ bosons and represents the host for the impurity species B and C, where $N_B = N_C = 1$. For simplicity, a mass-balanced system, i.e., $m_A = m_B = m_C \equiv m = 1$, is assumed. Due to ultralow temperatures it is adequate to use a contact s-wave interaction potential of strength $g_{\sigma,\sigma'}$, where $\sigma, \sigma' \in \{A, B, C\}$, for two atoms of the same or different species [67]. It is known that the effective 1D interaction strengths $g_{\sigma\sigma'}$ depend on the respective three-dimensional scattering lengths $a^{3D}_{\sigma\sigma'}$ and the transverse confinement frequency $\omega_\perp$. The first can be tuned via Feshbach resonances [67,68] and the second leads to confinement-induced resonances [69]. The 1D nature of the emergent dynamics is ensured by utilizing an adequately large trap aspect ratio, e.g., $\omega_x/\omega_\perp = 0.01$ customary in 1D experiments [53,70] to prevent involvement of transversal excitations. Additionally, in view of the scope of the present work, namely, to reveal the potential presence of induced impurity-impurity interactions, we set $g_{BC} = 0$. The many-body dimensionless Hamiltonian of this three-component setting is given by

$$\begin{aligned}\hat{H} = {} & \sum_{i=1}^{N_A} \hat{h}_A\big(x_i^A\big) + g_{AA} \sum_{i<j} \delta\big(x_i^A - x_j^A\big) \\ & + \hat{h}_B(x^B) + g_{AB} \sum_{i=1}^{N_A} \delta\big(x_i^A - x^B\big) \\ & + \hat{h}_C(x^C) + g_{AC} \sum_{i=1}^{N_A} \delta\big(x_i^A - x^C\big). \end{aligned} \tag{1}$$

Here, $\hat{h}_\sigma(x) = -(1/2)[(d^2/dx^2) - x^2]$ denote the σ-component single-particle Hamiltonian terms. In the above Hamiltonian we employ harmonic oscillator units in which the energy scales as $\hbar\omega$ and the length and interactions are expressed in units of $\sqrt{\hbar/m\omega}$ and $\sqrt{\hbar^3\omega/m}$, respectively. Experimentally, three-component mixtures have already been realized [8,52,54,71] and thus our system should be within reach, at least, in terms of the considered population imbalance among the components. For instance, a promising experimental setup to utilize would consist of two Rubidium isotopes where, e.g., ^{85}Rb represents the bath and two ^{87}Rb atoms in different hyperfine states emulate the impurities [72,73]. Similarly, employing a radiofrequency protocol as in Ref. [54] three different hyperfine states of ^{87}Rb could be populated with the required imbalance in order to realize our system.

In the following, the three-component system will be prepared in different correlated ground-state configurations with respect to the impurity-medium interaction strengths as outlined in Sec. IV. Consecutively, a time-dependent linear ramp from an initial to a final value characterized by a ramping rate τ triggers the nonequilibrium dynamics, see Sec. V, aiming to quantify emergent impurity-impurity mediated interactions. Specifically, the employed interaction ramp protocol reads

$$g_{A\sigma}(t) = \begin{cases} g^{0}_{A\sigma} + \frac{g^{\tau}_{A\sigma} - g^{0}_{A\sigma}}{\tau} t, & t < \tau, \\ g^{\tau}_{A\sigma}, & t \geqslant \tau, \end{cases} \tag{2}$$

where $g_{A\sigma}(t=0) \equiv g^{0}_{A\sigma}$ and $g_{A\sigma}(\tau \leqslant t) \equiv g^{\tau}_{A\sigma}$ with $\sigma = \{B, C\}$. Within the main text we shall mainly focus on ramp rates $\tau\omega = 1, 5$. These ensure that the interaction ramp is slower compared to the sudden quench and, thereby, leads to fewer high-energy excitations, but it is still far from being adiabatic (see also Appendix A). Experimentally, ramping between two interaction strengths at different rates can be realized by adjusting the magnetic field strength near a corresponding Feshbach resonance. Hence, it is possible to tune the respective intra or intercomponent scattering lengths with a finite ramp rate, e.g., as in the experiments of Refs. [74,75].

III. MANY-BODY COMPUTATIONAL METHOD

To simulate the ground-state and the nonequilibrium quantum dynamics of the aforementioned three-component system we resort to the *ab initio* multilayer multiconfiguration time-dependent Hartree method for atomic mixtures (ML-MCTDHX) [76–78]. In this context, the ansatz of the many-body wave function inherits a multilayer structure with time-dependent and variationally optimized basis functions such that all relevant intra and intercomponent correlations are taken into account. In particular, the first truncation of the many-body wave function $|\Psi(t)\rangle$ is performed on the so-called species layer. Namely, $|\Psi(t)\rangle$ is expanded in terms of D_σ time-dependent species functions, $\{|\Psi^{\sigma}_{i}(t)\rangle\}_{i=1}^{D_\sigma}$ with $\sigma = A, B, C$, and time-dependent $C_{ijk}(t)$ coefficients, i.e.,

$$|\Psi(t)\rangle = \sum_{ijk} C_{ijk}(t) \big|\Psi^{A}_{i}(t)\big\rangle \otimes \big|\Psi^{B}_{j}(t)\big\rangle \otimes \big|\Psi^{C}_{k}(t)\big\rangle. \tag{3}$$

Each $|\Psi^{\sigma}_{i}(t)\rangle$ describes the state of the entire σ species, which is achieved by the second truncation on the so-called particle layer. This means that $|\Psi^{\sigma}_{i}(t)\rangle$ is expressed with respect to bosonic number states $|\vec{n}(t)\rangle$ with time-dependent expansion coefficients $C^{\sigma}_{i,\vec{n}}(t)$. The number states themselves are constructed from d_σ time-dependent single-particle functions (SPFs), where the elements of $\vec{n} = (n_1, \ldots, n_{d_\sigma})$ quantify the particle occupation in each SPF satisfying $\sum_i n_i = N_\sigma$. Eventually, each SPF is expanded into a time-independent discrete variable representation referring to a spatial grid [79], that contains in our case $\mathcal{M}_r = 300$ grid points.

Importantly, from the tensor coefficients $C_{ijk}(t)$ appearing in Eq. (3) the eigenvalues of the species reduced density matrices can be derived [78]. They signify the contribution of each species function to the complete many-body wave function. Hence, they provide information about the entanglement among the three different species [80], see also Sec. VI for details about measuring bipartite entanglement between two subsystems.

Additionally, our ansatz is amenable to further reductions such that entanglement is ignored among all or specific components. As an extreme case example, if we deem to prohibit correlations among all species, then our ansatz in Eq. (3) contains $D_A = D_B = D_C = 1$, leading to a single product state, i.e., $|\Psi(t)\rangle = |\Psi^{A}(t)\rangle \otimes |\Psi^{B}(t)\rangle \otimes |\Psi^{C}(t)\rangle$ [78,81]. This process is dubbed species mean-field *sMF*, where each component acts as a mean-field-type effective potential to the others but intracomponent correlations are present since $d_\sigma > 1$. This treatment is well established for binary mixtures and has been used to uncover the effects stemming solely from interspecies correlations [82,83].

One feature that unveils the richness of the three-component mixture and renders it even more intriguing than the binary case is that it naturally allows for different types of entanglement which can be, for instance, explicated through distinct species mean-field ansatzes. For instance, let us consider a physical situation where entanglement between A and C subsystems is suppressed, but it still exists among A and B. In this case, our ansatz should include just one species function for the C impurity ($D_C = 1$), while for species A and B it holds that $D_A = D_B > 1$. Below, this ansatz will be referred to as *species mean field for the C component* (sMFC) since the latter cannot become entangled with the others. Here, from the perspective of the AB subsystem, impurity C acts as a mean-field-type potential. Along the same lines, it is possible to define the respective sMFA and sMFB ansatzes.

Finally, we remark that for our analysis additional calculations in terms of time-dependent effective one- and two-body models are performed. Indeed, for the single-particle model, described by $\hat{H}^{(1)}(x,t)$ (Sec. V B), the dynamics is obtained by numerical integration of the time-dependent one-body Schrödinger equation, i.e., $i\hbar\partial_t \Psi(x,t) = \hat{H}^{(1)}(x,t)\Psi(x,t)$. However, the time-dependent two-body problem is solved by expanding the two-body Hamiltonian $\hat{H}^{(2)}(x_1, x_2, t)$ (Sec. V C) in terms of product states of one-body solutions.

IV. GROUND-STATE CORRELATION REGIMES

Before delving into the dynamical behavior of the two impurities, we first provide a brief overview of the different ground-state correlation regimes which emerge upon varying the impurity-medium interaction strengths g_{AB} and g_{AC}. More elaborate discussions and analysis on these phases can be found in Ref. [50]. In practice, two types of induced impurity-impurity correlations can be discerned. Namely, impurities [Fig. 1(a)] bunching for $g_{AB}g_{AC} > 0$ and [Fig. 1(b)] antibunching occurring for $g_{AB}g_{AC} < 0$. If $g_{AB}g_{AC} = 0$, the B and C impurities remain uncorrelated. Recall that since $g_{BC} = 0$, any signature of correlation among the impurities is induced from their interaction with the medium.

A suitable observable to visualize this behavior is the spatially resolved two-body correlation function [50,84] of the impurities

$$\mathcal{G}_{BC}(x^B, x^C) = \rho^{(2)}_{BC}(x^B, x^C) - \rho^{(1)}_{B}(x^B)\rho^{(1)}_{C}(x^C). \tag{4}$$

Here, the unconditional probability $\rho^{(1)}_{B}(x^B)\rho^{(1)}_{C}(x^C)$ constructed from the respective impurities one-body densities is subtracted from the conditional probability of finding the impurities at positions x^B and x^C, i.e., the two-body reduced density matrix $\rho^{(2)}_{BC}(x^B_1, x^C_2)$ [34,78]. This way, we are able to definitively identify the impurities two-body configurations. Specifically, the impurities located at x^B and x^C are two-body correlated (anticorrelated) as long as $\mathcal{G}_{BC}(x^B, x^C) > 0$

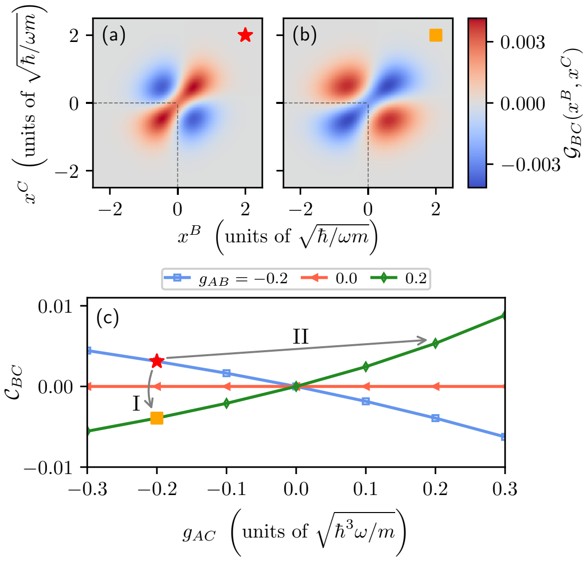

FIG. 1. (a) and (b) Ground-state two-body correlation profiles, $\mathcal{G}_{BC}(x^B, x^C)$, of the impurities quantifying their induced correlations since $g_{BC} = 0$. $\mathcal{G}_{BC}(x^B, x^C)$ shows the impurities are bunched (antibunched) at the same (different) position(s) as long as $g_{AB}g_{AC} > 0$ ($g_{AB}g_{AC} < 0$), see panel (a) for $(g_{AB}, g_{AC}) = (-0.2, -0.2)$, and panel (b) for $(g_{AB}, g_{AC}) = (-0.2, 0.2)$. (c) Integrating $\mathcal{G}_{BC}(x^B, x^C)$ over the region marked by the gray dashed lines in panels (a) and (b) provides information about the impurities two-body correlation content as quantified by $\mathcal{C}_{BC}$ for specific g_{AB} (see legend) and varying g_{AC}. The gray arrows designated by *I* and *II* illustrate the two quench protocols performed later on to induce the dynamics. In all cases, the impurities are coupled to a bosonic medium containing $N_A = 10$ atoms and interacting with $g_{AA} = 0.2$.

$[\mathcal{G}_{BC}(x^B, x^C) < 0]$ and are uncorrelated for $\mathcal{G}_{BC}(x^B, x^C) = 0$. Experimentally, the two-body correlation function can be observed in the following ways: (i) detect single atoms after a time-of-flight expansion [85]; (ii) analyze single-shot images as described in Ref. [86]; or (iii) through fluorescence measurements after freezing out the spatial degree's of freedom by ramping up a tight lattice confinement [87].

In Figs. 1(a) and 1(b) two characteristic correlation patterns of the impurities are presented for the interaction configurations $(g_{AB}, g_{AC}) = (-0.2, -0.2)$ and $(-0.2, 0.2)$, respectively. It can be readily seen that in the case of $g_{AB}g_{AC} > 0$ [Fig. 1(a)] the impurities are bunched, namely, they prefer to reside at the same location [see the diagonal of $\mathcal{G}_{BC}(x^B, x^C)$] and antibunched, i.e., they avoid each other, at different spatial regions [antidiagonal of $\mathcal{G}_{BC}(x^B, x^C)$]. In contrast, for $g_{AB}g_{AC} < 0$ the impurity-impurity correlation pattern is reversed showing antibunching along the diagonal and bunching in the antidiagonal, see Fig. 1(b). Hence, the impurities tend to avoid each other at the same spatial regions but rather prefer to stay symmetrically placed with respect to the trap center. Such a crossover from induced correlation to anticorrelation has been independently analyzed in terms of an effective two-body model and found to be associated with either attractive or repulsive effective contact interactions in Ref. [50].

To gain an overview of the impurities two-body correlation tendency upon different parametric variations, we subsequently measure the spatially integrated [see gray dashed lines in Figs. 1(a) and 1(b)] correlation function[1]

$$\mathcal{C}_{BC} = \int_{-\infty}^{0}\int_{-\infty}^{0} \mathrm{d}x^B \mathrm{d}x^C \mathcal{G}_{BC}(x^B, x^C). \tag{5}$$

Thereby, a negative (positive) value of $\mathcal{C}_{BC}$ is associated with induced impurity-impurity anticorrelations (correlations), while $\mathcal{C}_{BC} = 0$ indicates their absence. This observable is depicted in Fig. 1(c) for the ground state of the system as a function of g_{AC} and for fixed values of g_{AB}. A crossover from impurities antibunching to bunching is captured once the sign of $g_{AB}g_{AC}$ is reversed as it was originally reported in Ref. [50].

V. DYNAMICS OF THE DISTINGUISHABLE IMPURITIES AFTER A LINEAR QUENCH

Having exemplified the interaction combinations (g_{AB}, g_{AC}) for which the impurities are predominantly correlated or anticorrelated in their ground state, we aim to analyze the impurity dynamics after a time-dependent linear ramp of their intercomponent interactions. These interactions are linearly modified at a specific rate τ from their initial attractive values (g_{AB}^0, g_{AC}^0) to final ones $(g_{AB}^\tau, g_{AC}^\tau)$. Here, the overarching objective is to investigate the response of the impurity-impurity correlations when the related couplings are ramped from a correlated to an anticorrelated ground-state configuration as well as compare to scenarios at which the ramp is done between configurations with the same correlation behavior. For visualization purposes, these quench scenarios are illustrated in Fig. 1(c) with the gray arrows labeled with I and II.

A. Density response

The time evolution of the one-body density of component σ, $\rho_\sigma^{(1)}(x, t)$, after a linear interaction quench is presented in Fig. 2. Specifically, three paradigmatic linear interaction ramp protocols are utilized where either one or both impurity-medium interactions are ramped from attractive to repulsive values as depicted in Figs. 2(a1), 2(b1), and 2(c1) with a rate $\tau = 5$. The last value is adequately small to be close to the sudden quench and not large enough to approach the adiabatic limit where excitation processes are suppressed (cf. Appendix A).

An overall breathing motion of the cloud of each component is initiated by the intercomponent interaction ramp, as it can be seen from Fig. 2 even though in some cases [e.g., Figs. 2(a2), 2(a4), and 2(b2)] the breathing amplitude is relatively weak and thus the underlying collective motion becomes hardly visible.[2] The breathing motion manifests

---

[1] While in the ground state the integration area is always either positive or negative, during the evolution it may contain both positive and negative values due to more complicated correlation patterns. However, we find that even in this case $\mathcal{C}_{BC}$ remains a useful tool as long as these effects are not dominant.

[2] For a proper visualization of the breathing motion one can inspect, for instance, the variance of the one-body density (for brevity not shown here).

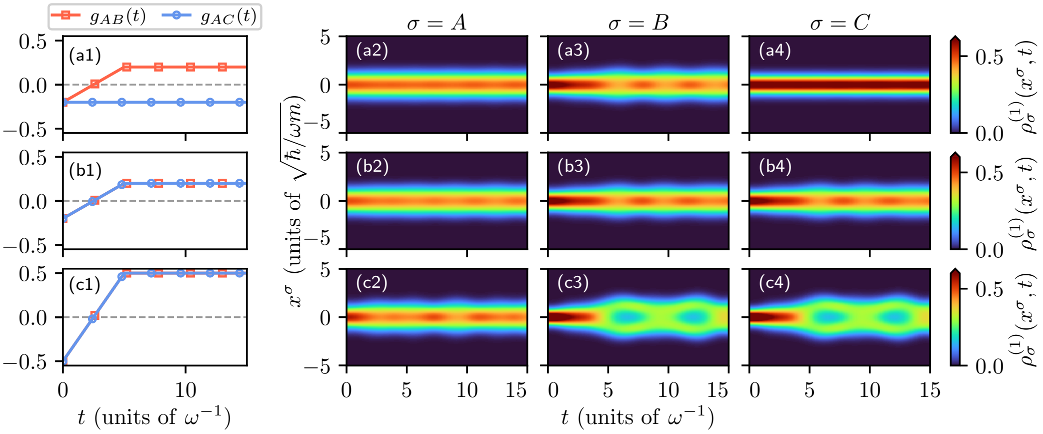

FIG. 2. Time evolution of the $\sigma \in \{A, B, C\}$ component one-body densities $\rho^{(1)}_\sigma(x,t)$ after linearly ramping up the impurity-medium interactions from (g^0_{AB}, g^0_{AC}) to $(g^\tau_{AB}, g^\tau_{AC})$ within $\tau\omega = 5$ as shown in panels (a1), (b1), and (c1). In particular, the interactions range (a1)-(a4) from $g^0_{AB} = -0.2$ to $g^\tau_{AB} = 0.2$ while $g^0_{AC} = g^\tau_{AC} = -0.2$, (b1)–(b4) from $g^0_{AB} = g^0_{AC} = -0.2$ to $g^\tau_{AB} = g^\tau_{AC} = 0.2$ and (c1)–(c4) from $g^0_{AB} = g^0_{AC} = -0.5$ to $g^\tau_{AB} = g^\tau_{AC} = 0.5$. The system is prepared in the ground state of two noninteracting B and C impurities immersed in a weakly coupled ($g_{AA} = 0.2$) bosonic medium A of $N_A = 10$ atoms. The depicted one-body densities are given in units of $\sqrt{m\omega/\hbar}$.

by the collective, weak amplitude, expansion, and contraction dynamics of the individual clouds. Specifically, for final impurity-medium interactions that do not exceed the intracomponent medium coupling as in Figs. 2(a1)–2(a4) and Figs. 2(b1)–2(b4) the components are miscible in the course of the evolution. Namely, they spatially overlap [7,88,89] with the impurities remaining within the host, see, in particular, the spatial scales of the densities which are the same in all cases during the evolution. This observation is important for the quasiparticle notion since, in addition to the formation of correlations, the finite overlap facilitates the impurity's dressing by the host excitations [28,82,90]. Notice also that in the special case where g_{AC} retains its original value (i.e., not quenched) the impurity C is only slightly perturbed which is hardly visible in Fig. 2(a4). This is attributed to the indirect action of the impurity B which through the finite change in g_{AB} slightly modifies the distribution of the medium. The dynamics of the latter for finite g_{AC} eventually also perturbs impurity C.

Turning to larger repulsive final impurity-medium interactions that overcome g_{AA}, following the quench, we observe a somewhat altered impurity response as shown in Figs. 2(c2)–2(c4). Here, dynamical miscibility is partially violated because the amplitude of the impurities ensuing breathing motion is arguably more pronounced due to stronger intercomponent repulsion. In this sense, at the time instants of maximum expansion of the impurities breathing motion a partial immiscibility between the impurities and the host clouds arise. As such, temporal phase-separation events among the impurities and the medium arise while the impurities remain miscible throughout the evolution. Note in passing, that for even larger repulsive intercomponent interactions phase-separation becomes prominent and the impurities escape their host leading to a temporal orthogonality catastrophe of the quasiparticle picture [91]. Still, in such repulsive interaction regimes the impurities, in the ground state of the system, can assemble outside of the bath in a Bell-type distribution as it was recently shown in Ref. [92].

To deepen our understanding on the above-described impurity response especially regarding the quasiparticles, i.e., Bose polarons, properties we subsequently construct effective descriptions to capture the dynamics of the two dressed impurities. To this end, we restrict ourselves to final intercomponent interactions being comparable with the intracomponent bath coupling $g_{AA} = 0.2$, see, in particular, Figs. 2(a1)–2(a4) and 2(b1)–2(b4), such that the impurities reside within the medium.

B. Effective one-body models

As a first step, we develop the one-body building blocks which are proven to be essential for the effective two-body model to be discussed in Sec. V C. The main idea is to compare the results obtained from the effective model for impurity B (C) to the ones predicted by the appropriate sMF ansatz $|\Psi^{\mathrm{sMF}C}(t)\rangle$ ($|\Psi^{\mathrm{sMF}B}(t)\rangle$). By doing so, the uncorrelated second impurity is seen by the other components only as a mean-field-type potential. Recall that within the sMFB (sMFC) ansatz only correlations between the medium and the impurity B (C) are prohibited which is achieved by requiring $D_A, D_C > 1$ and $D_B = 1$ ($D_A, D_B > 1$ and $D_C = 1$) in the many-body wave-function ansatz of Eq. (3). We choose such sMF ansatzes for calculating the reference many-body wave function to which we will compare the effective model predictions. This choice is already justified by inspecting the corresponding densities evolution within the fully correlated system [Figs. 2(a3) and 2(a4)] which are found to be qualitatively similar with the sMFB (sMFC) results (not shown for brevity). Thereby, we intentionally prohibit at this stage of the analysis the formation of induced correlations between the impurities since these effects are to be captured in a second step within the framework of an effective two-body model (Sec. V C).

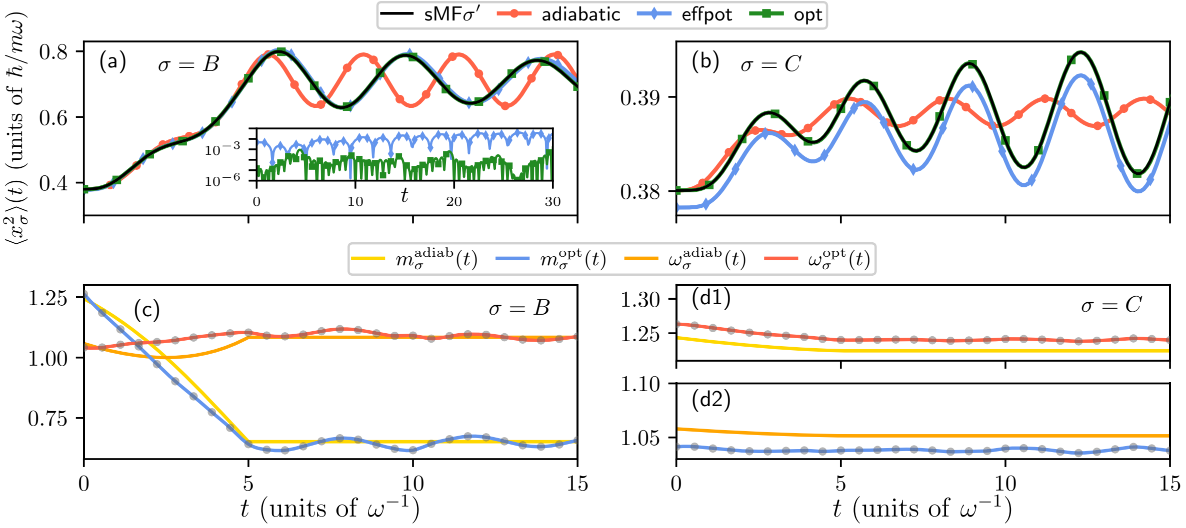

FIG. 3. Dynamics of the position variance for impurity (a) B and (b) C following a linear ramp of $g_{AB}(t)$ from -0.2 to 0.2 within $\tau\omega = 5$ while $g_{AC} = -0.2$ remains constant. The impurity dynamics within the sMFσ', where $\sigma' = C, B$, is compared to three different effective one-body models (see legend) described in the main text. For $t\omega \geqslant 15$, the impurity's position variance obtained within the effective potential model (*effpot*) starts to visibly deviate from the sMFσ' prediction (not shown). However, the variance following the optimization procedure (*opt*) shows adequate agreement with the sMFσ' outcome. For better visualization the inset of panel (a) depicts the relative differences between the variance of sMFσ' and *effpot* (green line) and *opt* (blue line), namely $|\langle x_B^{(2)}\rangle_{\mathrm{sMF}\sigma'} - \langle x_B^{(2)}\rangle_{\mathrm{effpot}}|/\langle x_B^{(2)}\rangle_{\mathrm{sMF}\sigma'}$ and $|\langle x_B^{(2)}\rangle_{\mathrm{sMF}\sigma'} - \langle x_B^{(2)}\rangle_{\mathrm{opt}}|/\langle x_B^{(2)}\rangle_{\mathrm{sMF}\sigma'}$, respectively. Both impurities are initially coupled to a weakly interacting, $g_{AA} = 0.2$, bosonic medium containing $N_A = 10$ atoms. Time-dependent effective masses and frequencies of impurity (c) B and (d1), (d2) C used in the *adiabatic* and *optimized* models (see legend).

In the following, we introduce three different one-body models whose purpose is to effectively describe the dynamics of one impurity interacting with the remaining system. This is done exemplarily for the scenario where both impurities are initially attractively coupled to the bath with $g_{AB}^0 = g_{AC}^0 = -0.2$ and then g_{AB} is ramped to $g_{AB}^\tau = 0.2$ within $\tau\omega = 5$, while $g_{AC}(t)$ is held fixed in this case.

1. Effective mass and frequency with an adiabatic ramp

Our first approach to effectively capture the impurity dynamics is to estimate for each time-dependent interaction configuration of the general form $[g_{AB}(t), g_{AC}(t)]$, a corresponding effective mass (m^{eff}) and frequency (ω^{eff}) from the respective ground states of the three-component setting, see Appendix B 1 for details and also Ref. [50]. In this way, it is possible to extract the interaction-dependent effective mass and frequency which will be referred to in the following as $m^{\mathrm{adiab}}(g_{AB}, g_{AC})$, $\omega^{\mathrm{adiab}}(g_{AB}, g_{AC})$. This means that these effective parameters practically describe the adiabatic polaron dynamics, namely, the case where the interaction ramp is performed within long timescales ($\tau \gg 1$) compared to the characteristic ones of the system. As such, the time-dependent effective one-body model characterized by $m_\sigma^{\mathrm{adiab}}[g_{AB}(t), g_{AC}(t)] \equiv m_\sigma^{\mathrm{adiab}}(t)$ and $\omega_\sigma^{\mathrm{adiab}}[g_{AB}(t), g_{AC}(t)] \equiv \omega_\sigma^{\mathrm{adiab}}(t)$, takes the form

$$\hat{H}_\sigma^{(1),\mathrm{adiab}}(t) = -\frac{\partial_x^2}{2m_\sigma^{\mathrm{adiab}}(t)} + \frac{1}{2}m_\sigma^{\mathrm{adiab}}(t)\big(\omega_\sigma^{\mathrm{adiab}}(t)\big)^2 x^2. \quad (6)$$

To testify the validity of $\hat{H}_\sigma^{(1),\mathrm{adiab}}(t)$, where $\sigma = B, C$, we invoke the impurities position variance $\langle x_\sigma^2\rangle(t)$ during the evolution. Specifically, the predictions of $\hat{H}_\sigma^{(1),\mathrm{adiab}}(t)$ and the corresponding sMFσ' ansatz with $\sigma' = C, B$ are demonstrated in Figs. 3(a) and 3(b). For completeness, the behavior of $m_\sigma^{\mathrm{adiab}}(t)$ and $\omega_\sigma^{\mathrm{adiab}}(t)$ is also provided in Figs. 3(c), 3(d1), and 3(d2).

As it can be seen, a rough agreement between the two approaches (adiabatic and species mean field) occurs on the level of the C impurity variance [cf. Fig. 3(b), note here the relatively small scales]. This is expected since only g_{AB} is ramped resulting in a weak dynamical response of the C component. However, the adiabatic effective model fails to qualitatively estimate the dynamics of the B impurity for $t\omega > 5$. This deviation originates from the fact that the chosen ramping time is far from the adiabatic limit, see also the discussion in Appendix A about the impact of τ on the impurities dynamics. Interestingly, however, $\hat{H}_\sigma^{(1),\mathrm{adiab}}(t)$ is able to describe the overall trend of $\langle x_B^2\rangle(t)$ throughout the evolution.

2. Time-dependent effective one-body potential

In the second effective model, we set $m_\sigma^{\mathrm{eff}}(t) = \omega_\sigma^{\mathrm{eff}}(t) = 1$ and consider the mean-field-type contribution of the bosonic medium to the bare one-body Hamiltonian $\hat{h}_\sigma$ appearing in Eq. (1). Here, the medium has the role of an external effective potential [28,34] and the resulting reduced model reads

$$\hat{H}_\sigma^{(1),\mathrm{effpot}}(t) = \hat{h}_\sigma + g_{A\sigma}(t)N_A\rho_A^{(1),\mathrm{sMF}\sigma'}(x,t), \quad (7)$$

where $\sigma = B, C$ and $\sigma' = C, B$. In particular, within this approach the one-body density of the medium is treated as a time-dependent mean-field potential which includes spatial deformations imprinted by the second impurity and it is weighted by the impurity-medium interaction strength $g_{A\sigma}(t)$. In the absence of interspecies correlations, i.e., for a full sMF ansatz, $\hat{H}_{\sigma}^{(1),\text{effpot}}(t)$ models exactly the one-body dynamics of the impurities.

The temporal evolution of $\langle x_{\sigma}^{2}\rangle(t)$ obtained from $\hat{H}_{\sigma}^{(1),\text{effpot}}(t)$ is presented in Figs. 3(a) and 3(b) for the impurity B and C, respectively. We find that this model captures very well the dynamics of the impurities even though impurity-medium correlation effects are only indirectly taken into account by $\rho_{A}^{(1),\text{sMF}\sigma'}(x,t)$ but are otherwise neglected [93]. This observation suggests that at these timescales and g_{AB} interactions the impact of AB entanglement on the spatial variance is suppressed. However, for longer timescales, i.e., for $t\omega\sim 30$, we observe that the effective potential model cannot adequately capture the characteristics of the oscillatory behavior of $\langle x_{B}^{2}\rangle(t)$ obtained via the sMFC method [see the inset in Fig. 3(a)]. This discrepancy underlines the importance of the impurity-medium correlation effects for the accurate description of the dynamics at least for longer timescales and for the present interaction quench. In contrast, the agreement on $\langle x_{C}^{2}\rangle(t)$ is to a good degree anticipated since g_{AC} retains its initial value. We have also confirmed that upon considering smaller ramping times, i.e., approaching the sudden quench scenario, the deviations among the predicted position variances take place at smaller timescales which is traced back to the larger amount of excitations induced by the quench.

3. *Time-dependent optimization of the effective mass and frequency*

The structure of the third effective model corresponds to the one given by Eq. (6). However, instead of the effective mass and frequency measured from the (adiabatically followed) ground state (or equivalently the adiabatic ramp), here they are acquired by following a time-dependent optimization method. Hence, $m_{\sigma}^{\text{adiab}}(t)$ and $\omega_{\sigma}^{\text{adiab}}(t)$ are replaced by $m_{\sigma}^{\text{opt}}(t)$ and $\omega_{\sigma}^{\text{opt}}(t)$ in Eq. (6). We refer to the respective optimized one-body Hamiltonian as $\hat{H}_{\sigma}^{(1),\text{opt}}(t)$.

The optimization process is initiated by solving the time-dependent one-body Schrödinger equation for $\hat{H}_{\sigma}^{(1),\text{opt}}(t)$ where the paths of $m_{\sigma}^{\text{opt}}(t)$ and $\omega_{\sigma}^{\text{opt}}(t)$ are dictated by a set of initial interpolation points. Meanwhile, a cost function $c_{\text{opt}}^{\text{1body}}$ (see below) is evaluated determining the quality of the effective wave function. Then, a gradient-based optimization algorithm [94,95] determines a new set of interpolation points for the paths $m_{\sigma}^{\text{opt}}(t)$ and $\omega_{\sigma}^{\text{opt}}(t)$ leading to a new value of the cost function. This procedure is repeated until further varying the interpolation points does not improve the overlap of the effective and many-body wave functions (see also Appendix C). For our purposes, we choose the cost function $c_{\text{opt}}^{\text{1body}}=\frac{1}{N_t}\sum_{i=1}^{N_t}[|\langle x_{\sigma}^{2}\rangle_{\text{sMF}\sigma'}(t_i)-\langle x^{2}\rangle_{\text{eff}}(t_i)|/\langle x_{\sigma}^{2}\rangle_{\text{sMF}\sigma'}(t_i)+\int dx|\rho_{\sigma}^{(1),\text{sMF}\sigma'}(x,t_i)-\rho_{\text{eff}}^{(1)}(x,t_i)|^{2}]$, where $t_{i+1}-t_i=0.1$ denotes the time step and N_t is the total number of timesteps. An optimization routine varies then the interpolation points such that the cost function becomes minimal.

By applying this procedure, we enforce the time-dependent wave function of the effective model to match the one of the many-body Hamiltonian (here extracted within the sMFC method). By design, this process leads to a quantitatively excellent agreement among the two approaches as exemplarily shown for the respective impurities position variances in Figs. 3(a) and 3(b). The extracted time-dependent behavior of $m_{\sigma}^{\text{opt}}(t)$ and $\omega_{\sigma}^{\text{opt}}(t)$ using $N_{\text{interp}}=28$ is illustrated in Figs. 3(c), 3(d1), and 3(d2). It becomes apparent that both $m_{\sigma}^{\text{opt}}(t)$ and $\omega_{\sigma}^{\text{opt}}(t)$ resemble to a certain degree $m_{\sigma}^{\text{adiab}}(t)$ and $\omega_{\sigma}^{\text{adiab}}(t)$ but they also exhibit additional time-dependent features caused by the quench and not captured by the adiabatic dynamics. In particular, the optimized parameters $m_{\sigma}^{\text{opt}}(t)$ and $\omega_{\sigma}^{\text{opt}}(t)$ depicted in Fig. 3(c) fluctuate at times $t\geqslant\tau$ around the constant values of $m_{\sigma}^{\text{adiab}}(t)$ and $\omega_{\sigma}^{\text{adiab}}(t)$. These additional dynamical features of the optimized parameters unveil the nonadiabatic time evolution of the system after the interaction ramp. They are intuitively expected since the interaction ramp imposes a breathing-type motion on the different species (cf. Fig. 2 where the complete many-body wave function is employed) and thus time-dependent effective parameters are required for an accurate description. Moreover, in the case of the B impurity, and in both the adiabatic and optimized approaches, the effective mass decreases with time while the frequency slightly increases. This behavior is attributed to the presence of the harmonic trap and it is in accordance with Refs. [28,91]. Here, the postquench repulsive impurity-medium coupling leads to a gradual delocalization of the impurity towards the trap edges in the course of the evolution. This can also be inferred from the apparent increase of the impurity's position variance. In this sense, the effective mass decreases [50] since the impurity's dressing is reduced.

However, a time-dependent quench from repulsive to attractive impurity-medium interactions leads to the inverse behavior, i.e., to the gradual increase of the effective mass during the evolution (not shown). Note, in passing, that in homogeneous setups an increase of effective mass should be expected as described in Refs. [96,97]. We also remark that this optimization method is able to effectively capture arising correlation effects emerging at longer timescales imprinted, for instance, as modulations in the time-dependent effective mass and frequency.

C. Effective two-body models

The success of the one-body effective description (especially with the optimization process) to estimate the effective mass and frequency of the generated polaron during the evolution motivates the consecutive investigation of the two noninteracting impurities dynamics. This process is, of course, more involved due to the occurrence of induced correlations and for this reason their effective interaction potential needs to be carefully chosen. As such, the effective two-body model has the form

$$\hat{H}^{(2),\text{eff}}(t)=\hat{H}_{B}^{(1),\text{opt}}(t)+\hat{H}_{C}^{(1),\text{opt}}(t)+\hat{V}_{BC}^{\text{int}}(t). \quad (8)$$

In this expression, the time evolution of each polaron separately is described by $\hat{H}_{\sigma}^{(1),\text{opt}}(t)$ incorporating $m_{\sigma}^{\text{opt}}(t)$ and $\omega_{\sigma}^{\text{opt}}(t)$, see also Sec. V B 3, while induced impurity-impurity interactions are captured via the interaction potential $\hat{V}_{BC}^{\text{int}}(t)$. Below, we elaborate on the applicability of three different forms of this time-dependent two-body effective potential by comparing with the many-body results obtained within the

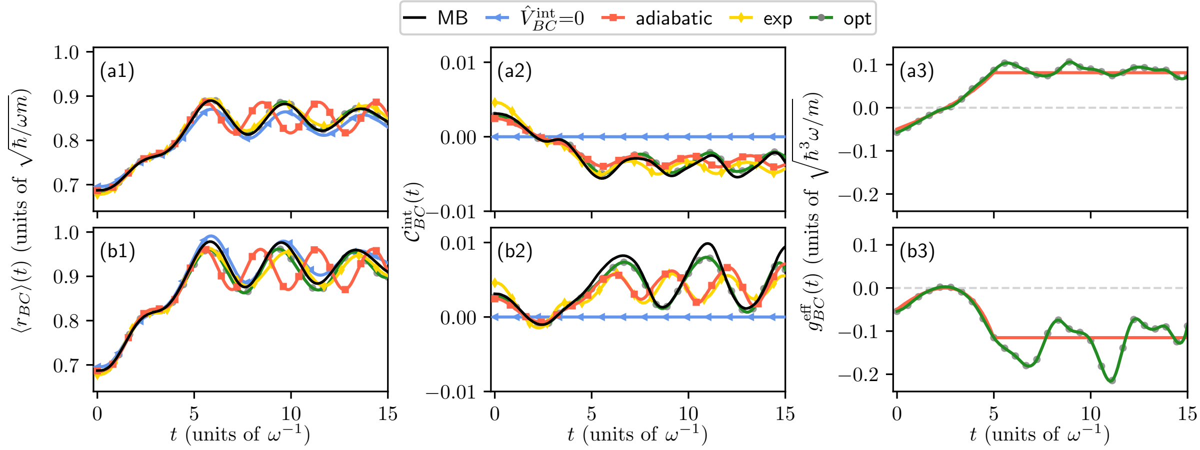

FIG. 4. Comparison of three effective two-body models (see main text) to the many-body dynamics (labeled as *MB*) of two distinguishable and noninteracting impurities B and C coupled to a weakly interacting bosonic medium with $N_A = 10$ atoms and $g_{AA} = 0.2$. The impurities couple initially attractively to the bath with $(g^0_{AB}, g^0_{AC}) = (-0.2, -0.2)$ and are then linearly ramped within $\tau\omega = 5$ either towards $(g^\tau_{AB}, g^\tau_{AC}) = (0.2, -0.2)$ (top row) or to $(g^\tau_{AB}, g^\tau_{AC} = (0.2, 0.2)$ (bottom row) [cf. arrows in Fig. 1(c)]. The prediction of the different methods are compared with respect to the impurities (a1), (b1) relative distance and (a2), (b2) integrated correlation function. The correlation function features a transition from a correlated to an anticorrelated behavior following the first quench and it remains correlated for the second quench. The time-dependent effective interaction strength used in the *adiabatic* and the *optimized* models are shown in panels (a3), (b3). The gray circles denote the interpolation points of the optimization method and the gray dashed lines mark the noninteracting case, i.e., when $g^{\rm eff}_{BC} = 0$.

full many-body ML-MCTDHX method where all correlations (including induced two-body ones) are considered. To validate the choice of $\hat{V}^{\rm int}_{BC}(t)$ we employ, as case examples, two quench protocols. Namely, the first facilitates the crossover from initially correlated impurities to anticorrelated ones [cf. arrow I in Fig. 1(c)], while in the second case we ramp the impurity-medium interactions between two correlated states [cf. arrow II in Fig. 1(c)].

To justify the necessity of the inclusion of the two-body interaction potential we compare the many-body ML-MCTDHX results to the solutions of $\hat{H}^{(2),\rm eff}(t)$ with $\hat{V}^{\rm int}_{BC}(t) = 0$. For this purpose, we use two representative two-body observables. The first is the impurities relative distance [34,98] defined by

$$\langle r_{BC}\rangle(t) = \frac{1}{N_B N_C}\int {\rm d}x^B {\rm d}x^C |x^B - x^C|\rho^{(2)}_{BC}(x^B, x^C, t), \qquad (9)$$

where the corresponding dynamics for both of the above-described quench protocols and approaches is presented in Figs. 4(a1) and 4(b1). It can be readily seen that the uncoupled model adequately captures the dynamics of $\langle r_{BC}\rangle(t)$ implying that the impact of two-body effects is comparatively small at this level. However, this picture changes drastically when one inspects the integrated impurity-impurity correlation function, $\mathcal{C}^{\rm int}_{BC}(t)$, see Figs. 4(a2) and 4(b2). Indeed, since interparticle correlations are vanishing within the uncoupled model it holds that $\mathcal{C}^{\rm int}_{BC}(t) = 0$, which is in contrast to the predictions of the fully correlated approach. In this later case, the evolution of $\mathcal{C}^{\rm int}_{BC}(t)$ reflects the characteristics of the pre and postquench ground states. In fact, $\mathcal{C}^{\rm int}_{BC}(t)$ transits from a correlated to an anticorrelated behavior for the first quench [Fig. 4(a2)], while it remains positive in the second quench scenario [Fig. 4(b2)] evincing a robust correlated trend. In this sense, these observations set the stage for searching a suitable two-body interaction potential.

1. Two-body potential with effective interactions from the adiabatic ramp

Here, $\hat{V}^{\rm int}_{BC}(t)$ contains an effective impurity-impurity coupling that is estimated (as in Sec. V B 1) from each ground-state configuration encountered along the corresponding adiabatic path of the linear ramp protocol. To determine these effective couplings $g^{\rm adiab}_{BC}(g_{AB}, g_{AC})$, we demand the matching of the two-body correlation functions among the static effective model and the ground state (or equivalently the adiabatic solution) of the many-body method, see details in Appendix B 2. In this sense, we refer to the effective two-body model based on the adiabatic approximation as $\hat{H}^{(2),\rm adiab}(t)$ and set $\hat{V}^{\rm int}_{BC}(t) = g^{\rm adiab}_{BC}(t)\delta(x^B - x^C)$.

The quench-induced dynamics of either $\langle r_{BC}\rangle(t)$ [Figs. 4(a1) and 4(b1)] or $\mathcal{C}^{\rm int}_{BC}(t)$ [Figs. 4(a2) and 4(b2)] shows an adequate agreement between the effective approach and the many-body method for $t \lesssim \tau$. However, deviations exist at later evolution times especially so in the case that both impurity-medium interactions are ramped up. These aberrations partly stem from the fact that the applied interaction ramp cannot be considered to be adiabatic. Therefore, also the rather complex dynamics of the induced correlations after the quench is unlikely to be well captured by $g^{\rm adiab}_{BC}(t)$, which for these times is constant [Figs. 4(a3) and 4(b3)]. It is also interesting to note here that the effective interaction exhibits a complementary behavior to the correlation function. For instance, as expected from the ground state, attractive effective interactions go in sync with the correlated two-body behavior and vice versa.

2. Exponential interaction potential

As a second attempt for modeling the impurities effective two-body interaction potential we consider an exponential Yukawa-type potential. Such an interaction potential has been used to describe the induced interaction in the ground state of polarons with a homogeneous background in Refs. [21,36,40,41,46], but has also been recently applied to the case of a harmonically trapped medium [50]. It reads

$$\hat{V}_{BC}^{\mathrm{int}}(r_{BC},t) = -\frac{g_{AB}(t)g_{AC}(t)m_A}{\sqrt{\gamma}}e^{-2r_{BC}/\xi_A}, \tag{10}$$

where $r_{BC} = |x^B - x^C|$ denotes the impurities' distance and $\gamma = m_A g_{AA}/[N_A \rho_A^{(1)}(0)]$. Here, the time dependence is inherited by the linearly ramped coupling parameters $g_{AB}(t)$ and $g_{AC}(t)$. Furthermore, it is required that $r_{BC} \lesssim \xi_A$ meaning that the impurities' distance should be comparable to the healing length of the medium $\xi_A \approx 1/\sqrt{2m_A g_{AA} N_A \rho_A^{(1)}(0)} \approx 0.7$.

Substituting $\hat{V}_{BC}^{\mathrm{int}}(r_{BC},t)$ in Eq. (8) we construct the effective two-body Hamiltonian dubbed $\hat{H}^{(2),\mathrm{exp}}(t)$. This is numerically solved to extract $\langle r_{BC}\rangle(t)$ and $\mathcal{C}_{BC}^{\mathrm{int}}(t)$, which are subsequently compared to the predictions of the ML-MCTDHX method, see Figs. 4(a1) and 4(b1). It can be deduced that $\hat{H}^{(2),\mathrm{exp}}(t)$ is indeed able to qualitatively describe the evolution of the impurities' relative distance for both quenches much better than $\hat{H}^{(2),\mathrm{adiab}}(t)$. Regarding $\mathcal{C}_{BC}^{\mathrm{int}}(t)$, the $\hat{H}^{(2),\mathrm{exp}}(t)$ approach shows a similar behavior as $\hat{H}^{(2),\mathrm{adiab}}(t)$. This means a qualitative good agreement with the many-body evolution for $t \lesssim \tau$ and a growing deviation at longer times. Still, it appears that the nonlocal character of the applied interaction potential plays a crucial role and captures the oscillation frequency of the relative distance during the evolution much better when compared to the adiabatic approach. Deviations observed for longer times are partially traced back to the fact that after the quench this potential is static and hence cannot account for dynamical deformations that exist.

3. Time-dependent optimization of the contact interaction potential

The third approach to estimate the effective strength of the impurities induced interactions is to follow an optimization procedure similar to the one used in Sec. V B 3 for identifying the polaron effective mass and frequency. This will allow to determine the optimal time-dependent induced coupling $g_{BC}^{\mathrm{opt}}(t)$ by minimizing the cost function of the two-body impurity correlations. Here, the effective Hamiltonian $\hat{H}^{(2),\mathrm{opt}}(t)$ [Eq. (8)] encapsulates the interaction potential $\hat{V}_{BC}^{\mathrm{int}}(t) = g_{BC}^{\mathrm{opt}}(t)\delta(x^B - x^C)$, where $g_{BC}^{\mathrm{opt}}(t)$ is represented by a finite set of interpolation points N_{interp}.[3] Specifically, considering an initial set of equidistant interpolation points we evaluate the cost function $c_{\mathrm{opt}}^{\mathrm{2body}} = \frac{1}{N_t}\sum_{i=1}^{N_t}\iint \mathrm{d}x^B \mathrm{d}x^C |\mathcal{G}_{BC}(x^B,x^C,t_i) - \mathcal{G}_{BC}^{\mathrm{eff,opt}}(x^B,x^C,t_i)|$ with $\mathcal{G}_{BC}(x^B,x^C,t_i)$ obtained from the full many-body approach. Note that the timesteps $t_{i+1} - t_i = 0.1$ and N_t is the total number of timesteps. Based on the outcome of the value of the cost function a gradient-based optimization routine varies the amplitudes of the time-wise fixed number of interpolation points such that $c_{\mathrm{opt}}^{\mathrm{2body}}$ is minimized. Namely, upon further varying the interpolation points does not lead to a smaller cost value.

The optimized $g_{BC}^{\mathrm{opt}}(t)$ is shown in Figs. 4(a3) and 4(b3) together with $N_{\mathrm{interp}} = 28$ (gray dots). It is evident that the optimized path of $g_{BC}^{\mathrm{opt}}(t)$ agrees well with $g_{BC}^{\mathrm{adiab}}(t)$ for $t \lesssim \tau$. This reflects the equally good description of $\langle r_{BC}\rangle(t)$ and $\mathcal{C}_{BC}^{\mathrm{int}}(t)$ within this time interval [see Figs. 4(a1), 4(b1) and 4(a2), 4(b2), respectively]. Turning to $t > \tau$, where $\mathcal{C}_{BC}^{\mathrm{int}}(t)$ features a more complex behavior only the optimized effective description is able to correctly describe the impurities correlation dynamics since the other effective models (as argued above) neglect certain correlation channels. At this point, it would be instructive to remark that we have also checked the performance of the optimization with respect to a time-dependent exponential interaction potential of the form of Eq. (10). In this case, both the factor and the exponent of the Yukawa-type interaction potential are optimized. Thereby, we find that the respective two-body model yields a similar agreement with the complete many-body ansatz predictions as compared to the effective model characterized by an optimized contact interaction potential. This observation indicates that accounting for the exponential tails of the interaction potential is not decisive for a quantitatively accurate description in the harmonically trapped case. Instead, one has to deploy interaction potentials which depend on both impurity coordinates and not solely on their relative difference [38,99].

Summarizing, it is found that the optimization scheme is able to adequately describe the induced correlation dynamics of the impurities throughout the evolution. An intriguing feature of the time-dependent effective coupling strength is that it exhibits a crossover from attractive to repulsive induced interactions (already known on the ground-state level [50]). This can explain the observed transition of the impurities' two-body correlation from a correlated to an anticorrelated behavior. Another imprint of this interesting induced correlation aspect is the dynamical evolution of the bipartite entanglement, see Sec. VI about similarities of the von Neumann entropy involving the medium and the impurities entanglement. Furthermore, it is interesting to note that a shorter ramp rate may trigger a repeated crossing from induced attraction to repulsion and vice versa. Such a case is investigated in more detail in Appendix E, elaborating also on the expansion coefficients of the impurities' correlation function.

VI. DYNAMICS OF BIPARTITE ENTANGLEMENT MEASURES

The existence of bipartite entanglement among the impurities subsystem with the medium is essential for the buildup of impurities induced correlations mediated by their host. A frequently used measure for estimating the degree of bipartite entanglement of pure states is the von Neumann entropy [80]. To calculate the von Neumann entropy between the medium and the two distinguishable impurities, we express the many-body wave function given by Eq. (3) as a truncated Schmidt decomposition [100,101] of rank $D_s = \min\{D_A, D_B \cdot D_C\}$.

---

[3] N_{interp} determines the accuracy of $g_{BC}^{\mathrm{opt}}(t)$ as briefly discussed in Appendix C.

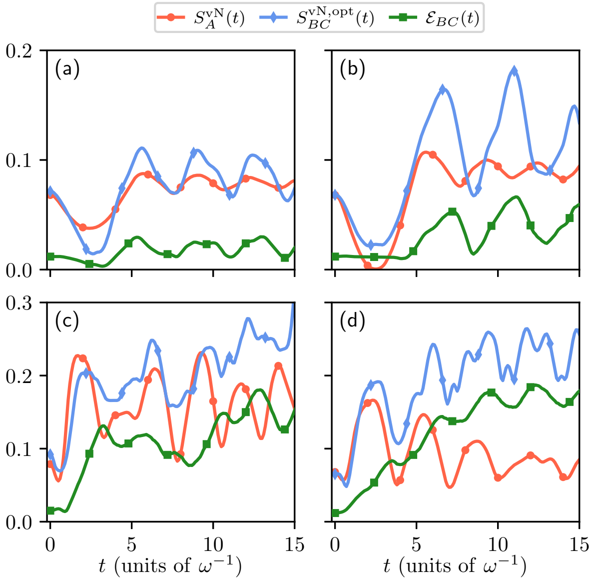

FIG. 5. Dynamical response of the von Neumann entropy quantifying entanglement among the medium and the two impurities subsystems, $S_A^{\rm vN}(t)$, the impurities' logarithmic negativity, $\mathcal{E}_{BC}(t)$, and the von Neumann entropy obtained from the effective two-body wave function $S_{BC}^{\rm vN,opt}(t)$ (see also Sec. VI for further details on the extraction of these observables). Independently of the measure, the impurity-impurity entanglement is finite justifying the presence of induced interactions. To induce the dynamics the impurity-medium interaction strengths are linearly ramped (a) from $(g_{AB}^0, g_{AC}^0) = (-0.2, -0.2)$ to $(g_{AB}^\tau, g_{AC}^\tau) = (0.2, -0.2)$ with rate $\tau = 5$, (b) from $(g_{AB}^0, g_{AC}^0) = (-0.2, -0.2)$ to $(g_{AB}^\tau, g_{AC}^\tau) = (0.2, 0.2)$ with $\tau = 5$, (c) from $(g_{AB}^0, g_{AC}^0) = (-0.2, 0.2)$ to $(g_{AB}^\tau, g_{AC}^\tau) = (0.2, -0.2)$ using $\tau = 1$, and (d) from $(g_{AB}^0, g_{AC}^0) = (-0.2, -0.2)$ to $(g_{AB}^\tau, g_{AC}^\tau) = (-0.2, 0.2)$ with $\tau = 1$.

Namely,

$$|\Psi(t)\rangle = \sum_{i=1}^{D_s} \sqrt{\lambda_i(t)}\,\big|\tilde{\Psi}_i^A\big\rangle \otimes \big|\tilde{\Psi}_i^{BC}\big\rangle, \tag{11}$$

where λ_i are the so-called Schmidt coefficients. These coefficients are the crucial ingredients of the von Neumann entropy which reads

$$S_A^{\rm vN}(t) = -\sum_{i=1}^{D_s} \lambda_i(t) \ln \lambda_i(t). \tag{12}$$

Apparently, $S_A^{\rm vN}(t)$ (or equivalently entanglement) becomes maximal within our Hilbert space truncation if all Schmidt coefficients are equally populated, i.e., $\lambda_i = 1/D_s$. Otherwise, $S_A^{\rm vN}(t)$ vanishes if only one Schmidt coefficient is nonzero implying that the two subsystems are described by a product state. It turns out that due to the hierarchical ordering of the time-dependent Schmidt coefficients for the considered dynamical cases in our setup (not shown for brevity) the maximally allowed entropy (due to truncation) is never reached. In fact, its upper bound lies well above the observed values of the von Neumann entropy shown in Fig. 5.

The time evolution of $S_A^{\rm vN}(t)$ is presented in Fig. 5 where the upper panels show the entanglement following the time-dependent quench protocols discussed in Sec. V C 3 and the lower panels refer to the protocols illustrated in Figs. 8(a1) and 8(b1) discussed in Appendix D. It can be seen that the impurities-medium entanglement [as captured through $S_A^{\rm vN}(t)$] is finite in all cases even at $t = 0$, thus justifying the presence of impurity-impurity induced correlations already from the ground state of the system but also evincing their systematic build-up during the dynamics. Notice also here, for completeness, that the response of $S_A^{\rm vN}(t)$ partially follows the time evolution of the medium's variance $\langle x_A^2\rangle(t)$ and the mean relative distance between the impurities and the medium $[\langle r_{AB}\rangle(t) + \langle r_{AC}\rangle(t)]/2$ (not shown).

However, instead of exploiting the impurities integrated correlation function (to infer the nature of their induced correlations) another possibility to quantify the impurities' entanglement is represented by the so-called logarithmic negativity [102] denoting an entanglement monotone [103]. It measures the bipartite entanglement of a mixed state and has been already successfully applied, e.g., in Refs. [50,64,104–108]. To compute this observable, we first trace out the medium's (subsystem A) degrees of freedom from $|\Psi(t)\rangle\langle\Psi(t)|$. This process leads to a two-component density matrix describing the impurities' subsystem

$$\begin{aligned}\rho_{BC}^{(2),\rm spec}(t) &= {\rm Tr}_A(|\Psi(t)\rangle\langle\Psi(t)|) &\text{(13a)}\\ &= \sum_{jkmn}\sum_i C_{ijk}(t)C_{imn}^*(t)\\ &\quad\times \big|\Psi_j^B(t)\big\rangle\big\langle\Psi_m^B(t)\big| \otimes \big|\Psi_k^C(t)\big\rangle\big\langle\Psi_n^C(t)\big|, &\text{(13b)}\end{aligned}$$

where $|\Psi_j^B\rangle$ and $|\Psi_k^C\rangle$ denote the species functions of impurity B and C, respectively, while $C_{ijk}(t)$ are the time-dependent expansion coefficients. If the impurity B is not entangled with C then the two-component mixture is separable and the eigenvalues of the partially transposed two-component density matrix, $(\rho_{BC}^{(2),\rm spec}(t)|_{jkmn})^{T_B} = \rho_{BC}^{(2),\rm spec}(t)|_{mkjn}$, are always positive. This is known as the positive partial transpose (PPT) criterion [80,109]. As such, one pathway to reveal the presence of entanglement is to search for negative eigenvalues[4] in the spectrum of $(\rho_{BC}^{(2),\rm spec}(t)|_{jkmn})^{T_B}$ [110,111]. Accordingly, the presence of bipartite entanglement is testified by the logarithmic negativity

$$\mathcal{E}_{BC}(t) = \log_2[1 + 2\mathcal{N}(t)], \tag{14}$$

where $\mathcal{N}$ refers to the sum of the negative eigenvalues of $(\rho_{BC}^{(2),\rm spec}(t)|_{jkmn})^{T_B}$ multiplied by (-1).

An alternative way to estimate impurities bipartite entanglement is via the von Neumann entropy that is calculated from the two-body wave function obtained by solving the effective two-body model within the optimization procedure as described in Sec. V C 3. The resulting time-dependent wave

---

[4] Note that the reverse case, i.e., the presence of entanglement leads to negative eigenvalues of $\rho_{BC}^{(2),\rm spec}(t)$, is only true for small dimensions, namely (2×2) or (2×3), of $\rho_{BC}^{(2),\rm spec}(t)$ which does not apply here [109].

function is a pure state from which the von Neumann entropy denoted by $S_{BC}^{\mathrm{vN,opt}}(t)$ can be extracted via Eq. (12). The two measures describing the impurities induced entanglement, i.e., $\mathcal{E}_{BC}(t)$ and $S_{BC}^{\mathrm{vN,opt}}(t)$ are shown in Fig. 5. We observe that both measures exhibit a qualitative similar oscillatory dynamics and are, therefore, both capable of providing adequate information about the induced bipartite entanglement between the impurities. Another interesting observation can be made by comparing the dynamics of $S_A^{\mathrm{vN}}(t)$, i.e., the entanglement between the medium and the impurities, with the behavior of the impurity-impurity entanglement captured by $S_{BC}^{\mathrm{vN,opt}}(t)$ and $\mathcal{E}_{BC}(t)$ for the interaction ramps presented in Figs. 5(a)–5(c). It is evident that an increase (decrease) of the induced entanglement among the impurities is accompanied by a similar increasing (decreasing) trend of the impurity-medium correlations. This hints to an indirect relation between the respective types of entanglement. However, in Fig. 5(d) we find opposite trends between the impurities-medium and the impurity-impurity entanglements. This can be attributed, in part, to the fact that, in this case, the impurity-medium interaction remains intact.

We also remark that a similar qualitative behavior between $S_A^{\mathrm{vN}}(t)$ and the impurity-medium relative distance $[\langle r_{AB}\rangle(t) + \langle r_{AC}\rangle(t)]/2$ as well as among $S_{BC}^{\mathrm{vN,opt}}(t)$ and the impurities' relative distance $\langle r_{BC}\rangle(t)$ is observed for times $t > \tau$ (not shown for brevity). However, to develop a better understanding on the link between the dynamical response of $S_A^{\mathrm{vN}}(t)$ and $S_{BC}^{\mathrm{vN,opt}}(t)$ with the aforementioned relative distances more systematic studies (both numerically covering the available parametric space and analytically whenever possible) on the relevant measures are certainly required. Along the same lines, another interesting future research direction would be the systematic study of the interplay between the impurity-medium entanglement and the induced impurity-impurity entanglement.

VII. CONCLUSION AND PERSPECTIVES

We studied the validity of various one- and two-body effective models for describing the dynamical response of two noninteracting distinguishable impurities immersed in a bosonic medium. This is achieved by a direct comparison to the predictions of a full many-body numerical approach at parameter regions where analytical solutions are absent. The composite three-component system is confined in an external harmonic trap and it is restricted in one dimension. Due to the noninteracting nature of the impurities correlations among them are solely induced by their medium, while their dressing by the excitations of the bosonic host leads to the formation of Bose polarons.

As a first step, we categorize the emergent induced correlation regimes between the impurities, appearing in the system's ground state, for varying the individual impurity-medium couplings. In this sense, it is possible to associate that an induced correlated (anticorrelated) behavior as captured by the impurities integrated correlation function occurs for positive (negative) values of the product of the impurities-medium interactions. The knowledge of the above-correlated patterns serves as a guide for triggering the dynamics by using linear impurity-medium interaction ramps between distinct or within the same correlation regimes.

Specifically, to identify the effective mass and frequency of the Bose polaron we consider the case where one of the impurities interacts only in a mean-field manner with the medium while the other one can become correlated with its host. Here, three different one-body models were constructed. The first is based on the assumption of adiabatically ramping up the interaction such that the system instantaneously follows its ground-state configuration. Within the second model the host plays the role of an external time-dependent mean-field potential to the impurity. Finally, for the third reduced approach a time-dependent optimization routine is employed. According to the optimization routine, the time-dependent effective mass and frequency are fitting parameters ensuring that characteristic one-body observables predicted in the effective model match the ones obtained in the many-body method. This time-dependent optimized model leads to the most accurate description of the polaron characteristics.

The estimation of each polaron effective mass and frequency is crucial for understanding the impurities induced correlations. This is accomplished by an effective two-body model, which for each impurity combines the appropriate optimized effective one-body model and additionally includes a two-body interaction potential. This potential is modeled either through a time-dependent exponentially decaying interaction term or a contact interaction potential whose coupling is obtained either via an adiabatic interaction ramp or by following an optimization scheme. We find that, similarly to the one-body case, the optimized effective two-body model provides the best agreement with the impurities time-evolved correlation function predicted within the many-body approach. Moreover, we showcase the presence of finite impurity-medium and impurity-impurity entanglement by calculating the corresponding von Neumann entropy and logarithmic negativity using a decomposition of the effective two-body impurities wave function.

Our results pave the way for future studies aiming to reduce the dynamics of a complex highly particle-imbalanced many-body system into effective one- or two-body models and ultimately engineer the polaron characteristics and induced correlations. This knowledge might be also proven useful for relevant extensions to higher dimensions. Possible future directions include, for instance, the treatment of mass-imbalanced three-component settings where either two heavy impurities are coupled to a lighter bosonic medium or the distinguishable impurities have different masses. Especially in the later case, understanding the interplay of the effective mass with the induced interactions would be worth pursuing. Another interesting extension is to consider species selective trapping geometries such as a homogeneous or lattice trapped bath.

ACKNOWLEDGMENTS

The authors would like to thank I. Englezos, K. Goswami, and A. Siemens for valuable discussions. S.I.M. is supported by the University of Missouri Science and Technology, Department of Physics, Startup fund.

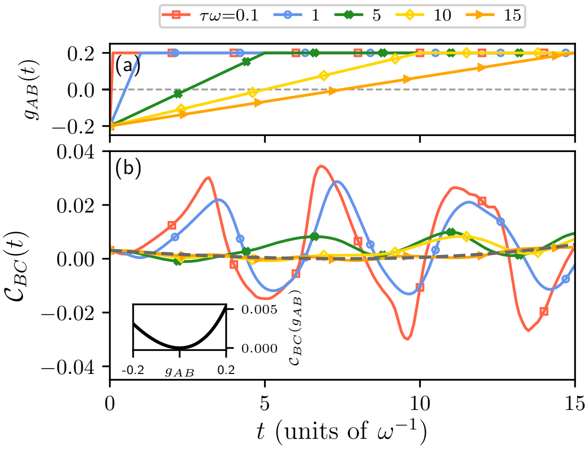

FIG. 6. (a) Dependence on the ramp rate of the linear impurity-medium interaction quench protocol from $g^0_{AB} = g^0_{AC} = -0.2$ to $g^\tau_{AB} = g^\tau_{AC} = 0.2$. (b) Time evolution of the impurities induced correlations described by their integrated correlation function $\mathcal{C}_{BC}(t)$ [Eq. (5)]. Inset of panel (b) depicts the corresponding adiabatic evolution of $\mathcal{C}_{BC}(t)$ following the above protocol when $\tau \to \infty$, which also appears as a gray dashed line in the main panel. An excellent agreement with the linear quench characterized by a rate $\tau\omega = 15$ is observed. The system consists of two distinguishable noninteracting B and C impurities immersed in a bosonic medium with $N_A = 10$ and $g_{AA} = 0.2$.

APPENDIX A: IMPACT OF THE RAMP RATE

In the following, we explicate the effect of the ramp rate τ of the linear interaction quench [Eq. (2)] on the resulting induced correlation dynamics as captured by $\mathcal{C}_{BC}(t)$ [see Eq. (5)]. For this investigation, we invoke a paradigmatic quench protocol, namely, ramping the impurity-medium couplings from $g^0_{AB} = g^0_{AC} = -0.2$ to $g^\tau_{AB} = g^\tau_{AC} = 0.2$ for various τ as illustrated in Fig. 6(a). Notice that a similar phenomenology occurs also for other postquench interactions not shown for brevity.

The emergent time evolution of the impurities integrated correlation function, $\mathcal{C}_{BC}(t)$, is demonstrated in Fig. 6(b). As expected, we observe that relatively small ramp rates, i.e., $\tau\omega = 0.1, 1$, lead to the most pronounced dynamical response of $\mathcal{C}_{BC}(t)$ manifested by its enhanced amplitude oscillatory behavior. However, induced correlations appear to be weaker when using longer ramp rates. A such, it is possible to infer that for an increasing quench rate, e.g., $\tau\omega = 15$ in Fig. 6(b), the correlation dynamics approaches its ideal adiabatic behavior which practically refers to $\tau \to \infty$. Indeed, during its adiabatic evolution the system remains always in its ground state and hence the respective $\mathcal{C}_{BC}$ is equivalent to the corresponding static solution characterized by specific g_{AB}, g_{AC} (or for the employed quench protocol only by g_{AB}). The $\mathcal{C}_{BC}$ of the ground-state system configurations passing through the respective adiabatic evolution can be seen in the inset of Fig. 6(b) and also in the main panel of Fig. 6(b) as a dashed gray line. It becomes apparent that it nearly coincides with $\mathcal{C}_{BC}(t)$ for $\tau\omega = 15$ further verifying the approach to the adiabatic limit. Therefore, the rates of $\tau\omega = 1$ and 5 which are employed in the main text induce a more prominent dynamical response that is closer to the sudden quench scenario.

APPENDIX B: DETERMINATION OF THE GROUND-STATE EFFECTIVE PARAMETERS

1. Effective mass and frequency of the one-body model

The effective mass and frequency of the ground-state Bose polaron [50] are calculated as follows. The system of two distinguishable and noninteracting impurities coupled to a bosonic medium is numerically solved within a species mean-field ansatz (Sec. III). This accounts only for the correlations of one impurity with the bath, while the other impurity acts as a mean-field potential. Afterwards, we determine the effective mass and frequency of the impurity $\sigma = B$ (C) for a specific (g_{AB}, g_{AC}) combination. This is done by fitting the energy and position variance predicted by the effective one-body model

$$\hat{H}^{(1)}\left(m^{\text{eff}}_\sigma, \omega^{\text{eff}}_\sigma\right) = -\frac{\partial^2_x}{2m^{\text{eff}}_\sigma} + \frac{1}{2}m^{\text{eff}}_\sigma\left(\omega^{\text{eff}}_\sigma\right)^2 x^2, \tag{B1}$$

to the ones evaluated by the suitable species mean-field ansatz. Thereby, the effective mass and frequency $(m^{\text{eff}}_\sigma, \omega^{\text{eff}}_\sigma)$ are chosen such that the cost function $c^{\text{1body}}_{\text{gs}} = \Delta E_\sigma + \Delta x^2_\sigma$ becomes vanishingly small of the order of 10^{-9}. Here, $\Delta E_\sigma = |E^{\text{sMF}\sigma'}_\sigma - E^{\text{eff}}_\sigma|^2$ is the difference between the energy of the effective one-body model E^{eff}_σ and the energy of the impurity-bath system described by the appropriate species mean-field ansatz. Namely, $E^{\text{sMF}\sigma'}_\sigma = \langle\Psi^{\text{sMF}\sigma'}|\hat{h}_\sigma|\Psi^{\text{sMF}\sigma'}\rangle$, where $\sigma' = C$ (B) and $\hat{h}_\sigma$ is the one-body Hamiltonian appearing in Eq. (1). Likewise, we define $\Delta x^2_\sigma = |\langle x^2_\sigma\rangle_{\text{sMF}\sigma'} - \langle x^2_\sigma\rangle_{\text{eff}}|^2$.

2. Effective two-body interaction strength of the two-body model

Having at hand the effective mass and frequency of the polaron it is possible to also find the impurities' effective interaction strength for each interaction configuration (g_{AB}, g_{AC}). Here, one should rely on the time-independent version of the effective two-body model of Eq. (8). Then, the only free parameter is the effective contact interaction strength g^{eff}_{BC}, appearing in $\hat{V}^{\text{int}}_{BC}(t) = g^{\text{eff}}_{BC}\delta(x^B, x^C)$ [Eq. (8)]. The value of g^{eff}_{BC} is the one which minimizes the cost function $\Delta\mathcal{G}_{BC} = \iint dx^B dx^C |\mathcal{G}_{BC}(x^B, x^C) - \mathcal{G}^{\text{eff,gs}}_{BC}(x^B, x^C)|^2$. In this expression, $\mathcal{G}^{\text{eff,gs}}_{BC}(x^B, x^C)$ $[\mathcal{G}_{BC}(x^B, x^C)]$ is the impurity-impurity correlation function [Eq. (4)] obtained with the effective (full many-body) approach. To calculate the static two-body solution in the effective model we expand the two-body wave function in terms of one-body states and diagonalize the respective two-body Hamiltonian (known as the exact diagonalization method).

APPENDIX C: CONVERGENCE BEHAVIOR OF THE APPLIED OPTIMIZATION ROUTINE

The convergence behavior of the optimization routine used to determine the time-dependent effective mass and frequency of the polaron as well as the effective coupling of two distinguishable polarons (Secs. V B 3 and V C 3) depends on the

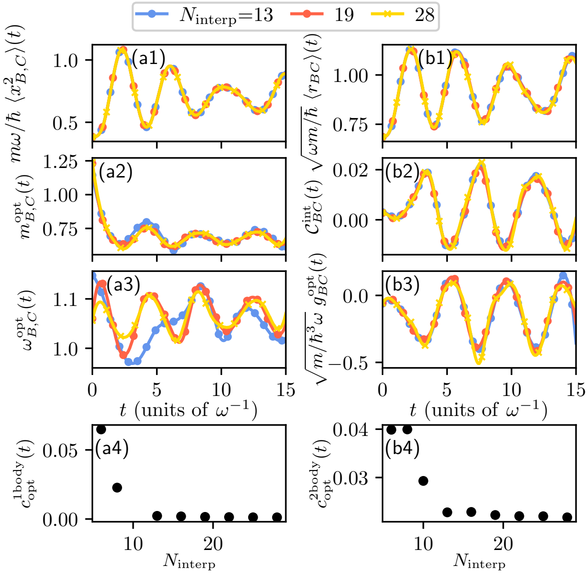

FIG. 7. Convergence study of different observables extracted from (a1)–(a4) the optimized one-body model as well as (b1)–(b4) the optimized two-body model. (a1)–(a3) Dynamical evolution of the variance, effective mass, and frequency, respectively, for a varying number of interpolation points used in the optimization procedure (see Sec. V B 3). (b1)–(b3) Time evolution of the impurities' relative difference, integrated correlation function, and effective induced interaction, respectively, obtained within the optimization routine described in Sec. V C 3. (a4), (b4) Cost value of the optimized one- and two-body effective model, respectively, in dependence of the number of interpolation points. We consider two noninteracting impurities coupled to a bosonic medium with $N_A = 10$ atoms interacting among each other with $g_{AA} = 0.1$. The dynamics is induced by ramping the impurity-medium interaction strengths at the same time from $g^0_{AB} = g^0_{AC} = -0.2$ to $g^\tau_{AB} = g^\tau_{AC} = 0.2$ within a ramp time of $\tau\omega = 1$.

number of interpolation points N_{interp}. This effect is demonstrated in Fig. 7 for linear interactions ramps from $g^0_{AB} = g^0_{AC} = -0.2$ to $g^\tau_{AB} = g^\tau_{AC} = 0.2$ within $\tau = 1$. In both optimization routines the aim is to approach the time-dependent path for which the observables of interest do not change, at least to a certain accuracy, by successively increasing N_{interp}. Simultaneously, the cost functions $c^{\text{1body}}_{\text{opt}}$ and $c^{\text{2body}}_{\text{opt}}$ (Secs. V B 3 and V C 3) should exhibit a decreasing trend for larger N_{interp}.

Inspecting the convergence behavior of the optimized effective mass and frequency, shown in Figs. 7(a2) and 7(a3), we can infer numerical convergence of the individual observables with the optimization method for $N_{\text{interp}} > 19$. It is worth mentioning here that the cost function $c^{\text{1body}}_{\text{opt}}$ saturates already for $N_{\text{interp}} > 12$ [Fig. 7(a4)], and the same holds for the respective variance $\langle x^2_{B,C}\rangle(t)$ in Fig. 7(a1). Thus, in such studies it is important to ensure convergence not only of the cost function but also of the effective parameters and the observables of interest. The same behavior can be also observed when inspecting the results obtained by optimizing the effective interaction strength, shown in Figs. 7(b1)–7(b4). However, here $c^{\text{2body}}_{\text{opt}}$ saturates at a finite value even upon considering a larger number of interpolation points as shown here. This implies that we reached the limitation of the optimization procedure for higher-order observables.

APPENDIX D: VALIDITY OF THE OPTIMIZATION METHOD INDEPENDENTLY OF THE QUENCH PROTOCOL

Let us demonstrate the applicability of the employed optimization routines (outlined in Secs. V B 3 and V C 3) irrespective of the used interaction ramp. Exemplary time-dependent interaction ramps of $g_{AB}(t)$ and $g_{AC}(t)$ are illustrated in Figs. 8(a1)–8(e1). The respective temporal evolution of the integrated correlation function obtained from the full many-body method $\mathcal{C}^{\text{MB}}_{BC}(t)$, and the one calculated from the two-body optimization routine with the aid of the reduced two-body model described in Sec. V C 3, $\mathcal{C}^{\text{opt}}_{BC}(t)$, is presented in Figs. 8(a2)–8(e2). Of course, preceding this two-body optimization routine, we estimated the underlying time-dependent effective mass and frequencies as discussed in Sec. V B 3 (not shown). To ease the visualization of the above observables we invert the sign of $g^{\text{opt}}_{BC}(t)$ such that a positive (negative) value of $\mathcal{C}^{\text{opt}}_{BC}$, associated with correlated (anticorrelated) impurities is accompanied by negative (positive) values of $-g^{\text{opt}}_{BC}(t)$. The quality of the optimization routines is judged by comparing $\mathcal{C}^{\text{opt}}_{BC}(t)$ and $\mathcal{C}^{\text{MB}}_{BC}(t)$. Overall, we find a very good agreement which validates the outcomes of the effective one- and two-body models. We finally remark that in the course of the dynamics quench-induced excitation patterns may be imprinted in the correlation function whose integration could oversimplify such a complex pattern. Still, in the considered cases we find that the integrated correlation function provides a reliable estimate about the impurities induced correlation behavior.

APPENDIX E: DECOMPOSING THE TWO-BODY DYNAMICS

To gain a deeper understanding on the participating microscopic processes responsible for the observed induced impurity-impurity correlation dynamics we shall next carefully inspect the ingredient of the correlation function. As a characteristic case example we focus on interaction ramps from $g^0_{AB} = g^0_{AC} = -0.2$ to $g^\tau_{AB} = g^\tau_{AC} = 0.2$ with rate $\tau\omega = 1$. As it will be showcased below, reducing the ramp rate to $\tau\omega = 1$ triggers a more complex response where induced correlations switch from a correlated to an anticorrelated behavior and vice versa even for $\tau \leqslant t$. As such, this allows to provide a more general argumentation for the behavior of correlations. Snapshots of $\mathcal{G}_{BC}(x^B, x^C; t)$ within the full many-body method at short evolution times are depicted in Figs. 9(a)–9(c). Also, the respective time evolution of the integrated correlation, $\mathcal{C}^{\text{MB}}_{BC}(t)$, is illustrated in Fig. 9(e). The oscillatory trend of $\mathcal{C}^{\text{MB}}_{BC}(t)$ taking positive and negative values indicates the periodic appearance of correlated and anticorrelated patterns which are also evident in the spatially resolved correlation provided in Figs. 9(a)–9(c). We remark that such an oscillatory correlation behavior cannot be observed for larger ramp rates, see Fig. 4(b2) and Appendix A further justifying our choice for the rate.

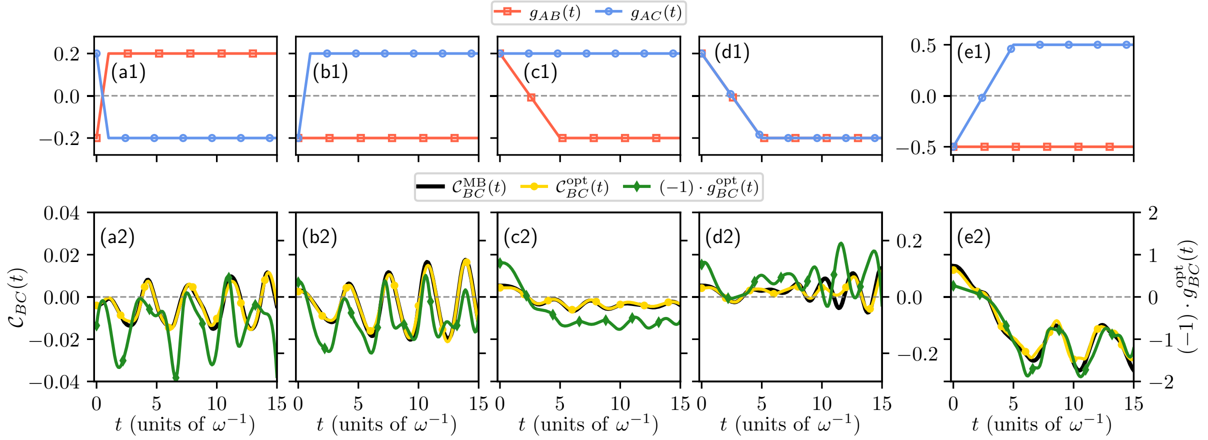

FIG. 8. (a1)–(e1) Schematic representation of different linear impurity-medium interaction ramps characterized by rates (a1), (b1) $\tau\omega = 1$, (c1)–(e1) $\tau\omega = 5$. The initial $(g^0_{AB}, g^0_{AC}) = (\pm 0.2, \pm 0.2)$ and final $(g^\tau_{AB}, g^\tau_{AC}) = (\pm 0.2, \pm 0.2)$ interaction combinations are shown in the panels (a1)–(d1), while in panel (e1) they correspond to $(g^0_{AB}, g^0_{AC}) = (-0.5, -0.5)$ and $(g^\tau_{AB}, g^\tau_{AC}) = (-0.5, 0.5)$. (a2)–(e2) Time evolution of the impurities integrated two-body correlation function within different approaches following the interaction ramps illustrated in panels (a1)–(e1). For comparison, we provide the integrated correlation functions $\mathcal{C}^{\rm opt}_{BC}(t)$ and $\mathcal{C}^{\rm MB}_{BC}(t)$, obtained with the effective optimized two-body model and the full many-body approach (see legend). It becomes evident that the correlation function deduced from the optimization process of the two-body model leads to a very good agreement with the one from the many-body method. In all cases, we consider two noninteracting distinguishable impurities B and C coupled to a bosonic medium of $N_A = 10$ interacting atoms with $g_{AA} = 0.2$.

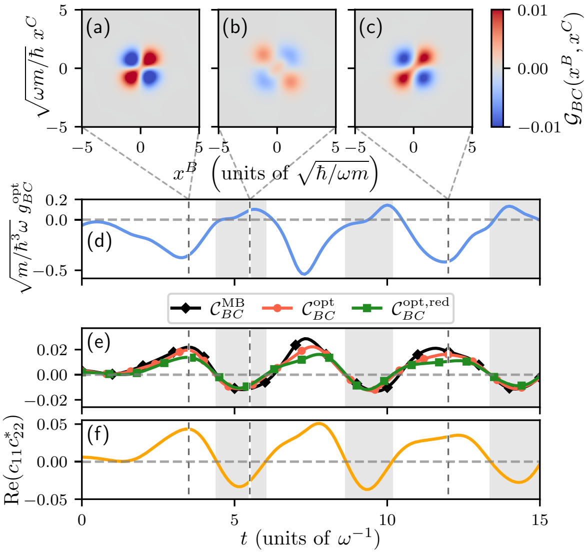

FIG. 9. (a)–(c) Snapshots of the impurity-impurity correlation function $\mathcal{G}_{BC}(x^B, x^C)$, at times $t\omega = 3.5, 5.5, 12$. (d) Time evolution of the effective impurity-impurity induced interaction $g^{\rm opt}_{BC}$, retrieved by fitting a two-body model to the many-body dynamics (Sec. V C 3). (e) Integrated correlation function obtained within the many-body dynamics $\mathcal{C}^{\rm MB}_{BC}$ and the effective two-body model $\mathcal{C}^{\rm opt}_{BC}$ compared to the reduced optimized integrated correlation function $\mathcal{C}^{\rm opt,red}_{BC}$. (f) Real part of the product of expansion coefficients $c_{11}c^*_{22}$ signifying the decisive role of the correlation expansion coefficients in the interpretation of the two-body correlation behavior. In all cases, the two noninteracting impurities B and C are coupled to the bosonic medium with $N_A = 10$ and $g_{AA} = 0.2$. The dynamics is induced by a linear ramp of the impurity-medium coupling from $g^0_{AB} = g^0_{AC} = -0.2$ to $g^\tau_{AB} = g^\tau_{AC} = 0.2$ with rate $\tau\omega = 1$.

To track the induced impurities interactions we deploy their effective two-body optimized description (Sec. V C 3) where the underlying interaction potential contains a time-dependent interaction strength as shown in Fig. 9(d). It can be seen that the resulting integrated correlation function $\mathcal{C}^{\rm opt}_{BC}(t)$ [Fig. 9(e)] agrees qualitatively well with $\mathcal{C}^{\rm MB}_{BC}(t)$. Hence, this effective two-body model captures the aforementioned alternating induced correlation behavior traced back to the alternating sign of the induced interaction strength $g^{\rm opt}_{BC}(t)$, see Fig. 9(d).

The effective two-body wave function can be expressed in terms of the time-dependent single-particle basis of harmonic oscillator eigenstates $|\phi^B_i(t)\rangle$ and $|\phi^C_j(t)\rangle$. These are determined through the optimization scheme yielding the time-dependent polaron effective masses and frequencies, i.e., $m^{\rm opt}_\sigma(t)$ and $\omega^{\rm opt}_\sigma(t)$. As such

$$\left|\Psi^{\rm opt}_{BC}(t)\right\rangle = \sum_{ij} c_{ij}(t)\left|\phi^B_i(t)\right\rangle \otimes \left|\phi^C_j(t)\right\rangle. \tag{E1}$$

Utilizing this wave-function expansion the impurities' two-body optimized correlation function can be approximated as

$$\mathcal{G}^{\rm opt}_{BC}(t) \approx \sum_{ijkl} c_{ij}(t)c^*_{kl}(t)\mathcal{G}^{\rm opt}_{ijkl}, \tag{E2}$$

with

$$\mathcal{G}^{\rm opt}_{ijkl} = \rho^{(2),\rm opt}_{ijkl}(t) - \int \rho^{(2),\rm opt}_{ijkl}(t)\mathrm{d}x^C \int \rho^{(2),\rm opt}_{ijkl}(t)\mathrm{d}x^B. \tag{E3}$$

Here, the matrix elements of the two-body reduced density matrix are given by $\rho^{(2),\rm opt}_{ijkl}(t) = \phi^B_i(t)\phi^C_j(t)\phi^{B,\dagger}_k(t)\phi^{C,\dagger}_l(t)$ and, for simplicity, we dropped the spatial coordinates x^B and x^C. Also, the last term in Eq. (E3) is extracted to eliminate the unconditional probability [see also Eq. (4)]. Notice that by doing this individually in each expansion term $\rho^{(2),\rm opt}_{ijkl}(t)$ of the actual two-body density is already an approximation for $\mathcal{G}_{BC}^{\mathrm{opt}}(t)$ since we obtain the unconditional probability individually for each expansion term instead of retrieving it from the complete two-body density. It turns out that within this simplification

$$\mathcal{G}_{ijkl}^{\mathrm{opt}}(t) = \begin{cases} 0, & i = k \text{ and } j = l, \\ \rho_{ijkl}^{(2),\mathrm{opt}}(t), & \text{else}, \end{cases} \tag{E4}$$

which is a direct consequence of the orthonormality relation of the one-body basis functions. Further integrating $\mathcal{G}_{ijkl}^{\mathrm{opt}}(t)$ according to Eq. (5) yields $\mathcal{C}_{ijkl}^{\mathrm{opt}}(t)$. Here, we numerically identify certain $ijkl$ combinations for which the elements of $\mathcal{C}_{ijkl}^{\mathrm{opt}}(t)$ are suppressed, e.g., for $ijkl = 1113$ where the positive and negative portions of the orbitals building up $\rho_{ijkl}^{(2),\mathrm{opt}}$ cancel each other when integrating. Taking all these findings into account, we find that a good approximation for $\mathcal{C}_{BC}^{\mathrm{opt}}(t)$ is represented by

$$\mathcal{C}_{BC}^{\mathrm{opt,red}}(t) = 2\mathrm{Re}[\mathrm{c}_{11}(\mathrm{t})\mathrm{c}_{22}^{*}(\mathrm{t})]\mathcal{C}_{1122}. \tag{E5}$$

To validate these approximations, the reduced integrated two-body correlation function $\mathcal{C}_{BC}^{\mathrm{opt,red}}(t)$ is shown together with the one obtained from the optimization process in Fig. 9(e). A direct comparison reveals a good qualitative agreement between the two, thus verifying our arguments.

Importantly, within this approximative picture it is possible to trace the origin of the alternating sign of the impurities induced interaction and correlations. This is explained by the time evolution of the $c_{11}(t)c_{22}^{*}(t)$ coefficients which is presented in Fig. 9(f). In particular, notice the gray shaded areas in Figs. 9(d)–9(f) marking the time intervals where $\mathrm{Re}[\mathrm{c}_{11}(\mathrm{t})\mathrm{c}_{22}^{*}(\mathrm{t})] < 0$ which correspond to an anticorrelated impurities behavior and repulsive induced interactions.

---

[1] I. Bloch, J. Dalibard, and W. Zwerger, Rev. Mod. Phys. **80**, 885 (2008).

[2] M. A. Cazalilla, R. Citro, T. Giamarchi, E. Orignac, and M. Rigol, Rev. Mod. Phys. **83**, 1405 (2011).

[3] T. Langen, R. Geiger, and J. Schmiedmayer, Annu. Rev. Condens. Matter Phys. **6**, 201 (2015).

[4] M. Haas, V. Leung, D. Frese, D. Haubrich, S. John, C. Weber, A. Rauschenbeutel, and D. Meschede, New J. Phys. **9**, 147 (2007).

[5] K. Henderson, C. Ryu, C. MacCormick, and M. G. Boshier, New J. Phys. **11**, 043030 (2009).

[6] A. J. Barker, S. Sunami, D. Garrick, A. Beregi, K. Luksch, E. Bentine, and C. J. Foot, J. Phys. B: At. Mol. Opt. Phys. **53**, 155001 (2020).

[7] S. B. Papp, J. M. Pino, and C. E. Wieman, Phys. Rev. Lett. **101**, 040402 (2008).

[8] C.-H. Wu, I. Santiago, J. W. Park, P. Ahmadi, and M. W. Zwierlein, Phys. Rev. A **84**, 011601(R) (2011).

[9] T. Hewitt, T. Bertheas, M. Jain, Y. Nishida, and G. Barontini, Quantum Sci. Technol. **9**, 035039 (2024).

[10] F. Serwane, G. Zürn, T. Lompe, T. B. Ottenstein, A. N. Wenz, and S. Jochim, Science **332**, 336 (2011).

[11] B. J. Lester, Y. Lin, M. O. Brown, A. M. Kaufman, R. J. Ball, E. Knill, A. M. Rey, and C. A. Regal, Phys. Rev. Lett. **120**, 193602 (2018).

[12] T. Sowiński and M. Ángel García-March, Rep. Prog. Phys. **82**, 104401 (2019).

[13] L. D. Landau, Phys. Z. Sowjetunion **3**, 644 (1933).

[14] P. Massignan, M. Zaccanti, and G. M. Bruun, Rep. Prog. Phys. **77**, 034401 (2014).

[15] R. Schmidt, M. Knap, D. A. Ivanov, J.-S. You, M. Cetina, and E. Demler, Rep. Prog. Phys. **81**, 024401 (2018).

[16] N. Spethmann, F. Kindermann, S. John, C. Weber, D. Meschede, and A. Widera, Phys. Rev. Lett. **109**, 235301 (2012).

[17] M.-G. Hu, M. J. Van de Graaff, D. Kedar, J. P. Corson, E. A. Cornell, and D. S. Jin, Phys. Rev. Lett. **117**, 055301 (2016).

[18] N. B. Jørgensen, L. Wacker, K. T. Skalmstang, M. M. Parish, J. Levinsen, R. S. Christensen, G. M. Bruun, and J. J. Arlt, Phys. Rev. Lett. **117**, 055302 (2016).

[19] M. G. Skou, T. G. Skov, N. B. Jørgensen, K. K. Nielsen, A. Camacho-Guardian, T. Pohl, G. M. Bruun, and J. J. Arlt, Nat. Phys. **17**, 731 (2021).

[20] K. Seetharam, Y. Shchadilova, F. Grusdt, M. B. Zvonarev, and E. Demler, Phys. Rev. Lett. **127**, 185302 (2021).

[21] F. Grusdt, N. Mostaan, E. Demler, and L. A. P. Ardila, arXiv:2410.09413.

[22] A. Schirotzek, C.-H. Wu, A. Sommer, and M. W. Zwierlein, Phys. Rev. Lett. **102**, 230402 (2009).

[23] C. Kohstall, M. Zaccanti, M. Jag, A. Trenkwalder, P. Massignan, G. M. Bruun, F. Schreck, and R. Grimm, Nature (London) **485**, 615 (2012).

[24] D. J. McCabe, D. G. England, H. E. L. Martay, M. E. Friedman, J. Petrovic, E. Dimova, B. Chatel, and I. A. Walmsley, Phys. Rev. A **80**, 033404 (2009).

[25] M. Cetina, M. Jag, R. S. Lous, I. Fritsche, J. T. M. Walraven, R. Grimm, J. Levinsen, M. M. Parish, R. Schmidt, M. Knap, and E. Demler, Science **354**, 96 (2016).

[26] V. Pastukhov, Phys. Rev. A **96**, 043625 (2017).

[27] F. Grusdt, G. E. Astrakharchik, and E. Demler, New J. Phys. **19**, 103035 (2017).

[28] S. I. Mistakidis, A. G. Volosniev, N. T. Zinner, and P. Schmelcher, Phys. Rev. A **100**, 013619 (2019).

[29] J. Jager, R. Barnett, M. Will, and M. Fleischhauer, Phys. Rev. Res. **2**, 033142 (2020).

[30] L. A. Peña Ardila and S. Giorgini, Phys. Rev. A **92**, 033612 (2015).

[31] F. Grusdt, R. Schmidt, Y. E. Shchadilova, and E. Demler, Phys. Rev. A **96**, 013607 (2017).

[32] P. Naidon, J. Phys. Soc. Jpn. **87**, 043002 (2018).

[33] D. Huber, H.-W. Hammer, and A. G. Volosniev, Phys. Rev. Res. **1**, 033177 (2019).

[34] S. I. Mistakidis, G. M. Koutentakis, G. C. Katsimiga, T. Busch, and P. Schmelcher, New J. Phys. **22**, 043007 (2020).

[35] S. I. Mistakidis, A. G. Volosniev, and P. Schmelcher, Phys. Rev. Res. **2**, 023154 (2020).

[36] A. Recati, J. N. Fuchs, C. S. Peça, and W. Zwerger, Phys. Rev. A **72**, 023616 (2005).

[37] A. I. Pavlov, J. van den Brink, and D. V. Efremov, Phys. Rev. B **98**, 161410(R) (2018).

[38] A. S. Dehkharghani, A. G. Volosniev, and N. T. Zinner, Phys. Rev. Lett. **121**, 080405 (2018).

[39] A. Camacho-Guardian and G. M. Bruun, Phys. Rev. X **8**, 031042 (2018).

[40] B. Reichert, A. Petković, and Z. Ristivojevic, Phys. Rev. B **99**, 205414 (2019).

[41] B. Reichert, Z. Ristivojevic, and A. Petković, New J. Phys. **21**, 053024 (2019).

[42] G. E. Astrakharchik, L. A. P. Ardila, K. Jachymski, and A. Negretti, Nat. Commun. **14**, 1647 (2023).

[43] R. Paredes, G. Bruun, and A. Camacho-Guardian, Phys. Rev. A **110**, 030101 (2024).

[44] W. Casteels, J. Tempere, and J. T. Devreese, Phys. Rev. A **88**, 013613 (2013).

[45] A. Camacho-Guardian, L. A. Peña Ardila, T. Pohl, and G. M. Bruun, Phys. Rev. Lett. **121**, 013401 (2018).

[46] M. Will, G. E. Astrakharchik, and M. Fleischhauer, Phys. Rev. Lett. **127**, 103401 (2021).

[47] J. Jager and R. Barnett, New J. Phys. **24**, 103032 (2022).

[48] M. Schecter and A. Kamenev, Phys. Rev. Lett. **112**, 155301 (2014).

[49] F. Brauneis, H.-W. Hammer, M. Lemeshko, and A. Volosniev, SciPost Phys. **11**, 008 (2021).

[50] F. Theel, S. I. Mistakidis, and P. Schmelcher, SciPost Phys. **16**, 023 (2024).

[51] S. De and I. B. Spielman, Appl. Phys. B **114**, 527 (2014).

[52] M. Taglieber, A.-C. Voigt, T. Aoki, T. W. Hänsch, and K. Dieckmann, Phys. Rev. Lett. **100**, 010401 (2008).

[53] S. Lannig, C.-M. Schmied, M. Prüfer, P. Kunkel, R. Strohmaier, H. Strobel, T. Gasenzer, P. G. Kevrekidis, and M. K. Oberthaler, Phys. Rev. Lett. **125**, 170401 (2020).

[54] T. M. Bersano, V. Gokhroo, M. A. Khamehchi, J. D'Ambroise, D. J. Frantzeskakis, P. Engels, and P. G. Kevrekidis, Phys. Rev. Lett. **120**, 063202 (2018).

[55] Y. Ma, C. Peng, and X. Cui, Phys. Rev. Lett. **127**, 043002 (2021).

[56] G. Bighin, A. Burchianti, F. Minardi, and T. Macrì, Phys. Rev. A **106**, 023301 (2022).

[57] Y. Ma and X. Cui, arXiv:2312.15846.

[58] A. Barman and S. Basu, J. Phys. B: At. Mol. Opt. Phys. **48**, 055301 (2015).

[59] C. Liu, P. Chen, L. He, and F. Xu, Phys. Rev. A **108**, 013309 (2023).

[60] E. Compagno, G. De Chiara, D. G. Angelakis, and G. M. Palma, Sci. Rep. **7**, 2355 (2017).

[61] F. K. Abdullaev and R. M. Galimzyanov, J. Phys. B: At. Mol. Opt. Phys. **53**, 165301 (2020).

[62] A. Boudjemâa, N. Guebli, M. Sekmane, and S. Khlifa-Karfa, J. Phys.: Condens. Matter **32**, 415401 (2020).

[63] K. Keiler, S. I. Mistakidis, and P. Schmelcher, Phys. Rev. A **104**, L031301 (2021).

[64] J. Becker, M. Pyzh, and P. Schmelcher, Phys. Rev. A **106**, 053314 (2022).

[65] K. Abbas and A. Boudjemâa, J. Phys.: Condens. Matter **34**, 125102 (2022).

[66] S. Mistakidis, A. Volosniev, R. Barfknecht, T. Fogarty, Th. Busch, A. Foerster, P. Schmelcher, and N. Zinner, Phys. Rep. **1042**, 1 (2023).

[67] C. Chin, R. Grimm, P. Julienne, and E. Tiesinga, Rev. Mod. Phys. **82**, 1225 (2010).

[68] T. Köhler, K. Góral, and P. S. Julienne, Rev. Mod. Phys. **78**, 1311 (2006).

[69] M. Olshanii, Phys. Rev. Lett. **81**, 938 (1998).

[70] A. Romero-Ros, G. C. Katsimiga, S. I. Mistakidis, S. Mossman, G. Biondini, P. Schmelcher, P. Engels, and P. G. Kevrekidis, Phys. Rev. Lett. **132**, 033402 (2024).

[71] J. R. Williams, E. L. Hazlett, J. H. Huckans, R. W. Stites, Y. Zhang, and K. M. O'Hara, Phys. Rev. Lett. **103**, 130404 (2009).

[72] A. Álvarez, J. Cuevas, F. R. Romero, C. Hamner, J. J. Chang, P. Engels, P. G. Kevrekidis, and D. J. Frantzeskakis, J. Phys. B: At. Mol. Opt. Phys. **46**, 065302 (2013).

[73] M. Egorov, B. Opanchuk, P. Drummond, B. V. Hall, P. Hannaford, and A. I. Sidorov, Phys. Rev. A **87**, 053614 (2013).

[74] C. A. Regal, C. Ticknor, J. L. Bohn, and D. S. Jin, Nature (London) **424**, 47 (2003).

[75] B. J. DeSalvo, K. Patel, G. Cai, and C. Chin, Nature (London) **568**, 61 (2019).

[76] L. Cao, S. Krönke, O. Vendrell, and P. Schmelcher, J. Chem. Phys. **139**, 134103 (2013).

[77] S. Krönke, L. Cao, O. Vendrell, and P. Schmelcher, New J. Phys. **15**, 063018 (2013).

[78] L. Cao, V. Bolsinger, S. I. Mistakidis, G. M. Koutentakis, S. Krönke, J. M. Schurer, and P. Schmelcher, J. Chem. Phys. **147**, 044106 (2017).

[79] J. C. Light, I. P. Hamilton, and J. V. Lill, J. Chem. Phys. **82**, 1400 (1985).

[80] R. Horodecki, P. Horodecki, M. Horodecki, and K. Horodecki, Rev. Mod. Phys. **81**, 865 (2009).

[81] L. Pitaevskii and S. Stringari, *Bose-Einstein Condensation* (Oxford University Press, Oxford, 2003).

[82] S. I. Mistakidis, F. Grusdt, G. M. Koutentakis, and P. Schmelcher, New J. Phys. **21**, 103026 (2019).

[83] F. Theel, K. Keiler, S. I. Mistakidis, and P. Schmelcher, New J. Phys. **22**, 023027 (2020).

[84] F. Theel, K. Keiler, S. I. Mistakidis, and P. Schmelcher, Phys. Rev. Res. **3**, 023068 (2021).

[85] R. G. Dall, A. G. Manning, S. S. Hodgman, W. RuGway, K. V. Kheruntsyan, and A. G. Truscott, Nat. Phys **9**, 341 (2013).

[86] J. H. V. Nguyen, M. C. Tsatsos, D. Luo, A. U. J. Lode, G. D. Telles, V. S. Bagnato, and R. G. Hulet, Phys. Rev. X **9**, 011052 (2019).

[87] R. Yao, S. Chi, M. Wang, R. J. Fletcher, and M. Zwierlein, arXiv:2411.08780.

[88] E. Timmermans, Phys. Rev. Lett. **81**, 5718 (1998).

[89] M. Pyzh and P. Schmelcher, Phys. Rev. A **102**, 023305 (2020).

[90] S. P. Rath and R. Schmidt, Phys. Rev. A **88**, 053632 (2013).

[91] S. I. Mistakidis, G. C. Katsimiga, G. M. Koutentakis, Th. Busch, and P. Schmelcher, Phys. Rev. Lett. **122**, 183001 (2019).

[92] T. D. Anh-Tai, T. Fogarty, S. de María-García, T. Busch, and M. A. García-March, Phys. Rev. Res. **6**, 043042 (2024).

[93] K. Keiler and P. Schmelcher, Phys. Rev. A **100**, 043616 (2019).

[94] R. H. Byrd, P. Lu, and J. Nocedal, SIAM J. Sci. Comput. **16**, 1190 (1995).

[95] C. Zhu, R. H. Byrd, P. Lu, and J. Nocedal, ACM Trans. Math. Softw. **23**, 550 (1997).

[96] S. Nascimbène, N. Navon, K. J. Jiang, L. Tarruell, M. Teichmann, J. McKeever, F. Chevy, and C. Salomon, Phys. Rev. Lett. **103**, 170402 (2009).

[97] L. A. Peña Ardila, G. E. Astrakharchik, and S. Giorgini, Phys. Rev. Res. **2**, 023405 (2020).

[98] S. I. Mistakidis, G. C. Katsimiga, G. M. Koutentakis, and P. Schmelcher, New J. Phys. **21**, 043032 (2019).

[99] J. Chen, J. M. Schurer, and P. Schmelcher, Phys. Rev. Lett. **121**, 043401 (2018).

[100] E. Schmidt, Math. Ann. **63**, 433 (1907).

[101] A. Ekert and P. L. Knight, Am. J. Phys. **63**, 415 (1995).

[102] G. Vidal and R. F. Werner, Phys. Rev. A **65**, 032314 (2002).

[103] M. B. Plenio, Phys. Rev. Lett. **95**, 090503 (2005).

[104] C. Hörhammer and H. Büttner, Phys. Rev. A **77**, 042305 (2008).

[105] O. S. Duarte and A. O. Caldeira, Phys. Rev. A **80**, 032110 (2009).

[106] T. Zell, F. Queisser, and R. Klesse, Phys. Rev. Lett. **102**, 160501 (2009).

[107] K. Shiokawa, Phys. Rev. A **79**, 012308 (2009).

[108] C. Charalambous, M. A. Garcia-March, A. Lampo, M. Mehboud, and M. Lewenstein, SciPost Phys. **6**, 010 (2019).

[109] A. Peres, Phys. Rev. Lett. **77**, 1413 (1996).

[110] K. Życzkowski, P. Horodecki, A. Sanpera, and M. Lewenstein, Phys. Rev. A **58**, 883 (1998).

[111] D. Braun, Phys. Rev. Lett. **89**, 277901 (2002).

arXiv:2503.20624v1 [cond-mat.quant-gas] 26 Mar 2025

Effective two- and three-body interactions between dressed impurities in a tilted double-well potential

F. Theel,[1] A. G. Volosniev,[2] D. Diplaris,[1, 3] F. Brauneis,[4] S. I. Mistakidis,[5] and P. Schmelcher[1, 3]
[1] *Center for Optical Quantum Technologies, University of Hamburg, Department of Physics, Luruper Chaussee 149, D-22761, Hamburg, Germany*
[2] *Center for Complex Quantum Systems, Department of Physics and Astronomy, Aarhus University, Ny Munkegade 120, DK-8000 Aarhus C, Denmark*
[3] *The Hamburg Centre for Ultrafast Imaging, University of Hamburg, Luruper Chaussee 149, D-22761, Hamburg, Germany*
[4] *Department of Physics, Technische Universität Darmstadt, 64289 Darmstadt, Germany*
[5] *Department of Physics, Missouri University of Science and Technology, Rolla, MO 65409, USA*

(Dated: March 27, 2025)

We explore the impact and scaling of effective interactions between two and three impurity atoms, induced by a bosonic medium, on their density distributions. To facilitate the detection of mediated interactions, we propose a setup where impurities are trapped in a tilted double-well potential, while the medium is confined to a ring. The tilt of the potential breaks the spatial inversion symmetry allowing us to exploit the population of the energetically elevated well as a probe of induced interactions. For two impurities, the interaction with the medium reduces the impurity population at the energetically elevated well, which we interpret as evidence of induced impurity-impurity attraction. Furthermore, the impact of an induced three-body interaction is unveiled by comparing the predictions of an effective three-body model with many-body simulations. We extend our study for induced interactions to a three-component mixture containing distinguishable impurities. Our results suggest pathways to detect and tune induced two- and three-body interactions.

I. INTRODUCTION

An impurity in a quantum medium is a crucial model for understanding polarized many-body systems, with the polaron quasiparticle offering a theoretical framework for its description [1, 2]. The state-of-the-art approach for testing this framework and going beyond it, is based on quantum simulators that can be realized in cold-atom laboratories [3–7]. They permit elaborated investigations of both static [8–10] and dynamical [11–13] properties of an impurity in three-dimensional systems. Furthermore, they allow to assess more exotic one-dimensional geometries [14] and the associated impurity physics [15, 16].

Systems involving more than a single impurity provide insights into the phenomenon of medium-induced correlations between dressed particles [17]. This is anticipated to be especially important in one spatial dimension (1D) where the role of interactions is often considered enhanced in comparison to higher dimensions [18]. Theoretical modeling clearly shows that induced attraction [19–23] lowers the energy and leads to clustering of two impurities in 1D in free space [24–26], in a lattice potential [27–30], and in a harmonic trap [31–35]. These effects, however, are relatively weak posing a challenge for modern experiments.

One strategy for observing the effect of weak mediated interactions is by bringing the system close to a transition point where even slight perturbations can lead to dramatic effects [36]. Ideally, the measurement should rely on the density of the impurity cloud, which is a routinely available observable experimentally. The transition point implies a certain energy landscape that can be simulated in cold-atom experiments by tailoring, for instance, an external potential [37–39].

In this work, we propose an arguably simple design of a 1D Bose gas with a few impurities in such an energy landscape: The impurities being trapped in a tilted double-well potential are coupled to a Bose gas, which is confined to a ring potential. The tilt of the potential is an experimentally available knob [40, 41] that can introduce a small energy scale into the problem – the energy gap between the two minima of the potential. To investigate this model, we focus on a few-body system. These systems are of particular interest [42–44] because they allow for accurate numerical solutions and for studying the emergence of many-body concepts, such as the medium-induced interactions, from the underlying microscopic physics.

The numerical investigation of the ground-state properties is performed using the *ab-initio* Multi-Layer Multi-Configuration Time Dependent Hartree method for atomic mixtures (ML-MCTDHX) [45–47]. This grants access to mixtures consisting of two to three distinguishable and indistinguishable impurities immersed in a Bose gas. It is found that the density population of impurities at the energetically higher double-well site is sensitive to variations of the impurity-medium interaction strength. To interpret this observation, we devise two- and three-body effective models characterized by suitable two- and three-body induced contact interaction contributions. Although, the parameters of these models are determined by fitting to the energies of the many-body system, it is demonstrated that they also describe other observables such as densities. Our analysis confirms the importance of two-body effective interactions. The lesser-known three-body induced interactions play a less significant role in the regime of weak interactions, where the concept of induced interactions is most useful. This aligns with our expectations. In all cases, the scaling of the induced two- and three-body interactions is numerically extracted and corroborated by perturbation theoretic arguments.

This work unfolds as follows. In Section II we introduce our multicomponent setup and the concept of induced interactions. Section III discusses the key ingredients of the employed many-body variational method. Impurity-impurity induced interactions along with the effective two- and three-body models are analyzed in Sec. IV for two indistinguishable bosonic impurities and in Sec. V for three impurities. Generalizations of our results to a three-component system are provided in Sec. VI. We conclude and discuss future extensions of our findings in Sec. VII.

Additional technical details are presented in five appendices. Appendix A explicates the exact diagonalization method used for the effective models. Appendix B discusses the localization behavior of a single impurity. Appendix C reveals the role of the quasi-particle effective mass in single-particle observables. Appendix D focuses on the impact of correlations on different observables. Finally, Appendix E elaborates on the inherent logarithmic divergent behavior of the three-body interaction term and how it is circumvented.

II. MULTICOMPONENT SETUP AND INDUCED INTERACTIONS

A. Impurity-in-a-medium setting

To study the induced two- and three-body interactions, we consider a bosonic medium consisting of N_A atoms on a ring. The mass of a boson is m_A; the boson-boson interaction is parametrized by the standard contact interaction potential of strength g_{AA} [48]. In the other component, we have up to three bosonic impurities with mass m_B confined in a tilted 1D double-well potential [49–51]. A free-space impurity-impurity contact interaction potential of strength g_{BB} is assumed. The coupling strength is experimentally adjustable via either Fano-Feshbach tuning that changes the three-dimensional s-wave scattering length [52] or by modifying the transverse confinement [48]. The later is assumed to be so tight that the transverse excitations are frozen out as in typical quasi-1D experiments, see, e.g., Refs. [53–55].

The corresponding many-body Hamiltonian has the form,

$$\hat{H} = \hat{H}_A + \hat{H}_B + \hat{H}_{AB}, \tag{1}$$

where $\hat{H}_\sigma$ denotes the Hamiltonian of component $\sigma = \{A, B\}$ and $\hat{H}_{AB}$ represents the intercomponent interaction of effective strength g_{AB}. Specifically,

$$\hat{H}_A = -\sum_{i=1}^{N_A} \frac{\hbar^2}{2m_A}\partial_x^2 + g_{AA}\sum_{i<j}\delta(x_i^A - x_j^A), \tag{2a}$$

$$\hat{H}_B = \sum_{i=1}^{N_B} \hat{h}_B^{(1)}(x_i^B) + g_{BB}\sum_{i<j}\delta(x_i^B - x_j^B), \tag{2b}$$

$$\hat{H}_{AB} = g_{AB}\sum_{i=1}^{N_A}\sum_{j=1}^{N_B}\delta(x_i^A - x_j^B). \tag{2c}$$

The Hamiltonian $\hat{h}_B^{(1)}(x_i^B) = -\frac{\hbar^2}{2m_B}\partial_x^2 + V_B(x_i^B)$ describes a single impurity in a tilted double-well external trap. The latter is modeled by a superposition of a harmonic oscillator with frequency ω, a Gaussian potential of width w and height h, and a linear tilting potential of strength α,

$$V_B(x) = \frac{1}{2}m_B\omega x^2 + \frac{h}{w\sqrt{2\pi}}\exp\left(-\frac{x^2}{2w^2}\right) + \alpha x. \tag{3}$$

It is illustrated in Fig. 1(a) along with characteristic density distributions of the medium A and the three impurities for repulsive impurity-medium couplings. The presence of a small α breaks the inversion symmetry of the problem and leads to an energy offset between the two double-well sites. The tilted double-well can be readily implemented in experiments by imposing a bias potential [40], while the ring trap is realized using time-averaged potentials [56, 57].

For simplicity, we study a mass-balanced mixture, namely it holds that $m_A = m_B \equiv m = 1$, and employ harmonic oscillator units. Accordingly, the energy scales are expressed in units of $\hbar\omega$, while the length and interaction scales are in terms of $\sqrt{\hbar/m\omega}$ and $\sqrt{\hbar^3\omega/m}$, respectively. Typically, our bath component consists of $N_A = 12$ bosonic particles featuring "weak" intracomponent repulsion, $g_{AA} = g_{BB} = 0.1$. By varying the parameter g_{AB}, we explore the strength of induced impurity-impurity interactions. In our numerical simulations all atoms of the medium reside on a ring of length $L = 12\sqrt{\hbar/m\omega}$ (the pre-factor here is given by N_A) ensuring that $L \gg \sqrt{\hbar/(m\omega)}$. This requirement reduces the role of finite-size effects in our study. Finally, throughout this work we employ a double-well characterized by $\omega = 1$, $w = 0.3\sqrt{\hbar/m\omega}$ and $h = 3\sqrt{\hbar m\omega}$, while the energy offset parameter is considered to be $\alpha = 0.06\sqrt{\hbar m\omega}$.

Our multicomponent systems can be experimentally implemented, for instance, with different hyperfine states of a ^{87}Rb gas. As an example the impurities may be realized using the state $|F = 1, m_F = 1\rangle$ while the bosons are in the $|F = 2, m_F = 1\rangle$ state [58]. For the three-component mass-balanced system discussed in Section VI A, it is possible to utilize an additional hyperfine state, e.g., $|F = 1, m_F = -1\rangle$ of ^{87}Rb [53].

Within this work we devise two- and three-body models which employ effective two- and three-body interaction parameters to effectively describe the behavior of the impurities interacting with the majority species, see Figs. 1(b) and (c) for a sketch.

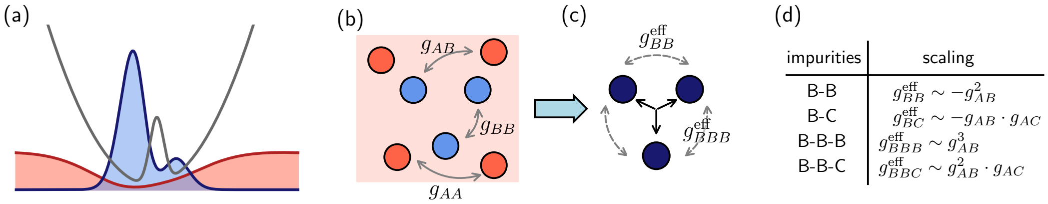

impurities	scaling
B-B	$g^{\text{eff}}_{BB} \sim -g^2_{AB}$
B-C	$g^{\text{eff}}_{BC} \sim -g_{AB} \cdot g_{AC}$
B-B-B	$g^{\text{eff}}_{BBB} \sim g^3_{AB}$
B-B-C	$g^{\text{eff}}_{BBC} \sim g^2_{AB} \cdot g_{AC}$

Figure 1. Sketch of our impurity-medium setup. (a) One-body densities of the medium A (red) and the three bosonic impurities (blue) for repulsive impurity-medium interactions. The medium, which consists of $N_A = 12$ weakly interacting bosonic particles, is confined to a ring with periodic boundary conditions. The impurities are trapped by a tilted double-well potential (gray line). (b) The medium particles (red circles) interact via a contact interaction of strength g_{AA}. The impurities (blue circles) repel each other with strength g_{BB}. The boson-impurity interaction is denoted by g_{AB}. (c) The induced interactions between the three impurities are parameterized by the effective two-body (g^{eff}_{BB}) as well as three-body (g^{eff}_{BBB}) effective couplings. (d) Overview of the identified scaling behavior of the mediated two- and three-body interaction strengths between two or three impurities belonging to species B and C.

B. Induced interactions

As the focus of this paper is induced interactions, we briefly introduce this concept here, first for a system with two impurities. Our results are applicable to any external trapping of the impurities as long as the bosonic medium is confined to a ring potential of length L. We utilize perturbation theory to calculate the correction to the non-interacting energy due to interactions [59]

$$\delta E = M_{gg} + \sum_e \frac{|M_{eg}|^2}{E_g - E_e} + \ldots \,, \tag{4}$$

where $M_{ij} = \langle i|\hat{H}_{AB}|j\rangle$ is the non-interacting matrix element between the states i and j; the index g (e) denotes the ground (excited) state of the non-interacting system characterized by the energy E_g (E_e). Using indistinguishability of particles, we write the matrix element in the coordinate space representation as

$$M_{eg} = g_{AB} N_A N_B \int \mathrm{d}x^A_1 \mathrm{d}x^B_1 \Psi_g \delta(x^A_1 - x^B_1)\Psi_e. \tag{5}$$

Induced interactions is an intuitive method to interpret the energy difference $\delta E_2 = \delta E(N_B = 2) - 2\delta E(N_B = 1)$, which is in general nonzero. To demonstrate this, note that for $N_B = 1$ [$N_B = 2$] the non-interacting ground state can be written as: $\Psi_g = \phi_g(x^B_1)\prod_i \psi_g(x^A_i)$ [$\Psi_g = \phi_g(x^B_1)\phi_g(x^B_2)\prod_i \psi_g(x^A_i)$], where we assume that all bosons occupy the same orbital, ψ_g; ϕ_g is the ground state of $\hat{h}^{(1)}_B$. For bosons on a ring, it holds that $\psi_g(x^B_i) = 1/\sqrt{L}$. Furthermore, we consider only excitations of the medium, as these are essential for induced interactions. The corresponding excited states read: $\Psi_e = \phi_g(x^B_1)\sum_i \psi_e(x^A_i)/\sqrt{N_A L^{N_A-1}}$ [$\Psi_e = \phi_g(x^B_1)\phi_g(x^B_2)\sum_i \psi_e(x^A_i)/\sqrt{N_A L^{N_A-1}}$]. Using these expressions in Eq. (5) the energy difference becomes

$$\delta E_2 \simeq 2 g^2_{AB} \frac{N_A}{L} \int \mathrm{d}x^B_1 \mathrm{d}x^B_2 |\phi_g(x^B_1)|^2 |\phi_g(x^B_2)|^2 V_{II}, \tag{6}$$

with the function V_{II} defined as follows

$$V_{II}(x^B_1, x^B_2) = \sum_e \frac{\psi^*_e(x^B_2)\psi_e(x^B_1)}{E_g - E_e}. \tag{7}$$

Note that the expression in Eq. (6) is equivalent to the first-order perturbative correction to the energy of two non-interacting impurities assuming that V_{II} is a perturbation. The fact that V_{II} does not depend on the state of the impurity enforces the interpretation of V_{II} in terms of an effective two-body interaction. Note that the leading-order contribution to the energy from the two-body induced interaction is proportional to g^2_{AB}, see also Fig. 1(d). It is always attractive as it stems from second-order perturbation theory.

We remark that Eq. (7) is also the correction to the non-interacting Bose gas perturbed by two static impurity potentials located at x^B_1 and x^B_2. This allows one to calculate V_{II} using the theoretical methods presented in Refs. [19, 22, 23, 25, 33] (see also Refs. [60–63] for relevant works in higher dimensions). In particular, one can approximate[1] $V_{II} \simeq -\delta(x^B_1 - x^B_2)L/(2g_{AA}N_A)$ for weak interactions in the thermodynamic limit ($N_A \to \infty, N_A/L \to \text{const}$) [44].

For three impurities, one introduces a three-body effective interaction to interpret the energy difference $\delta E_3 = \delta E(N_B = 3) - 3\delta E_2(N_B = 2) - 3\delta E(N_B = 1)$. Here, the factor 3 in front of $\delta E_2(N_B = 2)$ accounts for the number of interacting pairs. Alternatively, one can think that this factor is chosen so that δE_3 vanishes at the level of second order perturbation theory. Therefore, it is necessary to consider the energy correction within third-order perturbation theory

$$\delta_3 = \sum_{e \neq e'} \frac{M_{ge} M_{ee'} M_{e'g}}{(E_g - E_e)(E_g - E'_e)} - \sum_e \frac{M_{gg}|M_{eg}|^2}{(E_g - E_e)^2}. \tag{8}$$

We shall only analyze overall features of this expression. To this end, we consider the following excited states $\Psi_e =$

---

[1] Note that here we disregard the long-range part of the potential [21, 64], which is irrelevant for small trapped systems [33].

$\phi_g(x_1^B)\phi_g(x_2^B)\phi_g(x_3^B)\sum_i \psi_e(x_i^A)/\sqrt{N_A L^{N_A-1}}$, which are motivated by our discussion of V_{II}. Using these states, we write the contribution to the energy due to the first term in Eq. (8) that can be interpreted as a result of three-body induced interactions: $\frac{6g_{AB}^3 N_A}{L}\int \mathrm{d}x_1^B \mathrm{d}x_2^B \mathrm{d}x_3^B |\phi_g(x_1^B)|^2|\phi_g(x_2^B)|^2|\phi_g(x_3^B)|^2 V_{III}$, where

$$V_{III}(x_1^B, x_2^B, x_3^B) = \sum_{e,e'} \frac{\psi_e(x_1^B)\psi_e^*(x_2^B)\psi_{e'}^*(x_3^B)\psi_{e'}(x_2^B)}{(E_g - E_e)\,(E_g - E_e')}. \tag{9}$$

Note that V_{III} is a product of two-body interactions, i.e., $V_{III}(x_1^B, x_2^B, x_3^B) = V_{II}(x_1^B, x_2^B)V_{II}(x_2^B, x_3^B)$. For weak interactions in the thermodynamic limit, we can therefore write $V_{III}(x_1^B, x_2^B, x_3^B) = \delta(x_1^B - x_2^B)\delta(x_2^B - x_3^B)L^2/(4g_{AA}^2 N_A^2)$. As the three-body induced interactions is proportional to g_{AB}^3 in the leading order, we expect it to be repulsive for $g_{AB} > 0$ and attractive for $g_{AB} < 0$, see also Fig 1(d). Note that the last term in Eq. (8) gives rise to an effective two-body interaction in g_{AB}^3-order that depends on the number of impurities. Having introduced the general features of induced interactions, we explicate them further in Sections IV and V for the cases with $N_B = 2$ and $N_B = 3$, respectively.

III. MANY-BODY APPROACH

To study the ground state properties of our quantum many-body system, we employ the *ab-initio* ML-MCTDHX method [45–47]. A main facet of this approach is that the full many-body wave function is expressed in a multi-layer structure with time-dependent and variationally optimized basis functions. This process is tailored to account for the relevant intra- and intercomponent correlations of multicomponent cold atom settings. Detailed discussions on the ingredients, successful applicability and reductions of this method for a plethora of cold atom systems can be found in the recent reviews [44, 65].

Below, we mainly elaborate on the structure of the many-body wave function for the most general three-component setting used in our analysis. Comments on the reduction of this scheme to the two-component setup are provided whenever appropriate, see also [66, 67] for more detailed discussions. For a three-component system the wave function is firstly expanded in the truncated basis comprising of D_σ, with $\sigma = A, B, C$, orthonormal time-dependent species functions, $|\Psi_i^\sigma(t)\rangle$, as follows

$$|\Psi^{MB}(t)\rangle = \sum_i^{D_A}\sum_j^{D_B}\sum_k^{D_C} A_{ijk}(t)|\Psi_i^A(t)\rangle|\Psi_j^B(t)\rangle|\Psi_k^C(t)\rangle. \tag{10}$$

Here, $A_{ijk}(t)$ represent the time-dependent expansion coefficients. This expansion grants access to intercomponent correlations. Specifically, the expansion coefficients referring to the contribution of each species function provide information about the intercomponent entanglement, see also Refs. [68], since they allow the evaluation of the eigenvalues of the species reduced density matrices [67, 69, 70]. In the case of a binary mixture, the above expansion reduces to a truncated Schmidt decomposition [71, 72], see for instance the works [73–75] and references therein.

Next, in order to incorporate intracomponent correlations into our ansatz, each of the species functions, $|\Psi_i^\sigma(t)\rangle$, is expanded in terms of the bosonic number states $|\vec{n}_t^\sigma\rangle$. The latter are weighted by the time-dependent coefficients $C_{i,\vec{n}^\sigma}^\sigma(t)$. This yields

$$|\Psi_i^\sigma(t)\rangle = \sum_{\vec{n}|N_\sigma} C_{i,\vec{n}^\sigma}^\sigma(t)|\vec{n}^\sigma(t)\rangle, \tag{11}$$

where N_σ bosons are allowed to occupy d_σ single-particle functions (SPFs) $|\phi_j^\sigma(t)\rangle$. The vector $\vec{n}^\sigma = (n_1^\sigma, \dots, n_{d_\sigma}^\sigma)$ indicates the occupation number of each SPF. Finally, the SPFs are expanded with respect to a time-independent basis consisting of $\mathcal{M}_{pr}$ grid points[2]. The ML-MCTDHX equations of motion for the above-described coefficients are derived, e.g., by using the Dirac-Frenkel variational principle $\langle\delta\Psi|(i\hbar\partial_t - \hat{H})|\Psi\rangle = 0$. A limiting case is to set $D_A = D_B = D_C = 1$, which leads to a single product state in Eq. (10) neglecting intercomponent correlations, but still including intracomponent ones. In addition, using $d_A = d_B = d_C = 1$, the method reduces to the standard mean-field approach where all correlations are absent. We will exploit in Appendix D different reduction ansatzes in order to unravel the impact of two- and three-component correlations on one- and two-body observables.

IV. TWO BOSONIC IMPURITIES

We start our investigation on induced interactions with a system containing two bosonic impurities, i.e., $N_B = 2$. In what follows, the many-body ML-MCTDHX computations of the corresponding impurity-medium setting are analyzed and subsequently compared with an effective two-body model and the standard mean-field approximation.

A. One-body density configurations

By choosing to work with a tilted double-well potential, we intentionally break the system's inversion symmetry. This creates an energy offset between the two wells of the double-well potential. Consequently, the impurities prefer to occupy the energetically lower well. In Figs. 2(a) and (b) we present the one-body densities $\rho_\sigma^{(1)}(x^\sigma)$ of species $\sigma = A, B$, respectively, as a function of the impurity-medium interaction strength g_{AB}, for fixed $g_{AA} = g_{BB} = 0.1$. Our

---

[2] For a given $\mathcal{M}_{pr}$, ML-MCTDHX is numerically exact when $d_\sigma = \mathcal{M}_{pr}$ and D_σ equals the number of bosonic configurations, i.e. $\binom{N_\sigma+d_\sigma-1}{d_\sigma-1}$.

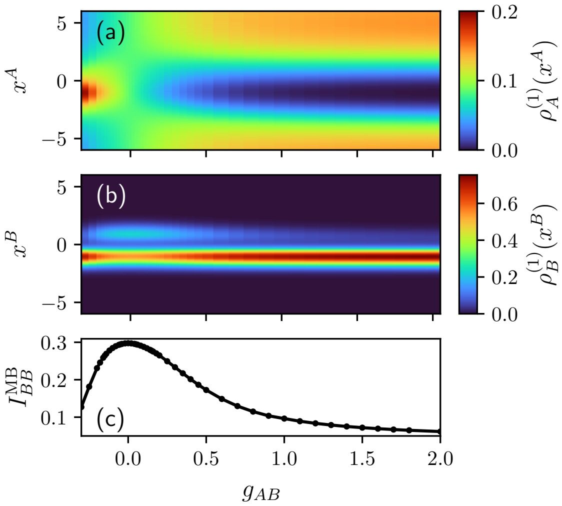

Figure 2. Ground-state one-body densities of (a) the medium and (b) the two bosonic impurities as a function of the interspecies interaction strength g_{AB}. (c) Population of impurities at the energetically elevated double-well site (located at $x^B > 0$), I_{BB}^{MB}, see Eq. (12) for the definition, with respect to g_{AB}. The simulations are performed within the many-body approach ML-MCTDHX. The two repulsively interacting ($g_{BB} = 0.1$) impurities experience a tilted double-well potential and are coupled to a bosonic medium with $N_A = 12$ and $g_{AA} = 0.1$.

choice of g_{BB} is somewhat arbitrary; we select it to match the value of g_{AA}. Note that for the induced interactions to exist in the thermodynamic limit, g_{AA} should be finite, see Sec. II B.

As it can be readily seen from Fig. 2(b), the population imbalance of the impurities is evident already in the non-interacting case, $g_{AB} = 0$. This behavior becomes gradually more prominent with increasing intercomponent interaction $|g_{AB}|$ eventually leading in the strongly interacting case ($g_{AA}, g_{BB} \ll g_{AB}$) to a complete depopulation of the energetically higher site from the impurities. As expected, depending on the sign of g_{AB} the density of the medium features a depletion (hump) for $g_{AB} > 0$ ($g_{AB} < 0$), as shown in Fig. 2(a), at the location of the impurities. Indeed, as long as $g_{AB} > 0$ the medium atoms prefer to avoid the impurities, while if $g_{AB} < 0$ the bosons accumulate in the vicinity of the impurities.

To quantify the depopulation process of the impurities we integrate $\rho_B^{(1)}(x^B)$ over the energetically higher double-well site (located at $x^B > 0$):

$$I_{BB} = \int_0^{L/2} \rho_B^{(1)}(x^B)\mathrm{d}x^B, \tag{12}$$

where the upper integration limit is set by the length L of the ring potential. A typical profile of this quantity is presented in Fig. 2(c) with respect to g_{AB} and labeled as I_{BB}^{MB} to indicate that this observable has been obtained within the full many-body approach (cf. Section III). Here, the largest population at the energetically higher site occurs at $g_{AB} = 0$ and then reduces for finite values of g_{AB}, thus implying that the impurities move to the energetically lower site at $x^B < 0$.

In the following our goal is to construct an effective model that captures the above-discussed depopulation mechanism. Thereby, we construct an effective two-body model whose parameters are determined on the basis of the polaron and bipolaron energies. [In this paper, we use the terms ‘polaron’ and ‘bipolaron’ to refer to a Bose gas with a single and two impurities, respectively. This terminology became standard, even when working with a few-body system [30, 32, 35].] To validate this effective model, we compare its predictions regarding the integrated density with those of the many-body approach, I_{BB}^{MB}, and of the mean-field approximation, I_{BB}^{MF}.

B. Effective two-body model

In the previous section we have seen that finite impurity-medium coupling strengths g_{AB} lead to a depletion of the impurities' density at the energetically higher double-well site. There are two plausible mechanisms for this behavior. First, it may be attributed to the increase of the effective mass of the impurity, which leads to spatial localization, see also Appendix B. Second, this behavior can be interpreted as an additional mediated interaction between the impurities induced by their coupling (g_{AB}) with the medium.

To construct an effective two-body model, we first define the energy cost of adding the impurity to the system, E_B^{pol} [6, 7],

$$E_B = E_A^{(0)} + E_B^{\mathrm{pol}}. \tag{13}$$

Here, E_B is the total energy of the impurity-bath system, and $E_A^{(0)}$ denotes (throughout this work) the energy of the bath without any impurities. Note that E_B and therefore $E_B^{\mathrm{pol}} = E_B - E_A^{(0)}$ depend on g_{AB}. The total energy is used, together with the undisturbed impurity Hamiltonian $\hat{h}_B^{(1)}$ [Eq. (2b)], to formulate the effective model

$$\hat{H}_B^{\mathrm{eff}}(x) = \epsilon_B^{\mathrm{pol}} + \hat{h}_B^{(1)}(x), \tag{14}$$

where $\epsilon_B^{\mathrm{pol}} = E_B^{\mathrm{pol}} - E^{(1\mathrm{body})}$ is chosen such that the ground state energy of $\hat{H}_B^{\mathrm{eff}}$ matches the energy E_B^{pol}. $E^{(1\mathrm{body})}$ is the ground-state energy of the one-body Hamiltonian $\hat{h}_B^{(1)}(x)$. In this effective one-body model we explicitly consider the bare impurity mass m_B as it turns out that the effective two-body model predictions are improved in the absence of the effective mass for $g_{AB} > 0$. More details about this fact can be found in Appendix B where the effective mass is determined, and in Appendix C at which the behavior of the induced two-body interaction accounting for the effective mass is reported.

Let us now consider two impurities. Each impurity contributes with E_B^{pol} to the energy of the undisturbed

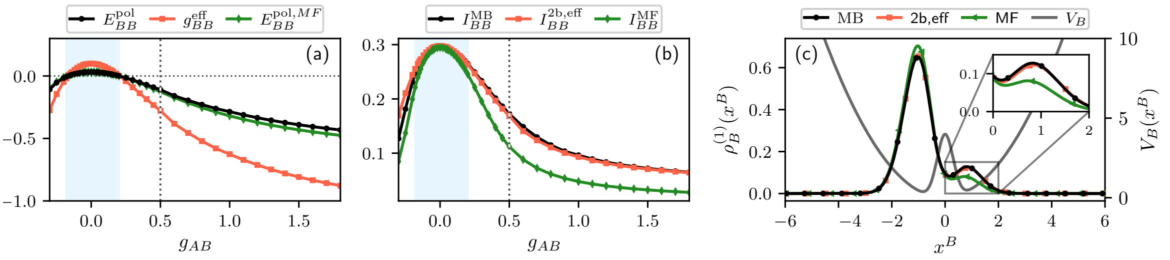

Figure 3. (a) The energy E_{BB}^{pol} (in units of $\hbar\omega$) and the corresponding effective interaction strength g_{BB}^{eff} (in units of $\sqrt{\hbar^3\omega/m}$) in terms of g_{AB}. The energies are obtained either using the many-body approach, E_{BB}^{pol}, or the mean-field approximation, $E_{BB}^{\mathrm{pol,MF}}$ (see legend). Notice that the predictions of the two approaches agree well. (b) Integrated one-body density [Eq. (12)] determined via the many-body approach I_{BB}^{MB}, the effective two-body model [Eq. (16)], I_{BB}^{eff}, and the mean-field approximation, I_{BB}^{MF}. The blue shaded areas in panels (a) and (b) mark the interaction region where the relative deviation between I_{BB}^{MB} and I_{BB}^{MF} is smaller than 0.1. (c) One-body density of the impurities within the many-body approach (MB), the effective two-body model (2b,eff) and the mean-field approximation (MF), see also legend. The double-well potential is also shown and the inset illustrates the impurities' density within the right well as predicted for the different methods. Here, $g_{AB} = 0.5$, see the vertical dotted lines in panels (a) and (b). Other system parameters are $N_A = 12$ and $g_{AA} = g_{BB} = 0.1$.

bath, $E_A^{(0)}$. The total energy, E_{BB}, of a system consisting of a bath coupled to two impurities can then be decomposed [28, 30, 76] (note the resemblance to the perturbative analysis presented in Sec. II B), as

$$E_{BB} = E_A^{(0)} + 2E_B^{\mathrm{pol}} + E_{BB}^{\mathrm{pol}}. \tag{15}$$

In this expression, E_{BB}^{pol} appears due to the direct and effective interactions between the impurity atoms. In Fig. 3(a), we present the many-body results of E_{BB}^{pol} for $g_{BB} = 0.1$. For weak impurity-medium couplings, the positive value of g_{BB} implies that $E_{BB}^{\mathrm{pol}} > 0$. However, for $g_{AB} \gtrsim g_{AA}$, induced attractive interactions dominate [44]. In this regime $E_{BB}^{\mathrm{pol}} < 0$, which suggests clustering of impurities[3]. To capture this effect, we design an effective two-body model that incorporates an effective interaction of strength g_{BB}^{eff} induced by the medium

$$\hat{H}_{BB}^{\mathrm{eff}} = \sum_{i=1}^{2} \hat{H}_B^{\mathrm{eff}}(x_i) + g_{BB}^{\mathrm{eff}}\delta(x_1 - x_2). \tag{16}$$

For simplicity we consider here a contact effective interaction, which is motivated by the discussion in Sec. II B. We anticipate that a 'simple' delta-function potential form cannot capture the physics of strong interactions in full detail [31, 33]. Still, as we shall argue below it provides an adequate starting approximation even in this case.

To calculate g_{BB}^{eff}, the condition that the ground state energy, E_{BB}^{eff}, of $\hat{H}_{BB}^{\mathrm{eff}}$ matches our many-body results is imposed, namely

$$E_{BB}^{\mathrm{eff}} \overset{!}{=} 2E_B^{\mathrm{pol}} + E_{BB}^{\mathrm{pol}}. \tag{17}$$

In practice, the free parameter g_{BB}^{eff} is varied until Eq. (17) is satisfied. To solve the two-body model, and later on the three-body one, we expand the respective wave function in terms of number states which are composed of a set of static single-particle functions, see Appendix A for more details.

In Fig. 3(a), g_{BB}^{eff} is illustrated for $g_{BB} = 0.1$ as a function of g_{AB}. Apparently, for $g_{AB} = 0$, induced impurity-impurity interactions are absent and it holds that $g_{BB}^{\mathrm{eff}} = g_{BB}$[4]. Although, the effective model was established using purely energy considerations, it also turns out to be useful for calculating other observables. This fact is shown in Fig. 3(b), (c) where we compare the impurities integrated one-body densities and a characteristic spatial profile obtained with the effective two-body model, $I_{BB}^{\mathrm{2b,eff}}$, and the many-body approach, I_{BB}^{MB}. A good agreement between the two methods is observed for the aforementioned population of the energetically higher double-well site and the density configuration itself. However, non-negligible deviations occur for increasing impurity-medium attractions.

To study the impact of correlations on the employed one-body observables, we perform a comparison of our results to the outcome of the standard mean-field approximation. Inspecting Figs. 3(a) and (b) it turns out that the mean-field results are accurate for weak intercomponent interactions. However, for larger val-

---

[3] In the homogeneous case the induced interaction between two impurities is approximately given by $g_{BB}^{\mathrm{eff}} - g_{BB} \simeq -\frac{g_{AB}^2}{g_{AA}}$ [44], see also Section II B. The induced attraction is roughly equal to the internal impurity-impurity repulsion ($g_{BB} = g_{BB}^{\mathrm{eff}}$) when $g_{AB} \simeq g_{AA}$. We have checked that the mediated interaction g_{BB}^{eff} determined via the fitting procedure indeed approaches this prediction if (i) $g_{AB} \ll g_{AA}$ and (ii) the healing length of the Bose gas is much smaller than L.

[4] In fact, the effective model at $g_{AB} = 0$ yields a g_{BB}^{eff} which matches up to the third digit $g_{BB} = 0.1$. This deviation marks the accuracy of the employed exact diagonalization method when fitting to the ML-MCTDHX data.

ues of $|g_{AB}|$ the mean-field predictions for the one-body density start to deviate from the many-body results indicating an increasing role of correlations in the system, see in particular Figs. 3(b), (c). This deviation implies that it is possible to study the strength of induced impurity-impurity interactions by observing the one-body density. For convenience, the interaction region ($-0.18 < g_{AB} < 0.2$) where the mean-field treatment yields accurate results (within 10% accuracy) for the integrated density is marked by a blue shaded area in Figs. 3(a) and (b). The origin of the deviation between the many-body and the mean-field results is linked to interspecies correlations, see Appendix D for more details.

V. THREE BOSONIC IMPURITIES

Next, we investigate three bosonic impurities coupled to a bosonic medium. Besides an effective two-body interaction discussed in the previous section, the system can experience an effective three-body force (cf. Ref. [26]). To quantify its effect, it is necessary to extend the effective model given by Eq. (16).

Similar to the two-impurity case, the extended effective model is developed using energy considerations. Namely, the total energy is re-arranged as follows

$$E_{BBB} = E_A^{(0)} + 3E_B^{\text{pol}} + 3E_{BB}^{\text{pol}} + E_{BBB}^{\text{pol}}. \tag{18}$$

This expression includes the unperturbed bath energy $E_A^{(0)}$ and three times E_B^{pol}. The higher-order contributions enter via the two-body polaron energy E_{BB}^{pol}, and the three-polaron one, E_{BBB}^{pol}. The coefficient 3 in front of E_{BB}^{pol} reflects the number of interacting impurity-impurity pairs. It also follows from the analysis based upon perturbation theory, see Section II B.

We incorporate induced three-body interactions in an effective three-body Hamiltonian as follows[5]

$$\hat{H}_{BBB}^{\text{eff}} = \sum_{i=1}^{3} H_B^{\text{eff}}(x_i) + g_{BB}^{\text{eff}} \sum_{\substack{i,j=1 \\ i\neq j}}^{3} (x_i - x_j) + g_{BBB}^{\text{eff}}\delta(x_1 - x_2)\delta(x_2 - x_3), \tag{19}$$

where the shape of the last term is motivated by the discussion in Sec. II B. The parameter g_{BB}^{eff} is determined within the effective two-body model introduced in Sec. IV B. To compute the strength of the effective three-body interaction, we enforce the condition that the ground-state energy of $\hat{H}_{BBB}^{\text{eff}}$, namely E_{BBB}^{eff}, matches the energy of the three dressed impurities,

$$E_{BBB}^{\text{eff}} \overset{!}{=} 3E_B^{\text{pol}} + 3E_{BB}^{\text{pol}} + E_{BBB}^{\text{pol}}. \tag{20}$$

As in Eq. (18), the one-body term here refers to the single-polaron energy E_B^{pol}. The two-body interaction term accounts for the impurity-impurity correlations and E_{BBB}^{pol} implies the presence of the three-impurity induced interactions.

The analysis of a three-impurity system is shown in Fig. 4 for varying g_{AB} and constant $g_{BB} = 0.1$. For weak interactions (i.e. $g_{AB} \to 0$), E_{BBB}^{pol} and g_{BBB}^{eff} appear to scale as g_{AB}^3, see Fig. 4 (a), in agreement with the perturbative predictions discussed in Sec. II B. Also, despite the fact that the effective model of Eq. (19) is constructed through energy considerations, it turns out to be useful for other observables (see below).

Figure 4(b) depicts the integrated one-body density using I_{BBB}^{MB}, obtained from the many-body treatment, as a reference. First, we determine the integrated one-body density from the effective model in the absence of three-body effects, i.e., setting $g_{BBB}^{\text{eff}} = 0$ in Eq. (19) which we refer to as $I_{BBB}^{\text{3b,eff,0}}$. It is found that $I_{BBB}^{\text{3b,eff,0}}$ agrees well with I_{BBB}^{MB} only for small impurity-medium coupling strengths, and that $g_{BBB}^{\text{eff}} \neq 0$ leads in general to more accurate results. Indeed, for larger values of g_{AB}, the integrated density of the impurities in either of the effective models deviates from the many-body result as can be readily seen in Fig. 4(b). This implies that the assumed effective interactions capture only approximately induced correlations between particles. This conclusion is further supported by investigating the one-body density for $g_{AB} = 0.5$, see Fig. 4(c) and its inset.

We conclude that while three-body effects are clearly present, their analysis appears to be more involved than those for two impurities. To interpret this observation, note that according to Section II B, the interaction strength g_{BB}^{eff} should be modified to account for the presence of the third impurity. Finally, it is worth noticing that the mean-field approximation leads to accurate results for the one-body densities and the energy, comparable to those of the effective model but not the many-body approach, see Fig. 4(a)-(c). The lack of agreement between the mean-field approach with the many-body one indicates that inter-particle correlations have a significant impact on the one-body observables.

VI. INDUCED INTERACTIONS IN THREE-COMPONENT MIXTURES WITH IMPURITIES

In the following, we examine the impact of mediated interactions on the behavior of two distinguishable impurities and two bosonic impurities plus one distinguishable impurity. Such a scenario presumes a three-component ultra-cold mixture. In our case, this consists of a medium A confined to a ring and two distinct impurity species B and C trapped in a double-well potential. The many-body Hamiltonian of Eq. (1) is readily extended to the three-component

---

[5] Note that our three-body interaction term leads to divergences similar to the two-dimensional contact interaction, see Ref. [77] and Appendix E. We renormalize this interaction potential by fitting in a finite Hilbert space.

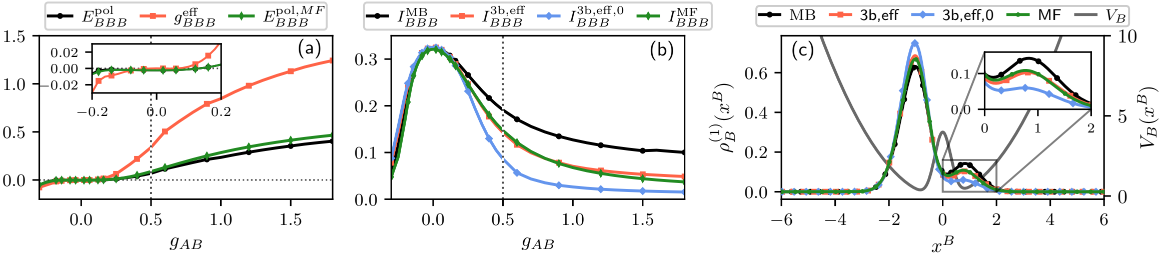

Figure 4. (a) The energy E^{pol}_{BBB} and the effective three-impurity interaction strength g^{eff}_{BBB} calculated by fitting the effective model to E^{pol}_{BBB} (see main text). E^{pol}_{BBB} is compared to $E^{\text{pol},MF}_{BBB}$, which is computed within the mean-field approach. (b) Integrated one-body density of the impurities, I_{BBB}, computed within the many-body (MB) method, the mean-field (MF) approximation and the three-body effective model with and without a three-body interaction potential, labeled as (3b,eff) and (3b,eff,0), respectively. (c) Ground-state density distribution of the impurities within four different approaches (see legend) for fixed $g_{AB} = 0.5$ indicated also by vertical gray dotted lines in panels (a) and (b). The inset provides a magnification of the densities for the right well of the double well (see also the right axis of panel (c)) emphasizing the degree of agreement among the different approaches. Other system parameters are $N_A = 12$, $N_B = 3$, $g_{AA} = 0.1$ and $g_{BB} = 0.1$.

case:

$$\hat{H} = \hat{H}_A + \hat{H}_B + \hat{H}_C + \hat{H}_{AB} + \hat{H}_{AC}. \tag{21}$$

For simplicity, we consider a mass-balanced system, $m_A = m_B = m_C = 1$, whilst the impurities interact with $g_{BB} = g_{BC} = 0.1$.

Analogously to the setup containing indistinguishable bosonic impurities discussed in Sections IV and V, our aim is to examine the impact of the mediated interactions between the impurities in a double-well potential. This will be again achieved by analyzing the effect of interactions on the one-body densities within the many-body method and the suitable effective model. A key difference from the previously studied scenarios is the possibility to independently tune the impurity-medium interaction strengths. This gives rise to a substantial change in the character of the induced interactions. In particular, coupling one impurity attractively to the bath, while the other repels it, induces repulsive interactions between the impurities as was also argued in Refs. [21, 22, 67, 78].

A. Two distinguishable impurities

In the following, we consider two distinguishable impurities, $N_B = 1$ and $N_C = 1$. We start by examining the integrated one-body density of the B-impurity, $I^{\text{MB},B}_{BC}$, determined within the many-body approach, see Fig. 5(a). Comparing the region where $g_{AB} = g_{AC} = 0$ with the upper left (lower right) corner of Fig. 5(a), we find an increase of the B impurity population in the energetically higher double-well site, while the regions corresponding to the upper right (lower left) corner show a reduction of $I^{\text{MB},B}_{BC}$. This signals the presence of a mediated repulsive (attractive) interaction between the impurities characterized by $g_{AB}g_{AC} < 0$ ($g_{AB}g_{AC} > 0$) in agreement with Refs. [21, 22, 67, 78], see also the discussion below.

Following Section IV B, we quantify this induced interaction using an effective two-body model

$$\hat{H}^{\text{eff}}_{BC} = \hat{H}^{\text{eff}}_B(x^B) + \hat{H}^{\text{eff}}_C(x^C) + g^{\text{eff}}_{BC}\delta(x^B - x^C), \tag{22}$$

where the effective one-body Hamiltonian, $\hat{H}^{\text{eff}}_\sigma$ (with $\sigma = B, C$), is constructed similarly to the one described in Eq. (14). The effective two-body interaction strength g^{eff}_{BC} is tuned such that the ground-state energy of this effective model, E^{eff}_{BC}, coincides with the expansion that contains one-body energies, i.e., $E^{\text{eff}}_{BC} \overset{!}{=} E^{\text{pol}}_B + E^{\text{pol}}_C + E^{\text{pol}}_{BC}$. Here, E^{pol}_{BC} parametrizes correlations between two impurities. Figure 5(b) presents the effective two-body interaction strength g^{eff}_{BC} along the parametric $g_{AB} - g_{BC}$ plane. As it can be seen, the prediction made from the behavior of $I^{\text{MB},B}_{BC}$ shown in Fig. 5(a), i.e., that $g^{\text{eff}}_{BC} - g_{BC} \sim -g_{AB}g_{AC}$, is readily confirmed.

To judge the quality of the applied effective model, in Figs. 5(c) and (d) we analyze the integrated densities of impurities B and C, respectively, for fixed $g_{AB} = 0.2$ and variable g_{AC}. We find reasonable agreement in the weakly- to intermediate-interacting regions marked by the blue shaded areas in panels (c) and (d). The many-body and effective model predictions deviate from the corresponding mean-field calculations, in some cases even qualitatively. This observation is consistent with the case of two B impurities, see Fig. 3.

To quantify the deviations of the effective two-body model from the many-body results, we sum over the relative differences of the integrated densities

$$\mathcal{E}^{\text{2b,eff}}_{BC} = \frac{\delta I^{\text{2b,eff},B}_{BC} + \delta I^{\text{2b,eff},C}_{BC}}{2}, \tag{23}$$

with $\delta I^{\text{2b,eff},\sigma}_{BC} = |I^{\text{MB},\sigma}_{BC} - I^{\text{2b,eff},\sigma}_{BC}|/I^{\text{MB},\sigma}_{BC}$. We estimate the deviations between the many-body and mean-field results in an analogous way, i.e., with $\mathcal{E}^{\text{MF}}_{BC}$ involving $\delta I^{\text{MF},\sigma}_{BC}$. In Fig. 5 (b) depicting g^{eff}_{BC}, we encircle the parametric regions where $\mathcal{E}^{\text{2b,eff}}_{BC} < 0.03$

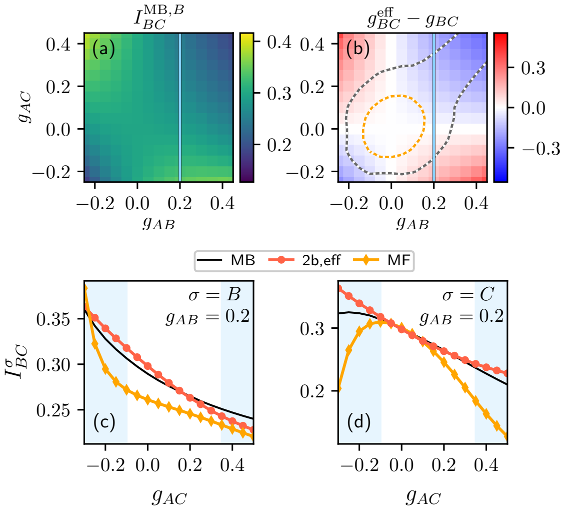

Figure 5. (a) Integrated one-body density of the impurity B (in the energetically higher well) as a function of the impurity-medium coupling strengths g_{AB} and g_{AC}. (b) Effective two-body interaction strength (subtracting g_{BC}) obtained from an effective two-body model [cf. Eq. (16)]. Integrated density of the (c) B and (d) C impurities for varying g_{AC} and fixed $g_{AB} = 0.2$ [see the vertical blue solid lines in panels (a) and (b)] obtained within the many-body (MB), mean-field (MF) and effective two-body model (2b,eff). The encircled parametric regions in panel (b) where $\mathcal{E}^{\mathrm{MF}}_{BC} < 0.03$ (orange-white dotted line) and where $\mathcal{E}^{\mathrm{2b,eff}}_{BC} < 0.03$ (gray-white dotted line) signify an extended range of validity of the effective two-body model compared to the mean-field results. The blue shaded areas in panels (c), (d) denote $\mathcal{E}^{\mathrm{2b,eff}}_{BC} > 0.03$. In all panels, the system consists of a weakly-interacting bosonic ultracold gas in a ring potential coupled to two impurities B and C interacting with $g_{BC} = 0.1$.

with a gray-white dotted line, while the ones characterized by $\mathcal{E}^{\mathrm{MF}}_{BC} < 0.03$ lie within the orange-white dotted line. It becomes apparent that the region of validity of the effective model is larger than that of the mean-field approximation. For the three-impurity system studied in the next section, we consider the parametric region where $\mathcal{E}^{\mathrm{2b,eff}}_{BC} < 0.03$ as the area where the two-body model provides a reliable starting point for investigation.

B. Two bosonic impurities and one distinguishable one

Finally, we consider a three-component mixture consisting of a bath A coupled to two bosonic B and one C impurities. Similarly to the case of three indistinguishable impurities (Section V), our goal here is to identify qualitative features of effective three-body interactions among the impurities, mediated by the bath. However, the important advantage of the present setting is that it encompasses two adjustable interaction parameters and not just one. This means that, besides g_{AB}, it is possible to also tune the interaction strength g_{AC}. Below, we analyze weakly-interacting impurities with $g_{BB} = g_{BC} = 0.1$.

As a first step, we examine the integrated one-body densities of the B and C impurities, see Figs. 6(a) and (b). A prominent difference between $I^{\mathrm{MB},B}_{BBC}$ and $I^{\mathrm{MB},C}_{BBC}$ is that the latter is larger in amplitude for $g_{AB}g_{AC} < 0$. This behavior does not necessarily allude to a three-body effect, since in these parameter regions we expect an induced two-body repulsion [22, 67, 78] among the B and C impurities. Repulsion implies that the two B impurities push the single C-impurity into the energetically higher site and hence $I^{\mathrm{MB},C}_{BBC}$ becomes larger. Therefore, in order to grasp the effects of a mediated three-body interaction on the one-body density, we need an effective three-body model.

We construct such a model by decomposing the energy of the system with three impurities $E^{(3)}_{BBC}$ in analogy to Eq. (18):

$$E^{(3)}_{BBC} = E^{(0)}_{A} + 2E^{\mathrm{pol}}_{B} + E^{\mathrm{pol}}_{C} + E^{\mathrm{pol}}_{BB} + 2E^{\mathrm{pol}}_{BC} + E^{\mathrm{pol}}_{BBC}. \tag{24}$$

In this expression, E^{pol}_{B}, E^{pol}_{C} are the energies of a single dressed impurity; E^{pol}_{BB} and E^{pol}_{BC} describe the impurity-impurity and E^{pol}_{BBC} the three-impurity energies. These energies are computed using the recipe of Section V. In particular, the single impurity energies are fitted to the effective one-body Hamiltonians $\hat{H}^{\mathrm{eff}}_{B}$ and $\hat{H}^{\mathrm{eff}}_{C}$. The energies E^{pol}_{BB} and E^{pol}_{BC} as well as the parameters g^{eff}_{BB}, g^{eff}_{BC} are obtained from the corresponding two-body models.

The three-impurity effective Hamiltonian reads

$$\begin{aligned}\hat{H}^{\mathrm{eff}}_{BBC} = &\sum_{i=1}^{2} \hat{H}^{\mathrm{eff}}_{B}(x^B_i) + \hat{H}^{\mathrm{eff}}_{C}(x^C) \\ &+ g^{\mathrm{eff}}_{BB}\delta(x^B_1 - x^B_2) + g^{\mathrm{eff}}_{BC}\sum_{i=1}^{2}\delta(x^B_i - x^C) \\ &+ g^{\mathrm{eff}}_{BBC}\delta(x^B_1 - x^B_2)\delta(x^B_2 - x^C).\end{aligned} \tag{25}$$

The last term describes the induced three-impurity correlations. The respective three-body interaction strength is tuned so that the ground-state energy of the effective model, E^{eff}_{BBC}, matches the right-hand side of Eq. (24).

In Figures 6(c) and (d) we present the three-polaron energy and the effective three-body interaction strength respectively, as a function of g_{AB} and g_{AC}. It can be discerned that the sign of the three-body interaction strength qualitatively obeys the relation $g^{\mathrm{eff}}_{BBC} \sim g^2_{AB}g_{AC}$. This property can be understood as a generalization of the case with three indistinguishable bosonic impurities where the sign of the three-body interaction strength follows $g^{\mathrm{eff}}_{BBB} \sim g^3_{AB}$. Note that the sign of the energy in Fig. 6(c) does not follow the simple prescription $g^2_{AB}g_{AC}$. Although the exact origin of this behavior is not clear, our interpretation is the following. In general, an accurate description of the system with three impurities (counterintuitively) requires a modification of the two-body

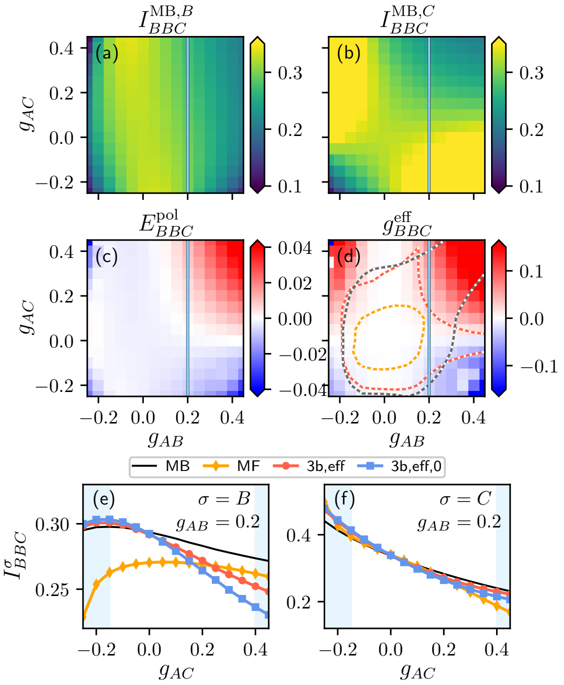

Figure 6. Integrated one-body density (across the energetically higher well) of the impurities (a) B and (b) C as a function of the impurity-medium coupling strengths g_{AB} and g_{AC}. (c) Three-polaron energy calculated from Eq. (24). (d) Effective three-body interaction strength in the parametric plane $g_{AB} - g_{AC}$, computed within the effective three-body model described by Eq. (25). Integrated density of impurities (e) B and (f) C for varying g_{AC} and fixed $g_{AB} = 0.2$ (see also blue lines in panels (a)-(d)) obtained within the many-body (MB), the mean-field (MF) and the effective three-body model with (3b,eff) and without (3b,eff,0) the three-body interaction term. In panel (d), we encircle the regions where $\mathcal{E}^{\mathrm{MF}}_{BBC} < 0.03$ (orange-white dotted line) and $\mathcal{E}^{\mathrm{3b,eff}}_{BBC} < 0.03$ (red-white dotted line). The region encircled by the gray dashed line denotes the range of applicability of the effective two-body model, where $\mathcal{E}^{\mathrm{2b,eff}}_{BBC} < 0.03$ holds. The blue shaded areas in (e) and (f) mark $\mathcal{E}^{\mathrm{2b,eff}}_{BBC} > 0.03$. The three-component system comprises of a weakly-interacting bosonic ultracold gas on a ring potential coupled to two B-impurities and one C-impurity with $g_{BB} = g_{BC} = 0.1$.

interaction, see the last term in Eq. (8). This interpretation is in agreement with our results in Fig. 4 where the three-impurity model does not describe the data accurately.

To explicate the impact of g^{eff}_{BBC} on the accuracy of the effective three-body model, in Figs. 6 (e) and (f), we compare its predictions in the presence ($I^{\mathrm{3b,eff},\sigma}_{BBC}$) and absence ($I^{\mathrm{3b,eff},0,\sigma}_{BBC}$) of the three-body term for the integrated one-body density to the many-body prediction ($I^{\mathrm{MB},\sigma}_{BBC}$), where $\sigma = B, C$. The results are shown for varying g_{AB} and fixed $g_{AB} = 0.2$. In view of the integrated densities of species B and C, it can be seen that including the three-body term always improves the model's prediction for the integrated one-body density, provided that the effective two-body model is accurate. The parameter region where the two-body model is judged to be adequate corresponds to the region defined by $\mathcal{E}^{\mathrm{2b,eff}}_{BBC} = (\delta I^{\mathrm{2b,eff},B}_{BC} + \delta I^{\mathrm{2b,eff},C}_{BC} + \delta I^{\mathrm{2b,eff},B}_{BB})/3 < 0.03$, see gray-white dotted line in Fig. 6(d). The regions where the two-body model looses its accuracy are marked by blue shaded areas in Figs. 6(e) and (f), where $\mathcal{E}^{\mathrm{2b,eff}}_{BBC} > 0.03$ holds. The region where the effective three-body model produces qualitatively good predictions for the integrated one-body densities corresponds to the region where $\mathcal{E}^{\mathrm{3b,eff}}_{BBC} = (\delta I^{\mathrm{3b,eff},B}_{BBC} + \delta I^{\mathrm{3b,eff},C}_{BBC})/2 < 0.03$, being encircled with a red-white dotted line in Fig. 6(d).

Finally, in order to further reveal the role of correlations we compare the many-body with the mean-field results and estimate the region where $\mathcal{E}^{\mathrm{MF}}_{BBC} = (\delta I^{\mathrm{MF},B}_{BBC} + \delta I^{\mathrm{MF},C}_{BBC})/2 < 0.03$, see the parametric region surrounded by the orange-white dotted line in Fig. 6(d). Similar to the two-impurity case (Section VI A), the region where the mean-field predictions are in good agreement with the many-body results for three impurities is limited to weak impurity-medium interactions g_{AB} and g_{AC}.

VII. CONCLUSIONS AND PERSPECTIVES

We have studied the emergence of two- and three-body mediated interactions for a few impurity atoms. These atoms are trapped by a tilted double-well potential and immersed in a bosonic host, which is confined to a one-dimensional ring trap. This simple setup is suggested to be a prototype for detecting effects of induced interactions. To achieve a comprehensive description of the underlying induced interactions, two- and three-component mixture settings have been considered. Particular attention has been given to how the impurity-medium coupling strength influences the imbalance in impurity population at different sites of the double-well potential. To elucidate the strength of induced interactions and their scaling behavior, effective two- and three-body models have been devised according to which the mediated interaction between the impurities is approximated by effective two- and three-body contact potentials.

The associated effective interaction strengths, determined by fitting to the respective polaron energies of the many-body system, are found to be either attractive or repulsive depending on the impurity-medium coupling. It is showcased that the two-body model predictions are in good agreement with the results obtained from an *ab initio* many-body approach. At the same time, the three-body effective models replicate many-body calculations only qualitatively, which we interpret as a general feature of the simplest three-polaron models. Additionally, we have compared the many-body results with relevant mean-field calculations, highlighting deviations in energies and densities. These discrepancies naturally originate from the absence of interspecies correlations that are neglected within the mean-field framework. For instance, it is known that the mean-field approach results in a faster localization of the impurity [79–81], in our case, at the energetically lower double-well site.

There are a number of possible follow-up studies that we find worth-pursuing. First, it is important to investigate the effect of temperature on our results. In general, one can expect that tight trapping of the impurities can help to circumvent one of the main problems in observing induced interactions, namely, the temperature of the bath. Indeed, trapping minimizes the excitation energy of the impurity, enhancing the effect of weak interactions. Second, it appears interesting to study mixtures with larger atom numbers to testify the robustness of the effective interactions. As we have shown the simplest effective models fail to provide quantitatively accurate results already for three impurities. In a similar vein, another perspective is to construct methods that are able to operate within the interaction regime of stronger intercomponent attractions where the strength of the effective interactions may be enhanced.

The generalization of the effective models to higher spatial dimensions as well as to Fermi/Bose systems containing fermionic or bosonic impurities can be a non-trivial extension [82, 83]. Similarly, it might be interesting to understand the role of three-body induced interactions for charged impurities [84]. Finally, we note that the double-well potential without a tilt may contain information about induced impurity-impurity interactions in a two-body correlation function, see, e.g., Ref. [85]. It appears interesting to study the impact of the induced three-body interaction in such a setting assuming a fine-tuned regime where the effect of the two-body induced potential is balanced by two-body free-space interactions. It seems natural to design a suitable radiofrequency spectroscopy scheme, which would allow to reveal properties of the dressed states such as lifetime, residue, effective mass and importantly identify effects of induced two- and three-body interactions.

ACKNOWLEDGEMENTS

S.I.M. acknowledges support from the University of Missouri Science and Technology, Department of Physics, in the framework of a startup fund. A.G.V. has been supported in part by the Danish National Research Foundation through the Center of Excellence “CCQ” (DNRF152). D.D. and P.S. acknowledge funding by the Cluster of Excellence “Advanced Imaging of Matter” of the Deutsche Forschungsgemeinschaft (DFG) - EXC 2056 - project ID 39071599.

Appendix A: Exact diagonalization method

In the following, we describe our approach to numerically solve the effective two and three-body models, given by Eqs. (16), (19), (22) and (25). We employ an exact diagonalization method in which the two- and three-body Hamiltonian matrix is constructed using corresponding two- and three-body basis states. These basis states are used to build a wave function (see below) which is inserted in the time-independent Schrödinger equation leading to a set of coupled linear equations,

$$\hat{H}^{(N_B),\mathrm{eff}}\mathbf{C}_n = E_n\mathbf{C}_n. \tag{A1}$$

Here, $\mathbf{C}_n$ represents the coefficient vector to the n-th eigenenergy. After diagonalization it is possible to assess the ground state energy and wave function. Exact diagonalization is a versatile method which has been employed, for instance, to systems consisting of few-body Bose mixtures [35, 86] or impurities coupled to a bosonic bath in a lattice [30]. Below, we outline the construction of the aforementioned basis-states for either three indistinguishable bosonic impurities or two bosonic and one distinguishable impurities.

1. Many-body basis for indistinguishable bosonic impurities

Let us assume $N_B = 2,3$ bosonic impurities. The statistical properties of the impurities are treated by expanding their wave function, $\Psi^{\mathrm{eff}}_{BB(B)}$, in terms of bosonic number states,

$$|\Psi^{\mathrm{eff}}_{BB(B)}\rangle = \sum_{i=1}^{\mathcal{D}_B} C_i|\vec{n}_i^B\rangle, \tag{A2}$$

where $\vec{n}_i^B = (n_1,\ldots,n_{d_B})$. The latter denotes the occupation distribution of N_B impurities over d_B SPFs, while simultaneously satisfying the constraint $\sum_i n_i = N_B$. This leads to a total number of $\mathcal{D}_B = (d_B+N_B-1)!/[N_B!(d_B-1)!]$ number states. We ensure convergence of the applied method by providing a sufficient number of SPFs from which the number-state basis is formed. As SPFs we choose the first $d_B = 8$ energetically lowest eigenstates $\{\varphi_i^B(x)\}_{i=1}^{d_B}$ of the single-particle Hamiltonian $\hat{h}_B^{(1)}$ describing one atom in a 1D tilted double-well potential [Eq. (2b)].

2. Distinguishable bosonic impurities

Next, we turn to a setting containing $N_B = 1,2$ bosonic impurities and another distinguishable impurity of species C, i.e., $N_C = 1$. The corresponding wave function ansatz, $\Psi^{\mathrm{eff}}_{B(B)C}$, has the form,

$$|\Psi^{\mathrm{eff}}_{B(B)C}\rangle = \sum_{i=1}^{\mathcal{D}_B}\sum_{j=1}^{d_C} C_{ij}|\vec{n}_i^B\rangle\otimes|\varphi_j^C\rangle, \tag{A3}$$

where the impurity C is described in terms of the eigenfunctions $\{\varphi_i^C(x)\}_{i=1}^{d_C}$ of the single-particle Hamiltonian $\hat{h}_C^{(1)}$. Analogously to Eq. (A2), the B-impurities are expanded in terms of number states, which reduce, in the case of $N_B = 1$, to a one-body basis. Finally, to solve this two- or three-body system, we evaluate the respective linear equation system given by the Schrödinger equation [cf. Eq. (A1)]. Throughout this work we consider $d_B = d_C = 8$ SPFs, which ensure the convergence of our simulations.

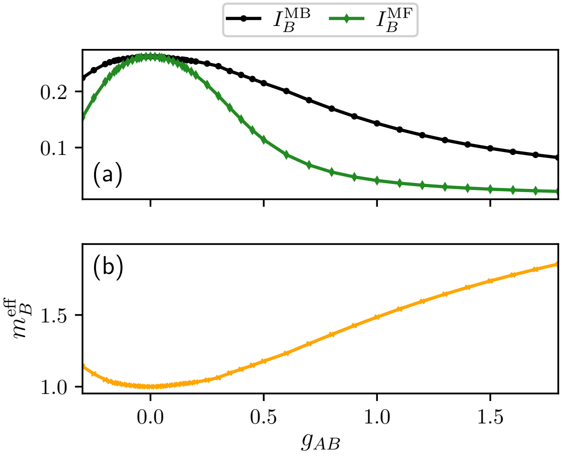

Figure 7. (a) Integrated one-body densities I_B^{MB} and I_B^{MF} computed within the many-body and mean-field approaches, respectively [see also Eq. (12)]. Here, a single impurity is trapped in a tilted double-well potential. The impurity is coupled via a contact interaction potential of strength g_{AB} to a weakly interacting bath ($g_{AA} = 0.1$) residing on a ring potential and containing $N_A = 12$ atoms. (b) Effective mass of the impurity extracted by fitting the integrated one-body density of an effective one-body model [Eq. (B1)] to I_B^{MB}.

Appendix B: A single impurity coupled to the bosonic host

For completeness, we investigate the scenario of a majority species A confined in a ring potential and being coupled to a single impurity B trapped in a tilted double-well potential. This system allows for explicit comparisons with the two (or three) impurity settings ultimately hinting towards the necessity to account for induced interactions.

The respective integrated one-body densities I_B^{MB} (over the energetically higher site) obtained from the many-body approach as a function of g_{AB} are presented in Fig. 7(a). As it can be seen, the density portion in the energetically elevated double-well site decreases as $|g_{AB}|$ increases indicating a localization of the impurity at the energetically lower site. Recall that a similar trend of the integrated density takes place for two or three bosonic impurities, see e.g. Fig. 3(b) and Fig. 4(b). Comparing the behaviors of the one- and two-impurity cases, I_B^{MB} and I_{BB}^{MB}, respectively, we find that the localization trend is stronger in the case of two non-interacting impurities (not shown) than the one of a single impurity. This suggests the presence of an induced attractive interaction. Moreover, this behavior is compared to I_B^{MF}, i.e., the integrated density obtained within a mean-field approximation. It is found that in general $I_B^{\mathrm{MF}} < I_B^{\mathrm{MB}}$ implying that correlations impede (but not eventually prevent) the impurity's localization Ref. [80, 81]).

Another important aspect of the dressed impurity that has not been estimated thus far is its effective mass. This may support the localization tendency of the impurities for varying interactions but also improve the agreement of the effective models with the many-body computations (see also Appendix C). For this reason, we construct an effective one-body description which in fact has been intensively used before and argued to provide an adequate approximation both for the static but also the dynamical properties of a single impurity [33, 87]. It reads

$$\hat{H}_B^{\mathrm{eff}'} = \epsilon_B^{\mathrm{pol}'} - \frac{\hbar^2}{2m_B^{\mathrm{eff}}}\partial_x^2 + V_B(x), \qquad \text{(B1)}$$

where $V_B(x)$ denotes the tilted double-well potential [Eq. (3)]. The energy difference $\epsilon_B^{\mathrm{pol}'}$ is chosen such that the ground-state energy of the effective model $\hat{H}_B^{\mathrm{eff}'}$ matches the polaron energy E_B^{pol} [Eq. (13)].

The crucial difference with the model described by Eq. (14) is the presence of the effective mass, m_B^{eff}. The latter is determined by varying m_B^{eff} such that the integrated one-body density of the effective model ($I_B^{\mathrm{1b,eff}}$) coincides with the many-body result (I_B^{MB}). This is achieved by minimizing the cost function $|I_B^{\mathrm{MB}} - I_B^{\mathrm{1b,eff}}|^2$. An overall accuracy of $\sim 10^{-10}$ is ensured within our simulations. In Fig. 7(b) we present the results for the effective mass as a function of g_{AB}. As shown, increasing $|g_{AB}|$ leads to a larger effective mass which is in accordance with the observed localization behavior of the impurities in the main text. Recall that within the main we argued that considering the bare impurity mass in the effective models improves the agreement with the many-body results. Below, in Appendix C, we exemplify the impact of the effective mass on the outcome of the effective two-body model.

Appendix C: Impact of the effective mass on the two-impurity behavior

Having at hand m_B^{eff} (see Appendix B) it is instructive to study its impact on the accuracy of the applied effective two-body model described in Section IV B. Indeed, the effective mass may be utilized to construct a corresponding effective two-body model,

$$\hat{H}_{BB}^{\mathrm{eff}'} = \sum_{i=1}^{2} \hat{H}_B^{\mathrm{eff}'}(x_i) + g_{BB}^{\mathrm{eff}'}\delta(x_1 - x_2), \qquad \text{(C1)}$$

where $\hat{H}_B^{\mathrm{eff}'}$ refers to the one-body Hamiltonian of Eq. (B1). Similarly to the prescription followed in Section IV B, the effective two-body interaction strength $g_{BB}^{\mathrm{eff}'}$ is estimated by demanding a matching of the ground-state energy of $\hat{H}_{BB}^{\mathrm{eff}'}$ with the energy $2E_B^{\mathrm{pol}} + E_{BB}^{\mathrm{pol}}$. In Fig. 8(a) we directly compare the effective two-body interaction strengths, g_{BB}^{eff} and $g_{BB}^{\mathrm{eff}'}$, corresponding to the two-body models without [Eq. (16)] and with [Eq. (C1)] an effective mass, respectively. It is evident that for small impurity-medium interaction strengths, g_{AB}, of either sign the effective coupling parameters extracted for the aforementioned different models agree well with each other while deviating for

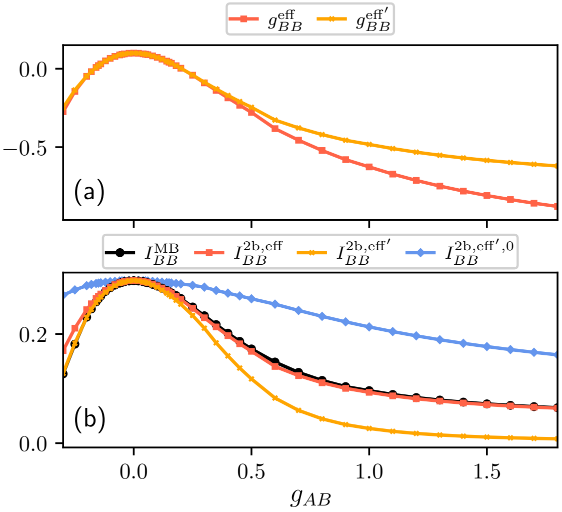

Figure 8. (a) Effective two-body interaction strengths g_{BB}^{eff} and $g_{BB}^{\mathrm{eff}'}$ extracted from the two-body models given by Eq. (16) and Eq. (C1), respectively. (b) Integrated one-body density obtained within the many-body approach (I_{BB}^{MB}) and with an effective two-body model which considers the bare impurity mass [$I_{BB}^{\mathrm{2b,eff}}$, Eq. (16)] and an effective mass [$I_{BB}^{\mathrm{2b,eff}'}$, Eq. (C1)]. The effect of the induced interaction is highlighted by a comparison to $I_{BB}^{\mathrm{eff}',0}$ corresponding to an effective two-body model which includes the effective mass but neglects the induced interaction, i.e., in Eq. (C1) we set $g_{BB}^{\mathrm{eff}'} \equiv g_{BB} = 0.1$. We consider two interacting ($g_{BB} = 0.1$) bosonic impurities, which are coupled to a bath consisting of $N_A = 12$ bosons featuring $g_{AA} = 0.1$.

larger repulsive g_{AB}. In particular, it appears that $g_{BB}^{\mathrm{eff}'}$ takes smaller absolute values than g_{BB}^{eff}.

To judge the quality of the applied methods, we additionally compare the respective integrated one-body densities, see Fig. 8(b). For repulsive g_{AB}, we find that the best agreement compared to the many-body results, I_{BB}^{MB}, occur for the integrated one-body density ($I_{BB}^{\mathrm{2b,eff}}$) calculated with the model described in Section IV B where the effective mass has been neglected. On the other hand, the integrated density corresponding to the model in Eq. (C1), $I_{BB}^{\mathrm{2b,eff}'}$, underestimates the many-body results for repulsive g_{AB}. However, for attractive g_{AB}, including the effective mass results in a better agreement between $I_{BB}^{\mathrm{eff}'}$ and I_{BB}^{MB}, while I_{BB}^{eff} overestimates the target results. This result is not straightforward, since a-priori one would expect an improvement of the model predictions when including the effective mass. Such an effect may emanate from different sources such as the rather complex potential landscape employed, or the fact that we operate far from the thermodynamic limit. To resolve this issue a careful analysis is required going even beyond the currently employed methods to exemplify the origin of this discrepancy which is left for future endeavors.

To reveal the effect of the induced interaction $g_{BB}^{\mathrm{eff}'}$ on the integrated density, we additionally calculate the observable $I_{BB}^{\mathrm{2b,eff}',0}$, obtained from an effective two-body model which includes the effective mass but does not consider the effects of the mediated interactions, i.e., in Eq. (C1) we set $g_{BB}^{\mathrm{eff}'} \equiv g_{BB} = 0.1$. It can be readily seen from Fig. 8(b), that $I_{BB}^{\mathrm{eff}',0}$ clearly deviates from I_{BB}^{MB} for $g_{AB} \neq 0$ and in fact yields (at least within the considered parameter range) always larger values than I_{BB}^{MB}. This indicates that, indeed, an attractive induced interaction strength is required to correctly capture the many-body results.

Appendix D: Correlation impact on one-body and two-body observables

In the following, we employ different ansatzes for the many-body wave function in order to unravel the role of correlations on one- and two-body observables. The many-body wave function of a general three-component mixture (see also Section III) is firstly expanded in terms of different D_A, D_B and D_C species functions. Setting $D_A = D_B = D_C = 1$, all intercomponent correlations are neglected rendering the total wave function [Eq. (10)] a single product state where each species is represented by a single species wave function. Note that each species wave function is expanded in terms of different SPFs accounting for intracomponent correlations. This approach is referred to as *species mean-field* (sMF) [67]. A step beyond this sMF ansatz is to allow entanglement formation solely between two of the species, while correlations with the third species are suppressed. This is accomplished, e.g. through $D_B = 1$ and $D_A, D_C > 1$, meaning that species A and C are correlated, experiencing a mean-field type potential from species B. We will dub this approach *species mean-field of species B* (sMFB). Analogously, one can define sMFA and sMFC.

As such it is possible to extract the impact of correlations between two different species on an arbitrary observable $\hat{O}$. For instance, to reveal the impact of correlations between species A and B, we calculate,

$$\Delta_{AB} = \langle \hat{O} \rangle_{\mathrm{sMFC}} - \langle \hat{O} \rangle_{\mathrm{sMF}}, \tag{D1}$$

where $\langle \hat{O} \rangle_X$ denotes the expectation value of $\hat{O}$ using the method $X = \mathrm{MB}, \mathrm{sMF}, \mathrm{sMFA}, \ldots$. In a next step, we can decompose the expectation value calculated within the full many-body method, i.e. $\langle \hat{O} \rangle_{\mathrm{MB}}$, in terms of contributions of different correlation orders as follows,

$$\langle \hat{O} \rangle_{\mathrm{MB}} = \langle \hat{O} \rangle_{\mathrm{sMF}} + \Delta_{\mathrm{2spec}} + \Delta_{\mathrm{3spec}}. \tag{D2}$$

Here, the expectation value $\langle \hat{O} \rangle_{\mathrm{MB}}$, which includes all relevant interspecies correlations, splits into a species mean-field part, $\langle \hat{O} \rangle_{\mathrm{sMF}}$, as well as a second- and third-order correlation term, $\Delta_{\mathrm{2spec}} = \Delta_{AB} + \Delta_{AC} + \Delta_{BC}$ and Δ_{3spec}. Specifically, we calculate Δ_{3spec} by subtracting the species mean-field and the second-order contribution from the many-body result $\langle \hat{O} \rangle_{\mathrm{MB}}$. More detailed discussions about such a decomposition can be found in Ref. [67].

Below, we focus on the setup of Section VI A, i.e., two distinguishable impurities B and C coupled to a

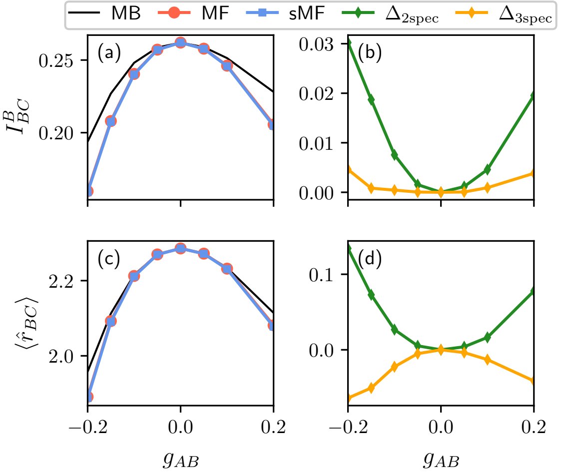

Figure 9. (a) Integrated one-body density of impurity B, I^B_{BC} [Eq. (12)], obtained within the full many-body (MB), mean-field (MF) and species mean-field (sMF) ansatz. (b) Contributions of the second- and third-order correlations on I^B_{BC}, see Eq. (D2). Impurities' relative distance, $\langle \hat{r}_{BC} \rangle$, by (c) using different numerical approaches (see legend) and (d) distinguishing second- and third-order correlation effects. We consider two distinguishable impurities B and C trapped in a tilted double-well potential coupled to a weakly interacting majority species A on a ring potential with $g_{BC} = 0$ and $g_{AB} = g_{AC}$.

bosonic majority species A where $g_{BC} = 0$. The integrated one-body density of species B, I^B_{BC} obtained within the many-body (MB), mean-field (MF) and sMF methods is presented in Fig. 9(a) as a function of $g_{AB} = g_{AC}$. As it can be seen, the MF and sMF predictions show a very good agreement indicating that the presence of correlations among the particles of species A do not play a decisive role for the behavior of the integrated density I^B_{BC}. Interestingly, a close comparison among the results obtained with the sMF and the MB approaches, unveils that the absence of interspecies correlations leads to a faster decrease of the density at the energetically higher double-well site. This clearly showcases that interspecies correlations hinder the impurities localization. In Figure 9(b) we resolve the discrepancy between the MB and sMF calculations in terms of two- and three-body effects. It turns out, that both contributions lead to an increase of the integrated density with the two-body ones naturally exhibiting the larger participation.

Next, we aim to generalize our observations by comparing correlation effects imprinted on two-body observables such as the impurities' relative distance $\langle \hat{r}_{BC} \rangle$ [32, 34]. Also inspection of this observable explicates that the presence of all correlations leads to an increase of the impurities relative distance, see Fig. 9(c). However, when resolving the impact of correlations in terms of second- and third order terms, we find that only two-component correlations are associated with an increase of $\langle \hat{r}_{BC} \rangle$, while the third order contribution is negative, see Fig. 9(d). This third-order mechanism is attributed to an induced effect, where the majority species A mediates correlations between the non-interacting impurities B and C. In particular, the shrinking of $\langle \hat{r}_{BC} \rangle$ can be interpreted as a correlation-induced attraction, which is in accordance with the effects reported in Refs. [67, 88].

Appendix E: Diverging three-body interaction

Here, we will show that the three-body interaction used in the main text, see Eq. (19), diverges logarithmically – similar to the contact interaction in 2D (see, e.g., Refs. [89, 90] and references therein). Therefore, we start with the following Hamiltonian of three particles in 1D with periodic boundary conditions:

$$H = -\frac{1}{2}\sum_{i=1}^{3}\frac{\partial^2}{\partial x_i^2} + g\delta(x_1 - x_2)\delta(x_2 - x_3). \tag{E1}$$

Since all interactions are translationally invariant, the total momentum of the system, P, is conserved. We can use this to eliminate one of the three coordinates by writing [87, 91, 92]

$$\Psi(x_2, x, y) = \tilde{\Psi}(x, y)e^{iPx_2}, \tag{E2}$$

where $x = x_1 - x_2 + \theta(x_2 - x_1)$, $y = x_3 - x_2 + \theta(x_2 - x_3)$ with $\theta(x)$ the Heaviside step function. This approach leads to the following Hamiltonian

$$H = -\left(\frac{\partial^2}{\partial x^2} + \frac{\partial^2}{\partial y^2} + \frac{\partial}{\partial y}\frac{\partial}{\partial x}\right) - g\delta(x)\delta(y). \tag{E3}$$

Note that this Hamiltonian is reminiscent of the Hamiltonian of a particle with mass $m = 2$ and a contact potential together with the additional mixed derivative term $\frac{\partial}{\partial x}\frac{\partial}{\partial y}$.

Next, we solve the Schrödinger equation in momentum space to show that this Hamiltonian diverges logarithmically,

$$k^2\Phi(\vec{k}) + k_x k_y \Phi(\vec{k}) + g\Psi(0) = E\Phi(\vec{k}). \tag{E4}$$

Rewriting this expression, inserting $\Psi(0) = \int \frac{d^2k'}{(2\pi)^2}\Phi(\vec{k}')$ and integrating over both sides in $\vec{k}$ we can write:

$$\begin{aligned} \int \frac{d^2k}{(2\pi)^2}\Phi(\vec{k}) &= \int \frac{d^2k}{(2\pi)^2}\frac{g}{-k^2 - k_x k_y + E}\int \frac{d^2k'}{(2\pi)^2}\Phi(\vec{k}') \\ 1 &= \int \frac{d^2k}{(2\pi)^2}\frac{g}{-k^2 - k_x k_y + E}. \end{aligned} \tag{E5}$$

With this expression, we can easily see that the integral is diverging logarithmically. We only run into problems for large values of $|k|$:

$$\int \frac{d^2k}{(2\pi)^2}\frac{g}{-k^2 - k_x k_y + E} \approx \int \frac{d^2k}{(2\pi)^2}\frac{g}{-k^2 - k_x k_y}. \tag{E6}$$

Next, we introduce polar coordinates to write

$$\int \frac{d^2k}{(2\pi)^2} \frac{g}{-k^2 - k_x k_y} = \int_0^\infty \frac{dkk}{(2\pi)^2} \times \int_0^{2\pi} d\phi \frac{g}{-k^2 - k^2 \sin\phi\cos\phi} = -\frac{g}{\sqrt{3}\pi} \int_0^\infty dk/k. \tag{E7}$$

It becomes apparent that this integral indeed diverges logarithmically.

As mentioned briefly in the main text, this is however not problematic for our approach. Since we solve the Schrödinger equation numerically with a fixed cutoff, the latter regularizes the above integral. We renormalize it by matching the three-body interaction strength g_{BBB} to the energy of the three quasiparticles. This approach is similar to common renormalization methods for Configuration-Interaction calculations in two-dimensional cold atom systems with contact interaction. In this context, the strength of the two-body interaction is determined by matching the bare value of the contact interaction strength to reproduce the same two-body ground state energy for each cutoff, see e.g. Ref. [89, 93].

[1] L. D. Landau, Über die bewegung der elektronen in kristallgitter, Phys. Z. Sowjetunion **3**, 3 (1933).

[2] S. I. Pekar, Autolocalization of the electron in an inertially polarizable dielectric medium, Zh. Eksp. Teor. Fiz **16**, 335 (1946).

[3] F. Chevy and C. Mora, Ultra-cold polarized fermi gases, Rep. Prog. Phys. **73**, 112401 (2010).

[4] P. Massignan, M. Zaccanti, and G. M. Bruun, Polarons, dressed molecules and itinerant ferromagnetism in ultracold Fermi gases, Rep. Prog. Phys. **77**, 034401 (2014).

[5] F. Scazza, M. Zaccanti, P. Massignan, M. M. Parish, and J. Levinsen, Repulsive Fermi and Bose Polarons in Quantum Gases, Atoms **10**, 55 (2022).

[6] F. Grusdt, N. Mostaan, E. Demler, and L. A. P. Ardila, Impurities and polarons in bosonic quantum gases: a review on recent progress, arXiv:2410.09413.

[7] P. Massignan, R. Schmidt, G. E. Astrakharchik, A. İmamoglu, M. Zwierlein, J. J. Arlt, and G. M. Bruun, Polarons in atomic gases and two-dimensional semiconductors, arXiv:2501.09618.

[8] A. Schirotzek, C.-H. Wu, A. Sommer, and M. W. Zwierlein, Observation of Fermi Polarons in a Tunable Fermi Liquid of Ultracold Atoms, Phys. Rev. Lett. **102**, 230402 (2009).

[9] M.-G. Hu, M. J. Van de Graaff, D. Kedar, J. P. Corson, E. A. Cornell, and D. S. Jin, Bose Polarons in the Strongly Interacting Regime, Phys. Rev. Lett. **117**, 055301 (2016).

[10] N. B. Jørgensen, L. Wacker, K. T. Skalmstang, M. M. Parish, J. Levinsen, R. S. Christensen, G. M. Bruun, and J. J. Arlt, Observation of Attractive and Repulsive Polarons in a Bose-Einstein Condensate, Phys. Rev. Lett. **117**, 055302 (2016).

[11] M. Cetina, M. Jag, R. S. Lous, J. T. M. Walraven, R. Grimm, R. S. Christensen, and G. M. Bruun, Decoherence of Impurities in a Fermi Sea of Ultracold Atoms, Phys. Rev. Lett. **115**, 135302 (2015).

[12] M. Cetina, M. Jag, R. S. Lous, I. Fritsche, J. T. M. Walraven, R. Grimm, J. Levinsen, M. M. Parish, R. Schmidt, M. Knap, and E. Demler, Ultrafast many-body interferometry of impurities coupled to a fermi sea, Science **354**, 96 (2016).

[13] M. G. Skou, T. G. Skov, N. B. Jørgensen, K. K. Nielsen, A. Camacho-Guardian, T. Pohl, G. M. Bruun, and J. J. Arlt, Non-equilibrium quantum dynamics and formation of the Bose polaron, Nat. Phys. **17**, 731 (2021).

[14] I. Bloch, J. Dalibard, and W. Zwerger, Many-body physics with ultracold gases, Rev. Mod. Phys. **80**, 885 (2008).

[15] J. Catani, G. Lamporesi, D. Naik, M. Gring, M. Inguscio, F. Minardi, A. Kantian, and T. Giamarchi, Quantum dynamics of impurities in a one-dimensional Bose gas, Phys. Rev. A **85**, 023623 (2012).

[16] A. N. Wenz, G. Zürn, S. Murmann, I. Brouzos, T. Lompe, and S. Jochim, From few to many: Observing the formation of a fermi sea one atom at a time, Science **342**, 457 (2013).

[17] R. Paredes, G. Bruun, and A. Camacho-Guardian, Interactions mediated by atoms, photons, electrons, and excitons, Phys. Rev. A **110**, 030101 (2024).

[18] Y. Kuramoto, *Quantum Many-Body Physics: A Perspective on Strong Correlations* (Springer Japan, 2020).

[19] A. Recati, J. N. Fuchs, C. S. Peça, and W. Zwerger, Casimir forces between defects in one-dimensional quantum liquids, Phys. Rev. A **72**, 023616 (2005).

[20] M. Bruderer, A. Klein, S. R. Clark, and D. Jaksch, Polaron physics in optical lattices, Phys. Rev. A **76**, 011605 (2007).

[21] M. Schecter and A. Kamenev, Phonon-Mediated Casimir Interaction between Mobile Impurities in One-Dimensional Quantum Liquids, Phys. Rev. Lett. **112**, 155301 (2014).

[22] F. Brauneis, H.-W. Hammer, M. Lemeshko, and A. Volosniev, Impurities in a one-dimensional Bose gas: The flow equation approach, SciPost Phys. **11**, 008 (2021).

[23] A. Petković and Z. Ristivojevic, Mediated interaction between polarons in a one-dimensional Bose gas, Phys. Rev. A **105**, L021303 (2022).

[24] D. Huber, H.-W. Hammer, and A. G. Volosniev, In-medium bound states of two bosonic impurities in a one-dimensional fermi gas, Phys. Rev. Research **1**, 033177 (2019).

[25] M. Will, G. E. Astrakharchik, and M. Fleischhauer, Polaron Interactions and Bipolarons in One-Dimensional Bose Gases in the Strong Coupling Regime, Phys. Rev. Lett. **127**, 103401 (2021).

[26] Y. Guo and H. Tajima, Medium-induced bosonic clusters in a bose-fermi mixture: Toward simulating cluster formations in neutron-rich matter, Phys. Rev. A **109**, 013319 (2024).

[27] S. Dutta and E. J. Mueller, Variational study of polarons and bipolarons in a one-dimensional bose lattice gas in both the superfluid and the mott-insulator regimes, Phys. Rev. A **88**, 053601 (2013).

[28] M. Pasek and G. Orso, Induced pairing of fermionic impurities in a one-dimensional strongly correlated

Bose gas, Phys. Rev. B **100**, 245419 (2019).

[29] K. Keiler, S. I. Mistakidis, and P. Schmelcher, Doping a lattice-trapped bosonic species with impurities: From ground state properties to correlated tunneling dynamics, New J. Phys. **22**, 083003 (2020).

[30] F. Isaule, A. Rojo-Francàs, and B. Juliá-Díaz, Bound impurities in a one-dimensional Bose lattice gas: Low-energy properties and quench-induced dynamics, SciPost Phys. Core **7**, 049 (2024).

[31] A. S. Dehkharghani, A. G. Volosniev, and N. T. Zinner, Coalescence of Two Impurities in a Trapped One-dimensional Bose Gas, Phys. Rev. Lett. **121**, 080405 (2018).

[32] S. I. Mistakidis, G. C. Katsimiga, G. M. Koutentakis, and P. Schmelcher, Repulsive Fermi polarons and their induced interactions in binary mixtures of ultracold atoms, New J. Phys. **21**, 043032 (2019).

[33] S. I. Mistakidis, A. G. Volosniev, and P. Schmelcher, Induced correlations between impurities in a one-dimensional quenched Bose gas, Phys. Rev. Research **2**, 023154 (2020).

[34] S. I. Mistakidis, G. M. Koutentakis, G. C. Katsimiga, T. Busch, and P. Schmelcher, Many-body quantum dynamics and induced correlations of Bose polarons, New J. Phys. **22**, 043007 (2020).

[35] T. D. Anh-Tai, T. Fogarty, S. de María-García, T. Busch, and M. A. García-March, Engineering impurity bell states through coupling with a quantum bath, Phys. Rev. Research **6**, 043042 (2024).

[36] B. J. DeSalvo, K. Patel, G. Cai, and C. Chin, Observation of fermion-mediated interactions between bosonic atoms, Nature **568**, 61 (2019).

[37] A. L. Gaunt, T. F. Schmidutz, I. Gotlibovych, R. P. Smith, and Z. Hadzibabic, Bose-einstein condensation of atoms in a uniform potential, Phys. Rev. Lett. **110**, 200406 (2013).

[38] R. Folman, P. Krüger, D. Cassettari, B. Hessmo, T. Maier, and J. Schmiedmayer, Controlling cold atoms using nanofabricated surfaces: Atom chips, Phys. Rev. Lett. **84**, 4749 (2000).

[39] P. Krüger, S. Hofferberth, I. E. Mazets, I. Lesanovsky, and J. Schmiedmayer, Weakly interacting bose gas in the one-dimensional limit, Phys. Rev. Lett. **105**, 265302 (2010).

[40] S. Fölling, S. Trotzky, P. Cheinet, M. Feld, R. Saers, A. Widera, T. Müller, and I. Bloch, Direct observation of second-order atom tunnelling, Nature **448**, 1029 (2007).

[41] S. Levy, E. Lahoud, I. Shomroni, and J. Steinhauer, The ac and dc josephson effects in a bose–einstein condensate, Nature **449**, 579 (2007).

[42] T. Sowiński and M. Ángel García-March, One-dimensional mixtures of several ultracold atoms: A review, Rep. Prog. Phys. **82**, 104401 (2019).

[43] A. Minguzzi and P. Vignolo, Strongly interacting trapped one-dimensional quantum gases: Exact solution, AVS Quantum Science **4**, 027102 (2022).

[44] S. Mistakidis, A. Volosniev, R. Barfknecht, T. Fogarty, Th. Busch, A. Foerster, P. Schmelcher, and N. Zinner, Few-body Bose gases in low dimensions—A laboratory for quantum dynamics, Phys. Rep. **1042**, 1 (2023).

[45] L. Cao, V. Bolsinger, S. I. Mistakidis, G. M. Koutentakis, S. Krönke, J. M. Schurer, and P. Schmelcher, A unified ab initio approach to the correlated quantum dynamics of ultracold fermionic and bosonic mixtures, J. Chem. Phys. **147**, 044106 (2017).

[46] L. Cao, S. Krönke, O. Vendrell, and P. Schmelcher, The multi-layer multi-configuration time-dependent Hartree method for bosons: Theory, implementation, and applications, J. Chem. Phys. **139**, 134103 (2013).

[47] S. Krönke, L. Cao, O. Vendrell, and P. Schmelcher, Non-equilibrium quantum dynamics of ultra-cold atomic mixtures: The multi-layer multi-configuration time-dependent Hartree method for bosons, New J. Phys. **15**, 063018 (2013).

[48] M. Olshanii, Atomic Scattering in the Presence of an External Confinement and a Gas of Impenetrable Bosons, Phys. Rev. Lett. **81**, 938 (1998).

[49] D. R. Dounas-Frazer, A. M. Hermundstad, and L. D. Carr, Ultracold Bosons in a Tilted Multilevel Double-Well Potential, Phys. Rev. Lett. **99**, 200402 (2007).

[50] L. D. Carr, D. R. Dounas-Frazer, and M. A. Garcia-March, Dynamical realization of macroscopic superposition states of cold bosons in a tilted double well, Europhys. Lett. **90**, 10005 (2010).

[51] J. Erdmann, S. I. Mistakidis, and P. Schmelcher, Correlated tunneling dynamics of an ultracold Fermi-Fermi mixture confined in a double well, Phys. Rev. A **98**, 053614 (2018).

[52] C. Chin, R. Grimm, P. Julienne, and E. Tiesinga, Feshbach resonances in ultracold gases, Rev. Mod. Phys. **82**, 1225 (2010).

[53] T. M. Bersano, V. Gokhroo, M. A. Khamehchi, J. D'Ambroise, D. J. Frantzeskakis, P. Engels, and P. G. Kevrekidis, Three-component soliton states in spinor F=1 Bose-Einstein condensates, Phys. Rev. Lett. **120**, 063202 (2018).

[54] S. Lannig, C.-M. Schmied, M. Prüfer, P. Kunkel, R. Strohmaier, H. Strobel, T. Gasenzer, P. G. Kevrekidis, and M. K. Oberthaler, Collisions of Three-Component Vector Solitons in Bose-Einstein Condensates, Phys. Rev. Lett. **125**, 170401 (2020).

[55] A. Romero-Ros, G. C. Katsimiga, S. I. Mistakidis, S. Mossman, G. Biondini, P. Schmelcher, P. Engels, and P. G. Kevrekidis, Experimental Realization of the Peregrine Soliton in Repulsive Two-Component Bose-Einstein Condensates, Phys. Rev. Lett. **132**, 033402 (2024).

[56] B. E. Sherlock, M. Gildemeister, E. Owen, E. Nugent, and C. J. Foot, Time-averaged adiabatic ring potential for ultracold atoms, Phys. Rev. A **83**, 043408 (2011).

[57] T. A. Bell, J. A. P. Glidden, L. Humbert, M. W. J. Bromley, S. A. Haine, M. J. Davis, T. W. Neely, M. A. Baker, and H. Rubinsztein-Dunlop, Bose–Einstein condensation in large time-averaged optical ring potentials, New J. Phys. **18**, 035003 (2016).

[58] M. Egorov, B. Opanchuk, P. Drummond, B. V. Hall, P. Hannaford, and A. I. Sidorov, Measurement of s-wave scattering lengths in a two-component Bose-Einstein condensate, Phys. Rev. A **87**, 053614 (2013).

[59] L. D. Landau and E. M. Lifshitz, *Quantum mechanics*, 3rd ed., edited by J. Menzies (Butterworth-Heinemann, Oxford, England, 1981).

[60] P. Naidon, Two Impurities in a Bose–Einstein Condensate: From Yukawa to Efimov Attracted Polarons, J. Phys. Soc. Jpn. **87**, 043002 (2018).

[61] G. Panochko and V. Pastukhov, Static impurities in a weakly interacting Bose gas, Atoms **10**, 19 (2022).

[62] J. Jager and R. Barnett, The effect of boson–boson interaction on the bipolaron formation, New J. Phys. **24**, 103032 (2022).

[63] M. Drescher, M. Salmhofer, and T. Enss, Medium-induced interaction between impurities in a bose-einstein condensate, Phys. Rev. A **107**, 063301 (2023).

[64] B. Reichert, Z. Ristivojevic, and A. Petković, The Casimir-like effect in a one-dimensional Bose gas, New J. Phys. **21**, 053024 (2019).

[65] A. U. J. Lode, C. Lévêque, L. B. Madsen, A. I. Streltsov, and O. E. Alon, Colloquium: Multiconfigurational time-dependent hartree approaches for indistinguishable particles, Rev. Mod. Phys. **92**, 011001 (2020).

[66] K. Keiler, S. I. Mistakidis, and P. Schmelcher, Polarons and their induced interactions in highly imbalanced triple mixtures, Phys. Rev. A **104**, L031301 (2021).

[67] F. Theel, S. I. Mistakidis, and P. Schmelcher, Crossover from attractive to repulsive induced interactions and bound states of two distinguishable Bose polarons, SciPost Phys. **16**, 023 (2024).

[68] R. Horodecki, P. Horodecki, M. Horodecki, and K. Horodecki, Quantum entanglement, Rev. Mod. Phys. **81**, 865 (2009).

[69] G. Vidal and R. F. Werner, Computable measure of entanglement, Phys. Rev. A **65**, 032314 (2002).

[70] M. B. Plenio, Logarithmic Negativity: A Full Entanglement Monotone That is not Convex, Phys. Rev. Lett. **95**, 090503 (2005).

[71] E. Schmidt, Zur Theorie der linearen und nichtlinearen Integralgleichungen: I. Teil: Entwicklung willkürlicher Funktionen nach Systemen vorgeschriebener, Math. Ann. **63**, 433 (1907).

[72] A. Ekert and P. L. Knight, Entangled quantum systems and the Schmidt decomposition, Am. J. Phys. **63**, 415 (1995).

[73] S. I. Mistakidis, F. Grusdt, G. M. Koutentakis, and P. Schmelcher, Dissipative correlated dynamics of a moving impurity immersed in a Bose–Einstein condensate, New J. Phys. **21**, 103026 (2019).

[74] F. Theel, K. Keiler, S. I. Mistakidis, and P. Schmelcher, Entanglement-assisted tunneling dynamics of impurities in a double well immersed in a bath of lattice trapped bosons, New J. Phys. **22**, 023027 (2020).

[75] M. Pyzh and P. Schmelcher, Breathing dynamics of the few-body Bose polaron in a species-selective harmonic trap, Phys. Rev. A **105**, 043304 (2022).

[76] A. Camacho-Guardian and G. M. Bruun, Landau Effective Interaction between Quasiparticles in a Bose-Einstein Condensate, Phys. Rev. X **8**, 031042 (2018).

[77] L. Pricoupenko, Three-body pseudopotential for atoms confined in one dimension, Phys. Rev. A **99**, 012711 (2019).

[78] B. Reichert, A. Petković, and Z. Ristivojevic, Field-theoretical approach to the Casimir-like interaction in a one-dimensional Bose gas, Phys. Rev. B **99**, 205414 (2019).

[79] E. Timmermans, Phase Separation of Bose-Einstein Condensates, Phys. Rev. Lett. **81**, 5718 (1998).

[80] L. Zschetzsche and R. E. Zillich, Suppression of polaron self-localization by correlations, Phys. Rev. Research **6**, 023137 (2024).

[81] D. Breu, E. Vidal Marcos, M. Will, and M. Fleischhauer, Impurities in a trapped one-dimensional bose gas of arbitrary interaction strength: Localization-delocalization transition and absence of self-localization, Phys. Rev. A **111**, 023326 (2025).

[82] H. Tajima, J. Takahashi, S. Mistakidis, E. Nakano, and K. Iida, Polaron Problems in Ultracold Atoms: Role of a Fermi Sea across Different Spatial Dimensions and Quantum Fluctuations of a Bose Medium, Atoms **9**, 18 (2021).

[83] C. Baroni, B. Huang, I. Fritsche, E. Dobler, G. Anich, E. Kirilov, R. Grimm, M. A. Bastarrachea-Magnani, P. Massignan, and G. M. Bruun, Mediated interactions between Fermi polarons and the role of impurity quantum statistics, Nat. Phys. **20**, 68–73 (2023).

[84] G. E. Astrakharchik, L. A. P. Ardila, K. Jachymski, and A. Negretti, Many-body bound states and induced interactions of charged impurities in a bosonic bath, Nat. Commun. **14**, 1647 (2023).

[85] F. Theel, S. I. Mistakidis, K. Keiler, and P. Schmelcher, Counterflow dynamics of two correlated impurities immersed in a bosonic gas, Phys. Rev. A **105**, 053314 (2022).

[86] T. D. Anh-Tai, M. A. García-March, T. Busch, and T. Fogarty, Quantum correlations and spatial localization in trapped one-dimensional ultra-cold Bose-Bose-Bose mixtures, arXiv:2501.15358.

[87] S. I. Mistakidis, A. G. Volosniev, N. T. Zinner, and P. Schmelcher, Effective approach to impurity dynamics in one-dimensional trapped Bose gases, Phys. Rev. A **100**, 013619 (2019).

[88] J. Chen, J. M. Schurer, and P. Schmelcher, Entanglement Induced Interactions in Binary Mixtures, Phys. Rev. Lett. **121**, 043401 (2018).

[89] M. Rontani, G. Eriksson, S. Åberg, and S. Reimann, On the renormalization of contact interactions for the configuration-interaction method in two-dimensions, J. Phys. B: At. Mol. Opt. Phys. **50**, 065301 (2017).

[90] S.-L. Nyeo, Regularization methods for delta-function potential in two-dimensional quantum mechanics, Am. J. Phys. **68**, 571 (2000).

[91] E. Gross, Motion of foreign bodies in boson systems, Ann. Phys. **19**, 234 (1962).

[92] M. D. Girardeau, Reduction of a quantum n-body problem to an (n-1)-body problem, Phys. Rev. A **28**, 3635 (1983).

[93] F. Brauneis, H.-W. Hammer, S. M. Reimann, and A. G. Volosniev, Comparison of renormalized interactions using one-dimensional few-body systems as a testbed, Phys. Rev. A **111**, 013303 (2025).

arXiv:2412.01517v2 [cond-mat.quant-gas] 16 Dec 2024

Chirally-protected state manipulation by tuning one-dimensional statistics

F. Theel,[1] M. Bonkhoff,[2] P. Schmelcher,[1, 3] T. Posske,[2, 3] and N.L. Harshman[4]
[1] *Center for Optical Quantum Technologies, Department of Physics,*
University of Hamburg, Luruper Chaussee 149, 22761 Hamburg Germany
[2] *I. Institute for Theoretical Physics, Universität Hamburg, Notkestraße 9, 22607 Hamburg, Germany*
[3] *The Hamburg Centre for Ultrafast Imaging, University of Hamburg,*
Luruper Chaussee 149, 22761 Hamburg, Germany
[4] *Physics Department, American University, Washington, DC 20016, USA*

Chiral symmetry is broken by typical interactions in lattice models, but the statistical interactions embodied in the anyon-Hubbard model are an exception. It is an example of a correlated hopping model in which chiral symmetry protects a degenerate zero-energy subspace. Complementary to the traditional approach of anyon braiding in real space, we adiabatically evolve the statistical parameter in the anyon-Hubbard model and we find non-trivial Berry phases and holonomies in this chiral subspace. The corresponding states possess stationary checkerboard pattern in their N-particle densities which are preserved under adiabatic manipulation. We give an explicit protocol for how these chirally-protected zero energy states can be prepared, observed, validated, and controlled.

In two dimensions, Abelian braid anyons with fractional exchange statistics arise from the topological analysis of two-body interactions [1–6], and non-Abelian anyons of various forms have been proposed as the working material for robust topological quantum computing protocols [7, 8]. However, non-standard exchange statistics are not an exclusively two-dimensional phenomenon. Their key features have been proposed and investigated in one-dimensional systems since the beginning of the field [1, 9–19], leading to experimental proposals [20–25] and recent realizations in Raman-coupled Bose-Einstein condensates [26, 27]. This, for the first time, opens the possibility to tune the statistical angle of anyons in an experimentally accessible platform.

The anyon-Hubbard model provides the platform for this exploration [15, 28–30]. It realizes exchange statistics with a statistical angle θ that interpolates between bosons $\theta = 0$ and fermions $\theta = \pi$ are implemented on a one-dimensional lattice using Floquet-manipulated Rb atoms in quantum gas microscopes [31] by density-dependent Peierls phases [32–34]. Such phases lead to intriguing effects, including statistically induced phase transitions [15, 28, 35], quasi-condensation at finite momenta [15, 28], emerging Friedel oscillations [29, 30, 36], as well as asymmetrical transport and expansion dynamics. [37, 38].

Although the anyons realized by the anyon-Hubbard model are Abelian, their non-standard exchange statistics reveals topological structures in configuration space which we propose to be exploited for non-Abelian state manipulation. To motivate this, consider that the density-dependent Peierls phases which implement the statistical interaction can induce synthetic magnetic fluxes through plaquettes in configuration space [19, 31]. In the anyon-Hubbard model, these fluxes provide a phase $\exp(\pm i\theta)$ depending on the order in which the particles exchange; see Fig. 1(a). Many models in which underlying canonical particles experience correlated hopping processes share this feature, including [32, 33, 38–42]. Such correlated hopping processes can be engineered to break parity and time-reversal symmetry [43]. However, correlated hopping models with only nearest-neighbor hopping processes, such as the anyon-Hubbard model, preserve the chiral symmetry associated with bipartite lattices, a symmetry that is broken when non-statistical interactions are included [44, 45]. As a result, theorems about bipartite spatial lattices [46–49] can be generalized from real space to configuration space in models with chirally symmetric interactions and particle number conservation.

In this article, we show that one-dimensional lattice anyons with only statistical interactions host a degenerate zero energy subspace protected by chiral symmetry. Adiabatically tuning the statistical angle θ from 0 to 2π varies all energy levels in the spectrum except for the zero-energy modes, as shown in Fig. 1(b1-b2). In this space, the variation generates nontrivial holonomies [50, 51], i.e., unitary transformations similar to braiding non-Abelian two-dimensional anyons around each other [8]. This scheme can be used for chiral-protected non-Abelian state preparation. Building on theorems of Lieb and Sutherland [46, 47], we find that these results hold for the experimentally accessible anyon-Hubbard model and extend to chirally symmetric correlated hopping models of bosons with particle number conservation. In these models, chiral symmetry equips the configuration space with a stationary checkerboard pattern that can be experimentally revealed by the N-body density correlations and the spatially off-diagonal correlation functions of zero energy states and the quasi-momentum distribution. We furthermore show how these zero energy states can be prepared from typical initial states and manipulated by steering the statistical angle.

Chiral symmetry and correlated hopping.— For a particle-number conserving bosonic system, a chiral sym-

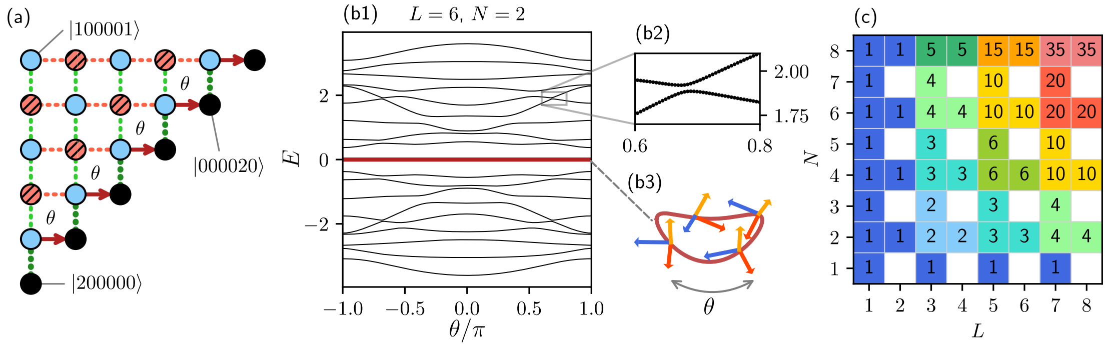

	1	2	3	4	5	6	7	8
8	1	1	5	5	15	15	35	35
7	1		4		10		20	
6	1	1	4	4	10	10	20	20
5	1		3		6		10	
4	1	1	3	3	6	6	10	10
3	1		2		3		4	
2	1	1	2	2	3	3	4	4
1	1		1		1		1	

FIG. 1. Configuration space representation of the anyon-Hubbard model and its chirally-protected zero energy subspace $\mathcal{H}_0$. (a) Bosonic configuration space for $N = 2$ particles on $L = 6$ sites. Each dot represents a bosonic number state with doubly-occupied sites (black) and singly-occupied (not black) and with positive chirality (black, red hashed) or negative chirality (plain blue). The edges represent hopping processes with amplitude $-J$ (thin), $-\sqrt{2}J$ (thick, dotted), and $-\sqrt{2}Je^{i\theta}$ (arrow). Boundary plaquettes have a flux with a density-dependent Peierls phase θ through them. (b1) Energy spectrum as a function of the statistical angle θ. The zero energy subspace has dimension $d_0 = 3$ for $N = 2$ and $L = 6$ (red line) without avoided crossings (inset (b2)). (b3) Schematic rotation of $\mathcal{H}_0$ by cyclic manipulation of θ. (c) The minimal degeneracy d_0 of $\mathcal{H}_0$.

metry corresponds to a unitary operator $\hat{S}$ that anticommutes with the Hamiltonian $[\hat{S}, \hat{H}]_+ = -\hat{H}$ [52–54]. Such an operator is an involution $\hat{S}^2 = 1$ that partitions the finite-dimensional Hilbert space into chiral eigenspaces $\mathcal{H} = \mathcal{H}_+ \oplus \mathcal{H}_-$ with eigenvalues $\chi = \pm 1$ and dimensions $\dim \mathcal{H}_\pm = d_\pm$. $\hat{H}$ is anti-block diagonal in the chiral basis and has a symmetric spectrum. Therefore, the zero energy eigenspace $\mathcal{H}_0$ has dimension $d_0 \geq |d_+ - d_-|$ [46–49, 55]. This minimal degeneracy of the zero energy subspace d_0 does not depend on the details of the Hamiltonian and is protected against perturbations that preserves chiral symmetry.

For N spinless bosons on a one-dimensional lattice with L sites, the operator $\hat{S}$ that realizes chiral symmetry for nearest-neighbor correlated-hopping models is [44, 45, 53]:

$$\hat{S} = \exp\left(i\pi \sum_{k=1}^{L} k\hat{n}_k\right), \tag{1}$$

where $\hat{n}_k = \hat{b}_k^\dagger \hat{b}_k$ is the number operator on site k. The operator $\hat{S}$ transforms bosonic operators as $\hat{S}\hat{b}_k\hat{S} = (-1)^k \hat{b}_k$ and acts like a local gauge transformation in configuration space that assigns opposite chirality to adjacent number states, i.e., number states that differ by a single hop have opposite chirality. See Fig. 1(a) for a depiction of $L = 6$ and $N = 2$, where the chiral operator partitions the 21-site configuration space lattice into a checkerboard of sublattices with $d_+ = 12$ and $d_- = 9$ chiral number states, respectively. Chiral symmetry together with particle-number conservation guarantees that this system has at least $d_0 = |d_+ - d_-| = 3$ zero-energy states with positive chirality, although the specific subspace $\mathcal{H}_0 \subset \mathcal{H}_+$ spanned by these three states depends on the Hamiltonian. Note that additional pairwise zero energy subspace degeneracies can only appear due to other non-Abelian symmetries or special accidental degeneracies. In particular, the non-interacting Bose-Hubbard model with $L = 8$ and $N \geq 3$ has additional degeneracies at $E = 0$ because of the trigonometric relation $\cos(\pi/9) + \cos(5\pi/9) + \cos(7\pi/9) = 0$. These accidental, cyclotomic degeneracies are akin to the Pythagorean degeneracies of the infinite square well. They occur in pairs that split upon variation from $\theta = 0$ and are therefore not chirally-protected.

On the zero energy subspace, the chiral operator $\hat{S}$ is promoted to an actual symmetry, because $\mathcal{H}_0$ is a subspace of the majority chirality eigenspace $\mathcal{H}_\pm$ [46, 47, 49, 55]. This implies that all correlation functions vanish which are not invariant with respect to $\hat{S}$. For example, the operator $\hat{b}_j^\dagger \hat{b}_{j+1}$ has odd chirality and therefore has a vanishing expectation value for every state in $\mathcal{H}_0$. Remarkably, we find for $N < L$ an analogous pattern in the N-particle densities. States in the zero energy subspace have support exclusively on the majority sublattice [46, 47, 56], forming an higher-dimensional generalization of a checkerboard pattern. The scenario of spontaneous symmetry breaking in the thermodynamic limit is ruled out by Elitzur's theorem [57–59].

For general N and L, the dimension of the chirally-protected zero energy subspace can be derived using combinatorics [49, 60, 61] and is depicted in Fig. 1(c):

$$d_0 = \begin{cases} 0 & \text{for } N \text{ odd and } L \text{ even} \\ \frac{(\lceil L/2 \rceil + \lfloor N/2 \rfloor - 1)!}{(\lceil L/2 \rceil - 1)! \lfloor N/2 \rfloor !} & \text{else,} \end{cases} \tag{2}$$

where $\lfloor A \rfloor$ and $\lceil A \rceil$ are the floor and ceiling function of A, respectively. The majority chiral subspace is $\mathcal{H}_+$ for N even and $\mathcal{H}_-$ for N odd and L odd.

Model.— The statistical interactions of the anyon-Hubbard model are chirally symmetric, in contrast to ordinary Hubbard-type interactions. They embody momentum-dependent interactions that are periodic in the statistical angle θ. The model is defined in terms of anyonic operators $\hat{a}_j$ with deformed commutation relations that obey fractional exchange statistics

$$\begin{aligned} \hat{a}_j\hat{a}_k^\dagger - e^{-i\theta \mathrm{sgn}(j-k)}\hat{a}_k^\dagger\hat{a}_j &= \delta_{jk} \\ \hat{a}_j\hat{a}_k - e^{i\theta \mathrm{sgn}(j-k)}\hat{a}_k\hat{a}_j &= 0. \end{aligned} \tag{3}$$

The Hamiltonian with L sites takes the form

$$H(\theta) = -J\sum_{j=1}^{L-1}\left(\hat{a}_{j+1}^\dagger\hat{a}_j + \mathrm{h.c.}\right). \tag{4}$$

The model is mapped to canonical bosons by a fractional Jordan-Wigner transformation $\hat{a}_j = \hat{b}_j e^{i\theta\sum_{l<j}\hat{n}_l}$ [15]:

$$\hat{H}(\theta) = -J\sum_{j=1}^{L-1}\left(\hat{b}_{j+1}^\dagger e^{-i\theta\hat{n}_j}\hat{b}_j + \mathrm{h.c}\right). \tag{5}$$

This results in a correlated hopping process mediated by a density-dependent Peierls phase.

Properties of the zero energy subspace.— We investigate the properties of the zero energy subspace by exact diagonalization and find the dimension of the zero energy subspace d_0 typically assumes its minimal value according to Eq. (2) as expected when the only symmetries are Abelian. Additional accidental degeneracies appear for special N and L at $\theta = 0$ that are not chirally-protected and unsuitable for adiabatic manipulation.

We first construct a convenient basis for the zero energy subspace at $\theta = 0$ (non-interacting bosons) and use this as a experimentally-verifiable starting point for state manipulation. The single-particle operators

$$\hat{c}_\nu = \sqrt{\frac{2}{L+1}}\sum_{k=1}^{L}\sin(q_\nu k)\,\hat{b}_k, \quad q_\nu = \frac{\pi\nu}{L+1} \tag{6}$$

diagonalize the Hamiltonian $\hat{H} = \sum_{\nu=1}^{L}\epsilon_\nu\hat{c}_\nu^\dagger\hat{c}_\nu$ with $\epsilon_\nu = -2J\cos(q_\nu)$. These operators satisfy the chirality relation $\hat{S}^\dagger\hat{c}_\nu\hat{S} = \hat{c}_{L-\nu+1}$ with $\epsilon_\nu = -\epsilon_{L-\nu+1}$.

From these L single-particle states, we can construct a d_0-dimensional basis of N-particle non-interacting states with zero energy and definite chirality. First, note that for L odd the single-particle state $|s\rangle \equiv c_{(L+1)/2}^\dagger|0\rangle$ has zero energy and chirality $\chi_s = -1$. Second, two-particle states of the form

$$|p(\mu)\rangle \equiv \hat{S}^\dagger\hat{c}_\mu^\dagger\hat{S}\hat{c}_\mu^\dagger|0\rangle \text{ for } \mu \in \lfloor L/2\rfloor \tag{7}$$

have zero energy and chirality $\chi_p = +1$. There are precisely d_0 ways to distribute N indistinguishable bosons among these chiral pair states $|p(\mu)\rangle$ and chiral single-particle states $|s\rangle$, and from these a standard basis for the zero energy subspace can be built.

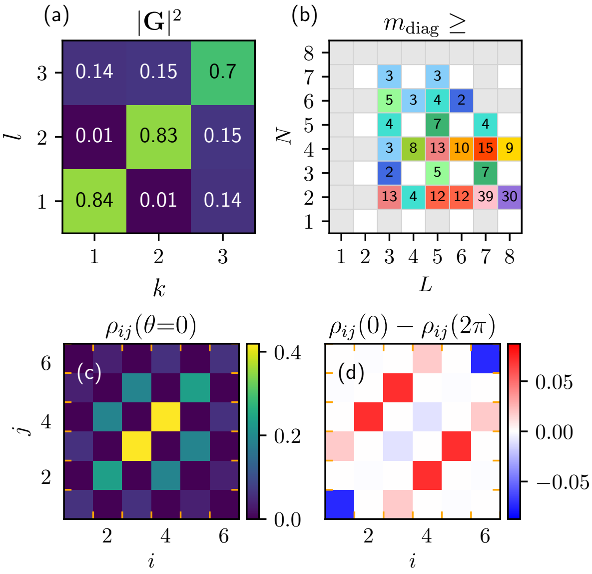

FIG. 2. Holonomies for adiabatic evolutions from $\theta = 0$ to 2π. (a) The holonomy matrix $\mathbf{G}$ in pair basis $|p(\mu)\rangle$ (Eq. (7)) reveals non-trivial adiabatic holonomies (here $N = 2$, $L = 6$, and $N_\theta = 10^4$ in Eq. (8), error $\sim 10^{-3}$, see [62]). (b) The smallest integer m_{diag} such that $G^{m_{\mathrm{diag}}}$ is diagonal (within the error bounds) quantifies how nontrivial $\hat{G}$ is. m_{diag} increases strongly with system size. The two-body density of an initial zero energy state (c), here $|p(1)\rangle$, alters significantly during the adiabatic evolution (d).

Adiabatic manipulation of the zero energy subspace.— The periodic dependency in the statistical angle θ invites the question how the zero energy subspace is affected under cyclic adiabatic variation of θ. As the statistical angle is tuned, the zero energy subspace $\mathcal{H}_0$ moves and rotates within the larger subspace $\mathcal{H}_\pm$ with majority chirality $\chi = \pm1$. Similar to the Aharonov-Bohm effect on a ring, the zero energy subspace accumulates topological Berry phases and nontrivial holonomies. These act as unitary transformations on the above-given standard basis vectors when tuning θ from 0 to 2π, as schematically depicted in Fig. 1(b3).

We propagate the zero energy subspace from $\theta = 0$ to $\theta = 2\pi$ using Kato's adiabatic evolution [50, 63]

$$\hat{G} = \lim_{N_\theta\to\infty}\prod_{j=1}^{N_\theta}\hat{P}_j, \tag{8}$$

where $\hat{P}_j = \sum_{\mu=1}^{d_0}|\psi_\mu(2\pi j/N_\theta)\rangle\langle\psi_\mu(2\pi j/N_\theta)|$ is the projector onto the zero energy subspace at the statistical angle $2\pi j/N_\theta$ and $|\psi_\mu\rangle$ is an orthonormal basis for the chiral zero energy subspace; see [62] for numerical details. The unitary matrix $\mathbf{G}_{\mu\mu'} = \langle\psi_{\mu'}|\hat{G}|\psi_\mu\rangle$ then embodies the adiabatic holonomy for a complete loop.

For $L = 2$ the zero energy subspace is non-degenerate and we calculate the (Abelian) Berry phase $\mathbf{G} = \pm 1$ exactly and find the nontrivial value of -1 for consecutive odd-integer coefficients in the Gauss sum $\sum_{k=1}^{N/2} k$, see [62]. We investigate the non-Abelian holonomies of larger systems by exact diagonalization [62, 64, 65]. As an example, in Fig. 2(a), we present the holonomy matrix $\mathbf{G}$ in the chiral pair basis $|p(\mu)\rangle$ at $\theta = 0$ for a system with $N = 2$ and $L = 6$ and $d_0 = 3$. The adiabatic evolution causes a significant non-trivial rotation of the zero energy subspace during the adiabatic evolution, which we indicate by $\rho^{\nu}_{ij}(\theta) = \langle \nu(\theta)|\hat{b}^{\dagger}_i \hat{b}^{\dagger}_j \hat{b}_j \hat{b}_i|\nu(\theta)\rangle$, an observable accessible in the corresponding experiments [31]. For example, we can take the initial two-body density $\rho^{\nu}_{ij}(\theta = 0)$ of the basis state $|p(1)\rangle$ [Fig. 2(c)] and compare with $\rho^{\nu}_{ij}(\theta = 2\pi)$, i.e., the two-body density corresponding to the adiabatically propagated state $\hat{G}|p(1)\rangle$. This yields a significant difference in the densities, see Fig. 2(d). Interestingly, for variations of parameters other than θ that preserve chiral symmetry, such as local variations in hopping strength J, we find that the connection is flat, meaning that $\hat{G}$ is not altered. Therefore, the results for the holonomy matrix $\mathbf{G}$ are robust against fluctuations in the adiabatic manipulation.

Tuning the statistical angle therefore implements a topologically protected operation on the zero energy subspace, a concept which has been extensively explored in the context of Majorana modes and other non-Abelian anyons [8]. To quantify the nontriviality of $\mathbf{G}$, we determine the smallest integer m_{diag} such that $\mathbf{G}^{m_{\text{diag}}}$ is diagonal, i.e., trivial in the context of state manipulation. Also, at least m_{diag} states in the computational space can be prepared from an initial state by repeated application of this operation. For instance, the braiding of Majorana modes becomes diagonal for $m_{\text{Maj.}} = 2$ and trivial with $G^4_{\text{Maj.}} = 1$ [8]. Within our error bounds, we find $m_{\text{diag}} > 4$ for various particle numbers and system sizes, particularly for large ones, see Fig. 2(b) and [62].

This idea can be elevated to non-Abelian holonomies if we implement the site-dependent statistical parameter θ_j. This leads to a generalized anyonic exchange algebra $a^{\dagger}_j a_k = \hat{a}_i \hat{a}^{\dagger}_j - e^{i\theta_{i,j}} \hat{a}^{\dagger}_j \hat{a}_i = \delta_{i,j}$ with $\theta_{i,j} = \theta_j$ for $i > j$, $\theta_{i,j} = -\theta_i$ for $i < j$, and $\theta_{i,i} = 0$. For different exchange phases θ_L in the left and θ_R in the right part of the system [62, 66], we generally find $[\mathbf{G}_L, \mathbf{G}_R] \neq 0$, meaning the fluctuation-protected state manipulation depends on which statistical angle is altered first [62].

Steering to the zero energy subspace.— The basis states for $\theta = 0$ can be prepared by temporal variation of $\theta = \theta(t)$ [31]. As a simple, accessible initial state, we consider two bosonic particles at the central sites of a lattice with $L = 6$ sites, i.e., $|\Psi(t = 0)\rangle = |001100\rangle$. In order to find a path for $\theta(t)$ which maximizes the overlap of the propagated wave function at time t_f with a chiral pair target state, $\mathcal{O}(t_f) = |\langle p(\mu)|\Psi(t_f)\rangle|^2$, we represent $\theta(t)$ with M interpolation points (for details see [62]). These M points serve as an input for a gradient based optimization algorithm which updates the path $\theta(t)$ until $\mathcal{O}(t_f)$ becomes maximal [67–69].

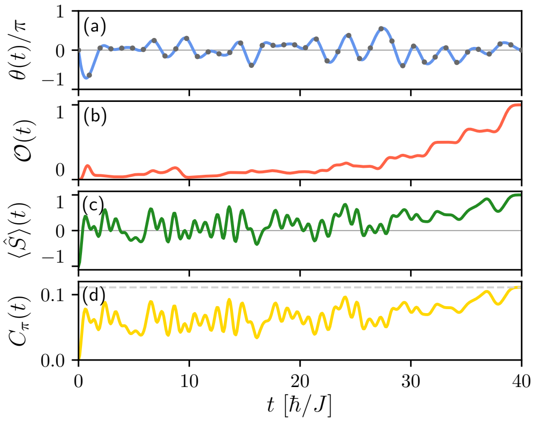

FIG. 3. Steering to the zero energy subspace, starting with $N = 2$ bosons at the center of $L = 6$ sites. (a) The statistical phase $\theta(t)$ is dynamically varied along 60 optimized interpolation points (gray) such that (b) the overlap $\mathcal{O}(t_f)$ of the time-evolved state with the zero energy state $|p(1)\rangle$ (Eq. (7)) is maximal, reaching a final overlap of $1-10^{-4}$. The time evolution of (c) the chirality and (d) the static structure factor $C_\pi(t)$, which approaches its maximal value N^2/L^2 (dashed line) indicating the emergence of a checkerboard pattern, the signature of the zero energy subspace.

In Fig. 3, we present details of the optimization routine for $M = 40$ and $t_f = 40$. The chosen path for $\theta(t)$ shown in Fig. 3(a) reaches a fidelity $\mathcal{O}(t_f) = 1 - 10^{-4}$ in Fig. 3(b), which can be further increased for larger M and t_f. As a measure whether the final state converges to the zero energy subspace, we monitor the expectation value of the chiral operator $\hat{S}$ in Fig. 3(c) and investigate the steering of the structure factor [70] in Fig. 3(d)

$$C_q(t) = \frac{1}{L^2} \sum_{jk} e^{iq(j-k)} \langle \Psi(t)|\hat{n}_j \hat{n}_k|\Psi(t)\rangle. \tag{9}$$

We find a dominant signal at $q = 0, \pi$ that signals the presence of the checkerboard pattern in the N-particle density correlation for $L > N$, which is conveniently experimentally accessible in few-particle systems, see Fig. 2(c) [71, 72]. For large particle numbers, we instead propose to probe the one-body density matrix $\langle\psi|\hat{b}^{\dagger}_i \hat{b}_j|\psi\rangle$ directly by the Fourier transform of the quasi-momentum distribution $\langle \tilde{b}^{\dagger}_k \tilde{b}_k\rangle$.

Conclusions.— We have shown that chiral-symmetric number-preserving correlated hopping models with bosons accommodate at least d_0 degenerate zero energy states. The dimension of this space of states is robust against any parameter variations that preserve chiral symmetry, although the space itself sweeps through the chiral majority subspace. For the free anyon-Hubbard model, states in the zero energy chiral subspace can be prepared from experimentally-accessible initial states and detected by the characteristic checkerboard pattern in configuration space with current quantum gas microscopy techniques [31]. As the statistical angle is adiabatically tuned, the zero energy space picks up a non-Abelian holonomy for each cycle. This paradigm of non-Abelian state preparation could find further applications within the space of chiral symmetric correlated hopping models by tuning more than one cyclic parameter. As an example, we propose implementing this non-Abelian state preparation scheme within a spatially-inhomogeneous anyon-Hubbard model. More generally, we believe that Floquet-driven density-dependent Peierls phases offer a rich perspective for future exploration. Such models contain synthetic magnetic fluxes in few-body configuration space, and they provide an alternate path to understanding topological interactions in low dimensional systems. We propose a generalized anyon-Hubbard model with inhomogeneous statistical angles as one example of wider class of bosonic Hamiltonians with density-dependent Peierls phases, possibly without anyonic interpretation, but relevant to experiments and topological control via adiabatic holonomies.

The authors thank André Eckardt and Peter Græns Larsen for discussions on correlated hopping models and Joyce Kwan and Bryce Bakkani-Hassani for discussions of their anyon-Hubbard model experiment. T.P. thanks Ingo Runkel for comments on the local varying statistical angles. M.B. and T.P. acknowledge funding by the European Union (ERC, QUANTWIST, project number 101039098). The views and opinions expressed are however those of authors only and do not necessarily reflect those of the European Union or the European Research Council, Executive Agency. T.P. and P.S. acknowledge support by the Cluster of Excellence "CUI: Advanced Imaging of Matter" of the Deutsche Forschungsgemeinschaft (DFG) – EXC 2056 – project ID 390715994 and T.P. acknowledges funding of the DFG project No. 420120155. Additionally, N.H. was supported by the Deutscher Akademischer Austauschdienst, the Centre for Ultrafast Imaging: Advanced Imaging of Matter of the University of Hamburg.

[1] J. M. Leinaas and J. Myrheim, Il Nuovo Cimento B (1971-1996) **37**, 1 (1977).
[2] G. A. Goldin, R. Menikoff, and D. H. Sharp, Journal of Mathematical Physics **21**, 650 (1980).
[3] F. Wilczek, Physical Review Letters **49**, 957 (1982).
[4] Y.-S. Wu, Physical Review Letters **52**, 2103 (1984).
[5] L. Biedenharn, E. Lieb, B. Simon, and F. Wilczek, Physics Today **43**, 90 (1990).
[6] A. Khare, *Fractional Statistics and Quantum Theory*, 2nd ed. (World Scientific, Hackensack, N.J, 2005).
[7] A. Kitaev, Annals of Physics **321**, 2 (2006).
[8] C. Nayak, S. H. Simon, A. Stern, M. Freedman, and S. Das Sarma, Reviews of Modern Physics **80**, 1083 (2008).
[9] F. D. M. Haldane, Physical Review Letters **67**, 937 (1991).
[10] T. Hansson, J. Leinaas, and J. Myrheim, Nuclear Physics B **384**, 559 (1992).
[11] U. Aglietti, L. Griguolo, R. Jackiw, S.-Y. Pi, and D. Seminara, Physical Review Letters **77**, 4406 (1996).
[12] A. Kundu, Physical Review Letters **83**, 1275 (1999).
[13] K.-V. Pham, M. Gabay, and P. Lederer, Le Journal de Physique IV **10**, Pr3 (2000).
[14] M. T. Batchelor, X.-W. Guan, and J.-S. He, Journal of Statistical Mechanics: Theory and Experiment **2007**, P03007 (2007).
[15] T. Keilmann, S. Lanzmich, I. McCulloch, and M. Roncaglia, Nature Communications **2**, 361 (2011).
[16] T. Posske, B. Trauzettel, and M. Thorwart, Physical Review B **96**, 195422 (2017).
[17] M. Greiter, Inference: International Review of Science **7**, 10.37282/991819.22.27 (2022).
[18] N. L. Harshman and A. C. Knapp, Physical Review A **105**, 052214 (2022).
[19] S. Nagies, B. Wang, A. C. Knapp, A. Eckardt, and N. L. Harshman, SciPost Physics **16**, 086 (2024).
[20] S. Longhi and G. D. Valle, Optics Letters **37**, 2160 (2012).
[21] C. Yannouleas and U. Landman, Physical Review A **100**, 013605 (2019).
[22] C. Schweizer, F. Grusdt, M. Berngruber, L. Barbiero, E. Demler, N. Goldman, I. Bloch, and M. Aidelsburger, Nature Physics **15**, 1168 (2019).
[23] F. Görg, K. Sandholzer, J. Minguzzi, R. Desbuquois, M. Messer, and T. Esslinger, Nature Physics **15**, 1161 (2019).
[24] W. Zhang, L. Qian, H. Sun, and X. Zhang, Communications Physics **6**, 1 (2023).
[25] M. Bonkhoff, S. B. Jäger, I. Schneider, A. Pelster, and S. Eggert, Physical Review B **108**, 155134 (2023).
[26] C. S. Chisholm, A. Frölian, E. Neri, R. Ramos, L. Tarruell, and A. Celi, Physical Review Research **4**, 043088 (2022).
[27] A. Frölian, C. S. Chisholm, E. Neri, C. R. Cabrera, R. Ramos, A. Celi, and L. Tarruell, Nature **608**, 293 (2022).
[28] S. Greschner and L. Santos, Physical Review Letters **115**, 053002 (2015).
[29] C. Sträter, S. C. L. Srivastava, and A. Eckardt, Physical Review Letters **117**, 205303 (2016).
[30] M. Bonkhoff, K. Jägering, S. Eggert, A. Pelster, M. Thorwart, and T. Posske, Physical Review Letters **126**, 163201 (2021).
[31] J. Kwan, P. Segura, Y. Li, S. Kim, A. V. Gorshkov, A. Eckardt, B. Bakkali-Hassani, and M. Greiner, Science **386**, 1055 (2024).
[32] S. Greschner, G. Sun, D. Poletti, and L. Santos, Physical Review Letters **113**, 215303 (2014).
[33] L. Cardarelli, S. Greschner, and L. Santos, Physical Review A **94**, 023615 (2016).
[34] L. W. Clark, B. M. Anderson, L. Feng, A. Gaj, K. Levin, and C. Chin, Physical Review Letters **121**, 030402 (2018).
[35] F. Lange, S. Ejima, and H. Fehske, Physical Review Let-

ters **118**, 120401 (2017).

[36] F. Lange, S. Ejima, and H. Fehske, Physical Review A **95**, 063621 (2017).

[37] F. Liu, J. R. Garrison, D.-L. Deng, Z.-X. Gong, and A. V. Gorshkov, Physical Review Letters **121**, 250404 (2018).

[38] S. Greschner, L. Cardarelli, and L. Santos, Physical Review A **97**, 053605 (2018).

[39] M. D. Liberto, C. E. Creffield, G. I. Japaridze, and C. M. Smith, Physical Review A **89**, 013624 (2014).

[40] A. Hudomal, I. Vasić, N. Regnault, and Z. Papić, Communications Physics **3**, 99 (2020).

[41] A. Chu, A. P. Orioli, D. Barberena, J. K. Thompson, and A. M. Rey, Physical Review Research **5**, L022034 (2023).

[42] P. Brighi, M. Ljubotina, and M. Serbyn, SciPost Phys. **15**, 093 (2023).

[43] M. Robnik and M. V. Berry, Journal of Physics A: Mathematical and General **19**, 669 (1986).

[44] B. Damski and J. Zakrzewski, Physical Review A **74**, 043609 (2006).

[45] F. Grusdt, M. Höning, and M. Fleischhauer, Physical Review Letters **110**, 260405 (2013).

[46] B. Sutherland, Physical Review B **34**, 5208 (1986).

[47] E. H. Lieb, Physical Review Letters **62**, 1201 (1989).

[48] A. Ramachandran, A. Andreanov, and S. Flach, Physical Review B **96**, 161104 (2017).

[49] C. P. Chen, M. Szyniszewski, and H. Schomerus, Phys. Rev. Res. **2**, 023118 (2020).

[50] T. Kato, Journal of the Physical Society of Japan **5**, 435 (1950).

[51] F. Wilczek and A. Zee, Physical Review Letters **52**, 2111 (1984).

[52] A. W. W. Ludwig, Physica Scripta **2016**, 014001 (2015).

[53] J. Yu, N. Sun, and H. Zhai, Physical Review Letters **119**, 225302 (2017).

[54] R. Xiao and Y. X. Zhao, Nature Communications **15**, 3787 (2024).

[55] V. Karle, M. Serbyn, and A. A. Michailidis, Physical Review Letters **127**, 060602 (2021).

[56] Y. Hatsugai, Annals of Physics **435**, 168453 (2021).

[57] S. Elitzur, Physical Review D **12**, 3978 (1975).

[58] C. D. Batista and Z. Nussinov, Physical Review B **72**, 045137 (2005).

[59] B. I. Halperin, Journal of Statistical Physics **175**, 521 (2019).

[60] V. Karle, M. Serbyn, and A. A. Michailidis, Phys. Rev. Lett. **127**, 060602 (2021).

[61] L. Zhang, Y. Ke, and C. Lee, arXiv:2410.22778.

[62] F. Theel, M. Bonkhoff, T. Posske, P. Schmelcher, and N. L. Harshman, (2024), supplemental material [url] will be inserted by the publisher.

[63] K. G. Wilson, Phys. Rev. D **10**, 2445 (1974).

[64] A. Weiße and H. Fehske, in *Computational Many-Particle Physics*, Vol. 739, edited by H. Fehske, R. Schneider, and A. Weiße (Springer Berlin Heidelberg) pp. 529–544.

[65] P. Virtanen, R. Gommers, T. E. Oliphant, M. Haberland, T. Reddy, D. Cournapeau, E. Burovski, P. Peterson, W. Weckesser, J. Bright, S. J. van der Walt, M. Brett, J. Wilson, K. J. Millman, N. Mayorov, A. R. J. Nelson, E. Jones, R. Kern, E. Larson, C. J. Carey, İ. Polat, Y. Feng, E. W. Moore, J. VanderPlas, D. Laxalde, J. Perktold, R. Cimrman, I. Henriksen, E. A. Quintero, C. R. Harris, A. M. Archibald, A. H. Ribeiro, F. Pedregosa, P. van Mulbregt, and SciPy 1.0 Contributors, Nature Methods **17**, 261 (2020).

[66] L. L. Lau and S. Dutta, Physical Review Research **4**, L012007 (2022).

[67] R. H. Byrd, P. Lu, J. Nocedal, and C. Zhu, SIAM Journal on Scientific Computing **16**, 1190 (1995).

[68] C. Zhu, R. H. Byrd, P. Lu, and J. Nocedal, ACM Transactions on Mathematical Software **23**, 550 (1997).

[69] F. L. Lewis, D. L. Vrabie, and V. L. Syrmos, *Optimal Control* (John Wiley & Sons, New York, 2012).

[70] M. Lewenstein, A. Sanpera, and V. Ahufinger, *Ultracold Atoms in Optical Lattices: Simulating Quantum Many-Body Systems* (Oxford University Press, 2012).

[71] T. D. Kühner, S. R. White, and H. Monien, Physical Review B **61**, 12474 (2000).

[72] P. Rosson, M. Kiffner, J. Mur-Petit, and D. Jaksch, Physical Review A **101**, 013616 (2020).

arXiv:2412.01517v2 [cond-mat.quant-gas] 16 Dec 2024

Supplemental Material for "Chirality-protected state manipulation by tuning one-dimensional statistics"

F. Theel,[1] M. Bonkhoff,[2] P. Schmelcher,[1,3] T. Posske,[2,3] and N.L. Harshman[4]
[1] *Center for Optical Quantum Technologies, Department of Physics, University of Hamburg, Luruper Chaussee 149, 22761 Hamburg Germany*
[2] *I. Institute for Theoretical Physics, Universität Hamburg, Notkestraße 9, 22607 Hamburg, Germany*
[3] *The Hamburg Centre for Ultrafast Imaging, University of Hamburg, Luruper Chaussee 149, 22761 Hamburg, Germany*
[4] *Physics Department, American University, Washington, DC 20016, USA*

In this Supplemental Material, we introduce the basic computational tools and discuss details of the key results discussed in the main text. In Sec. A, we discuss the numerical details of the diagonalization procedure. In Sections B and C, we comment on the convergence behavior of the adiabatic evolution and the error treatment relevant for potentiating the holonomy matrices. In Sec. D, we calculate the quantized geometric phase of the exactly solvable two-side model and extend the adiabatic manipulation to locally varying statistical angles in Sec. E. In Sec. F, we provide more details on the protocol used to steer an initial state into the zero-energy space.

Appendix A: Implementation of the Anyon-Hubbard model

Here, we provide details about the numerical implementation of the Anyon-Hubbard model. The objective is to solve the Hamiltonian $\hat{H}$ in Eq. (5) exactly via exact diagonalization [1]. Therefore, we express $\hat{H}$ in terms of the number state basis $|\mathbf{n}_i\rangle_{i=1}^{\mathcal{N}}$, which results in the matrix $\mathbf{H}_{ij} = \langle \mathbf{n}_i|\hat{H}|\mathbf{n}_j\rangle$. The number states, $\mathbf{n} = (n_1, \ldots, n_L)$, specify the occupation of N particles distributed on L lattice sites with $\sum_k n_k = N$. Assuming indistinguishable particles, there are $\mathcal{N} = (N+L-1)!/[N!(L-1)!]$ basis states which also defines the dimension of Hilbert space. The largest system size we consider in this work has a Hilbert space dimension of $\mathcal{N} = 6435$ which corresponds to the case where $L = 8$ and $N = 8$ and, thus, is well in the range of what is computationally feasible.

Apart from calculating the ground state properties, we also calculate the time evolution of an initial state for a time-dependent Hamiltonian as done within the steering process or for the adiabatic propagation. The time evolution is conducted by integrating the time-dependent Schrödinger equation, i.e., a set of coupled ordinary differential equations. We use an eighth-order Runge-Kutta method within the module `scipy.integrate.ode` with the `scipy` [2] version 1.10.1 and the input parameters *nsteps* $= 10^8$, *atol* $= 10^{-10}$ and *rtol* $= 10^{-10}$.

Appendix B: Convergence of the adiabatic evolution

In the following, we determine the accuracy of the method used for obtaining the holonomy matrix $\mathbf{G}$ outlined in the main text for a system with $L = 6$ lattice sites and $N = 2$ particles corresponding to a three-fold degenerate zero-energy space. Within this method, the zero-energy states of $H(\theta = 0)$ are adiabatically propagated by projecting the initial states consecutively onto zero-energy spaces lying on the path from $\theta = 0$ to 2π [3]. In the adiabatic limit, $N_\theta \to \infty$, the overlap between the initial and adiabatically propagated states defines the holonomy matrix $\mathbf{G}$ (see main text). This matrix is unitary, i.e., $\mathbf{G}\mathbf{G}^\dagger = \mathbf{1}$ where $\mathbf{1}$ is the identity matrix. This property can be probed for holonomy matrices $\tilde{\mathbf{G}}$ with a finite number of projection steps N_θ by measuring the distance $||\tilde{\mathbf{G}}\tilde{\mathbf{G}}^\dagger - \mathbf{1}||^2$. In Fig. S1(a), we show the convergence of this distance in dependence on the steps N_θ leading to a deviation from the unitary matrix around $\sim 10^{-4}$ for $N_\theta = 10^4$. As post process, we obtain the holonomy matrix $\mathbf{G}$ used for the analysis, by calculating the closest unitary matrix that is closest to the holonomy matrix $\tilde{\mathbf{G}}$ obtained with $N_\theta = 10^4$ projections. For this, we first perform a singular value decomposition on $\tilde{\mathbf{G}}$ such that we yield $\tilde{\mathbf{G}} = \mathbf{U}\mathbf{\Sigma}\mathbf{V}^\dagger$, where $\mathbf{U}$ and $\mathbf{V}$ are two unitary rotation matrices and $\mathbf{\Sigma}$ is a diagonal ma-

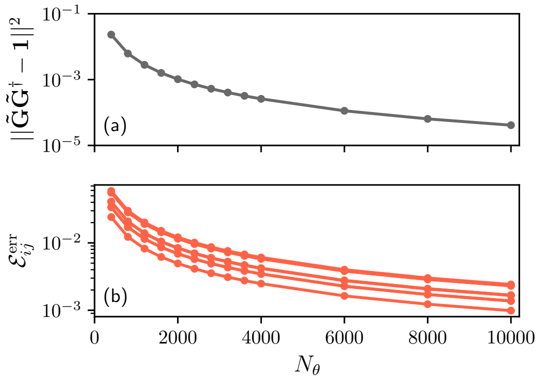

FIG. S1. Convergence of the adiabatic holonomy when altering the statistical angle θ from 0 to 2π ($L = 6$ and $N = 2$). (a) Distance of the holonomy matrix $\tilde{\mathbf{G}}$ to an unitary matrix. (b) Relative difference $\Delta\mathcal{E}_{ij}^{\mathrm{err}}$ between the entries of $\tilde{\mathbf{G}}$ obtained with N_θ projections and the unitary holonomy matrix, $\mathbf{G}$, obtained with $N_\theta = 10^4$, see text for procedure.

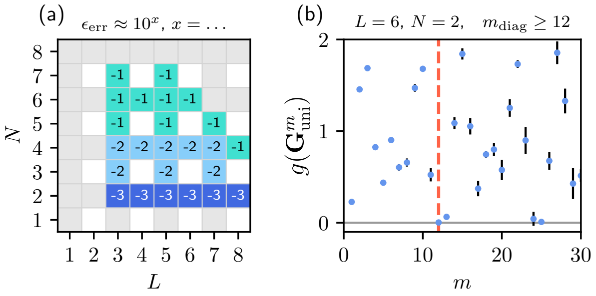

FIG. S2. (a) Error of the holonomy matrix, $\epsilon^{\rm proj}_{\rm err}$, in dependence on the lattice sites L and the particle number N. The error is defined as the largest deviation of the holonomy matrix obtained with $N_\theta = 10^4$ projections to the closest unitary matrix (see Sec. B). (b) Calculating the distance of the potentiated holonomy matrix $\mathbf{G}^m$ to the diagonal matrix illustrated by $g(\mathbf{G}^m)$ [see Eq. (C1)]. We define $m_{\rm diag}$ as the smallest value of m where $g(\mathbf{G}^m) - s_{g(\mathbf{G}^m)} < 0$, i.e., for which the potentiated matrix cannot be distinguished from a diagonal matrix for a given error $s_{g(\mathbf{G}^m_{\rm proj-uni})}$ (red dashed line) (see Sec. C).

trix. Then we define the unitary holonomy matrix as $\mathbf{G} = \mathbf{U}\mathbf{V}^\dagger$, which has the property $||\mathbf{G}\mathbf{G}^\dagger - \mathbf{1}||^2 = 0$.

On the basis of the unitary holonomy matrix, we analyze the convergence behavior of the single elements of $\tilde{\mathbf{G}}$ for different numbers of projections N_θ. In particular, we show in Fig. S1(b) the relative difference $\mathcal{E}^{\rm err}_{ij}(N_\theta) = |\tilde{G}^{N_\theta}_{ij} - G_{ij}|/|G_{ij}|$, which reveals the expected convergence behavior for increasing N_θ. Based on this we quantify the error of the holonomy matrix as,

$$\epsilon_{\rm err} = \max_{ij}\left(\mathcal{E}^{\rm err}_{ij}\right), \tag{B1}$$

i.e., as the largest deviation of the holonomy matrix obtained with $N_\theta = 10^4$ projections, $\tilde{\mathbf{G}}$, from its closest unitary matrix, $\mathbf{G}$. In Fig. S2(a) we show the order of the error in dependence of L and N (see also Sec. C).

Finally, we have compared the holonomy matrices obtained by applying projections as described to a method when the zero energy states are propagated in time. More precisely, each zero energy state in chiral pair basis representation is propagated in time while $\theta(t)$ is ramped linearly from $\theta(0) = 0$ to 2π within a total propagation time of t_f. The accuracy of this method increases with the final propagation time t_f and is exact in the adiabatic limit $t_f \to \infty$. We have verified that the holonomy matrices obtained with both methods are in agreement.

Appendix C: Potentiated holonomy matrices

In Fig. 2(b) of the main text, we present the minimal exponents $m_{\rm diag}$ of the holonomy matrix $\mathbf{G}$ in dependence of L and N for which the potentiated holonomy matrix, $\mathbf{G}^m$, cannot be distinguished from a unitary matrix. We judge the distance of the potentiated holonomy matrix to the diagonal matrix by calculating

$$g(\mathbf{G}^m) = \sum_{ij}\left||G^m_{ij}|^2 - \delta_{ij}\right|^2. \tag{C1}$$

The value of $m_{\rm diag}$ is the smallest exponent m for which $g(\mathbf{G}^m) - s_m < 0$, where s_m denotes the numerical error. We estimate s_m for a specific L-N combination stochastically. To this end, we first calculate the relative absolute difference between the holonomy matrix and its closest unitary matrix, $\mathcal{E}^{\rm err}_{ij}$ (see Sec. B). Then we collect the values of g for a set of purposely modified holonomy matrices, $(\mathcal{G}_k)_{ij} = G^{\rm uni}_{ij} + P^k_{ij}\Delta G_{ij}$, where $P^k_{ij} = \{-1, 1\}$. Thereby, g is calculated for maximally 1000 combinations of how to add/subtract the deviations $\mathcal{E}^{\rm err}_{ij}$ to/from G_{ij}. From the sample set $g(\mathcal{G}^m_k)$, we take the value with the largest absolute difference from $g(\mathbf{G}^m)$ as numerical error, i.e., $s_m = \max_k(|g(\mathcal{G}^m_k) - g(\mathbf{G}^m)|)$. Evidently, the error increases with increasing particle numbers, which is explains why the values for $m_{\rm diag}$ in these regimes are comparatively small, cf. Fig. 2(b). In Fig. S2(b), we representatively show the evolution of $g(\mathbf{G}^m)$ for $L = 6$ and $N = 2$ and mark $m_{\rm diag}$ by a red dashed line.

Appendix D: Exact Null State and Non-Degenerate Geometric Phase for $L = 2$ and $N = 2m$

In this section, we derive exact results for a system with two sites, $L = 2$, and an even number of particles, $N = 2m$ with $m \in \mathbb{N}$, to gain intuition and to compare to the general, numeric results in the main text. In this case, the zero-energy space in Eq. (2) is one-dimensional. In Ref. [4] it was shown that the anyon-Hubbard dimer and the integrable Bose-Hubbard dimer are dual to each other, so in the following, we use this duality relation to calculate the geometrical phase for this special case analytically. For $U = 0$ the zero energy state of the Bose-Hubbard dimer in Fourier space reads

$$\hat{H} = -2J(\hat{n}_0 - \hat{n}_1) \tag{D1}$$

$$|\Psi\rangle = \frac{1}{(N/2)!}(\hat{b}^\dagger_0)^{N/2}(\hat{b}^\dagger_1)^{N/2}|0, 0\rangle \tag{D2}$$

with

$$\hat{b}_n = \frac{1}{\sqrt{2}}\sum_{j=1}^{2} e^{ij\pi}\hat{b}_j, \quad n = 0, 1. \tag{D3}$$

Subsequently, we get the corresponding state of the anyon-Hubbard dimer in real space, with chirality $\chi = 1$

$$|\Psi\rangle = \frac{1}{2^{N/2}((N/2)!)^2}\sum_{l=0}^{N/2}(-1)^{N/2-l}\sqrt{(N-2l)!(2l!)}\binom{N/2}{l} e^{i\theta\hat{n}_1(1+\hat{n}_2)}e^{i\theta(N+1))(\hat{n}_1-\hat{n}_2)/4}|N-2l, 2l\rangle, \tag{D4}$$

by inversion of the Fourier modes and the usage of the duality transformation from Ref. [4]. Thereby, the modes

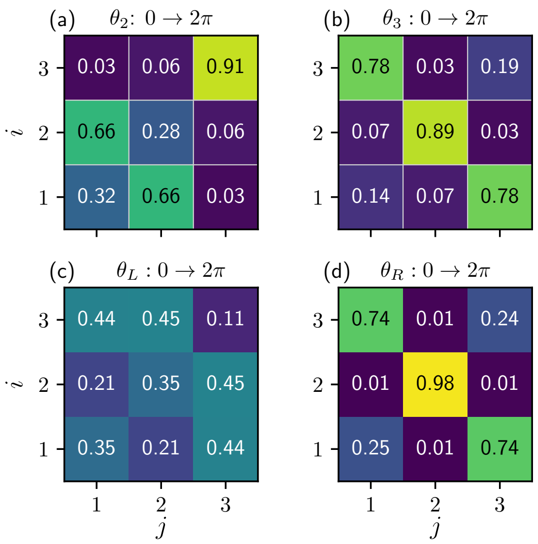

FIG. S3. Absolute squares of the holonomy matrices $|\mathbf{G}_{\theta_j}|^2$ obtained after adiabatically steering a single or multiple θ_j from 0 to 2π while the other statistical angles remain 0 ($L = 6$ sites and $N = 2$). (a), (b) Tuning one statistical angle. (c), (d) Tuning the left side $\theta_L = \theta_1 = \theta_2 = \theta_3$ and the right side $\theta_R = \theta_4 = \theta_5$ independently. The error of the shown holonomy matrices is everywhere of the order of 10^{-4}.

in Eq. (D3) have an equal occupation of $N/2 = m$, meaning that such states can exist only for even particle numbers in agreement with Eq. (2) of the main text. As the zero-energy state is non-degenerate, the non-abelian holonomy reduces to a single phase, i.e.,

$$\begin{aligned}\phi =& \frac{1}{i\pi}\int_0^{2\pi} d\theta \langle\Psi|\partial_\theta|\Psi\rangle \\ =& \frac{N/2\,(N/2+1)}{2},\end{aligned} \tag{D5}$$

that is indeed quantized as expected for chiral symmetric models [5, 6]. Interestingly, the value in Eq. (D5) is exactly the proportionality factor of the Casimir operator of $SU(2)$, which is the dynamical symmetry group of the two-site problem.

Appendix E: Locally varying θ

We next discuss a generalization of the adiabatic manipulation of statistical angles to multiple species of anyons and other chiral perturbations. To this end, we consider, the following Jordan-Wigner transformation with spatially varying θ_j [7], i.e.,

$$\hat{a}_j = \hat{b}_j e^{i\sum_{l<j}\theta_l \hat{n}_l}, \tag{E1}$$

such that the following relation holds

$$\begin{aligned}\tilde{H} &= -J\sum_j \hat{a}_j^\dagger \hat{a}_{j+1} + \text{h.c.} \\ &= -J\sum_j \hat{b}_j^\dagger \hat{b}_{j+1} e^{i\theta_j \hat{n}_j} + \text{h.c.}.\end{aligned} \tag{E2}$$

Subsequently, we obtain "generalized" deformed commutation relations for the $\hat{a}_i$ particles, i.e.,

$$\begin{aligned}\hat{a}_i\hat{a}_j^\dagger - e^{i\theta_{i,j}}\hat{a}_j^\dagger\hat{a}_i &= \delta_{i,j}, \\ \hat{a}_i\hat{a}_j - e^{-i\theta_{i,j}}\hat{a}_j\hat{a}_i &= 0, \\ \hat{a}_i^\dagger\hat{a}_j^\dagger - e^{-i\theta_{i,j}}\hat{a}_j^\dagger\hat{a}_i^\dagger &= 0,\end{aligned} \tag{E3}$$

with the statistical angle

$$\theta_{i,j} = \begin{cases} -\theta_i, & i < j, \\ \theta_j, & i > j, \\ 0, & \text{else} \end{cases} \tag{E4}$$

which generalize the deformed commutation relation for the particles in Eq. (4) in the main text.

For illustration, we calculate the holonomy matrices $\mathbf{G}_{\theta_j}$ for a system with $L = 6$ and $N = 2$ when one or several statistical angles θ_j are varied from 0 to 2π. In Fig. S3(a) and (b), we present the absolute squares of the holonomy matrix when either θ_2 or θ_3 is adiabatically tuned, respectively, while in (c) and (d) more than one θ_j is varied simultaneously, $\theta_1 = \theta_2 = \theta_3 \equiv \theta_L$ and $\theta_4 = \theta_5 \equiv \theta_R$, respectively. As shown, the holonomy matrices in Fig. S3 denote different rotations of the nullspace and are also to be distinguished from the case where all θ_j are tuned simultaneously, as shown in the main text in Fig. 2(a). Moreover, we have checked that the shown holonomy matrices $\mathbf{G}_{\theta_j}$ are pair-wise non-commuting, $\mathbf{G}_{\theta_j}\mathbf{G}_{\theta_k} - \mathbf{G}_{\theta_k}\mathbf{G}_{\theta_j} \neq 0$ for $j \neq k$.

The adiabatic evolution has been done by applying a series of $N_\theta = 10^4$ projections as discussed in Sec. B. We find for each shown holonomy matrix in Fig. S3 an error of $\epsilon_{\text{err}} \approx 10^{-4}$, following the procedure of Sec. B.

Appendix F: Steering process

In the following, we provide nuemrical details for the optimization routine employed for steering the system from a pure number state to an zero energy eigenstate by optimally varying the statistical parameter $\theta(t)$ in time. As mentioned in the main text, we represent $\theta(t)$ by a fixed number of $M_{\text{interp}} + 2$ time-wise equidistant interpolation points $\theta(t_i)$, where the first and last point remain fixed at $\theta = 0$, i.e., $\theta(t_1) = \theta(t_{M_{\text{interp}}+2}) = 0$. The interpolation employs a third degree spline function that passes through all interpolation points and is done with the module `scipy.interpolate.InterpolatedUnivariateSpline` from `scipy` [2] version 1.10.1. In the next step, we choose an initial state $|\Psi(t=0)\rangle$ which serves as starting point for each time-propagation and an initial guess for the path $\theta(t)$. For the latter we set all interpolation points, apart from the first and last, to $\theta(t_i) = 0.01$, where $1 < i < M_{\text{interp}} + 2$, and calculate the respective interpolation. The interpolation points are input to an optimization routine, where within each optimization step the corresponding time-propagation for $\theta(t)$ is calculated. After each propagation the overlap $\mathcal{O}(t_f)$ at the last time step between the propagated wave function with the target state is evaluated. The optimization routine varies the amplitudes of $\theta(t_i)$ after each propagation until the cost value $1 - \mathcal{O}(t_f)$ becomes minimal. As optimization routine, we use the module `scipy.optimize.minimize` from `scipy` version 1.10.1 and the *L-BFGS-B* method [8–10].

Note that altering the initial interpolation points can lead to different outcomes of the optimization routine regarding the final path of $\theta(t)$. Moreover, we have checked that this optimization routine can be also applied to smaller system sizes than $L = 6$, $N = 2$. Additionally, we considered different optimization routines such as a linear interpolation of θ (instead of a third degree spline) and a greedy optimization routine where the wave function is step-wise propagated according to the next optimal value for θ (instead of cyclically updating the optimal route for $\theta(t)$ after propagating the wave function from $t = 0$ to t_f). However, both attempts were not successful since they both heave led to significant smaller overlaps with the target state than the procedure described above. Another route we explored was to introduce onsite interactions $\frac{U(t)}{2}\sum_{i=1}^{L}\hat{n}_i(\hat{n}_i - 1)$ to the Hamiltonian in Eq. (5) in the main text and apply the optimization routine only to $U(t)$ and fix $\theta = 0$. However, also this method for the input parameters: $t_f = 40$, $M_{\text{interp}} = 40$ and an initial $U(t_i) = 0.1$ results in $\mathcal{O}(t_f) \approx 0.3$ for $L = 5$ and $N = 2$, while the procedure regarding an optimization with respect to $\theta(t)$ with the same input parameters leads to $\mathcal{O}(t_f) \approx 1 - 10^{-8}$. Note that varying only the hopping parameter $J(t)$ while $U = \theta = 0$ has no effect on the overlap which remains at $\mathcal{O} = 0$. We conclude that within our numerical studies varying θ dynamically remains the most promising method for zero-energy space state preparation.

---

[1] A. Weiße and H. Fehske, in *Computational Many-Particle Physics*, Vol. 739, edited by H. Fehske, R. Schneider, and A. Weiße (Springer Berlin Heidelberg) pp. 529–544.

[2] P. Virtanen, R. Gommers, T. E. Oliphant, M. Haberland, T. Reddy, D. Cournapeau, E. Burovski, P. Peterson, W. Weckesser, J. Bright, S. J. van der Walt, M. Brett, J. Wilson, K. J. Millman, N. Mayorov, A. R. J. Nelson, E. Jones, R. Kern, E. Larson, C. J. Carey, İ. Polat, Y. Feng, E. W. Moore, J. VanderPlas, D. Laxalde, J. Perktold, R. Cimrman, I. Henriksen, E. A. Quintero, C. R. Harris, A. M. Archibald, A. H. Ribeiro, F. Pedregosa, P. van Mulbregt, and SciPy 1.0 Contributors, Nature Methods **17**, 261 (2020).

[3] T. Kato, Journal of the Physical Society of Japan **5**, 435 (1950).

[4] M. Bonkhoff, S. B. Jäger, I. Schneider, A. Pelster, and S. Eggert, Physical Review B **108**, 155134 (2023).

[5] Y. Hatsugai, Journal of the Physical Society of Japan **75**, 123601 (2006).

[6] F. Grusdt, M. Höning, and M. Fleischhauer, Physical Review Letters **110**, 260405 (2013).

[7] L. L. Lau and S. Dutta, Physical Review Research **4**, L012007 (2022).

[8] R. H. Byrd, P. Lu, J. Nocedal, and C. Zhu, SIAM Journal on Scientific Computing **16**, 1190 (1995).

[9] C. Zhu, R. H. Byrd, P. Lu, and J. Nocedal, ACM Transactions on Mathematical Software **23**, 550 (1997).

[10] F. L. Lewis, D. L. Vrabie, and V. L. Syrmos, *Optimal Control* (John Wiley & Sons, New York, 2012).

Chapter 9

Conclusions and Outlook

In this cumulative thesis we have investigated the static and dynamical properties of impurities coupled to a bosonic medium confined in one dimension in the ultracold regime. In this sense, we have revealed unseen static and dynamical properties, with special emphasis on the study of the effective interactions and induced correlations mediated by the bosonic gas. In a separate direction, we have studied the static properties of the anyon-Hubbard model and revealed the presence of a chirally protected zero-energy space. This subspace exhibits a non-trivial holonomy matrix when adiabatically propagating the system in time while tuning the statistical angle in a closed loop in parameter space. In each section we begin by summarizing the main findings of the individual works followed by an outlook on possible further research directions.

9.1 Counterflow Dynamics of Impurities Coupled to a Bosonic Medium

In Ref. [FT1] we have analyzed a system consisting of two impurities trapped in a double-well potential and coupled to a bosonic majority species which is subjected to different trapping geometries. This work provides significant new insights into the field of strongly particle-imbalanced ultracold mixtures by exploring the correlated stationary and dynamical behavior of two impurities in various external trapping potentials [11, 153, 156, 158, 179, 186, 374, 375]. We have categorized the emerging patterns in terms of the spatially resolved two-body density, which allowed us to extract the corresponding phase diagrams for different trapping potentials of the medium. As it turned out, the external confinement of the medium has a crucial impact on the phase diagram, while the impurities behave qualitatively similar within the regimes. Among others, we have revealed a clustering and an anti-bunching behavior of the impurities. The clustering arises due to an induced attraction that can be controlled by tuning the impurity-medium interaction strength and counteracts the anti-bunching behavior caused by direct impurity-impurity repulsions [170]. Moreover, we studied the dynamical response upon lowering the central barrier of the impurities' double-well potential. The resulting dynamics showed a strong dependence on the impurity-medium coupling strength as well as the external confinement of the medium. Remarkably, for a harmonically trapped medium the impurities performed in the weak coupling regime a state transfer between an anti-bunching and a bunching behavior. We analyzed this behavior in terms of one- and two-body effective models, which enabled us to associate this state transfer with the population of higher excited two-body states.

A natural extension of this model would be to consider other types of trapping potentials for the bath, e.g., a ring or a periodic lattice potential. For instance, in Ref. [FT1] the finite size of the box potential has led to a reflection of the excitations of the bath at the boundaries and for sufficiently strong coupling strengths significantly impacted the dynamics of the impurities. This back-action could be omitted by considering a large ring potential for the medium.

Additionally, it would be intriguing to study the propagation of the excitations of the medium and investigate the possibility to even excite soliton trains in the medium [294, 376]. Besides the already studied potentials, confining the medium in a lattice potential is expected to induce spatial modulations of the latter, which will affect the correlation patterns of the impurities and eventually modify the ensuing phase diagram. In order to unravel the induced interaction, an effective two-body model could be devised on the basis of the procedures discussed in Refs. [FT2, FT3, 170]. Especially, for complex trapping geometries, such as lattice potentials, the usually employed contact interaction potential used to approximate the induced interaction could become insufficient and a more involved interaction potential might be required.

Another route consists of considering a three-component mixture with two distinguishable impurities coupled to a medium. This would open up the possibility to study the dynamical response of the impurities in terms of different masses or with different impurity-medium coupling strengths. In particular, if one impurity is coupled attractively and the other repulsively to the bath, the mediated interaction between the impurities is expected to be repulsive [FT2, 167, 177, 202] such that an anti-bunched scenario could be realized even in the case of non-interacting impurities. Another advantage of distinguishable impurities is that they can be trapped individually. In this sense, the impurities could be initially prepared in spatially separated harmonic oscillator potentials and, subsequently, the counterflow could be induced by quenching the respective trap centers to the same spatial position. For weak couplings and small displacements the resulting dynamics can be expected to resemble a dipole-like oscillation [153, FT8] which could be further analyzed by fitting the mean position to the motion of a damped oscillator in order to extract an effective mass or damping amplitude [FT8]. Alternatively, one can devise a time-dependent effective model similar to procedure employed in Ref. [FT3].

9.2 Induced Interactions between Impurities

In Refs. [FT2–FT4] we have focused on the induced interactions between impurities coupled to a one-dimensional Bose gas. The crucial difference to the majority of existing works is the consideration of two mobile distinguishable impurities which couple with individual interaction strengths to the majority species, in this way, giving rise to a three-component mixture.

9.2.1 Static Case

In Ref. [FT2] we have studied the ground state behavior for two non-interacting distinguishable impurities upon varying their individual interaction strength to the medium in the presence of an external harmonic confinement. By leaving the interaction strength between one impurity and the medium fixed at a repulsive value and tuning the coupling strength between the other impurity and the bath from attractive to repulsive values, we have observed a crossover from an induced anti-bunching to a bunching behavior diagnosed with the two-body correlation functions. By devising an effective two-body model, we were able to associate the bunching and anti-bunching behavior of the impurities with an effective attractive and repulsive interaction strength, respectively. Moreover, we found evidence for the formation of a bipolaron as well as a trimer state composed of one bath particle and the impurities [150, 175]. In this sense, this work generalizes the understanding of the induced interplay between two mobile impurities in terms of a three-component mixture and opens up a new avenue to study the well-known attractive induced interaction appearing in two-component setups [165, 167, 170, 171, 173], as well as the effects of an induced repulsive interaction.

In the publication [FT4] we have provided an alternative approach to the procedure employed in Refs. [FT2, FT3]. In the latter works, the effective interaction between two non-interacting impurities has been determined by fitting an effective model to the two-body correlation function. In contrast to these approaches, in Ref. [FT4] we have specified the induced interaction strengths by fitting the energies of corresponding effective models to the polaron and bipolaron energies obtained from many-body calculations. The impact of the mediated interaction on the impurities is subsequently studied in terms of the one-body density. In order to enhance the impact of mediated interaction on the one-body density, we consider for the impurities a tilted double-well potential and couple them to a majority species which is confined on a ring potential. In particular, the tilt has been applied to trigger a population imbalance between the two double-well sites. The quality of the effective models has been judged by comparing the calculated population imbalance with the results obtained from the ML-MCTDHX many-body method. We find for two distinguishable or indistinguishable impurities that the model is capable of adequately describing the population imbalance for varying impurity-medium coupling strengths. Extending to the case of three impurities, we have approximated the mediated three-body force by an effective contact interaction potential and analyzed its impact on the impurities' population imbalance. Moreover, we have studied the effect of correlations on the one-body density by comparing the many-body results to different types of mean-field approximations.

An intriguing extension would be to study the impact of the mass ratio between the three atomic species on the induced interplay between the impurities. For instance, from Ref. [202] it is known that there exists a repulsive induced interaction mediated between an infinitely heavy and impenetrable impurity and a static impurity with finite impurity-medium attractions. However, the dependence of the effective interaction strength on the impurity mass is by no means fully resolved yet. A step towards answering this question was made in Ref. [FT2], where we have found that the induced correlation between the impurities is enhanced when increasing the mass of one impurity. Due to the close relation between the correlation behavior and the effective interaction between the impurities, we expect that increasing the mass of the impurities will lead to an increase in the mediated interaction strength. Another intriguing path worth pursuing is to investigate the dependence of the induced interplay between the impurities on the size of the medium. Here, the leading thought is that the majority of the existing literature considers a bosonic medium with a large number of particles, namely much larger than the number of impurities. In this sense, it is of great interest to understand how the induced interactions and correlations are affected when the number of host particles is gradually increased from a few to a mesoscopic number. Another point would be to explore possibilities to improve the accuracy of the effective model. So far, we have considered that the effective interaction potential depends only on one parameter, namely, the relative difference between the impurities. However, this assumption is generally speaking only valid in a homogeneous scenario or for weak impurity-medium couplings [165, 170]. In this sense, it would intriguing to develop a simplified effective interaction potential that depends on two or three impurity coordinates in the hope to further improve the accuracy of the effective models.

9.2.2 Dynamical Regime

In Ref. [FT3] we have extended the stationary case discussed in Ref. [FT2] into the dynamical regime. Specifically, we have considered two indistinguishable impurities coupled to a harmonically trapped bosonic gas. The dynamics have been triggered by ramping the impurity-medium interaction strength individually from attractive to repulsive values or vice versa. The main scope was to explore the dynamical response of the induced correlation effects between the impurities and pursue the question whether these dynamics can be captured by an effective model. Depending on the applied quench protocol, a breathing-like dynamics has been induced which has been visualized by monitoring the spatial variance [377]. We devised several one-body models to effectively describe the dynamical response of one impurity. The best agreement with the many-body results has been achieved for a model that employs a time-dependent effective mass and frequency stemming from an optimization process. The time-dependent behavior of the effective parameters gave us then further insights into the dynamics of the dressed impurity. By monitoring the integrated two-body correlation function, we have observed a time-dependent crossover from an induced bunching to an anti-bunching behavior or vice versa depending on the applied ramp protocol. We found that this behavior can be appropriately captured by an effective two-body model consisting of a contact interaction potential with a time-dependent effective interaction strength. We found that the effective interaction strength qualitatively follows the dynamics of the two-body correlation function. Another important aspect of the optimized time-dependent effective one- and two-body model is their ability to capture the many-body dynamics even at long time scales, i.e., longer than the ramp time. This feature distinguishes these models from other ones that are based on static effective parameters [153, FT8].

The main emphasis of Ref. [FT3] has been put on understanding the dynamical evolution of the induced interactions between two impurities in terms of effective one- and two-body models. However, there are other techniques which can be applied to infer information about the polaronic properties of the dressed impurities, e.g., spectroscopic schemes allow the identification of excited polaronic states or deliver information about the presence of induced interactions [120, 331, 378]. Furthermore, in Ref. [FT1] we have demonstrated that the external trapping potential of the medium significantly impacts the dynamical response of the impurities. In this sense, it would be interesting to calculate the time-dependent effective parameters for systems, where the majority species is trapped in other external geometries, e.g. in a ring or lattice potential. In the former case, we would expect that the dressed impurities acquire always an effective mass heavier than their bare one [FT4, 143, 148]. However, apart from altering the external confinement of the medium, an interesting aspect would be to consider a two-component medium which might even form a quantum droplet [102–104]. Here, it would be intriguing to probe the stability of the droplet and the impact on the induced behavior between the impurities by applying different quench protocols [193]. Moreover, it has been shown that for strong impurity-bath coupling strengths and varying impurity-impurity interactions a strongly correlated state close to Bell-states can be formed [203]. In this setup a time-dependent quench protocol could be applied to dynamically control the formation of these strongly correlated states, which could serve as fundamental building blocks for more advanced state manipulation devices [194].

9.3 Zero-Energy Subspace of the One-Dimensional Anyon-Hubbard Model

In Ref. [FT5] we have investigated the spectral properties of the one-dimensional anyon-Hubbard model in terms of variations of the statistical parameter θ and found a degenerate subspace, build from the eigenvectors associated with zero energy. The dimension of the zero-energy subspace turned out to be a consequence of the underlying chiral symmetry of the system, which is conserved for vanishing on-site interactions and, importantly, for variations of the statistical parameter $\theta \neq 0$. Further analysis showed that this property is not unique to the anyon-Hubbard model, but holds for any particle-number conserving model with chiral symmetry. A key feature of the zero-energy states is the emergence of a checkerboard pattern in any correlation function that is not invariant with respect to the chiral symmetry as well as in the N-body density - a feature which is experimental accessible and absent for other eigenstates. We exploited the stability of the null-space dimension and tuned the zero-energy states adiabatically from $\theta = 0$ to 2π, i.e., from bosons to fermions and back to bosons. We found that this loop in parameter space leads to nontrivial Wilcek-Zee phases [379, 380] and holonomies that describe a nontrivial unitary transformation of the initial subspace. In fact, we argued that the cyclic adiabatic evolution describes a topological protected operation. For various system sizes we showed that this operation can be applied numerous times before becoming trivial in the context of state manipulation within a given error. Finally, we provided an experimentally accessible steering protocol, where we demonstrated the possibility to transfer an initial number state into an eigenstate with vanishing eigenenergy by varying the statistical parameter $\theta(t)$ optimally in time [213].

There exist several intriguing research directions worth to be pursued in the future. For instance, we have calculated in Ref. [FT5] the holonomy matrices, besides a globally varying θ, also for a locally varying θ, which again resulted in non-trivial and non-commuting holonomy matrices. Applying a combination of such state manipulation processes could efficiently convert the initial state into, e.g., a highly entangled target state. In general, more work is required to fully understand how the cyclic evolution of θ leads to a non-trivial holonomy matrix, where a first step could be made by analytically understanding the adiabatic evolution for the case corresponding to $N = 2$ particles distributed on $L = 3$ lattice sites [380]. Other directions involve the study of a system with periodic or twisted boundary conditions, where for specific system sizes degenerate zero-energy subspaces exist. Yet another path is given by exploring the adiabatic evolution in terms of two anyonic species [381] that are trapped in a lattice. Such a model would given then rise to a two-component anyon-Hubbard model [369]. Here, the relevant question would be whether degenerate subspaces can exist, and whether the dimension of the subspace is stable with respect to variations in θ. Besides the analysis of static or adiabatic properties, it would be interesting to monitor the expansion dynamics of two or more initially localized anyons over the lattice, when the statistical parameter is varied in time. For example, the asymmetric transport properties could be inverted by tuning θ from negative to positive values and vice versa [213, 233] or even more altered by periodically driving θ.

Bibliography

[1] M. H. Anderson, J. R. Ensher, M. R. Matthews, C. E. Wieman, and E. A. Cornell, “Observation of Bose-Einstein Condensation in a Dilute Atomic Vapor”, Science **269**, 198 (1995).

[2] K. B. Davis, M.-O. Mewes, M. R. Andrews, N. J. van Druten, D. S. Durfee, D. M. Kurn, and W. Ketterle, “Bose-Einstein Condensation in a Gas of Sodium Atoms”, Phys. Rev. Lett. **75**, 3969 (1995).

[3] P. O. Fedichev, Yu. Kagan, G. V. Shlyapnikov, and J. T. M. Walraven, “Influence of Nearly Resonant Light on the Scattering Length in Low-Temperature Atomic Gases”, Phys. Rev. Lett. **77**, 2913 (1996).

[4] C. Chin, R. Grimm, P. Julienne, and E. Tiesinga, “Feshbach resonances in ultracold gases”, Rev. Mod. Phys. **82**, 1225 (2010).

[5] S. Inouye, M. R. Andrews, J. Stenger, H.-J. Miesner, D. M. Stamper-Kurn, and W. Ketterle, “Observation of Feshbach resonances in a Bose–Einstein condensate”, Nature **392**, 151 (1998).

[6] T. Köhler, K. Góral, and P. S. Julienne, “Production of cold molecules via magnetically tunable Feshbach resonances”, Rev. Mod. Phys. **78**, 1311 (2006).

[7] J. Herbig, T. Kraemer, M. Mark, T. Weber, C. Chin, H.-C. Nägerl, and R. Grimm, “Preparation of a Pure Molecular Quantum Gas”, Science **301**, 1510 (2003).

[8] S. Dürr, T. Volz, A. Marte, and G. Rempe, “Observation of Molecules Produced from a Bose-Einstein Condensate”, Phys. Rev. Lett. **92**, 020406 (2004).

[9] M. Olshanii, “Atomic Scattering in the Presence of an External Confinement and a Gas of Impenetrable Bosons”, Phys. Rev. Lett. **81**, 938 (1998).

[10] I. Bloch, J. Dalibard, and W. Zwerger, “Many-body physics with ultracold gases”, Rev. Mod. Phys. **80**, 885 (2008).

[11] S. Mistakidis, A. Volosniev, R. Barfknecht, T. Fogarty, Th. Busch, A. Foerster, P. Schmelcher, and N. Zinner, “Few-body Bose gases in low dimensions—A laboratory for quantum dynamics”, Phys. Rep. **1042**, 1 (2023).

[12] N. Navon, R. P. Smith, and Z. Hadzibabic, “Quantum gases in optical boxes”, Nat. Phys. **17**, 1334 (2021).

[13] M. Albiez, R. Gati, J. Fölling, S. Hunsmann, M. Cristiani, and M. K. Oberthaler, “Direct Observation of Tunneling and Nonlinear Self-Trapping in a Single Bosonic Josephson Junction”, Phys. Rev. Lett. **95**, 010402 (2005).

[14] R. Gati and M. K. Oberthaler, “A bosonic Josephson junction”, J. Phys. B: At. Mol. Opt. Phys. **40**, R61 (2007).

[15] A. M. Kaufman, B. J. Lester, C. M. Reynolds, M. L. Wall, M. Foss-Feig, K. R. A. Hazzard, A. M. Rey, and C. A. Regal, “Two-particle quantum interference in tunnel-coupled optical tweezers”, Science **345**, 306 (2014).

[16] A. J. Barker, S. Sunami, D. Garrick, A. Beregi, K. Luksch, E. Bentine, and C. J. Foot, "Realising a species-selective double well with multiple-radiofrequency-dressed potentials", J. Phys. B: At. Mol. Opt. Phys. **53**, 155001 (2020).

[17] I. Bloch, "Ultracold quantum gases in optical lattices", Nat. Phys. **1**, 23 (2005).

[18] O. Morsch and M. Oberthaler, "Dynamics of Bose-Einstein condensates in optical lattices", Rev. Mod. Phys. **78**, 179 (2006).

[19] K. Henderson, C. Ryu, C. MacCormick, and M. G. Boshier, "Experimental demonstration of painting arbitrary and dynamic potentials for Bose–Einstein condensates", New J. Phys. **11**, 043030 (2009).

[20] S. Will, T. Best, U. Schneider, L. Hackermüller, D.-S. Lühmann, and I. Bloch, "Time-resolved observation of coherent multi-body interactions in quantum phase revivals", Nature **465**, 197 (2010).

[21] S. Will, T. Best, S. Braun, U. Schneider, and I. Bloch, "Coherent Interaction of a Single Fermion with a Small Bosonic Field", Phys. Rev. Lett. **106**, 115305 (2011).

[22] F. Serwane, G. Zürn, T. Lompe, T. B. Ottenstein, A. N. Wenz, and S. Jochim, "Deterministic Preparation of a Tunable Few-Fermion System", Science **332**, 336 (2011).

[23] A. N. Wenz, G. Zürn, S. Murmann, I. Brouzos, T. Lompe, and S. Jochim, "From Few to Many: Observing the Formation of a Fermi Sea One Atom at a Time", Science **342**, 457 (2013).

[24] S. Murmann, A. Bergschneider, V. M. Klinkhamer, G. Zürn, T. Lompe, and S. Jochim, "Two Fermions in a Double Well: Exploring a Fundamental Building Block of the Hubbard Model", Phys. Rev. Lett. **114**, 080402 (2015).

[25] A. M. Kaufman, B. J. Lester, M. Foss-Feig, M. L. Wall, A. M. Rey, and C. A. Regal, "Entangling two transportable neutral atoms via local spin exchange", Nature **527**, 208 (2015).

[26] M. Endres, H. Bernien, A. Keesling, H. Levine, E. R. Anschuetz, A. Krajenbrink, C. Senko, V. Vuletic, M. Greiner, and M. D. Lukin, "Atom-by-atom assembly of defect-free one-dimensional cold atom arrays", Science **354**, 1024 (2016).

[27] E. Altman et al., "Quantum Simulators: Architectures and Opportunities", PRX Quantum **2**, 017003 (2021).

[28] S. S. Szigeti, O. Hosten, and S. A. Haine, "Improving cold-atom sensors with quantum entanglement: Prospects and challenges", Appl. Phys. Lett. **118**, 140501 (2021).

[29] D. Jaksch and P. Zoller, "The cold atom Hubbard toolbox", Ann. Phys. **315**, 52 (2005).

[30] M. Lewenstein, A. Sanpera, V. Ahufinger, B. Damski, A. Sen(De), and U. Sen, "Ultracold atomic gases in optical lattices: mimicking condensed matter physics and beyond", Adv. Phys. **56**, 243 (2007).

[31] C. Gross and I. Bloch, "Quantum simulations with ultracold atoms in optical lattices", Science **357**, 995 (2017).

[32] G.-X. Su, H. Sun, A. Hudomal, J.-Y. Desaules, Z.-Y. Zhou, B. Yang, J. C. Halimeh, Z.-S. Yuan, Z. Papić, and J.-W. Pan, "Observation of many-body scarring in a Bose-Hubbard quantum simulator", Phys. Rev. Research **5**, 023010 (2023).

[33] L. Su et al., "Dipolar quantum solids emerging in a Hubbard quantum simulator", Nature **622**, 724 (2023).

[34] J. Léonard, A. Morales, P. Zupancic, T. Esslinger, and T. Donner, "Supersolid formation in a quantum gas breaking a continuous translational symmetry", Nature **543**, 87 (2017).

[35] L. Chomaz et al., "Long-Lived and Transient Supersolid Behaviors in Dipolar Quantum Gases", Phys. Rev. X **9**, 021012 (2019).

[36] L. Tanzi, E. Lucioni, F. Famà, J. Catani, A. Fioretti, C. Gabbanini, R. N. Bisset, L. Santos, and G. Modugno, "Observation of a Dipolar Quantum Gas with Metastable Supersolid Properties", Phys. Rev. Lett. **122**, 130405 (2019).

[37] Z. Davoudi, M. Hafezi, C. Monroe, G. Pagano, A. Seif, and A. Shaw, "Towards analog quantum simulations of lattice gauge theories with trapped ions", Phys. Rev. Research **2**, 023015 (2020).

[38] B. Yang, H. Sun, R. Ott, H.-Y. Wang, T. V. Zache, J. C. Halimeh, Z.-S. Yuan, P. Hauke, and J.-W. Pan, "Observation of gauge invariance in a 71-site Bose–Hubbard quantum simulator", Nature **587**, 392 (2020).

[39] H. Moritz, T. Stöferle, M. Köhl, and T. Esslinger, "Exciting Collective Oscillations in a Trapped 1D Gas", Phys. Rev. Lett. **91**, 250402 (2003).

[40] C. Pethick and H. Smith, *Bose-Einstein condensation in dilute gases*, 2nd ed. (Cambridge University Press, Cambridge, 2006), 402 pp., ISBN: 978-0-521-66194-2.

[41] S. Burger, K. Bongs, S. Dettmer, W. Ertmer, K. Sengstock, A. Sanpera, G. V. Shlyapnikov, and M. Lewenstein, "Dark Solitons in Bose-Einstein Condensates", Phys. Rev. Lett. **83**, 5198 (1999).

[42] J. Denschlag et al., "Generating Solitons by Phase Engineering of a Bose-Einstein Condensate", Science **287**, 97 (2000).

[43] A. Romero-Ros, G. C. Katsimiga, P. G. Kevrekidis, B. Prinari, G. Biondini, and P. Schmelcher, "On-demand generation of dark soliton trains in Bose-Einstein condensates", Phys. Rev. A **103**, 023329 (2021).

[44] K. E. Strecker, G. B. Partridge, A. G. Truscott, and R. G. Hulet, "Formation and propagation of matter-wave soliton trains", Nature **417**, 150 (2002).

[45] L. Khaykovich, F. Schreck, G. Ferrari, T. Bourdel, J. Cubizolles, L. D. Carr, Y. Castin, and C. Salomon, "Formation of a Matter-Wave Bright Soliton", Science **296**, 1290 (2002).

[46] P. G. Kevrekidis, R. Carretero-González, and D. J. Frantzeskakis, eds., *Emergent Nonlinear Phenomena in Bose-Einstein Condensates: Theory and Experiment*, Atomic, Optical, and Plasma Physics 45 (Springer-Verlag Berlin Heidelberg, Berlin, Heidelberg, 2008), ISBN: 978-3-540-73590-8.

[47] P. C. Haljan, I. Coddington, P. Engels, and E. A. Cornell, "Driving Bose-Einstein-Condensate Vorticity with a Rotating Normal Cloud", Phys. Rev. Lett. **87**, 210403 (2001).

[48] V. Schweikhard, I. Coddington, P. Engels, V. P. Mogendorff, and E. A. Cornell, "Rapidly Rotating Bose-Einstein Condensates in and near the Lowest Landau Level", Phys. Rev. Lett. **92**, 040404 (2004).

[49] D. R. Scherer, C. N. Weiler, T. W. Neely, and B. P. Anderson, "Vortex Formation by Merging of Multiple Trapped Bose-Einstein Condensates", Phys. Rev. Lett. **98**, 110402 (2007).

[50] M. W. Zwierlein, A. Schirotzek, C. H. Schunck, and W. Ketterle, "Fermionic Superfluidity with Imbalanced Spin Populations", Science **311**, 492 (2006).

[51] M. A. Cazalilla, R. Citro, T. Giamarchi, E. Orignac, and M. Rigol, "One dimensional bosons: From condensed matter systems to ultracold gases", Rev. Mod. Phys. **83**, 1405 (2011).

[52] M. Lewenstein, A. Sanpera Trigueros, and V. Ahufinger, *Ultracold atoms in optical lattices: simulating quantum many-body systems*, paperback (Oxford University Press, Oxford, 2016), 479 pp., ISBN: 978-0-19-878580-4.

[53] S. Zöllner, H.-D. Meyer, and P. Schmelcher, "Ultracold Few-Boson Systems in a Double-Well Trap", Phys. Rev. A **74**, 053612 (2006).

[54] A. N. Salgueiro, A. de Toledo Piza, G. B. Lemos, R. Drumond, M. C. Nemes, and M. Weidemüller, "Quantum dynamics of bosons in a double-well potential: Josephson oscillations, self-trapping and ultralong tunneling times", Eur. Phys. J. D **44**, 537 (2007).

[55] S. Zöllner, H.-D. Meyer, and P. Schmelcher, "Few-Boson Dynamics in Double Wells: From Single-Atom to Correlated Pair Tunneling", Phys. Rev. Lett. **100**, 040401 (2008).

[56] K. Sakmann, A. I. Streltsov, O. E. Alon, and L. S. Cederbaum, "Exact Quantum Dynamics of a Bosonic Josephson Junction", Phys. Rev. Lett. **103**, 220601 (2009).

[57] V. Jelic and F. Marsiglio, "The double-well potential in quantum mechanics: a simple, numerically exact formulation", Eur. J. Phys. **33**, 1651 (2012).

[58] Y. Liu and Y. Zhang, "Two atoms in a double well: Exact solution with a Bethe ansatz", Phys. Rev. A **91**, 053610 (2015).

[59] J. Dobrzyniecki and T. Sowiński, "Exact dynamics of two ultra-cold bosons confined in a one-dimensional double-well potential", Eur. Phys. J. D **70**, 83 (2016).

[60] F. Borselli et al., "Two-Particle Interference with Double Twin-Atom Beams", Phys. Rev. Lett. **126**, 083603 (2021).

[61] L. Pitaevskii and S. Stringari, *Bose-Einstein condensation* (Oxford University Press, Oxford, 2003), ISBN: 9780198507192.

[62] D. Jaksch, C. Bruder, J. I. Cirac, C. W. Gardiner, and P. Zoller, "Cold Bosonic Atoms in Optical Lattices", Phys. Rev. Lett. **81**, 3108 (1998).

[63] M. Greiner, O. Mandel, T. Esslinger, T. W. Hänsch, and I. Bloch, "Quantum phase transition from a superfluid to a Mott insulator in a gas of ultracold atoms", Nature **415**, 39 (2002).

[64] I. Spielman, W. Phillips, and J. Porto, "Mott-Insulator Transition in a Two-Dimensional Atomic Bose Gas", Phys. Rev. Lett. **98**, 080404 (2007).

[65] I. Spielman, W. Phillips, and J. Porto, "Condensate Fraction in a 2D Bose Gas Measured across the Mott-Insulator Transition", Phys. Rev. Lett. **100**, 120402 (2008).

[66] T. Stöferle, H. Moritz, C. Schori, M. Köhl, and T. Esslinger, "Transition from a Strongly Interacting 1D Superfluid to a Mott Insulator", Phys. Rev. Lett. **92**, 130403 (2004).

[67] B. Paredes, A. Widera, V. Murg, O. Mandel, S. Fölling, I. Cirac, G. V. Shlyapnikov, T. W. Hänsch, and I. Bloch, "Tonks–Girardeau gas of ultracold atoms in an optical lattice", Nature **429**, 277 (2004).

[68] J. K. Chin, D. E. Miller, Y. Liu, C. Stan, W. Setiawan, C. Sanner, K. Xu, and W. Ketterle, "Evidence for superfluidity of ultracold fermions in an optical lattice", Nature **443**, 961 (2006).

[69] G. Wirth, M. Ölschläger, and A. Hemmerich, "Evidence for orbital superfluidity in the P-band of a bipartite optical square lattice", Nat. Phys. **7**, 147 (2011).

[70] P. Soltan-Panahi, D.-S. Lühmann, J. Struck, P. Windpassinger, and K. Sengstock, "Quantum phase transition to unconventional multi-orbital superfluidity in optical lattices", Nat. Phys. **8**, 71 (2012).

[71] P. W. Anderson, “Absence of Diffusion in Certain Random Lattices”, Phys. Rev. **109**, 1492 (1958).

[72] G. Roati, C. D’Errico, L. Fallani, M. Fattori, C. Fort, M. Zaccanti, G. Modugno, M. Modugno, and M. Inguscio, “Anderson localization of a non-interacting Bose–Einstein condensate”, Nature **453**, 895 (2008).

[73] A. Lukin, M. Rispoli, R. Schittko, M. E. Tai, A. M. Kaufman, S. Choi, V. Khemani, J. Léonard, and M. Greiner, “Probing entanglement in a many-body–localized system”, Science **364**, 256 (2019).

[74] L. Fallani, J. E. Lye, V. Guarrera, C. Fort, and M. Inguscio, “Ultracold Atoms in a Disordered Crystal of Light: Towards a Bose Glass”, Phys. Rev. Lett. **98**, 130404 (2007).

[75] J.-C. Yu, S. Bhave, L. Reeve, B. Song, and U. Schneider, “Observing the two-dimensional Bose glass in an optical quasicrystal”, Nature **633**, 338 (2024).

[76] T. Sowiński and M. Ángel García-March, “One-dimensional mixtures of several ultracold atoms: a review”, Rep. Prog. Phys. **82**, 104401 (2019).

[77] C. Baroni, G. Lamporesi, and M. Zaccanti, “Quantum mixtures of ultracold gases of neutral atoms”, Nat. Rev. Phys. **6**, 736 (2024).

[78] M. Haas, V. Leung, D. Frese, D. Haubrich, S. John, C. Weber, A. Rauschenbeutel, and D. Meschede, “Species-selective microwave cooling of a mixture of rubidium and caesium atoms”, New J. Phys. **9**, 147 (2007).

[79] M. Taglieber, A.-C. Voigt, T. Aoki, T. W. Hänsch, and K. Dieckmann, “Quantum Degenerate Two-Species Fermi-Fermi Mixture Coexisting with a Bose-Einstein Condensate”, Phys. Rev. Lett. **100**, 010401 (2008).

[80] J. Catani, G. Barontini, G. Lamporesi, F. Rabatti, G. Thalhammer, F. Minardi, S. Stringari, and M. Inguscio, “Entropy Exchange in a Mixture of Ultracold Atoms”, Phys. Rev. Lett. **103**, 140401 (2009).

[81] G. Lamporesi, J. Catani, G. Barontini, Y. Nishida, M. Inguscio, and F. Minardi, “Scattering in Mixed Dimensions with Ultracold Gases”, Phys. Rev. Lett. **104**, 153202 (2010).

[82] C.-H. Wu, I. Santiago, J. W. Park, P. Ahmadi, and M. W. Zwierlein, “Strongly interacting isotopic Bose-Fermi mixture immersed in a Fermi sea”, Phys. Rev. A **84**, 011601 (2011).

[83] G. Modugno, M. Modugno, F. Riboli, G. Roati, and M. Inguscio, “Two Atomic Species Superfluid”, Phys. Rev. Lett. **89**, 190404 (2002).

[84] S. B. Papp, J. M. Pino, and C. E. Wieman, “Tunable Miscibility in a Dual-Species Bose-Einstein Condensate”, Phys. Rev. Lett. **101**, 040402 (2008).

[85] J. Catani, G. Lamporesi, D. Naik, M. Gring, M. Inguscio, F. Minardi, A. Kantian, and T. Giamarchi, “Quantum dynamics of impurities in a one-dimensional Bose gas”, Phys. Rev. A **85**, 023623 (2012).

[86] R. Scelle, T. Rentrop, A. Trautmann, T. Schuster, and M. K. Oberthaler, “Motional Coherence of Fermions Immersed in a Bose Gas”, Phys. Rev. Lett. **111**, 070401 (2013).

[87] B. J. DeSalvo, K. Patel, G. Cai, and C. Chin, “Observation of fermion-mediated interactions between bosonic atoms”, Nature **568**, 61 (2019).

[88] A. Schirotzek, C.-H. Wu, A. Sommer, and M. W. Zwierlein, “Observation of Fermi Polarons in a Tunable Fermi Liquid of Ultracold Atoms”, Phys. Rev. Lett. **102**, 230402 (2009).

[89] S. Palzer, C. Zipkes, C. Sias, and M. Köhl, "Quantum Transport through a Tonks-Girardeau Gas", Phys. Rev. Lett. **103**, 150601 (2009).

[90] E. Timmermans, "Phase Separation of Bose-Einstein Condensates", Phys. Rev. Lett. **81**, 5718 (1998).

[91] M. Pyzh and P. Schmelcher, "Phase separation of a Bose-Bose mixture: Impact of the trap and particle-number imbalance", Phys. Rev. A **102**, 023305 (2020).

[92] S. Zöllner, H.-D. Meyer, and P. Schmelcher, "Composite fermionization of one-dimensional Bose-Bose mixtures", Phys. Rev. A **78**, 013629 (2008).

[93] Y. Hao and S. Chen, "Density-functional theory of two-component Bose gases in one-dimensional harmonic traps", Phys. Rev. A **80**, 043608 (2009).

[94] M. A. García-March, B. Juliá-Díaz, G. E. Astrakharchik, T. Busch, J. Boronat, and A. Polls, "Quantum correlations and spatial localization in one-dimensional ultracold bosonic mixtures", New J. Phys. **16**, 103004 (2014).

[95] Z.-H. Luo, W. Pang, B. Liu, Y.-Y. Li, and B. A. Malomed, "A new form of liquid matter: Quantum droplets", Front. Phys. **16**, 32201 (2021).

[96] R. N. Bisset, L. A. Peña Ardila, and L. Santos, "Quantum Droplets of Dipolar Mixtures", Phys. Rev. Lett. **126**, 025301 (2021).

[97] D. S. Petrov, "Quantum Mechanical Stabilization of a Collapsing Bose-Bose Mixture", Phys. Rev. Lett. **115**, 155302 (2015).

[98] D. S. Petrov and G. E. Astrakharchik, "Ultradilute Low-Dimensional Liquids", Phys. Rev. Lett. **117**, 100401 (2016).

[99] T. D. Lee, K. Huang, and C. N. Yang, "Eigenvalues and Eigenfunctions of a Bose System of Hard Spheres and Its Low-Temperature Properties", Phys. Rev. **106**, 1135 (1957).

[100] C. R. Cabrera, L. Tanzi, J. Sanz, B. Naylor, P. Thomas, P. Cheiney, and L. Tarruell, "Quantum liquid droplets in a mixture of Bose-Einstein condensates", Science **359**, 301 (2018).

[101] G. Ferioli, G. Semeghini, L. Masi, G. Giusti, G. Modugno, M. Inguscio, A. Gallemí, A. Recati, and M. Fattori, "Collisions of Self-Bound Quantum Droplets", Phys. Rev. Lett. **122**, 090401 (2019).

[102] T. Mithun, S. I. Mistakidis, P. Schmelcher, and P. G. Kevrekidis, "Statistical mechanics of one-dimensional quantum droplets", Phys. Rev. A **104**, 033316 (2021).

[103] S. I. Mistakidis, T. Mithun, P. G. Kevrekidis, H. R. Sadeghpour, and P. Schmelcher, "Formation and quench of homonuclear and heteronuclear quantum droplets in one dimension", Phys. Rev. Research **3**, 043128 (2021).

[104] I. A. Englezos, S. I. Mistakidis, and P. Schmelcher, "Correlated dynamics of collective droplet excitations in a one-dimensional harmonic trap", Phys. Rev. A **107**, 023320 (2023).

[105] I. Morera, G. E. Astrakharchik, A. Polls, and B. Juliá-Díaz, "Quantum droplets of bosonic mixtures in a one-dimensional optical lattice", Phys. Rev. Research **2**, 022008 (2020).

[106] I. Morera, G. E. Astrakharchik, A. Polls, and B. Juliá-Díaz, "Universal Dimerized Quantum Droplets in a One-Dimensional Lattice", Phys. Rev. Lett. **126**, 023001 (2021).

[107] Y. Sekino and Y. Nishida, "Quantum droplet of one-dimensional bosons with a three-body attraction", Phys. Rev. A **97**, 011602 (2018).

[108] D. Yan, J. J. Chang, C. Hamner, M. Hoefer, P. G. Kevrekidis, P. Engels, V. Achilleos, D. J. Frantzeskakis, and J. Cuevas, "Beating dark–dark solitons in Bose–Einstein condensates", J. Phys. B: At. Mol. Opt. Phys. **45**, 115301 (2012).

[109] A. Álvarez, J. Cuevas, F. R. Romero, C. Hamner, J. J. Chang, P. Engels, P. G. Kevrekidis, and D. J. Frantzeskakis, "Scattering of atomic dark–bright solitons from narrow impurities", J. Phys. B: At. Mol. Opt. Phys. **46**, 065302 (2013).

[110] G. C. Katsimiga, J. Stockhofe, P. G. Kevrekidis, and P. Schmelcher, "Dark-bright soliton interactions beyond the integrable limit", Phys. Rev. A **95**, 013621 (2017).

[111] G. C. Katsimiga, G. M. Koutentakis, S. I. Mistakidis, P. G. Kevrekidis, and P. Schmelcher, "Dark–bright soliton dynamics beyond the mean-field approximation", New J. Phys. **19**, 073004 (2017).

[112] I. Danaila, M. A. Khamehchi, V. Gokhroo, P. Engels, and P. G. Kevrekidis, "Vector dark-antidark solitary waves in multicomponent Bose-Einstein condensates", Phys. Rev. A **94**, 053617 (2016).

[113] G. C. Katsimiga, S. I. Mistakidis, T. M. Bersano, M. K. H. Ome, S. M. Mossman, K. Mukherjee, P. Schmelcher, P. Engels, and P. G. Kevrekidis, "Observation and analysis of multiple dark-antidark solitons in two-component Bose-Einstein condensates", Phys. Rev. A **102**, 023301 (2020).

[114] A. Romero-Ros, G. C. Katsimiga, S. I. Mistakidis, B. Prinari, G. Biondini, P. Schmelcher, and P. G. Kevrekidis, "Theoretical and numerical evidence for the potential realization of the Peregrine soliton in repulsive two-component Bose-Einstein condensates", Phys. Rev. A **105**, 053306 (2022).

[115] A. Romero-Ros, G. C. Katsimiga, S. I. Mistakidis, S. Mossman, G. Biondini, P. Schmelcher, P. Engels, and P. G. Kevrekidis, "Experimental Realization of the Peregrine Soliton in Repulsive Two-Component Bose-Einstein Condensates", Phys. Rev. Lett. **132**, 033402 (2024).

[116] P. Massignan, M. Zaccanti, and G. M. Bruun, "Polarons, dressed molecules and itinerant ferromagnetism in ultracold Fermi gases", Rep. Prog. Phys. **77**, 034401 (2014).

[117] H. Tajima, J. Takahashi, S. Mistakidis, E. Nakano, and K. Iida, "Polaron Problems in Ultracold Atoms: Role of a Fermi Sea across Different Spatial Dimensions and Quantum Fluctuations of a Bose Medium", Atoms **9**, 18 (2021).

[118] F. Scazza, M. Zaccanti, P. Massignan, M. M. Parish, and J. Levinsen, "Repulsive Fermi and Bose Polarons in Quantum Gases", Atoms **10**, 55 (2022).

[119] F. Grusdt, N. Mostaan, E. Demler, and L. A. Ardila Peña, "Impurities and polarons in bosonic quantum gases: a review on recent progress", `10.48550/arXiv.2410.09413` (2024), preprint.

[120] N. B. Jørgensen, L. Wacker, K. T. Skalmstang, M. M. Parish, J. Levinsen, R. S. Christensen, G. M. Bruun, and J. J. Arlt, "Observation of Attractive and Repulsive Polarons in a Bose-Einstein Condensate", Phys. Rev. Lett. **117**, 055302 (2016).

[121] M.-G. Hu, M. J. Van de Graaff, D. Kedar, J. P. Corson, E. A. Cornell, and D. S. Jin, "Bose Polarons in the Strongly Interacting Regime", Phys. Rev. Lett. **117**, 055301 (2016).

[122] Z. Z. Yan, Y. Ni, C. Robens, and M. W. Zwierlein, "Bose polarons near quantum criticality", Science **368**, 190 (2020).

[123] C. Kohstall, M. Zaccanti, M. Jag, A. Trenkwalder, P. Massignan, G. M. Bruun, F. Schreck, and R. Grimm, "Metastability and coherence of repulsive polarons in a strongly interacting Fermi mixture", Nature **485**, 615 (2012).

[124] M. Koschorreck, D. Pertot, E. Vogt, B. Fröhlich, M. Feld, and M. Köhl, “Attractive and repulsive Fermi polarons in two dimensions”, Nature **485**, 619 (2012).

[125] N. Spethmann, F. Kindermann, S. John, C. Weber, D. Meschede, and A. Widera, “Dynamics of Single Neutral Impurity Atoms Immersed in an Ultracold Gas”, Phys. Rev. Lett. **109**, 235301 (2012).

[126] T. Fukuhara et al., “Quantum dynamics of a mobile spin impurity”, Nat. Phys. **9**, 235 (2013).

[127] F. Meinert, M. Knap, E. Kirilov, K. Jag-Lauber, M. B. Zvonarev, E. Demler, and H.-C. Nägerl, “Bloch oscillations in the absence of a lattice”, Science **356**, 945 (2017).

[128] Q. Bouton, J. Nettersheim, D. Adam, F. Schmidt, D. Mayer, T. Lausch, E. Tiemann, and A. Widera, “Single-Atom Quantum Probes for Ultracold Gases Boosted by Nonequilibrium Spin Dynamics”, Phys. Rev. X **10**, 011018 (2020).

[129] T. Hewitt, T. Bertheas, M. Jain, Y. Nishida, and G. Barontini, “Controlling the interactions in a cold atom quantum impurity system”, Quantum Sci. Technol. **9**, 035039 (2024).

[130] K. Sacha and E. Timmermans, “Self-localized impurities embedded in a one-dimensional Bose-Einstein condensate and their quantum fluctuations”, Phys. Rev. A **73**, 063604 (2006).

[131] M. Bruderer, A. Klein, S. R. Clark, and D. Jaksch, “Polaron physics in optical lattices”, Phys. Rev. A **76**, 011605 (2007).

[132] Y. E. Shchadilova, R. Schmidt, F. Grusdt, and E. Demler, “Quantum Dynamics of Ultracold Bose Polarons”, Phys. Rev. Lett. **117**, 113002 (2016).

[133] F. Grusdt, R. Schmidt, Y. E. Shchadilova, and E. Demler, “Strong-coupling Bose polarons in a Bose-Einstein condensate”, Phys. Rev. A **96**, 013607 (2017).

[134] M. Drescher, M. Salmhofer, and T. Enss, “Quench Dynamics of the Ideal Bose Polaron at Zero and Nonzero Temperatures”, Phys. Rev. A **103**, 033317 (2021).

[135] K. Seetharam, Y. Shchadilova, F. Grusdt, M. B. Zvonarev, and E. Demler, “Dynamical Quantum Cherenkov Transition of Fast Impurities in Quantum Liquids”, Phys. Rev. Lett. **127**, 185302 (2021).

[136] R. S. Christensen, J. Levinsen, and G. M. Bruun, “Quasiparticle Properties of a Mobile Impurity in a Bose-Einstein Condensate”, Phys. Rev. Lett. **115**, 160401 (2015).

[137] J. Levinsen, M. M. Parish, and G. M. Bruun, “Impurity in a Bose-Einstein Condensate and the Efimov Effect”, Phys. Rev. Lett. **115**, 125302 (2015).

[138] S. P. Rath and R. Schmidt, “Field-theoretical study of the Bose polaron”, Phys. Rev. A **88**, 053632 (2013).

[139] L. A. Peña Ardila and S. Giorgini, “Impurity in a Bose-Einstein condensate: Study of the attractive and repulsive branch using quantum Monte Carlo methods”, Phys. Rev. A **92**, 033612 (2015).

[140] N. Mostaan, N. Goldman, and F. Grusdt, “A unified theory of strong coupling Bose polarons: From repulsive polarons to non-Gaussian many-body bound states”, `10.48550/arXiv.2305.00835` (2023), preprint.

[141] M. Bruderer, W. Bao, and D. Jaksch, “Self-trapping of impurities in Bose-Einstein condensates: Strong attractive and repulsive coupling”, Europhys. Lett. **82**, 30004 (2008).

[142] W. Casteels, J. Tempere, and J. T. Devreese, “Polaronic properties of an impurity in a Bose-Einstein condensate in reduced dimensions”, Phys. Rev. A **86**, 043614 (2012).

[143] L. Parisi and S. Giorgini, “Quantum Monte Carlo study of the Bose-polaron problem in a one-dimensional gas with contact interactions”, Phys. Rev. A **95**, 023619 (2017).

[144] F. Grusdt, G. E. Astrakharchik, and E. Demler, “Bose polarons in ultracold atoms in one dimension: beyond the Fröhlich paradigm”, New J. Phys. **19**, 103035 (2017).

[145] V. Pastukhov, “Impurity states in the one-dimensional Bose gas”, Phys. Rev. A **96**, 043625 (2017).

[146] A. G. Volosniev and H.-W. Hammer, “Analytical approach to the Bose-polaron problem in one dimension”, Phys. Rev. A **96**, 031601R (2017).

[147] G. Panochko and V. Pastukhov, “Mean-field construction for spectrum of one-dimensional Bose polaron”, Ann. Phys. **409**, 167933 (2019).

[148] J. Jager, R. Barnett, M. Will, and M. Fleischhauer, “Strong-coupling Bose polarons in one dimension: Condensate deformation and modified Bogoliubov phonons”, Phys. Rev. Research **2**, 033142 (2020).

[149] G. M. Koutentakis, S. I. Mistakidis, and P. Schmelcher, “Pattern Formation in One-Dimensional Polaron Systems and Temporal Orthogonality Catastrophe”, Atoms **10**, 3 (2021).

[150] M. Will, G. E. Astrakharchik, and M. Fleischhauer, “Polaron Interactions and Bipolarons in One-Dimensional Bose Gases in the Strong Coupling Regime”, Phys. Rev. Lett. **127**, 103401 (2021).

[151] D. Breu, E. Vidal Marcos, M. Will, and M. Fleischhauer, “Impurities in a trapped one-dimensional Bose gas of arbitrary interaction strength: Localization-delocalization transition and absence of self-localization”, Phys. Rev. A **111**, 023326 (2025).

[152] S. Krönke, J. Knörzer, and P. Schmelcher, “Correlated quantum dynamics of a single atom collisionally coupled to an ultracold finite bosonic ensemble”, New J. Phys. **17**, 053001 (2015).

[153] S. I. Mistakidis, F. Grusdt, G. M. Koutentakis, and P. Schmelcher, “Dissipative correlated dynamics of a moving impurity immersed in a Bose–Einstein condensate”, New J. Phys. **21**, 103026 (2019).

[154] A. S. Popova, V. V. Tiunova, and A. N. Rubtsov, “Quantum Monte Carlo simulation of BEC-impurity tunneling”, Phys. Rev. B **103**, 155406 (2021).

[155] J. Chen, K. Keiler, G. Xianlong, and P. Schmelcher, “Impurity-induced quantum chaos for an ultracold bosonic ensemble in a double well”, Phys. Rev. A **104**, 033315 (2021).

[156] A. Klein, M. Bruderer, S. R. Clark, and D. Jaksch, “Dynamics, dephasing and clustering of impurity atoms in Bose–Einstein condensates”, New J. Phys. **9**, 411 (2007).

[157] K. Keiler, S. Krönke, and P. Schmelcher, “Correlation induced localization of lattice trapped bosons coupled to a Bose–Einstein condensate”, New J. Phys. **20**, 033030 (2018).

[158] N. A. Kamar, A. Kantian, and T. Giamarchi, “Dynamics of a mobile impurity in a two-leg bosonic ladder”, Phys. Rev. A **100**, 023614 (2019).

[159] K. Keiler and P. Schmelcher, “Interaction-induced single-impurity tunneling in a binary mixture of trapped ultracold bosons”, Phys. Rev. A **100**, 043616 (2019).

[160] S. I. Mistakidis, G. C. Katsimiga, G. M. Koutentakis, Th. Busch, and P. Schmelcher, “Quench Dynamics and Orthogonality Catastrophe of Bose Polarons”, Phys. Rev. Lett. **122**, 183001 (2019).

[161] A. Klein and M. Fleischhauer, “Interaction of impurity atoms in Bose-Einstein condensates”, Phys. Rev. A **71**, 033605 (2005).

[162] A. Recati, J. N. Fuchs, C. S. Peça, and W. Zwerger, "Casimir forces between defects in one-dimensional quantum liquids", Phys. Rev. A **72**, 023616 (2005).

[163] P. Wächter, V. Meden, and K. Schönhammer, "Indirect forces between impurities in one-dimensional quantum liquids", Phys. Rev. B **76**, 045123 (2007).

[164] A. I. Pavlov, J. Van Den Brink, and D. V. Efremov, "Phonon-mediated Casimir interaction between finite-mass impurities", Phys. Rev. B **98**, 161410 (2018).

[165] A. S. Dehkharghani, A. G. Volosniev, and N. T. Zinner, "Coalescence of Two Impurities in a Trapped One-dimensional Bose Gas", Phys. Rev. Lett. **121**, 080405 (2018).

[166] A. Camacho-Guardian, L. A. Peña Ardila, T. Pohl, and G. M. Bruun, "Bipolarons in a Bose-Einstein Condensate", Phys. Rev. Lett. **121**, 013401 (2018).

[167] B. Reichert, A. Petković, and Z. Ristivojevic, "Field-theoretical approach to the Casimir-like interaction in a one-dimensional Bose gas", Phys. Rev. B **99**, 205414 (2019).

[168] B. Reichert, Z. Ristivojevic, and A. Petković, "The Casimir-like effect in a one-dimensional Bose gas", New J. Phys. **21**, 053024 (2019).

[169] S. I. Mistakidis, G. M. Koutentakis, G. C. Katsimiga, T. Busch, and P. Schmelcher, "Many-body quantum dynamics and induced correlations of Bose polarons", New J. Phys. **22**, 043007 (2020).

[170] S. I. Mistakidis, A. G. Volosniev, and P. Schmelcher, "Induced correlations between impurities in a one-dimensional quenched Bose gas", Phys. Rev. Research **2**, 023154 (2020).

[171] A. Petković and Z. Ristivojevic, "Mediated interaction between polarons in a one-dimensional Bose gas", Phys. Rev. A **105**, L021303 (2022).

[172] G. E. Astrakharchik, L. A. Peña Ardila, K. Jachymski, and A. Negretti, "Many-body bound states and induced interactions of charged impurities in a bosonic bath", Nat. Commun. **14**, 1647 (2023).

[173] R. Paredes, G. Bruun, and A. Camacho-Guardian, "Interactions mediated by atoms, photons, electrons, and excitons", Phys. Rev. A **110**, 030101 (2024).

[174] W. Casteels, J. Tempere, and J. T. Devreese, "Bipolarons and multipolarons consisting of impurity atoms in a Bose-Einstein condensate", Phys. Rev. A **88**, 013613 (2013).

[175] A. Camacho-Guardian and G. M. Bruun, "Landau Effective Interaction between Quasiparticles in a Bose-Einstein Condensate", Phys. Rev. X **8**, 031042 (2018).

[176] J. Jager and R. Barnett, "The effect of boson–boson interaction on the bipolaron formation", New J. Phys. **24**, 103032 (2022).

[177] M. Schecter and A. Kamenev, "Phonon-Mediated Casimir Interaction between Mobile Impurities in One-Dimensional Quantum Liquids", Phys. Rev. Lett. **112**, 155301 (2014).

[178] J. Chen, J. M. Schurer, and P. Schmelcher, "Entanglement Induced Interactions in Binary Mixtures", Phys. Rev. Lett. **121**, 043401 (2018).

[179] K. Keiler, S. I. Mistakidis, and P. Schmelcher, "Doping a lattice-trapped bosonic species with impurities: from ground state properties to correlated tunneling dynamics", New J. Phys. **22**, 083003 (2020).

[180] A. S. Mellish, N. Kjærgaard, P. S. Julienne, and A. C. Wilson, "Quantum scattering of distinguishable bosons using an ultracold-atom collider", Phys. Rev. A **75**, 020701 (2007).

[181] A. Weller, J. P. Ronzheimer, C. Gross, J. Esteve, M. K. Oberthaler, D. J. Frantzeskakis, G. Theocharis, and P. G. Kevrekidis, "Experimental Observation of Oscillating and Interacting Matter Wave Dark Solitons", Phys. Rev. Lett. **101**, 130401 (2008).

[182] R. Thomas, M. Chilcott, C. Chisholm, A. B. Deb, M. Horvath, B. J. Sawyer, and N. Kjærgaard, "Quantum Scattering in an Optical Collider for Ultracold Atoms", J. Phys.: Conf. Ser. **875**, 012007 (2017).

[183] R. Thomas, M. Chilcott, E. Tiesinga, A. B. Deb, and N. Kjærgaard, "Observation of bound state self-interaction in a nano-eV atom collider", Nat. Commun. **9**, 4895 (2018).

[184] F. Köhler and P. Schmelcher, "Bosonic quantum dynamics following colliding potential wells", Phys. Rev. A **103**, 043326 (2021).

[185] C. Hamner, J. J. Chang, P. Engels, and M. A. Hoefer, "Generation of Dark-Bright Soliton Trains in Superfluid-Superfluid Counterflow", Phys. Rev. Lett. **106**, 065302 (2011).

[186] J. Akram, "Quantum dynamics of impurities in a Bose–Einstein condensate", Appl. Phys. B **127**, 108 (2021).

[187] J. Kwasniok, S. I. Mistakidis, and P. Schmelcher, "Correlated dynamics of fermionic impurities induced by the counterflow of an ensemble of fermions", Phys. Rev. A **101**, 053619 (2020).

[188] T. M. Bersano, V. Gokhroo, M. A. Khamehchi, J. D'Ambroise, D. J. Frantzeskakis, P. Engels, and P. G. Kevrekidis, "Three-component soliton states in spinor F=1 bose-einstein condensates", Phys. Rev. Lett. **120**, 063202 (2018).

[189] S. Lannig, C.-M. Schmied, M. Prüfer, P. Kunkel, R. Strohmaier, H. Strobel, T. Gasenzer, P. G. Kevrekidis, and M. K. Oberthaler, "Collisions of Three-Component Vector Solitons in Bose-Einstein Condensates", Phys. Rev. Lett. **125**, 170401 (2020).

[190] E. Compagno, G. De Chiara, D. G. Angelakis, and G. M. Palma, "Tunable Polarons in Bose-Einstein Condensates", Sci. Rep. **7**, 2355 (2017).

[191] A. Boudjemâa, N. Guebli, M. Sekmane, and S. Khlifa-Karfa, "Breathing modes of repulsive polarons in Bose–Bose mixtures", J. Phys.: Condens. Matter **32**, 415401 (2020).

[192] F. K. Abdullaev and R. M. Galimzyanov, "Bosonic impurity in a one-dimensional quantum droplet in the Bose–Bose mixture", J. Phys. B: At. Mol. Opt. Phys. **53**, 165301 (2020).

[193] K. Keiler, S. I. Mistakidis, and P. Schmelcher, "Polarons and their induced interactions in highly imbalanced triple mixtures", Phys. Rev. A **104**, L031301 (2021).

[194] J. Becker, M. Pyzh, and P. Schmelcher, "Interaction-controlled impurity transport in trapped mixtures of ultracold bosons", Phys. Rev. A **106**, 053314 (2022).

[195] K. Abbas and A. Boudjemâa, "Binary Bose–Einstein condensates in a disordered time-dependent potential", J. Phys.: Condens. Matter **34**, 125102 (2022).

[196] C. Liu, P. Chen, L. He, and F. Xu, "Ground-state properties of multicomponent bosonic mixtures: A Gutzwiller mean-field study", Phys. Rev. A **108**, 013309 (2023).

[197] G. Bighin, A. Burchianti, F. Minardi, and T. Macrì, "Impurity in a heteronuclear two-component Bose mixture", Phys. Rev. A **106**, 023301 (2022).

[198] Y. Ma, C. Peng, and X. Cui, "Borromean Droplet in Three-Component Ultracold Bose Gases", Phys. Rev. Lett. **127**, 043002 (2021).

[199] Y. Ma and X. Cui, "Shell-Shaped Quantum Droplet in a Three-Component Ultracold Bose Gas", Phys. Rev. Lett. **134**, 043402 (2025).

[200] T. D. Anh-Tai, M. A. García-March, T. Busch, and T. Fogarty, "Quantum correlations and spatial localization in trapped one-dimensional ultra-cold Bose-Bose-Bose mixtures", `10.48550/arXiv.2501.15358` (2025), preprint.

[201] C. Charalambous, M. Á. García-March, G. Muñoz-Gil, P. R. Grzybowski, and M. Lewenstein, "Control of anomalous diffusion of a Bose polaron", Quantum **4**, 232 (2020).

[202] F. Brauneis, H.-W. Hammer, M. Lemeshko, and A. Volosniev, "Impurities in a one-dimensional Bose gas: the flow equation approach", SciPost Phys. **11**, 008 (2021).

[203] T. D. Anh-Tai, T. Fogarty, S. De María-García, T. Busch, and M. A. García-March, "Engineering impurity Bell states through coupling with a quantum bath", Phys. Rev. Research **6**, 043042 (2024).

[204] L. Cao, S. Krönke, O. Vendrell, and P. Schmelcher, "The multi-layer multi-configuration time-dependent Hartree method for bosons: Theory, implementation, and applications", J. Chem. Phys. **139**, 134103 (2013).

[205] S. Krönke, L. Cao, O. Vendrell, and P. Schmelcher, "Non-equilibrium quantum dynamics of ultra-cold atomic mixtures: the multi-layer multi-configuration time-dependent Hartree method for bosons", New J. Phys. **15**, 063018 (2013).

[206] L. Cao, V. Bolsinger, S. I. Mistakidis, G. M. Koutentakis, S. Krönke, J. M. Schurer, and P. Schmelcher, "A unified ab initio approach to the correlated quantum dynamics of ultracold fermionic and bosonic mixtures", J. Chem. Phys. **147**, 044106 (2017).

[207] L. A. Peña Ardila and S. Giorgini, "Bose polaron problem: Effect of mass imbalance on binding energy", Phys. Rev. A **94**, 063640 (2016).

[208] D. R. Dounas-Frazer, A. M. Hermundstad, and L. D. Carr, "Ultracold Bosons in a Tilted Multilevel Double-Well Potential", Phys. Rev. Lett. **99**, 200402 (2007).

[209] L. D. Carr, D. R. Dounas-Frazer, and M. A. Garcia-March, "Dynamical realization of macroscopic superposition states of cold bosons in a tilted double well", Europhys. Lett. **90**, 10005 (2010).

[210] J. Erdmann, S. I. Mistakidis, and P. Schmelcher, "Correlated tunneling dynamics of an ultracold Fermi-Fermi mixture confined in a double well", Phys. Rev. A **98**, 053614 (2018).

[211] B. E. Sherlock, M. Gildemeister, E. Owen, E. Nugent, and C. J. Foot, "Time-averaged adiabatic ring potential for ultracold atoms", Phys. Rev. A **83**, 043408 (2011).

[212] T. A. Bell, J. A. P. Glidden, L. Humbert, M. W. J. Bromley, S. A. Haine, M. J. Davis, T. W. Neely, M. A. Baker, and H. Rubinsztein-Dunlop, "Bose–Einstein condensation in large time-averaged optical ring potentials", New J. Phys. **18**, 035003 (2016).

[213] J. Kwan, P. Segura, Y. Li, S. Kim, A. V. Gorshkov, A. Eckardt, B. Bakkali-Hassani, and M. Greiner, "Realization of one-dimensional anyons with arbitrary statistical phase", Science **386**, 1055 (2024).

[214] J. M. Leinaas and J. Myrheim, "On the theory of identical particles", Nuovo Cim B **37**, 1 (1977).

[215] G. A. Goldin, R. Menikoff, and D. H. Sharp, "Representations of a local current algebra in nonsimply connected space and the Aharonov–Bohm effect", J. Math. Phys. **22**, 1664 (1981).

[216] F. Wilczek, “Magnetic Flux, Angular Momentum, and Statistics”, Phys. Rev. Lett. **48**, 1144 (1982).

[217] D. C. Tsui, H. L. Stormer, and A. C. Gossard, “Two-Dimensional Magnetotransport in the Extreme Quantum Limit”, Phys. Rev. Lett. **48**, 1559 (1982).

[218] R. B. Laughlin, “Anomalous Quantum Hall Effect: An Incompressible Quantum Fluid with Fractionally Charged Excitations”, Phys. Rev. Lett. **50**, 1395 (1983).

[219] F. D. M. Haldane, ““Fractional statistics” in arbitrary dimensions: A generalization of the Pauli principle”, Phys. Rev. Lett. **67**, 937 (1991).

[220] B. I. Halperin, “Statistics of Quasiparticles and the Hierarchy of Fractional Quantized Hall States”, Phys. Rev. Lett. **52**, 1583 (1984).

[221] D. Arovas, J. R. Schrieffer, and F. Wilczek, “Fractional Statistics and the Quantum Hall Effect”, Phys. Rev. Lett. **53**, 722 (1984).

[222] H. Bartolomei et al., “Fractional statistics in anyon collisions”, Science **368**, 173 (2020).

[223] J. Nakamura, S. Liang, G. C. Gardner, and M. J. Manfra, “Direct observation of anyonic braiding statistics”, Nat. Phys. **16**, 931 (2020).

[224] T. D. Kühner and H. Monien, “Phases of the one-dimensional Bose-Hubbard model”, Phys. Rev. B **58**, R14741 (1998).

[225] T. D. Kühner, S. R. White, and H. Monien, “One-dimensional Bose-Hubbard model with nearest-neighbor interaction”, Phys. Rev. B **61**, 12474 (2000).

[226] J. Arcila-Forero, R. Franco, and J. Silva-Valencia, “Critical points of the anyon-Hubbard model”, Phys. Rev. A **94**, 013611 (2016).

[227] S. Greschner and L. Santos, “Anyon Hubbard Model in One-Dimensional Optical Lattices”, Phys. Rev. Lett. **115**, 053002 (2015).

[228] T. Posske, B. Trauzettel, and M. Thorwart, “Second quantization of Leinaas-Myrheim anyons in one dimension and their relation to the Lieb-Liniger model”, Phys. Rev. B **96**, 195422 (2017).

[229] C. Sträter, S. C. L. Srivastava, and A. Eckardt, “Floquet Realization and Signatures of One-Dimensional Anyons in an Optical Lattice”, Phys. Rev. Lett. **117**, 205303 (2016).

[230] A. Kundu, “Exact Solution of Double δ Function Bose Gas through an Interacting Anyon Gas”, Phys. Rev. Lett. **83**, 1275 (1999).

[231] M. Bonkhoff, K. Jägering, S. Eggert, A. Pelster, M. Thorwart, and T. Posske, “Bosonic Continuum Theory of One-Dimensional Lattice Anyons”, Phys. Rev. Lett. **126**, 163201 (2021).

[232] F. Lange, S. Ejima, and H. Fehske, “Anyonic Haldane Insulator in One Dimension”, Phys. Rev. Lett. **118**, 120401 (2017).

[233] F. Liu, J. R. Garrison, D.-L. Deng, Z.-X. Gong, and A. V. Gorshkov, “Asymmetric Particle Transport and Light-Cone Dynamics Induced by Anyonic Statistics”, Phys. Rev. Lett. **121**, 250404 (2018).

[234] A. Del Campo, “Fermionization and bosonization of expanding one-dimensional anyonic fluids”, Phys. Rev. A **78**, 045602 (2008).

[235] Y. Hao, Y. Zhang, and S. Chen, “Ground-state properties of hard-core anyons in one-dimensional optical lattices”, Phys. Rev. A **79**, 043633 (2009).

[236] Y. Hao and S. Chen, “Dynamical properties of hard-core anyons in one-dimensional optical lattices”, Phys. Rev. A **86**, 043631 (2012).

[237] G. Tang, S. Eggert, and A. Pelster, “Ground-state properties of anyons in a one-dimensional lattice”, New J. Phys. **17**, 123016 (2015).

[238] S. Dhar, B. Wang, M. Horvath, A. Vashisht, Y. Zeng, M. B. Zvonarev, N. Goldman, Y. Guo, M. Landini, and H.-C. Nägerl, “Anyonization of bosons”, `10.48550/arXiv.2412.21131` (2024), preprint.

[239] S. N. Bose, “Plancks Gesetz und Lichtquantenhypothese”, Z. Phys. **26**, 178 (1924).

[240] A. Einstein, in *Albert Einstein: Akademie-Vorträge*, edited by D. Simon, 1st ed. (Wiley, Dec. 16, 2005), pp. 245–257, ISBN: 978-3-527-60895-9.

[241] C. N. Cohen-Tannoudji, “Nobel Lecture: Manipulating atoms with photons”, Rev. Mod. Phys. **70**, 707 (1998).

[242] W. D. Phillips, “Nobel Lecture: Laser cooling and trapping of neutral atoms”, Rev. Mod. Phys. **70**, 721 (1998).

[243] S. Chu, “Nobel Lecture: The manipulation of neutral particles”, Rev. Mod. Phys. **70**, 685 (1998).

[244] H. J. Metcalf and P. Van Der Straten, *Laser Cooling and Trapping*, red. by R. S. Berry, J. L. Birman, J. W. Lynn, M. P. Silverman, H. E. Stanley, and M. Voloshin, Graduate Texts in Contemporary Physics (Springer New York, New York, NY, 1999), ISBN: 978-1-4612-1470-0.

[245] F. Schreck and K. V. Druten, “Laser cooling for quantum gases”, Nat. Phys. **17**, 1296 (2021).

[246] H. Son, J. J. Park, W. Ketterle, and A. O. Jamison, “Collisional cooling of ultracold molecules”, Nature **580**, 197 (2020).

[247] M. Drewsen, Ph. Laurent, A. Nadir, G. Santarelli, A. Clairon, Y. Castin, D. Grison, and C. Salomon, “Investigation of sub-Doppler cooling effects in a cesium magneto-optical trap”, Appl. Phys. B **59**, 283 (1994).

[248] C. G. Townsend, N. H. Edwards, C. J. Cooper, K. P. Zetie, C. J. Foot, A. M. Steane, P. Szriftgiser, H. Perrin, and J. Dalibard, “Phase-space density in the magneto-optical trap”, Phys. Rev. A **52**, 1423 (1995).

[249] K. Dieckmann, R. J. C. Spreeuw, M. Weidemüller, and J. T. M. Walraven, “Two-dimensional magneto-optical trap as a source of slow atoms”, Phys. Rev. A **58**, 3891 (1998).

[250] W. Ketterle and N. V. Druten, in *Advances In Atomic, Molecular, and Optical Physics*, Vol. 37 (Elsevier, 1996), pp. 181–236, ISBN: 978-0-12-003837-4.

[251] C.-L. Hung, X. Zhang, N. Gemelke, and C. Chin, “Accelerating evaporative cooling of atoms into Bose-Einstein condensation in optical traps”, Phys. Rev. A **78**, 011604 (2008).

[252] R. Grimm, M. Weidemüller, and Y. B. Ovchinnikov, “Optical Dipole Traps for Neutral Atoms”, Adv. At. Mol. Opt. Phys. **42**, 95 (2000).

[253] A. L. Gaunt, T. F. Schmidutz, I. Gotlibovych, R. P. Smith, and Z. Hadzibabic, “Bose-Einstein Condensation of Atoms in a Uniform Potential”, Phys. Rev. Lett. **110**, 200406 (2013).

[254] S. Peil, J. V. Porto, B. L. Tolra, J. M. Obrecht, B. E. King, M. Subbotin, S. L. Rolston, and W. D. Phillips, “Patterned loading of a Bose-Einstein condensate into an optical lattice”, Phys. Rev. A **67**, 051603 (2003).

[255] Z. Hadzibabic, S. Stock, B. Battelier, V. Bretin, and J. Dalibard, "Interference of an Array of Independent Bose-Einstein Condensates", Phys. Rev. Lett. **93**, 180403 (2004).

[256] Dalibard J., "Collisional dynamics of ultra-cold atomic gases", ENFI **140**, 321 (1999).

[257] M. Ueda, *Fundamentals and new frontiers of Bose-Einstein condensation* (World Scientific, New Jersey, 2010), 351 pp., ISBN: 978-981-283-959-6.

[258] K. Huang, *Statistical mechanics*, 2nd ed (Wiley, New York, 1987), 493 pp., ISBN: 978-0-471-81518-1.

[259] A. J. Moerdijk, B. J. Verhaar, and A. Axelsson, "Resonances in ultracold collisions of Li 6 , Li 7 , and Na 23", Phys. Rev. A **51**, 4852 (1995).

[260] G. Thalhammer, M. Theis, K. Winkler, R. Grimm, and J. H. Denschlag, "Inducing an optical Feshbach resonance via stimulated Raman coupling", Phys. Rev. A **71**, 033403 (2005).

[261] M. Yan, B. J. DeSalvo, B. Ramachandhran, H. Pu, and T. C. Killian, "Controlling Condensate Collapse and Expansion with an Optical Feshbach Resonance", Phys. Rev. Lett. **110**, 123201 (2013).

[262] S. Blatt, T. L. Nicholson, B. J. Bloom, J. R. Williams, J. W. Thomsen, P. S. Julienne, and J. Ye, "Measurement of Optical Feshbach Resonances in an Ideal Gas", Phys. Rev. Lett. **107**, 073202 (2011).

[263] T. L. Nicholson, S. Blatt, B. J. Bloom, J. R. Williams, J. W. Thomsen, J. Ye, and P. S. Julienne, "Optical Feshbach resonances: Field-dressed theory and comparison with experiments", Phys. Rev. A **92**, 022709 (2015).

[264] C. Chin, A. J. Kerman, V. Vuletić, and S. Chu, "Sensitive Detection of Cold Cesium Molecules Formed on Feshbach Resonances", Phys. Rev. Lett. **90**, 033201 (2003).

[265] C. A. Regal, C. Ticknor, J. L. Bohn, and D. S. Jin, "Creation of ultracold molecules from a Fermi gas of atoms", Nature **424**, 47 (2003).

[266] E. A. Donley, N. R. Claussen, S. T. Thompson, and C. E. Wieman, "Atom–molecule coherence in a Bose–Einstein condensate", Nature **417**, 529 (2002).

[267] S. B. Papp and C. E. Wieman, "Observation of Heteronuclear Feshbach Molecules from a Rb 85 – Rb 87 Gas", Phys. Rev. Lett. **97**, 180404 (2006).

[268] M. Duda, X.-Y. Chen, A. Schindewolf, R. Bause, J. Von Milczewski, R. Schmidt, I. Bloch, and X.-Y. Luo, "Transition from a polaronic condensate to a degenerate Fermi gas of heteronuclear molecules", Nat. Phys. **19**, 720 (2023).

[269] T. Kinoshita, T. Wenger, and D. S. Weiss, "Local Pair Correlations in One-Dimensional Bose Gases", Phys. Rev. Lett. **95**, 190406 (2005).

[270] E. H. Lieb and W. Liniger, "Exact Analysis of an Interacting Bose Gas. I. The General Solution and the Ground State", Phys. Rev. **130**, 1605 (1963).

[271] E. H. Lieb, "Exact Analysis of an Interacting Bose Gas. II. The Excitation Spectrum", Phys. Rev. **130**, 1616 (1963).

[272] C. N. Yang and C. P. Yang, "Thermodynamics of a One-Dimensional System of Bosons with Repulsive Delta-Function Interaction", J. Math. Phys. **10**, 1115 (1969).

[273] L. Tonks, "The Complete Equation of State of One, Two and Three-Dimensional Gases of Hard Elastic Spheres", Phys. Rev. **50**, 955 (1936).

[274] M. Girardeau, "Relationship between Systems of Impenetrable Bosons and Fermions in One Dimension", J. Math. Phys. **1**, 516 (1960).

[275] E. Haller, R. Hart, M. J. Mark, J. G. Danzl, L. Reichsöllner, M. Gustavsson, M. Dalmonte, G. Pupillo, and H.-C. Nägerl, "Pinning quantum phase transition for a Luttinger liquid of strongly interacting bosons", Nature **466**, 597 (2010).

[276] T. Busch, B.-G. Englert, K. Rzażewski, and M. Wilkens, "Two Cold Atoms in a Harmonic Trap", Found. Phys. **28**, 549 (1998).

[277] T. Stöferle, H. Moritz, K. Günter, M. Köhl, and T. Esslinger, "Molecules of Fermionic Atoms in an Optical Lattice", Phys. Rev. Lett. **96**, 030401 (2006).

[278] N. L. Harshman, "Symmetries of three harmonically trapped particles in one dimension", Phys. Rev. A **86**, 052122 (2012).

[279] M. A. García-March, B. Juliá-Díaz, G. E. Astrakharchik, J. Boronat, and A. Polls, "Distinguishability, degeneracy, and correlations in three harmonically trapped bosons in one dimension", Phys. Rev. A **90**, 063605 (2014).

[280] P. D'Amico and M. Rontani, "Three interacting atoms in a one-dimensional trap: a benchmark system for computational approaches", J. Phys. B: At. Mol. Opt. Phys. **47**, 065303 (2014).

[281] G. Bougas, S. I. Mistakidis, P. Giannakeas, and P. Schmelcher, "Few-body correlations in two-dimensional Bose and Fermi ultracold mixtures", New J. Phys. **23**, 093022 (2021).

[282] E. Tempfli, S. Zöllner, and P. Schmelcher, "Excitations of attractive 1D bosons: binding versus fermionization", New J. Phys. **10**, 103021 (2008).

[283] I. Brouzos and P. Schmelcher, "Construction of Analytical Many-Body Wave Functions for Correlated Bosons in a Harmonic Trap", Phys. Rev. Lett. **108**, 045301 (2012).

[284] L. Budewig, S. I. Mistakidis, and P. Schmelcher, "Quench dynamics of two one-dimensional harmonically trapped bosons bridging attraction and repulsion", Mol. Phys. **117**, 2043 (2019).

[285] I. Brouzos and P. Schmelcher, "Controlled excitation and resonant acceleration of ultracold few-boson systems by driven interactions in a harmonic trap", Phys. Rev. A **85**, 033635 (2012).

[286] R. Schmitz, S. Krönke, L. Cao, and P. Schmelcher, "Quantum breathing dynamics of ultracold bosons in one-dimensional harmonic traps: Unraveling the pathway from few- to many-body systems", Phys. Rev. A **88**, 043601 (2013).

[287] E. Haller, M. Gustavsson, M. J. Mark, J. G. Danzl, R. Hart, G. Pupillo, and H.-C. Nägerl, "Realization of an Excited, Strongly Correlated Quantum Gas Phase", Science **325**, 1224 (2009).

[288] A. Iu. Gudyma, G. E. Astrakharchik, and M. B. Zvonarev, "Reentrant behavior of the breathing-mode-oscillation frequency in a one-dimensional Bose gas", Phys. Rev. A **92**, 021601 (2015).

[289] L. D. Landau, "Über Die Bewegung der Elektronen in Kristallgitter", Phys. Z. Sowjetunion **3**, 644 (1933).

[290] A. S. Alexandrov and J. T. Devreese, *Advances in Polaron Physics*, Vol. 159, Springer Series in Solid-State Sciences (Springer Berlin Heidelberg, Berlin, Heidelberg, 2010), ISBN: 978-3-642-01896-1.

[291] S. I. Mistakidis, A. G. Volosniev, N. T. Zinner, and P. Schmelcher, "Effective approach to impurity dynamics in one-dimensional trapped Bose gases", Phys. Rev. A **100**, 013619 (2019).

[292] M. A. García-March, A. S. Dehkharghani, and N. T. Zinner, “Entanglement of an impurity in a few-body one-dimensional ideal Bose system”, J. Phys. B: At. Mol. Opt. Phys. **49**, 075303 (2016).

[293] S. Peotta, D. Rossini, M. Polini, F. Minardi, and R. Fazio, “Quantum Breathing of an Impurity in a One-Dimensional Bath of Interacting Bosons”, Phys. Rev. Lett. **110**, 015302 (2013).

[294] H. Kiehn, S. I. Mistakidis, G. C. Katsimiga, and P. Schmelcher, “Spontaneous generation of dark-bright and dark-antidark solitons upon quenching a particle-imbalanced bosonic mixture”, Phys. Rev. A **100**, 023613 (2019).

[295] H. B. G. Casimir and D. Polder, “The Influence of Retardation on the London-van der Waals Forces”, Phys. Rev. **73**, 360 (1948).

[296] V. R. Yordanov and F. Isaule, “Mobile impurities interacting with a few one-dimensional lattice bosons”, J. Phys. B: At. Mol. Opt. Phys. **56**, 045301 (2023).

[297] F. Isaule, A. Rojo-Francàs, and B. Juliá-Díaz, “Bound impurities in a one-dimensional Bose lattice gas: Low-energy properties and quench-induced dynamics”, SciPost Phys. Core **7**, 049 (2024).

[298] P. A. M. Dirac, “Note on Exchange Phenomena in the Thomas Atom”, Math. Proc. Camb. Philos. Soc. **26**, 376 (1930).

[299] J. Frenkel, *Wave Mechanics - Advanced General Theory* (Oxford University Press, Oxford, 1934).

[300] A. Raab, “On the Dirac–FrenkelrMcLachlan variational principle”, Chem. Phys. Lett. **319**, 674 (2000).

[301] J. C. Light, I. P. Hamilton, and J. V. Lill, “Generalized discrete variable approximation in quantum mechanics”, J. Chem. Phys. **82**, 1400 (1985).

[302] M. Beck, A. Jäckle, G. A. Worth, and H.-D. Meyer, “The multiconfiguration time-dependent Hartree (MCTDH) method: a highly efficient algorithm for propagating wavepackets”, Phys. Rep. **324**, 1 (2000).

[303] D. T. Colbert and W. H. Miller, “A novel discrete variable representation for quantum mechanical reactive scattering via the S-matrix Kohn method”, J. Chem. Phys. **96**, 1982 (1992).

[304] R. Meyer, “Trigonometric Interpolation Method for One-Dimensional Quantum-Mechanical Problems”, J. Chem. Phys. **52**, 2053 (1970).

[305] C. C. Marston and G. G. Balint-Kurti, “The Fourier grid Hamiltonian method for bound state eigenvalues and eigenfunctions”, J. Chem. Phys. **91**, 3571 (1989).

[306] D. Kosloff and R. Kosloff, “A fourier method solution for the time dependent Schrödinger equation as a tool in molecular dynamics”, J. Comput. Phys. **52**, 35 (1983).

[307] R. Kosloff, “Time-dependent quantum-mechanical methods for molecular dynamics”, J. Phys. Chem. **92**, 2087 (1988).

[308] *LAPACK users’ guide*, 3rd ed, Software, Environments, Tools (Society for industrial and applied mathematics, Philadelphia, 1999), ISBN: 978-0-89871-447-0.

[309] P. Virtanen et al., “SciPy 1.0: fundamental algorithms for scientific computing in Python”, Nat Methods **17**, 261 (2020).

[310] E. Hairer, S. P. Nørsett, and G. Wanner, *Solving Ordinary Differential Equations I: Nonstiff Problems*, 2nd ed., Springer Series in Computational Mathematics (Springer-Verlag, Berlin, Heidelberg, 1993), ISBN: 978-3-540-56670-0.

[311] E. Hairer and G. Wanner, *Solving Ordinary Differential Equations II: Stiff and Differential-Algebraic Problems*, 2nd ed., Springer Series in Computational Mathematics (Springer-Verlag, Berlin, Heidelberg, 1996), ISBN: 978-3-540-60452-5.

[312] D. Raventós, T. Graß, M. Lewenstein, and B. Juliá-Díaz, "Cold bosons in optical lattices: a tutorial for exact diagonalization", J. Phys. B: At. Mol. Opt. Phys. **50**, 113001 (2017).

[313] Z. Idziaszek and T. Calarco, "Two atoms in an anisotropic harmonic trap", Phys. Rev. A **71**, 050701 (2005).

[314] Z. Idziaszek and T. Calarco, "Analytical solutions for the dynamics of two trapped interacting ultracold atoms", Phys. Rev. A **74**, 022712 (2006).

[315] A. McLachlan, "A variational solution of the time-dependent Schrodinger equation", Mol. Phys. **8**, 39 (1964).

[316] H.-D. Meyer, U. Manthe, and L. Cederbaum, "The multi-configurational time-dependent Hartree approach", Chem. Phys. Lett. **165**, 73 (1990).

[317] U. Manthe, H.-D. Meyer, and L. S. Cederbaum, "Wave-packet dynamics within the multiconfiguration Hartree framework: General aspects and application to NOCl", J. Chem. Phys. **97**, 3199 (1992).

[318] A. D. Hammerich, U. Manthe, R. Kosloff, H.-D. Meyer, and L. S. Cederbaum, "Time-dependent photodissociation of methyl iodide with five active modes", J. Chem. Phys. **101**, 5623 (1994).

[319] G. A. Worth, H.-D. Meyer, and L. S. Cederbaum, "The effect of a model environment on the S 2 absorption spectrum of pyrazine: A wave packet study treating all 24 vibrational modes", J. Chem. Phys. **105**, 4412 (1996).

[320] H.-D. Meyer, "Studying molecular quantum dynamics with the multiconfiguration time-dependent Hartree method", WIREs Comput. Mol. Sci. **2**, 351 (2012).

[321] A. U. J. Lode, C. Lévêque, L. B. Madsen, A. I. Streltsov, and O. E. Alon, "*Colloquium*: Multiconfigurational time-dependent Hartree approaches for indistinguishable particles", Rev. Mod. Phys. **92**, 011001 (2020).

[322] J. Zanghellini, M. Kitzler, C. Fabian, T. Brabec, and A. Scrinzi, "An MCTDHF Approach to Multielectron Dynamics in Laser Fields", Laser Phys. **13** (2003).

[323] T. Kato and H. Kono, "Time-dependent multiconfiguration theory for electronic dynamics of molecules in an intense laser field", Chem. Phys. Lett. **392**, 533 (2004).

[324] M. Nest, T. Klamroth, and P. Saalfrank, "The multiconfiguration time-dependent Hartree–Fock method for quantum chemical calculations", J. Chem. Phys. **122**, 124102 (2005).

[325] A. I. Streltsov, O. E. Alon, and L. S. Cederbaum, "Role of Excited States in the Splitting of a Trapped Interacting Bose-Einstein Condensate by a Time-Dependent Barrier", Phys. Rev. Lett. **99**, 030402 (2007).

[326] O. E. Alon, A. I. Streltsov, and L. S. Cederbaum, "Multiconfigurational time-dependent Hartree method for bosons: Many-body dynamics of bosonic systems", Phys. Rev. A **77**, 033613 (2008).

[327] F. Köhler, K. Keiler, S. I. Mistakidis, H.-D. Meyer, and P. Schmelcher, "Dynamical pruning of the non-equilibrium quantum dynamics of trapped ultracold bosons", J. Chem. Phys. **151**, 054108 (2019).

[328] G. C. Katsimiga, S. I. Mistakidis, G. M. Koutentakis, P. G. Kevrekidis, and P. Schmelcher, "Many-body quantum dynamics in the decay of bent dark solitons of Bose–Einstein condensates", New J. Phys. **19**, 123012 (2017).

[329] J. H. V. Nguyen, M. C. Tsatsos, D. Luo, A. U. J. Lode, G. D. Telles, V. S. Bagnato, and R. G. Hulet, "Parametric Excitation of a Bose-Einstein Condensate: From Faraday Waves to Granulation", Phys. Rev. X **9**, 011052 (2019).

[330] V. J. Bolsinger, S. Krönke, and P. Schmelcher, "Beyond mean-field dynamics of ultracold bosonic atoms in higher dimensions: facing the challenges with a multi-configurational approach", J. Phys. B: At. Mol. Opt. Phys. **50**, 034003 (2017).

[331] S. I. Mistakidis, G. M. Koutentakis, F. Grusdt, H. R. Sadeghpour, and P. Schmelcher, "Radiofrequency spectroscopy of one-dimensional trapped Bose polarons: crossover from the adiabatic to the diabatic regime", New J. Phys. **23**, 043051 (2021).

[332] L. P. Pitaevskii, "Vortex lines in an imperfect Bose gas", Sov. Phys. JETP **13**, 451 (1961).

[333] E. P. Gross, "Hydrodynamics of a Superfluid Condensate", J. Math. Phys. **4**, 195 (1963).

[334] A. J. Leggett, "Bose-Einstein condensation in the alkali gases: Some fundamental concepts", Rev. Mod. Phys. **73**, 307 (2001).

[335] R. Kosloff and H. Tal-Ezer, "A direct relaxation method for calculating eigenfunctions and eigenvalues of the schrödinger equation on a grid", Chem. Phys. Lett. **127**, 223 (1986).

[336] H.-D. Meyer and G. A. Worth, "Quantum molecular dynamics: propagating wavepackets and density operators using the multiconfiguration time-dependent Hartree method", Theor. Chem. Acc. **109**, 251 (2003).

[337] H. Wang, "Iterative Calculation of Energy Eigenstates Employing the Multilayer Multiconfiguration Time-Dependent Hartree Theory", J. Phys. Chem. A **118**, 9253 (2014).

[338] H. Wang, "Multilayer Multiconfiguration Time-Dependent Hartree Theory", J. Phys. Chem. A **119**, 7951 (2015).

[339] R. Horodecki, P. Horodecki, M. Horodecki, and K. Horodecki, "Quantum entanglement", Rev. Mod. Phys. **81**, 865 (2009).

[340] J. Eisert, M. Cramer, and M. B. Plenio, "*Colloquium*: Area laws for the entanglement entropy", Rev. Mod. Phys. **82**, 277 (2010).

[341] A. K. Srivastava, G. Müller-Rigat, M. Lewenstein, and G. Rajchel-Mieldzioć, in *New Trends and Platforms for Quantum Technologies*, Vol. 1025, edited by R. Aguado, R. Citro, M. Lewenstein, and M. Stern (Springer Nature Switzerland, Cham, 2024), pp. 225–285, ISBN: 978-3-031-55657-9.

[342] G. Vidal and R. F. Werner, "Computable measure of entanglement", Phys. Rev. A **65**, 032314 (2002).

[343] O. Gühne and G. Tóth, "Entanglement detection", Phys. Rep. **474**, 1 (2009).

[344] M. B. Plenio, "Logarithmic Negativity: A Full Entanglement Monotone That is not Convex", Phys. Rev. Lett. **95**, 090503 (2005).

[345] C. Hörhammer and H. Büttner, "Environment-induced two-mode entanglement in quantum Brownian motion", Phys. Rev. A **77**, 042305 (2008).

[346] O. S. Duarte and A. O. Caldeira, "Effective quantum dynamics of two Brownian particles", Phys. Rev. A **80**, 032110 (2009).

[347] T. Zell, F. Queisser, and R. Klesse, "Distance Dependence of Entanglement Generation via a Bosonic Heat Bath", Phys. Rev. Lett. **102**, 160501 (2009).

[348] K. Shiokawa, "Non-Markovian dynamics, nonlocality, and entanglement in quantum Brownian motion", Phys. Rev. A **79**, 012308 (2009).

[349] C. Charalambous, M. A. Garcia-March, A. Lampo, M. Mehboud, and M. Lewenstein, "Two distinguishable impurities in BEC: squeezing and entanglement of two Bose polarons", SciPost Phys. **6**, 010 (2019).

[350] A. Peres, "Separability criterion for density matrices", Phys. Rev. Lett. **77**, 1413 (1996).

[351] K. Życzkowski, P. Horodecki, A. Sanpera, and M. Lewenstein, "Volume of the set of separable states", Phys. Rev. A **58**, 883 (1998).

[352] D. Braun, "Creation of Entanglement by Interaction with a Common Heat Bath", Phys. Rev. Lett. **89**, 277901 (2002).

[353] K. Sakmann, A. I. Streltsov, O. E. Alon, and L. S. Cederbaum, "Reduced density matrices and coherence of trapped interacting bosons", Phys. Rev. A **78**, 023615 (2008).

[354] M. Bonitz, *Quantum kinetic theory*, Teubner-Texte Zur Physik 33 (Teubner, Stuttgart Leipzig, 1998), 388 pp., ISBN: 978-3-519-00238-3.

[355] S. Krönke and P. Schmelcher, "The BBGKY hierarchy for ultracold bosonic systems", `10.48550/arXiv.1712.00819` (2018), preprint.

[356] S. I. Mistakidis, G. C. Katsimiga, P. G. Kevrekidis, and P. Schmelcher, "Correlation effects in the quench-induced phase separation dynamics of a two species ultracold quantum gas", New J. Phys. **20**, 043052 (2018).

[357] I. A. Englezos, P. Schmelcher, and S. I. Mistakidis, "Particle-imbalanced weakly interacting quantum droplets in one dimension", Phys. Rev. A **110**, 023324 (2024).

[358] S. Hofferberth, I. Lesanovsky, T. Schumm, A. Imambekov, V. Gritsev, E. Demler, and J. Schmiedmayer, "Probing quantum and thermal noise in an interacting many-body system", Nat. Phys. **4**, 489 (2008).

[359] S. S. Hodgman, R. G. Dall, A. G. Manning, K. G. H. Baldwin, and A. G. Truscott, "Direct Measurement of Long-Range Third-Order Coherence in Bose-Einstein Condensates", Science **331**, 1046 (2011).

[360] R. G. Dall, A. G. Manning, S. S. Hodgman, W. RuGway, K. V. Kheruntsyan, and A. G. Truscott, "Ideal n-body correlations with massive particles", Nat. Phys. **9**, 341 (2013).

[361] T. Schweigler, V. Kasper, S. Erne, I. Mazets, B. Rauer, F. Cataldini, T. Langen, T. Gasenzer, J. Berges, and J. Schmiedmayer, "Experimental characterization of a quantum many-body system via higher-order correlations", Nature **545**, 323 (2017).

[362] K. Sakmann and M. Kasevich, "Single-shot simulations of dynamic quantum many-body systems", Nature Phys. **12**, 451 (2016).

[363] R. Yao, S. Chi, M. Wang, R. J. Fletcher, and M. Zwierlein, "Measuring pair correlations in Bose and Fermi gases via atom-resolved microscopy", `10.48550/arXiv.2411.08780` (2024), preprint.

[364] A. Yu. Kitaev, "Fault-tolerant quantum computation by anyons", Ann. Phys. **303**, 2 (2003).

[365] C. Nayak, S. H. Simon, A. Stern, M. Freedman, and S. Das Sarma, "Non-Abelian anyons and topological quantum computation", Rev. Mod. Phys. **80**, 1083 (2008).

[366] T. Keilmann, S. Lanzmich, I. McCulloch, and M. Roncaglia, "Statistically induced phase transitions and anyons in 1D optical lattices", Nat. Commun. **2**, 361 (2011).

[367] M. Bonkhoff, "Advances in Luttinger liquid theory. Applications to lattice anyons and finite spin chains", PhD thesis (Technische Universität Kaiserslautern, Kaiserslautern (Germany), 2022).

[368] L. Yuan, M. Xiao, S. Xu, and S. Fan, "Creating anyons from photons using a nonlinear resonator lattice subject to dynamic modulation", Phys. Rev. A **96**, 043864 (2017).

[369] L. Cardarelli, S. Greschner, and L. Santos, "Engineering interactions and anyon statistics by multicolor lattice-depth modulations", Phys. Rev. A **94**, 023615 (2016).

[370] P. M. Preiss, R. Ma, M. E. Tai, A. Lukin, M. Rispoli, P. Zupancic, Y. Lahini, R. Islam, and M. Greiner, "Strongly correlated quantum walks in optical lattices", Science **347**, 1229 (2015).

[371] M. Pasek and G. Orso, "Induced pairing of fermionic impurities in a one-dimensional strongly correlated Bose gas", Phys. Rev. B **100**, 245419 (2019).

[372] T. Kato, "On the adiabatic theorem of quantum mechanics", J. Phys. Soc. Jpn. **5**, 435 (1950).

[373] K. G. Wilson, "Confinement of quarks", Phys. Rev. D **10**, 2445 (1974).

[374] A. G. Volosniev, H.-W. Hammer, and N. T. Zinner, "Real-time dynamics of an impurity in an ideal Bose gas in a trap", Phys. Rev. A **92**, 023623 (2015).

[375] S. I. Mistakidis, L. Hilbig, and P. Schmelcher, "Correlated quantum dynamics of two quenched fermionic impurities immersed in a Bose-Einstein Condensate", Phys. Rev. A **100**, 023620 (2019).

[376] A. Romero-Ros, G. C. Katsimiga, P. G. Kevrekidis, and P. Schmelcher, "Controlled generation of dark-bright soliton complexes in two-component and spinor Bose-Einstein condensates", Phys. Rev. A **100**, 013626 (2019).

[377] M. Pyzh and P. Schmelcher, "Breathing dynamics of the few-body Bose polaron in a species-selective harmonic trap", Phys. Rev. A **105**, 043304 (2022).

[378] S. I. Mistakidis, G. C. Katsimiga, G. M. Koutentakis, Th. Busch, and P. Schmelcher, "Pump-probe spectroscopy of Bose polarons: Dynamical formation and coherence", Phys. Rev. Research **2**, 033380 (2020).

[379] F. Wilczek and A. Zee, "Appearance of Gauge Structure in Simple Dynamical Systems", Phys. Rev. Lett. **52**, 2111 (1984).

[380] S. Sugawa, F. Salces-Carcoba, Y. Yue, A. Putra, and I. B. Spielman, "Wilson loop and Wilczek-Zee phase from a non-Abelian gauge field", npj Quantum Inf. **7**, 144 (2021).

[381] N. T. Zinner, "Strongly interacting mesoscopic systems of anyons in one dimension", Phys. Rev. A **92**, 063634 (2015).

Acknowledgements

At this point, I would like to thank everyone who has contributed, directly or indirectly, to the completion of my PhD. It has been an exciting journey for me with many joyful moments, but also with the usual challenges that are part of the life as a scientist.

First and foremost, I would like to thank my supervisor, Professor Dr. Peter Schmelcher, who not only gave me the chance to do my Master thesis in his group, but also encouraged me to continue my studies in the framework of a PhD. I am grateful for the excellent scientific environment he provided and the freedom I received to develop and pursue new research ideas. His enthusiasm and dedication towards science inspired me and kept me motivated throughout my PhD.

Furthermore, I thank all the current and former members of the group of Professor Schmelcher, whom I had the pleasure of getting to know , namely, Aditya, Alejandro, André, Anja, Ansgar, Dan, David, Dimitrios, Christian, Fanis, Fabian, Felipe, Felix, Frederic, Gagan, George, Georgios, Henryk, Ilias, Jie, Judith, Kapil, Kevin, Lia, Malte, Mathis, Maxim, Mirko, Nader, Rick, Rohan, Simos, Tomasz, Wieland and Zeki. I will keep fond memories of the very nice scientific and unscientific chats we had during and past the coffee break. Additional thanks goes to Ansgar and Ilias, who shared an office with me for most of the time, and of course Dan, who was always a welcome visitor to our humble workspace. Moreover, I am indebted to André, Dan, Dimitrios, Ilias, Martin and Simos for their careful proofreading of my thesis.

Furthermore, I would like to express my gratitude to Henryk and Mirko, who I had the pleasure of accompanying during their Bachelor and Master thesis, it was really fun! Moreover, I thank my collaborators Dr. Kevin Keiler and Professor Dr. Simos I. Mistakidis, who gave me guidance during my own Master thesis and all our fruitful collaborations. Especially, I would like to thank Simos for all his advice and support! Moreover, I would like to say thank you to Dimitrios Diplaris, Dr. Fabian Brauneis and Professor Dr. Artem Volosniev for their perseverance and the beautiful work on induced interactions. Additional thanks goes to Dr. Martin Bonkhoff, Professor Dr. Nathan L. Harshman and Dr. Thore Posske for introducing me to the exciting world of anyons, and of course for our very nice collaboration!

Finally, this work could not have been done without the endless support from my friends and family. I am indebted in my parents and my brothers, who always stand by my side. Most importantly, I wholeheartedly thank my wife Monicha, who supported me during my entire studies with her endless love and care. Thank you for your patience and your advice whenever I needed it! Finally, I thank my children Jasper and Charlotte, who remind me every day that it is the little things that matter the most.

Eidesstattliche Versicherung / Declaration of oath

Hiermit versichere ich an Eides statt, die vorliegende Dissertationsschrift selbst verfasst und keine anderen als die angegebenen Hilfsmittel und Quellen benutzt zu haben.

Sofern im Zuge der Erstellung der vorliegenden Dissertationsschrift generative Künstliche Intelligenz (gKI) basierte elektronische Hilfsmittel verwendet wurden, versichere ich, dass meine eigene Leistung im Vordergrund stand und dass eine vollständige Dokumentation aller verwendeten Hilfsmittel gemäß der Guten wissenschaftlichen Praxis vorliegt. Ich trage die Verantwortung für eventuell durch die gKI generierte fehlerhafte oder verzerrte Inhalte, fehlerhafte Referenzen, Verstöße gegen das Datenschutz- und Urheberrecht oder Plagiate.

Hamburg, den 14.04.2025

Friethjof Theel

Friethjof Theel